University of Nottingham
UK | CHINA | MALAYSIA

Selective Laser Melting of 18Ni-300 Maraging Steel: Influence of In-Process Parameters and Post-Processing on Microstructure Evolution, Mechanical Properties, and Plastic Strain Localisation

by
Wee King, Law (MEng)

Thesis
Submitted to the University of Nottingham Malaysia
for the degree of
Doctor of Philosophy (PhD)

Department of Mechanical, Materials, and Manufacturing Engineering
October 2025

Abstract

The use of selective laser melting (SLM) to fabricate 18Ni-300 maraging steel components for aerospace and mould making applications has attracted significant interest from both industry and academia. In particular, mould makers have utilised SLM to fabricate steel moulds with integrated conformal cooling channels, which provided enhanced cooling efficiency and reduced injection moulding cycle time compared to their conventional counterparts. However, its widespread application was hindered due to issues such as microstructural heterogeneity, mechanical anisotropy, and manufacturing defects. In the present thesis, the process-microstructure-properties relationships in SLM 18Ni-300 maraging steel were investigated to address these issues and facilitate the fabrication of additively manufactured steel moulds with mechanical properties comparable to their conventionally made counterparts.

An extensive literature review was conducted to understand how SLM process parameters (or in-process parameters) influence microstructure evolution and mechanical properties in SLM 18Ni-300 maraging steel and four other steel mould materials (i.e. H13, P20, AISI 420 stainless steel, and S136). This facilitated a novel comparative analysis of laser-powder interactions, rapid solidification, and intrinsic heat treatment across the five steel mould materials, and addressed the lack of comparative analysis specific to this topic. Complex laser-powder interactions such as the scanning motion of the laser during SLM process resulted in mechanical anisotropy and manufacturing defects, which may be mitigated via statistical process optimisation. Rapid solidification resulted in microstructural heterogeneity (i.e. variations in grain size and crystallographic texture), which was subsequently altered during post-processing heat treatment. Intrinsic heat treatment resulted in in situ precipitation hardening in SLM 18Ni-300 maraging steel and martensite tempering in the other four steel mould materials.

Experimental investigations were conducted to elucidate the process-microstructure-properties relationships in SLM 18Ni-300 maraging steel. Experiments on additively manufactured individual scan tracks and fully built samples revealed that increasing laser power (P), reducing the scanning speed (v), and reducing the hatch spacing (h) resulted in increased laser energy input (E_{linear} and $E_{volumetric}$) and reduced manufacturing defects. Following that, a combined statistical optimisation methodology featuring Taguchi's methods and grey relational analysis (GRA) was implemented to determine optimal SLM in-process parameters for the multi-response optimisation of mechanical properties. Statistical analysis indicated both P and v had an approximately equal influence on the mechanical properties, while the influence of h was less significant. The mechanical properties of samples fabricated using the optimal SLM in-process parameters have high relative density ($\rho_{relative}$ > 99 %) and were comparable with their conventionally made counterparts. Macroscale plastic strain localisation phenomena including propagation of Lüders bands and necking leading to ductile fracture in the fabricated samples were captured using optical imaging-based digital image correlation (optical-DIC).

The influence of microstructural heterogeneity (i.e. variations in grain size and crystallographic texture) on the microscale plastic strain localisation in SLM 18Ni-300 maraging steel was investigated using electron backscatter diffraction (EBSD), in situ uniaxial tensile experiments, and scanning electron microscope-based digital image

correlation (SEM-DIC). Sub-micron sized speckle patterns were created via magnetron sputtering, which facilitated high-resolution strain measurements via SEM-DIC and addressed the lack of established speckle creation methodology for SLM 18Ni-300 maraging steel. Custom MATLAB scripts were employed to digitally align and overlay the EBSD and SEM-DIC datasets. This methodology facilitated a novel grain-to-grain comparison of the microscale plastic strain localisation in relation to the microstructural heterogeneity, provided grain-level insights into the role of internal misorientations on slip activity in individual grains, as well as addressed the lack of SEM-DIC investigations specific to SLM 18Ni-300 maraging steel.

Experimental findings revealed that the microscale plastic strain localisation in SLM 18Ni-300 maraging steel was driven by the interplay between microstructural heterogeneity, Ni-based intermetallics, and the impediment of dislocation motion. The densely distributed equiaxed grains contributed to grain boundary strengthening in the as-built (AB) sample. After post-processing heat treatment, the precipitation of densely distributed Ni-based intermetallics contributed to strain hardening in the solution-aging treatment (SAT) sample. The main deformation mechanism was identified as dislocation slip. Slip preferentially occurred in grains with increased internal misorientation, and intersected regions that exhibited increased kernel average misorientation (KAM). Complex slip behaviour including discrete slip, diffuse slip, and possible cross-slip (or overlapping slip) was identified in the investigated grains of AB and SAT samples. The combined kinematics of the active slip systems were reflected in the in-plane deformation behaviour of the investigated grains. The findings of the present thesis provide fundamental insights into tailoring the microstructure of SLM 18Ni-300 maraging steel for optimised industrial performance.

Finally, potential future research directions for SLM 18Ni-300 maraging steel were suggested, including numerical modelling of microstructure evolution and investigation of microscale plastic strain localisation under complex loading conditions such as multiaxial loading and fatigue.

Publications

Journal papers:

1. **W.K. Law**, K.-C. Wong, H. Wang, Z. Sun, C.S. Lim, Microstructure Evolution in Additively Manufactured Steel Molds: A Review, J. Mater. Eng. Perform. 30 (2021) 6389–6405. https://doi.org/10.1007/s11665-021-05948-1.
2. **W.K. Law**, Z. Wu, C. Song, H. Wang, K.-C. Wong, C.S. Lim, Z. Sun, Optimization of Selective Laser Melting Process Parameters Via Taguchi's Methods and Gray Relational Analysis for 3D Printing of 18Ni-300 Maraging Steel, Steel Res. Int. 94 (2023). https://doi.org/10.1002/srin.202200203.
3. **W.K. Law**, H. Wang, C. Song, K.-C. Wong, C.S. Lim, Z. Sun, Influence of microstructural heterogeneity on the plastic strain localisation in selective laser melted 18Ni-300 maraging steel, Int. J. Plast. (2025) 104400. https://doi.org/10.1016/j.ijplas.2025.104400.

Conference papers:

4. **W.K. Law**, Z. Wu, K.-C. Wong, H. Wang, Z. Sun, C.S. Lim, Investigation of the Influence of Selective Laser Melting Process Parameters on the Microstructure and Mechanical Properties of 18Ni-300 Maraging Steel, Key Eng. Mater. 913 (2022) 259–264. https://doi.org/10.4028/p-2tysi2.
    - Presented at the 8th International Conference on Mechanics, Materials and Manufacturing (ICMMM 2021).
5. **W.K. Law**, H. Wang, C. Song, C.S. Lim, Z. Sun, K.-C. Wong, Influence of Magnetron Sputtering Parameters on Speckle Characteristics for Application in Microscale DIC of Maraging Steel, Mater. Sci. Forum. 1154 (2025) 37–42. https://doi.org/10.4028/p-Ht69Dm.
    - Presented at the 13th International Conference on Engineering and Innovative Materials (ICEIM 2024).

Acknowledgements

My PhD journey has been a long and winding one, spanning almost six years and fraught with challenges. As I reflect on this journey, I am reminded of the challenges I had faced, particularly those related to the availability and usage of experimental equipment, in addition to restrictions on travel and access to research facilities brought about by the COVID-19 lockdowns. Despite these challenges, I continued with my research work, which eventually resulted in the completion of the present thesis. I want to thank the people who have supported me throughout this journey, whose names are mentioned in the following paragraphs.

To begin, I would like to express my gratitude to Prof. Sun Zhenzhong, Dr. Wang Haoliang, and Dr. Song Chenghao from Dongguan University of Technology, Dongguan, China. Prof. Sun, thank you for allowing me to participate in the joint doctoral training program between Dongguan University of Technology and University of Nottingham Malaysia (DGUT-UNM), in addition to giving me the opportunity to study abroad in DGUT and conduct experiments there. Thanks again for your care and concern throughout my stay there. Dr. Wang, thank you for guiding me on the set-up for in situ tensile experiments and digital image correlation (DIC), in addition to giving me the opportunity to obtain invaluable practical experience in conducting experiments and operating the scanning electron microscope (SEM). Thanks again for giving me the chance to hone my skills and improve on previous experimental failures. Dr. Song, thank you for spending the time to discuss experimental plans and data analysis with me, in addition to helping me troubleshoot issues with my experiments. The suggestions you gave were quite helpful in improving the quality of my research work. Following that, I would like to thank Xiao Wu and Xiao Zeng, both Master's students who had helped me with my experiments during the COVID-19 lockdowns. Also, I would like to thank the other Master's students from Prof. Sun's research group who have helped me in various ways during my stay at DGUT. Thanks to Zhenshan, Xiao Su, and Liu Heng for your help.

Next, I would like to express my gratitude to Prof. Lim Chin Seong and Dr. Wong Kok-Cheong from the University of Nottingham Malaysia, Selangor, Malaysia. Thanks to both of you for taking the time to listen to my weekly progress updates and sharing your wisdom with me throughout my PhD journey. Prof. Lim, thank you for reminding me of the important things to focus on, helping me stay on track towards completion. Dr. Wong, thank you for sharing your expertise in academic writing with me. It has greatly improved my writing and helped me to articulate my ideas more clearly. Following that, I would like to thank my fellow PhD students for the time spent together, both in conducting experiments and engaging in recreational activities. Like me, they also faced numerous challenges in their respective PhD journeys, which were further exacerbated by the COVID-19 lockdowns. In particular, I want to thank Tiya, Adriel, and Hock Yee for the numerous discussions we had about our respective research work. Tiya, thank you for spending time with me and discussing our research work together. It has been quite insightful and interesting to hear your perspective during our discussions. Adriel, thank you for spending time with me to talk about our respective research works and for playing badminton together. I do appreciate the companionship that we shared during those challenging times. Hock Yee, thank you for helping me troubleshoot my experiments and for supporting me through some of the most difficult moments in my

PhD journey. You have been an invaluable friend and an awesome badminton partner. I hope we get to play more badminton and chit-chat in the future.

Lastly, I would like to express my heartfelt gratitude to my family, including my sister and my mom. Mom, thank you for your dedication and understanding throughout the years. I will forever be grateful for your unwavering care and support. Following that, I would like to dedicate my thesis in memory of my Dad and my Uncle Wan. Dad, thank you for giving me the chance to pursue this path. I will continue to do my best in the future. Uncle Wan, thank you for your care and support, I am very grateful for it. The end of my PhD journey also signals the beginning of the next phase in my career and in life. Thanks again to everyone who supported me throughout this journey, including those who were not mentioned here. I would also like to thank you, the reader, for taking the time to read until the end. I wish you all the best for the future!

Table of contents

List of figures

List of tables

List of abbreviations

AB	As-built condition (sample condition after fabrication via SLM)
AISI	American Iron and Steel Institute
AM	Additive manufacturing
AMMC(s)	Additively manufactured metal component(s)
ANOVA	Analysis of variance
BCC	Body-centered cubic
CAD	Computer-aided design
CAE	Computer-aided engineering
CCD	Charge-coupled device
CET	Columnar-to-equiaxed transition
CNC	Computer numerical control
CT	Computed tomography
DAT	Direct aging treatment (heat treatment condition)
DED	Directed energy deposition
DIC	Digital image correlation
DOF	Degree of freedom
DTEM	Dynamic transmission electron microscopy
EB-DED	Electron beam directed energy deposition
EBM	Electron beam melting
EB-PBF	Electron beam powder bed fusion
EBSD	Electron backscatter diffraction
EDM	Electrical discharge machining
EOS	Electro Optical Systems GmbH
FCC	Face-centered cubic
FEM	Finite element method
FOV	Field of view
GIA	Grey incidence analysis
GRA	Grey relational analysis
GRC	Grey relational coefficient
GRG	Grey relational grade
HIP	Hot isostatic pressed (heat treatment condition)
HT	Hardened and tempered (heat treatment condition)
IHT	Intrinsic heat treatment
L-DED	Laser-based directed energy deposition
L-PBF	Laser powder bed fusion

MRI	Magnetic resonance imaging
NASA	National Aeronautics and Space Administration
OM	Optical microscopy
PBF	Powder bed fusion
PC	Polycarbonate
PVC	Polyvinyl chloride
ROI	Region of interest
RSM	Response surface methodology
SAR	Synthetic aperture radar
SAT	Solution-aging treatment (heat treatment condition)
SEM	Scanning electron microscope
SEM-DIC	DIC data acquisition via SEM
SLM	Selective laser melting
SNR	Signal-to-noise ratio
SOL	Solution treatment (heat treatment condition)
SR	Stress relief (heat treatment condition)
SSLIP	Slip Systems based Local Identification of Plasticity
TEM	Transmission electron microscope
XRD	X-ray diffraction

Nomenclature

Symbol	Description [units]
Selective laser melting (SLM):	
P	Laser power [W]
v	Scanning speed [$\mathrm{mm\ s^{-1}}$]
h	Hatch spacing between scan tracks [mm]
t_{layer}	Layer thickness [mm]
E_{linear}	Linear energy density [$\mathrm{J\ m^{-1}}$]
$E_{volumetric}$	Volumetric energy density [$\mathrm{J\ mm^{-3}}$]
Surface tension-temperature gradient in the melt pool:	
$T_A, T_B, \text{and } T_C$	Temperatures at locations A, B, and C in the melt pool
$\gamma_A, \gamma_B, \text{and } \gamma_C$	Surface tensions at the corresponding locations
γ_{LV}	Surface tension at the liquid-vapour interface of the melt pool
$\frac{d\gamma_{LV}}{dT}$	Surface tension-temperature gradient in the melt pool
Relative density (according to ISO 3369):	
$\rho_{relative}$	Relative density [%]
m_{air}	Mass of samples when weighed in air [g]
$m_{submerged}$	Mass of displaced liquid when the samples are submerged in water [g]
Mechanical properties (according to ISO 6892-1 and ISO 148):	
R_m	Ultimate tensile strength [MPa]
R_e	Yield strength [MPa]
$R_{p0.2}$	0.2% proof strength [MPa]
E	Modulus of elasticity [GPa]
A_t	Elongation at fracture (or elongation at break), defined as percentage total extension at fracture in ISO 6892-1 [%]
KV_2	Charpy impact energy
Taguchi methods:	
η	Signal-to-noise ratio, SNR [-]
r	Number of readings [-]
y_i	Response obtained from experiments [-]
y_0	Reference response [-]
N	Number of occurrences of that parameter level in Taguchi array [-]
n	Total no. of SLM parameter config. in Taguchi orthogonal array [-]
L	No. of levels for each parameter [-]
S	Sum of squares
V	Variance
Grey relational analysis (GRA):	
γ_{GRC}	Grey relational coefficient, GRC [-]
Γ	Grey relational grade, GRG [-]
x_{ij}	Normalised value for the i-th parameter and j-th response in GRA [-]

y_{ij}	Response obtained from experiments in GRA [-]
Δ_{ij}	Absolute difference between the ideal and actual conditions in GRA [-]
ξ	Distinguishing coefficient in GRA [-]
ω_j	Weightage for the j-th response in GRA [-]

Magnetron sputtering:

$I_{sputter}$	Sputter current [mA]
$t_{sputter}$	Sputter duration [s]
$P_{sputter}$	Chamber pressure during magnetron sputtering [Pa]

Plastic strain localisation:

ε_{vM}	The von Mises surface strain [-]
ε_{eff}	Effective surface strain [-]
ε_{yy}	y-direction (vertical) engineering surface strain [-]
E_{yy}	Lagrange strain tensor in the y-direction (vertical) [-]

Kernel average disorientation (KAM):

$o_{i,j}$	The orientations at pixel position (i, j) obtained from EBSD datasets
$o_{k,l}$	The orientation of the neighbouring pixel position (k, l)
$\omega(o_{i,j}, o_{k,l})$	The misorientation angle between $o_{i,j}$ and $o_{k,l}$
$N(i,j)$	The set of all neighboring pixel positions
$\lvert N(i,j)\rvert$	The number of elements in $N(i,j)$

Scientific constants

Symbol	Description [value and units]
ρ_{MS}	Theoretical full density of 18Ni-300 maraging steel [8.1 g cm^{-3}, from literature]
ρ_{water}	Density of distilled water [0.997 g cm^{-3} at 25 ℃, from ISO 3369]

1. Introduction

1.1. Background and motivation

The advent of metal additive manufacturing (AM) technologies and its rapid development over the last two decades has opened up new possibilities and caused a drastic change in several industries. The metal AM technologies that have garnered significant interest include selective laser melting (SLM), electron beam melting (EBM), and directed energy deposition (DED). The layer-wise build strategy that is characteristic of metal AM technologies has enabled the fabrication of complex geometries with less material wastage as compared to conventional manufacturing technologies (e.g. casting, milling etc.). Attaran [1] reported the advantages of metal AM technologies include accelerating product development cycles by reducing lead times, streamlining supply chains by reducing inventory costs and time to market, in addition to enabling the batch production of highly customised products (i.e. mass customisation).

Aziz et al. [2] conducted a comparative analysis of the applications of SLM, EBM, and DED in fabricating 316L stainless steel engineering components. SLM was identified as well-suited for fabricating precision engineering components with near-full density and high dimensional accuracy, utilising metal powder as the feedstock material. However, its application in the industry was hindered by the presence of porosity and residual stress in the fabricated components. The fabrication of engineering components via EBM resulted in reduced residual stress due to the lower temperature gradient induced by higher processing temperatures. However, its application was limited to electrically conductive materials, as the fabrication process was dependent on electron transfer and required a vacuum chamber to maintain electron beam stability. DED was reported to be particularly suited for component repair and restoration due to its capability for multi-axis material deposition. However, further post-processing was often required to achieve a smooth surface finish. In the present thesis, SLM was selected for sample fabrication due to its capability to fabricate steel moulds with complex geometries and high dimensional accuracy.

Metal AM technologies have garnered significant popularity in various industries including medical, aerospace, automotive, and mould making [3–6]. This is due to its ability to fabricate fully functional engineering prototypes and end-use components with complex geometries. For example, in the aerospace industry, Sogeti High Tech collaborated with Electro Optical Systems (EOS) GmbH to redesign the vertical stabiliser bracket of a commercial aircraft (i.e. Airbus) for part consolidation and reduced weight [7]. The redesigned bracket was fabricated using SLM, and the material used was AlSi10Mg. The redesigned bracket features the consolidation of 30 components into one unified design, in addition to a 30 % weight reduction compared to its conventionally made counterpart. In the mould making industry, Innomia a.s. also collaborated with EOS GmbH to fabricate steel moulds with conformal cooling channels built inside it [8]. SLM was used for the fabrication of the mould, and the material used was 18Ni-300 maraging steel. These conformal cooling channels were designed to enable uniform cooling in the injection moulded component. The application of these additively manufactured steel moulds for polymer injection moulding of automobiles' armrests resulted in a 17 % reduction in injection moulding cycle time. Furthermore, deformation

in the injection moulded component (i.e. armrests) was reduced significantly due to uniform heat dissipation during the cooling process.

In academia, SLM's potential to become a mainstream industrial manufacturing technology has attracted considerable attention from several research communities. Researchers from the industrial manufacturing and materials science communities have exhibited great enthusiasm towards uncovering the underlying physics of the SLM process itself [9–12], in addition to understanding the process-microstructure-properties relationships in components fabricated via SLM [13–15]. By obtaining an in-depth understanding of the underlying physics that govern the SLM process, researchers would be able to construct numerical models for the real-time monitoring of the SLM process and make predictions on the quality of components fabricated by it. In addition, the in-depth understanding of the process-microstructure-properties relationships in components fabricated via SLM is equally important, as it enables researchers to tailor the component's microstructure and mechanical properties for enhanced functionality and reliability.

The 18Ni-300 grade of maraging steel was selected as the material of interest for the present thesis. Maraging steel is a special class of high-strength steel that is strengthened via precipitation of Ni-based intermetallics such as $\mathrm{Ni_3Ti}$ and $\mathrm{Ni_3Mo}$ [16,17]. The term 'maraging' refers to the age hardening of martensite after aging heat treatment. The principal alloying element for maraging steel is nickel (up to 18 wt. %), whereas carbon content is kept as low as possible. Maraging steel is often applied in aerospace and tooling industries due to its superior strength and toughness. In particular, the ultimate tensile strength, elongation at fracture, and hardness of SLM 18Ni-300 maraging steel was reported to be approximately 1943 MPa, 5.6 %, and 53.5 HRC after solution-aging treatment (SAT) [18].

Recently, researchers have explored using SLM to additively manufacture 18Ni-300 maraging steel moulds for polymer injection moulding [19–21]. However, it was reported that the additively manufactured samples contained manufacturing defects such as pores, cracks and incomplete fusion of powder material [22–24]. These manufacturing defects led to reduced relative density in samples and were detrimental to its mechanical performance. Furthermore, microstructural heterogeneity and mechanical anisotropy were identified in SLM 18Ni-300 maraging steel. These variations in microstructure and mechanical properties were identified to be directly influenced by the SLM process parameters (or in-process parameters) used during fabrication [25–27], and was further altered after post-processing heat treatment [28–30]. Following that, SLM 18Ni-300 maraging steel moulds exhibited higher defect content, lower density, and inferior mechanical properties as compared to their conventionally made counterparts. The differences in processing conditions (e.g. rapid solidification, intrinsic heat treatment) also contributed to greater variability in the microstructure and mechanical properties of the additively manufactured steel moulds. Collectively, these issues hinder the widespread application of SLM in the mould making industry. A comprehensive understanding of the process-microstructure-properties relationships in SLM 18Ni-300 maraging steel is essential to fully address these issues. However, knowledge of this subject is yet to be fully elucidated in current literature.

1.2. Research aim and objectives

The main aim of the present research is to establish a comprehensive understanding of the process-microstructure-properties relationships in SLM 18Ni-300 maraging steel. This research topic was chosen due to its potential industrial application in the additive manufacturing of 18Ni-300 maraging steel moulds for polymer injection moulding. Following that, the research objectives for the present research are listed in the following:

1. To conduct a comparative analysis to identify key trends and knowledge gaps regarding the influence of SLM process parameters (or in-process parameters) on microstructure evolution and mechanical properties of SLM 18Ni-300 maraging steel and four other steel mould materials (i.e. H13, P20, AISI 420 stainless steel, and S136).
2. To investigate the influence of SLM in-process parameters on the microstructure and mechanical properties of SLM 18Ni-300 maraging steel.
3. To determine optimal SLM in-process parameters for fabricating 18Ni-300 maraging steel samples with near-full density (i.e. relative density > 99 %) and mechanical properties comparable to their conventionally made counterparts.
4. To investigate the influence of porosity on the macroscale plastic strain localisation and fracture in SLM 18Ni-300 maraging steel subjected to uniaxial tensile loading.
5. To develop a methodology for depositing sub-micron sized speckle patterns on the samples' surface for investigating the microscale plastic strain localisation in SLM 18Ni-300 maraging steel.
6. To investigate the influence of microstructural heterogeneity on the microscale plastic strain localisation in SLM 18Ni-300 maraging steel subjected to uniaxial tensile loading.
7. To identify the main deformation mechanism(s) and active slip or twinning system(s) in SLM 18Ni-300 maraging steel subjected to uniaxial tensile loading.

Research objective no. 1 was devised to establish a common reference point for characterising and comparing the microstructure and mechanical properties of various steel mould materials processed via metal AM technologies. The comparative analysis was conducted via extensive literature review. The interdependence between metal AM process parameters and the mechanical properties of steel mould materials was discussed in terms of their microstructure evolution after solidification processing and after post-processing heat treatment. (**Chapter 2 Section 2.3**)**.**

The experimental investigations in the present thesis were designed taking into account the following considerations. The SLM process is driven by a wide range of in-process parameters, which are generally classified into four categories: laser related, scan related, powder related, and temperature related [31,32]. The SLM parameters investigated in the present thesis include laser power (P), scanning speed (v), and hatch spacing between scan tracks (h). These three SLM in-process parameters were selected due to their direct contribution towards the amount of laser energy transferred to the metal powder during the SLM process, and were determined based on the equation for volumetric energy density ($E_{volumetric}$). The influence of layer thickness (t_{layer}) was not investigated in the present thesis because the inclusion of another parameter would

have significantly increased the time and cost required to conduct additional experimental runs, with the risk that they may not yield additional meaningful results.

Following that, steel moulds for polymer injection moulding are often subjected to compressive, shear, and fatigue loading during operation [33]. These loading conditions arise from the pressure exerted by the injected polymer melt on the mould cavities. Current literature contains comparatively more data regarding the tensile properties of 18Ni-300 maraging steel and comparatively less data on its compressive properties. Thus, the experimental investigations in the present thesis were designed to focus on uniaxial tensile testing, as this allowed for direct comparison with existing literature. Investigations involving more complex loading conditions (e.g. compressive and fatigue loading) are recommended for future work.

Two different experiments were devised for research objective no. 2. The experiments using additively manufactured individual scan tracks were designed to study the effects of SLM parameters in isolation. A total of 6 SLM parameter configurations were studied, and the influence of P and v on the build quality of scan tracks were evaluated (**Chapter 3 Section 3.2**). On the other hand, the experiments using fully built samples were designed to study the combined effect of SLM parameters on their relative density and mechanical properties. A separate set of 6 SLM parameter configurations were studied, and the influence of v and h on the relative density and tensile properties of fully built samples were evaluated (**Chapter 3 Section 3.2**). The investigated tensile properties include ultimate tensile strength (R_m), 0.2% proof strength ($R_{p0.2}$), modulus of elasticity (E), and elongation at fracture (A_t) .

For research objective no. 3, a combined statistical optimisation methodology featuring Taguchi's methods [34] and grey relational analysis (GRA) [35] was implemented to determine the optimal SLM in-process parameters (i.e. combination of $P, v, \mathrm{and}\ h$) for the multi-response optimisation of several mechanical properties. The mechanical properties of interest include ultimate tensile strength (R_m), elongation at fracture (A_t), Vickers hardness, and Charpy impact energy (KV_2). Following that, the interplay between SLM in-process parameters and mechanical properties of SLM 18Ni-300 maraging steel were statistically analysed (**Chapter 3 Section 3.3**).

For research objective no. 4, a best-worst comparison was devised to characterise the influence of porosity. A best-worst comparison provides a clear indication of the variation in porosity (and in extension relative density) between the investigated samples, and how this variation influences macroscale plastic strain localisation in SLM 18Ni-300 maraging steel. The samples from research objective no. 3 (**Chapter 3 Section 3.3**) were used for comparison. Optical imaging-based digital image correlation (optical-DIC) was utilised to quantitatively and qualitatively track the surface deformation of samples in real time and generate strain distribution maps. The macroscale plastic strain localisation and fracture in SLM 18Ni-300 maraging steel were elucidated via strain distribution maps and fractography analysis (**Chapter 3 Section 3.4**).

For research objective no. 5, a new experiment methodology is needed for depositing sub-micron sized speckles on the surface of test samples for investigating the microscale plastic strain localisation in SLM 18Ni-300 maraging steel. Literature reported that magnetron sputtering (a type of physical vapour deposition process) could be utilised to achieve this objective [36]. However, a suitable speckle pattern for the present application is yet to be developed. Following that, experiments were conducted to investigate the influence of magnetron sputtering parameters on speckle

characteristics and determine suitable parameters for depositing sub-micron sized speckle patterns (**Chapter 4 Section 4.2**).

Research objective no. 6 was devised to establish an experimental correlation between the microstructural heterogeneity in SLM 18Ni-300 maraging steel and its microscale plastic strain localisation behaviour. The microstructural heterogeneity (i.e. variations in grain size and crystallographic texture) was characterised via electron backscatter diffraction (EBSD). In situ tensile experiments were conducted inside the scanning electron microscope (SEM), and the surface of test samples was deposited with sub-micron sized speckle pattern via magnetron sputtering using the methodology from research objective no. 5 (**Chapter 4 Section 4.2**). The test samples were fabricated using the optimal SLM in-process parameters identified in research objective no. 3 (**Chapter 3 Section 3.3**). A sequence of images depicting the microscale tensile deformation of test samples was captured via SEM and analysed via DIC, a methodology termed SEM-DIC. The application of SEM-DIC in the present investigation enabled the real-time tracking of the microscale plastic strain localisation at high spatial resolution. (**Chapter 4 Section 4.3**).

Research objective no. 7 was devised to elucidate the main deformation mechanism(s) and active slip or twining system(s) in SLM 18Ni-300 maraging steel. This knowledge is crucial for elucidating the material's plastic deformation behaviour and for predicting failure in engineering components fabricated using said material. To achieve this objective, custom MATLAB scripts [37,38] were used to digitally align and overlay the EBSD and SEM-DIC datasets from research objective no. 6 (**Chapter 4 Section 4.3**). This facilitated the identification of active slip systems in the individual grains of said material (**Chapter 4 Section 4.3**).

The findings of the present thesis have been published in peer-reviewed papers [39–43]. The contents of these publications were adapted to fit the structure of the present thesis. In particular, the discussions in the present thesis were updated to include recent findings in the literature (up to the time of writing), and the presentation of contents was updated to enhance coherence across the thesis chapters.

1.3. Significance and novelty of the present research

The findings of the present research would benefit the industry as well as academia. In the mould making industry, mould makers could utilise the findings for research objectives no. 2, 3, and 4 to additively manufacture 18Ni-300 maraging steel moulds that meet operational and performance expectations in the industry. Furthermore, mould makers could utilise the statistical optimisation methodology for research objective no. 3 (**Chapter 3 Section 3.3**) to determine optimal processing conditions for fabricating other grades of steel moulds via metal AM technologies. In academia, researchers could utilise the research findings presented in the present thesis to tailor the microstructure of additively manufactured 18Ni-300 maraging steel moulds to achieve better mechanical properties or enhanced functionality. In particular, the findings for research objectives no. 1, 6, and 7 could provide useful insights for the numerical prediction of microstructure evolution, plastic strain localisation and active slip systems in SLM 18Ni-300 maraging steel. Besides that, the findings for research objective no. 5 (**Chapter 4 Section 4.2**) could aid in developing sub-micron sized speckle patterns for high-resolution SEM-DIC investigations.

The present research advances the current understanding of SLM 18Ni-300 maraging steel through the following novel contributions:

1. The comparative analysis of the microstructure evolution and mechanical properties of SLM 18Ni-300 maraging steel and four other additively processed steel mould materials (i.e. H13, P20, AISI 420, S136). This topic has been partially addressed in the literature but not specifically in the context considered in the present thesis (**Chapter 2 Section 2.3**). This analysis also provides a novel comparison of how SLM in-process parameters influence the microstructure evolution and mechanical properties of these five additively processed steel mould materials.
2. The application of a combined statistical optimisation methodology (i.e. Taguchi methods and GRA) for the multi-response optimisation of mechanical properties in SLM 18Ni-300 maraging steel. This contribution extends beyond conventional single-response optimisation studies reported in literature by providing a more comprehensive optimisation framework, in addition to enabling the simultaneous optimisation of several mechanical properties (**Chapter 3 Section 3.3**).
3. The adaptation and development of a methodology for depositing sub-micron sized speckle patterns on the surface of test samples, which are essential for high-resolution strain measurements in scanning electron microscope-based digital image correlation (SEM-DIC) investigations of microscale plastic strain localisation in steels. This novel contribution addresses the lack of established speckle creation methodology specific to SLM 18Ni-300 maraging steel (**Chapter 4 Section 4.2**).
4. The in-depth characterisation and analysis of the microscale plastic strain localisation in SLM 18Ni-300 maraging steel in relation to its microstructural heterogeneity using SEM-DIC. This novel contribution elucidates the process-microstructure-properties relationships in said material at sub-micron scale spatial resolution, in addition to extending beyond prior investigations that were focused on other steels (**Chapter 4 Section 4.3**).

5. The identification and analysis of plastic deformation mechanisms and active slip systems in the individual grains of SLM 18Ni-300 maraging steel, including a comparative analysis between SLM as-built and heat-treated conditions. This novel contribution addresses the limited understanding of plastic deformation mechanisms specific to said material, in addition to relating the observed mechanisms to those reported in other steels (**Chapter 4 Section 4.3**).

2. Literature review

2.1. Additive manufacturing (AM) technologies

The emergence of additive manufacturing (AM) technologies has opened up new possibilities for innovation and prompted manufacturers to rethink current manufacturing workflows. The seven categories of AM technologies are illustrated in **Figure 1**. AM technologies differ from conventional manufacturing technologies such as casting and computer numerical control (CNC) machining due to their fabrication method [44]. AM technologies utilise the geometry information provided by 3D computer-aided design (CAD) models to fabricate an object in a layer-wise fashion. On the other hand, casting involves filling a hollow mould of the desired object with molten material, also known as formative manufacturing. CNC machining involves removing excess material to obtain the desired object shape, also known as subtractive manufacturing. The advantages of using AM technologies over conventional manufacturing technologies include reduced material wastage and product development costs, enhanced design freedom and complexity, in addition to accelerated product development cycles. Following that, the advantages and disadvantages of each AM category, its applications, and the materials it could process are summarised by Ahangar et al. [45] and not further discussed in the present section to maintain brevity.

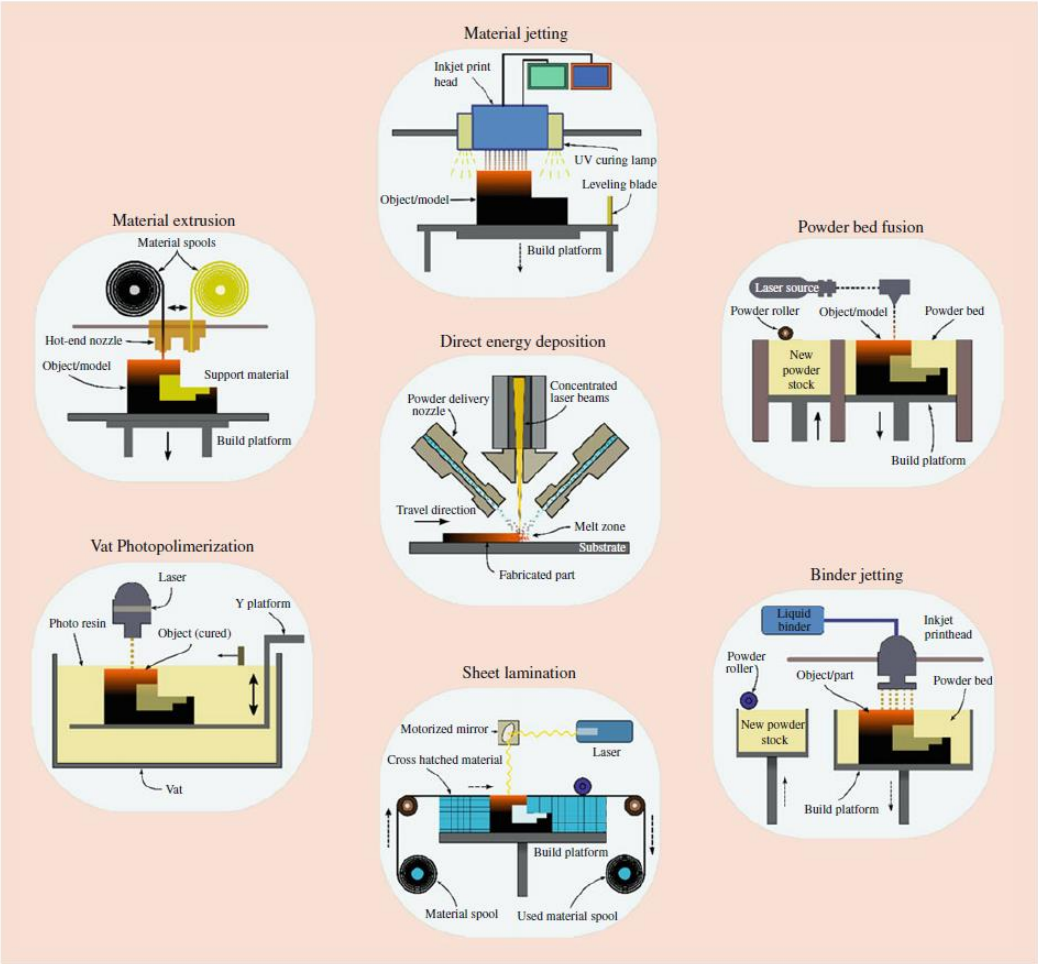

Figure 1: Schematics for the seven categories of AM technologies [44].

Among the seven categories of AM technologies, the directed energy deposition (DED) and powder bed fusion (PBF) categories have been applied for the fabrication of fully functional metal components in various industries, and are collectively referred to as metal AM technologies. DED utilises a heat source such as a laser beam (L-DED) or electron beam (EB-DED) to melt and fuse wire or powder material onto objects, creating a new layer of material on it. The wire or powder material is supplied via a nozzle. The nozzle is able to move in multiple directions, enabling freedom of motion not available in other AM technologies. It has been applied for the fabrication of engineering components that feature high geometric complexity, in addition to the repair of existing components [46].

There are two AM technologies within the PBF category that are able to process metals, namely selective laser melting (SLM) and electron beam melting (EBM). These two processes are commonly defined as laser powder bed fusion (L-PBF) and electron beam powder bed fusion (EB-PBF) in the literature [44]. The terms SLM and EBM are used throughout the present thesis to maintain consistency. The fabrication process begins by spreading metal powder on the build platform with the use of a roller. A heat source will then selectively melt and fuse regions of the powder bed to form a cross-section of the 3D component that is being fabricated. The process is repeated layer-by-layer until the 3D component is fully built. SLM utilises a high-powered laser as the heat source, while EBM utilises an electron beam instead. For SLM, the build chamber needs to be filled with inert gas (e.g. nitrogen) to prevent oxidation during fabrication, while EBM requires a vacuum environment. A review by Aziz et al. [2] highlighted that the fabrication of engineering components via EBM resulted in reduced residual stress compared to those fabricated via SLM. This was attributed to the higher processing temperatures in EBM, which facilitated a slower cooling rate compared to SLM. However, the application of EBM was limited to conductive materials only as the fabrication process was dependent on electron transfer and a vacuum chamber was required to maintain stability in the electron beam.

2.1.1. Implementation of metal AM technologies in various industries

Metal AM technologies, especially SLM have been applied to fabricate fully functional engineering components for use in the medical, aerospace, automotive, and mould making industries [3–6]. Yap et al. [47] reported that SLM is able to process a wide range of metals, and the frequently researched ones include steels, titanium alloys and nickel alloys. A review by Frazier [48] provided a broad perspective on the potential of various metal AM technologies. Also highlighted in the review are the advantages of using metal AM technologies as compared to conventional manufacturing technologies.

The implementation of AM technologies across various industries is shown in **Figure 2**, categorised according to its level of maturity [49]. In particular, the implementation of metal AM technologies in medical and aerospace industries has reached full maturity and is able to handle full-rate production (i.e. large-scale production that meets stringent quality control). This is because the medical and aerospace industries had incorporated metal AM technologies in their value creation process at an earlier stage compared to the other industries. On the other hand, metal AM technologies are gradually becoming mainstream in the automotive industry, and are currently in the low-rate production stage. (i.e. production of small batches for

testing and evaluation). The difference in implementation maturity of metal AM technologies in the automotive industry compared to medical and aerospace industries was due to high implementation costs and an unfavourable cost structure for high production volumes. Furthermore, the design optimisation of automotive components yielded less significant fuel savings compared to similar case studies in the aerospace industry, thus reducing the overall financial incentive for AM implementation in the automotive industry.

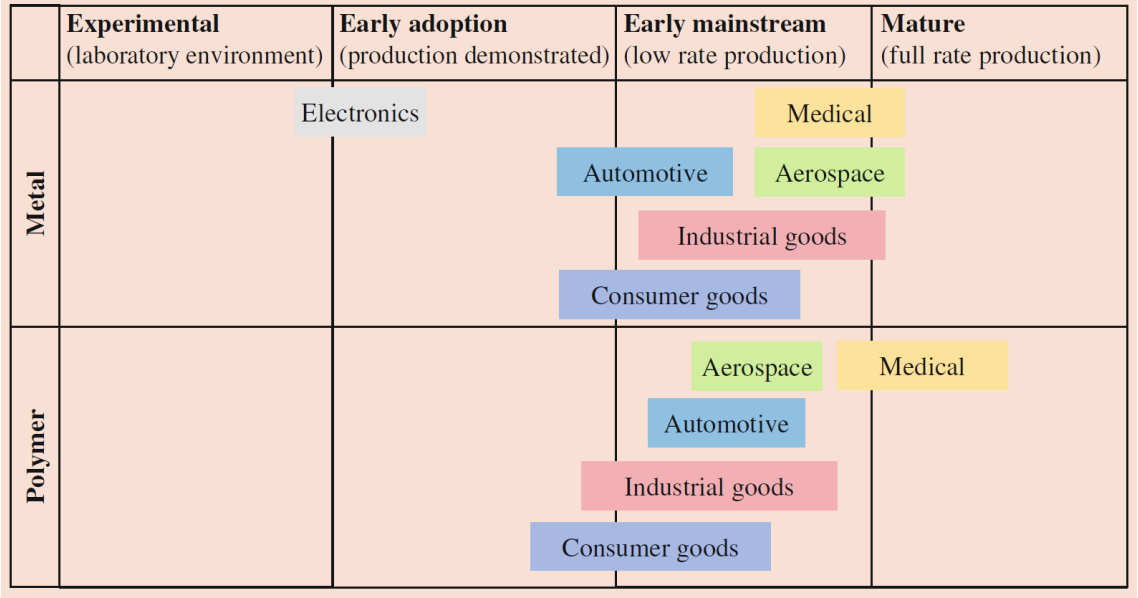

Figure 2: Implementation of AM technologies in various industries [49].

In the medical industry, metal AM technologies were found to be highly compatible for creating custom-made medical applications to suit the needs of individual patients [3]. For example, SLM was utilised to fabricate medical implants such as tibial baseplate and tibial cavity reinforcement for a patient's knee. The implants were made of titanium alloy (Ti-6Al-4V). The implants feature a porous surface for holding it in place and create a functional connection between it and the patient's knee (termed fixation and osseointegration). Besides that, metal AM technologies are able to utilise 3D medical datasets such as those obtained via computed tomography (CT) and magnetic resonance imaging (MRI) as the basis for designing and fabricating physical models for surgery planning and support, educating medical students, as well as for patient briefing [50]. Furthermore, it was reported that metal AM technologies (especially DED) could be applied for the repair of medical tools and instruments [51].

In the aerospace industry, the advantages of using metal AM technologies include functional integration and component consolidation, reduced component weight and aircraft fuel consumption, in addition to streamlining component design and development [4,52]. In terms of application, aerospace firm ArianeGroup has utilised SLM to fabricate an injector head for the Ariane 6 rocket engine [53]. The injector head was made using IN 718 nickel alloy, and features component consolidation by combining 248 elements into 1 additively manufactured component. The use of SLM also resulted in a 50 % reduction in production costs compared to conventional manufacturing routes. Besides that, the National Aeronautics and Space Administration (NASA) had utilised SLM to fabricate a turbopump that delivers liquid hydrogen fuel to rocket engines [54].

The additively manufactured turbopump has 45 % fewer parts compared to its conventionally made counterpart, and is able to deliver 4542 litres (or approx. 1200 gallons) of liquid hydrogen per minute. Other applications of metal AM technologies in the aerospace industry are comprehensively reviewed by Blakey-Milner et al. [4].

The implementation of metal AM technologies in the automotive industry is less mature compared to the medical and aerospace industries due to the following factors: component dimensions are relatively large, the need for high production volumes, and strict cost requirements [49]. Instead, metal AM technologies are currently utilised in the following applications: rapid prototyping for jigs and fixtures, production of personalised end-user components in small batches (i.e. mass customisation), and production of spare parts. Examples of automotive components fabricated via metal AM technologies include camshafts, carburettors and brake callipers [5]. Besides that, metal AM technologies were also applied in the motorsports industry. Rennteam Uni Stuttgart [55] had utilised SLM to additively manufacture a topology-optimised steering stub axle. The additively manufactured component features a 35 % weight reduction and 20 % increased rigidity as compared to its conventionally made counterpart. This resulted in faster lap times and reduced fuel consumption, which propelled their team to become champions of Formula Student Germany 2012.

Recently, metal AM technologies (i.e. DED) have been applied together with subtractive manufacturing technologies (i.e. CNC machining) to fabricate components with complex geometries and good surface finish [46]. This combined manufacturing methodology, termed hybrid manufacturing is illustrated in **Figure 3**. Hybrid manufacturing leverages the capabilities of both manufacturing technologies to implement a more flexible, efficient, and interconnected manufacturing environment. Hybrid manufacturing is known to excel in the following three applications: fabrication of near-net-shape (or fully built) components, repair of damaged components, and the joining of discretised geometry into a single component. For the fabrication of near-net-shape components, DED is used to deposit material on the substrate and create the component. Following that, CNC machining is used to create the desired features and surface finish on the component. Repair of damaged components is done by first removing the damaged portion via CNC machining, followed by deposition of new material on the damaged surface via DED to recreate the damaged features. For joining of discretised geometry, the final component geometry is first discretised into prefabricated blocks and then joined together via DED by depositing material over it.

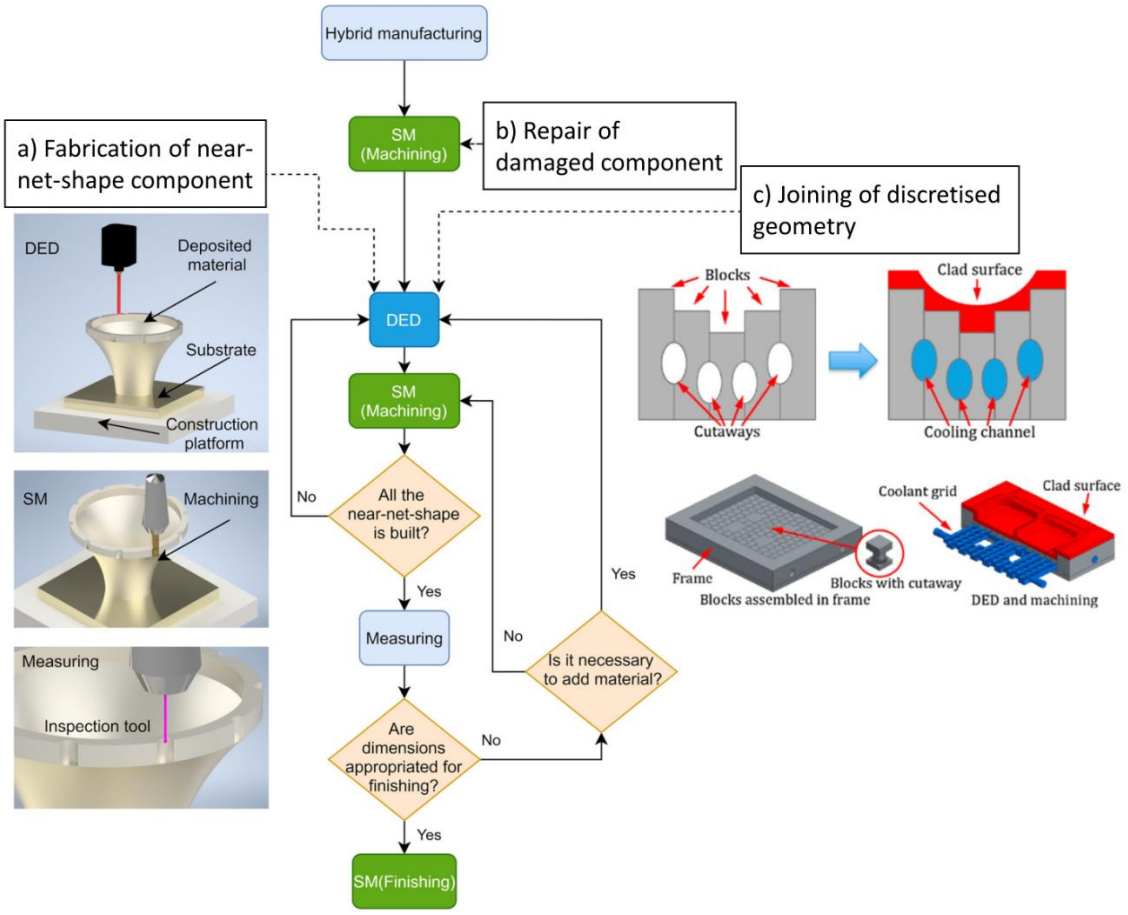

Figure 3: Methodology for hybrid manufacturing [46].

Despite the numerous capabilities that metal AM technologies possess, its processes and the components fabricated by it are required to undergo strict qualification and certification procedures before it could be fully adapted for use in the industry. A review by Chen et al. [56] summarised the main qualification procedures include evaluation of technical requirements and design specifications, review of metal AM materials and processes, in addition to component testing and inspection. The main certification procedures include witness and validation of test samples, verification of compliance to requirements and traceability, as well as documentation of compliance in the form of a certificate.

The present section has discussed the implementation of metal AM technologies in the medical [3], aerospace [4], and automotive industries [5], in addition to highlighting its role in hybrid manufacturing [46] and the need for qualification and certification [56]. The discussion regarding the implementation of metal AM technologies in the mould making industry is presented in **Section 2.2.2**, and is addressed together with the processing of steel mould materials via said technologies.

2.1.2. Issues found in additively manufactured metal components (AMMCs)

Significant heterogeneity in the microstructure and anisotropy in mechanical properties were identified in additively manufactured metal components (AMMCs). In particular, heterogeneity in the microstructure was caused by differences in grain morphologies, crystallographic textures (or grain orientations), phase transformations, solidification conditions, as well as grain coarsening [13,57]. Zhang et al. [57] reported that the microstructure of additively manufactured components exhibited significant differences compared to its conventionally made counterparts due to the rapid solidification and phase transformations that occur during metal AM processes. Kok et al. [13] reported that despite these differences in microstructure, the quasi-static mechanical properties (e.g. tensile strength, hardness) of additively manufactured components were found to be comparable with its conventionally made counterparts. However, subsequent surface machining and post-processing heat treatment are often required to obtain dynamic mechanical properties (e.g. fatigue) that are comparable with its conventionally made counterparts.

The anisotropy in mechanical properties of AMMCs was primarily influenced by microstructural heterogeneity, i.e. differences in grain size, grain morphology, and crystallographic texture. Kok et al. [13] reported that the presence of columnar grains and strong crystallographic texture in AMMCs resulted in direction-dependent deformation behavior due to the directional variation of the microstructure. Anisotropy was also caused by manufacturing defects, laser-powder interactions, and in-process parameters [9,13–15]. The micrographs of manufacturing defects such as pores, incomplete fusion of metal powder, cracks, and balling are shown in **Figure 4**. Zhang et al. [9] reported that the occurrence of manufacturing defects in AMMCs was directly influenced by the in-process parameters of metal AM technologies. In particular, the SLM in-process parameters include: laser power, scanning speed, hatch spacing, layer thickness, scanning pattern and volumetric energy density. The volumetric energy density is an integrated parameter used to indicate the amount of laser energy transferred to the metal powder during the SLM process. Furthermore, Sanaei and Fatemi [15] reported that these manufacturing defects resulted in anisotropy in mechanical properties of AMMCs due to them acting as crack initiation sites and exhibiting high stress concentration during loading.

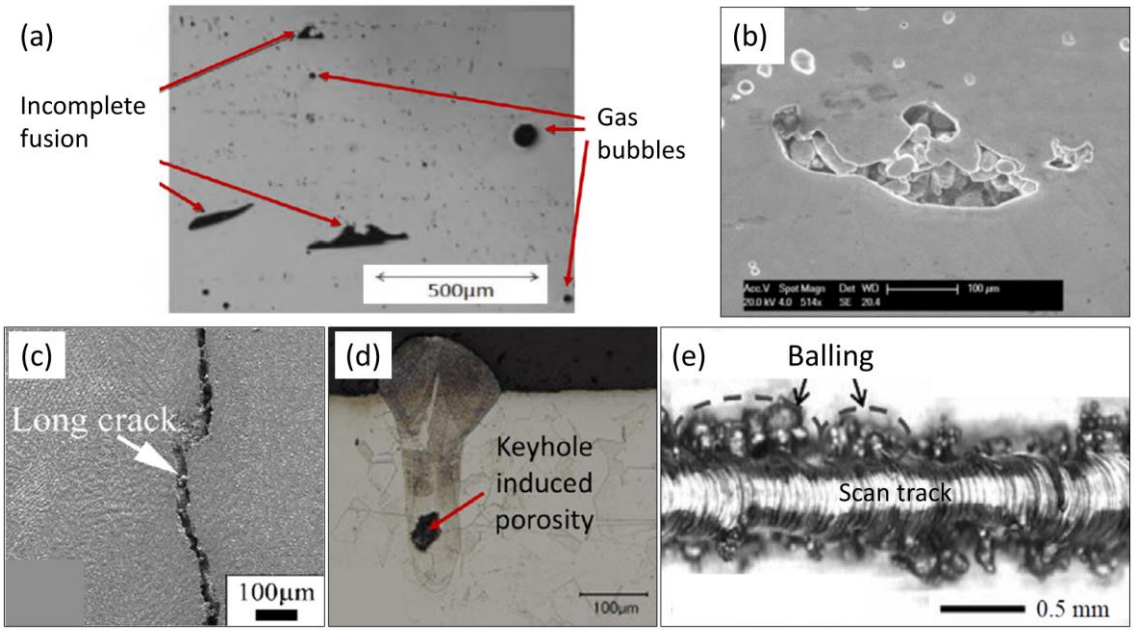

Figure 4: Manufacturing defects in additively manufactured metal components (AMMCs), including (a) porosity due to incomplete fusion of metal powder and trapped gas bubbles, (b) unmelted metal powder due to incomplete fusion, (c) cracks, (d) keyhole geometry together with induced porosity, and (e) balling along the sides of the scan track due to vaporisation of the melt pool [14].

SLM features complex laser-powder interaction phenomena, resulting in the formation of manufacturing defects such as keyhole induced porosity, spatter, balling, as well as residual stress in AMMCs [11,31,58]. Yang et al. [11] reported that keyhole induced porosity was formed due to the excessive laser energy supplied during the SLM process, which not only melted the metal powder but caused it to vaporise (especially metals with lower boiling point). The vaporisation of the melt pool resulted in recoil pressure which pushed the melt pool downwards to form a deep and narrow cavity, resembling a keyhole. Pores formed as a result of gas bubbles being trapped inside the keyhole-shaped melt pool after rapid solidification. Sun et al. [31] reported that vaporisation of the melt pool also resulted in spattering. This led to the expulsion of the melt pool's liquid and the non-melted metal powder due to recoil pressure. Balling was reported to be caused by several factors. The first factor is the capillary instability of the scan track, i.e. the scan track loses its continuity and breaks up into individual droplets at high scanning speeds. The second factor is the hydrodynamic instability driven by the Marangoni effect, i.e. variation in the melt pool's surface tension gradient. The third and the fourth factors are the reduced wettability due to high oxygen content in the atmosphere, as well as the vaporisation of the melt pool. Kruth et al. [58] reported that residual stress in AMMCs was caused by the large temperature gradient between the currently melted layer and the previously solidified layer. This was worsened by the slow heat conduction of the previous layer. Furthermore, the uneven cooling between the layers resulted in distortion, cracks and delamination in AMMCs.

It was identified that the laser-powder interaction phenomena in SLM process shared several similarities with those found in welding [31,59,60]. In particular, the Marangoni effect was identified in the melt pools of additively manufactured and welded samples, which is illustrated in **Figure 5**. The temperature at locations A, B, and

C in the melt pool are denoted as $T_A, T_B, \text{and } T_C$. The surface tension at the corresponding locations are denoted as $\gamma_A, \gamma_B, \text{and } \gamma_C$. The surface tension at the liquid-vapour interface of the melt pool is denoted as γ_{LV}. The surface tension-temperature gradient in the melt pool is denoted as $\frac{d\gamma_{LV}}{dT}$. Mills et al. [60] reported that the $\frac{\mathrm{d}\gamma_{LV}}{\mathrm{d}T}$ in the melt pool was influenced by the oxygen and sulphur content in it. Melt pools of steels with oxygen and sulphur content larger than 60 ppm would exhibit a positive gradient $\left(\frac{\mathrm{d}\gamma_{LV}}{\mathrm{d}T} > 0\right)$, resulting in a radially inward flow and a deeper and narrower melt pool (**Figure 5**(a)). In contrast, melt pools with radially outward flows exhibit a negative gradient $\left(\frac{\mathrm{d}\gamma_{LV}}{\mathrm{d}T} < 0\right)$, and the resultant melt pool was less deep and more wider in shape (**Figure 5**(b)). Melt pools with radially outward flows have more gas bubbles trapped within it due to reduced weld penetration, resulting in increased porosity after the melt pool has solidified.

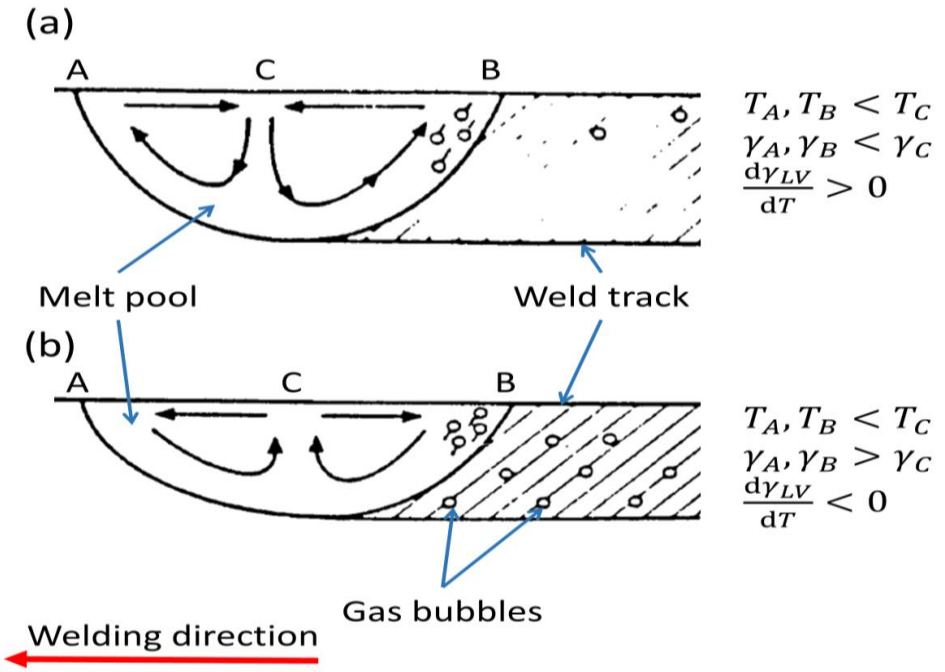

Figure 5: Marangoni effect in the melt pool of a weld due to variations in localised temperature and surface tension, where (a) shows positive and (b) shows negative surface tension-temperature gradient $\frac{d\gamma_{LV}}{dT}$ [60].

The influence of SLM in-process parameters on the build quality of AMMCs is illustrated in **Figure 6**. The four main SLM parameters that contribute towards the build quality include laser power, scanning speed, hatch spacing, and layer thickness. Bai et al. [61] reported that the use of high scanning speed and low laser power led to reduced energy being supplied to the metal powder during fabrication (i.e. low energy density), and resulted in balling (**Figure 6**(a)). The use of larger hatch spacing and layer thickness was reported to be detrimental to the build quality due to the reduced overlap between scan tracks, as well as reduced wetting area between melt pool and substrate (**Figure 6**(b and c)). Furthermore, the presence of manufacturing defects led to reduced relative density in AMMCs as compared to its conventionally made counterparts.

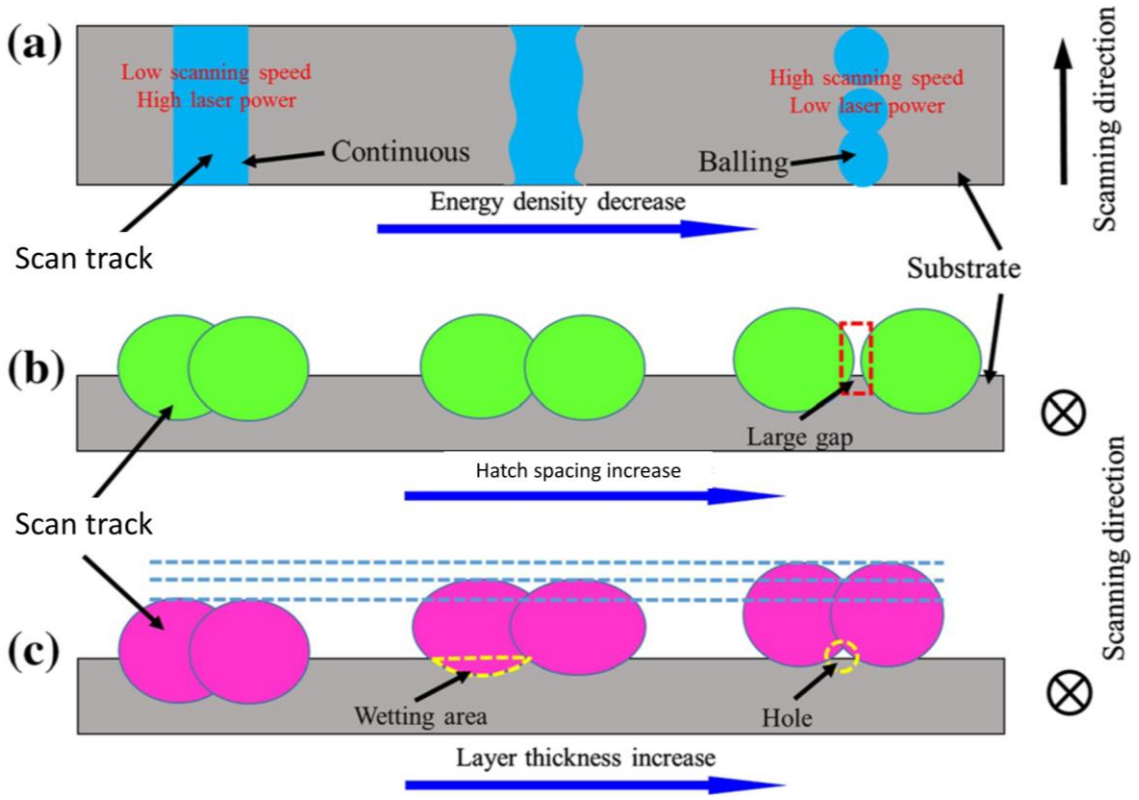

Figure 6: Influence of SLM process parameters (or in-process parameters) on the build quality of AMMCs when the (a) energy density, (b) hatch spacing, and (c) layer thickness are varied [61].

2.1.3. Statistical optimisation of metal AM processes

It was reported in literature that the occurrence of manufacturing defects in AMMCs could be minimised via statistical optimisation, but may not be fully eliminated [9,15]. Statistical optimisation of metal AM processes (e.g. SLM) often involves the design of experiments, in which the individual in-process parameters are systematically varied to evaluate their impact on the mechanical properties of AMMCs. The SLM process is driven by a wide range of in-process parameters, which were classified into four categories: laser related, scan related, powder related, and temperature related [31,32]. A conventional full factorial design of experiments is often impractical for optimising the SLM process, as the number of required experimental runs increases exponentially with the number of process parameters, leading to an inefficient use of resources. Furthermore, the interpretation of the experimental data can be challenging due to the large number of in-process parameters and the lack of clear analysis guidelines.

Following that, the Taguchi methods was conceptualised as a standardised design methodology for researchers and industrial practitioners interested in statistical optimisation of metal AM processes. The methodology offered a more efficient alternative to full factorial design of experiments for evaluating process parameters and obtaining statistically meaningful results with significantly fewer experimental runs [34]. This was achieved via the use of orthogonal arrays to plan experimental runs, followed by the conversion of experimental results to signal-to-noise ratios (SNRs) and analysing them via analysis of variance (ANOVA) to identify the most significant process parameter affecting the experimental results.

Other statistical optimisation methods of note include response surface methodology (RSM) and grey relational analysis (GRA). RSM may be used to quantify the influences of multiple process parameters on the response variable (or objective) to be optimised by fitting polynomial equations to model the relationship between them [62]. The experimental results may then be illustrated graphically via contour maps. In GRA, a grey relational coefficient is assigned to each experimental run to quantify its closeness to the desired response [35]. A grey relational grade is then calculated for each experimental run, with the highest grade indicating the most suitable combination of process parameters for achieving the desired response. It should be noted that GRA can be used for the simultaneous optimisation of several response variables (or multi-response optimisation), while RSM and Taguchi methods are limited to the optimisation of a single response variable (or single-response optimisation).

Recently, researchers have utilised statistical optimisation methods to determine optimal SLM process parameters (or in-process parameters) for fabricating 18Ni-300 maraging steel components with reduced manufacturing defects [28,63,64]. It should be noted that the investigations cited here are not exhaustive. Mutua et al. [28] utilised two full factorial design of experiments to investigate the influence of SLM parameters. The SLM parameters of interest include laser power (P), scanning speed (v), hatch spacing between scan tracks (h), volumetric energy density ($E_{volumtric}$), and overlap rate between scan tracks. The responses to be optimised include relative density ($\rho_{relative}$), surface roughness, and hardness of the fabricated samples. The layer thickness (t_{layer}) was fixed at 0.05 mm. The optimal SLM in-process parameters were identified as $P = 300\ \mathrm{W}, v = 700\ \mathrm{mm\ s^{-1}}, h = 0.12\ \mathrm{mm}, E_{volumtric} = 71.43\ \mathrm{J\ mm^{-3}}$, and a scan track overlap rate of 40 %. A $\rho_{relative}$ of 99.8 %, an average surface roughness

of $35\ \mu m$, and a hardness of 366.5 ± 36.5 HV (or 330–403 HV) was reported for the samples fabricated via the stated SLM parameter configuration. Furthermore, the ultimate tensile strength (R_m) and elongation at fracture (A_t) of the samples were reported as 1125 MPa and 10.38 %, respectively.

Ferreira et. al. [63] utilised RSM and ANOVA to statistically determine optimal SLM process parameters. The influence of P, v, and h on the $\rho_{relative}$ and hardness of samples were statistically analysed. It was concluded that the optimal SLM in-process parameters (combination of P, v, and h) for 3D printing samples with high $\rho_{relative}$ differed from those used to obtain high hardness. In particular, the optimal SLM in-process parameters for obtaining high $\rho_{relative}$ include: $P = 275.0\ W, v = 923.1\ mm\ s^{-1}, h = 0.110\ mm$. On the other hand, the optimal SLM in-process parameters for obtaining high hardness include: $P = 337.5\ W, v = 1333.3\ mm\ s^{-1}, h = 0.095\ mm$. It was reported that samples fabricated using the set of SLM in-process parameters optimised for high $\rho_{relative}$ achieved a $\rho_{relative}$ of 99.99 % and a hardness of 350 HV. A similar study was also conducted by Mao et al. [64], who reported their optimal SLM in-process parameters as $P = 283.86\ W, v = 867.5\ mm\ s^{-1}, and\ h = 0.081\ mm$. The t_{layer} was reported at 0.05 mm. The achieved $\rho_{relative}$ was reported as 99.45 %, and the R_m and A_t were reported as 1245 ± 3 MPa and 10.5 ± 0.5 %, respectively.

Following that, it was identified that the cited investigations [28,63,64] were focused on the optimisation of a single response variable, i.e. each response variable was optimised individually (i.e. single-response optimisation). To the best of the author's knowledge and at the time of writing, investigations that focused on the simultaneous optimisation of several response variables (or multi-response optimisation) for fabricating 18Ni-300 maraging steel components via SLM is yet to be reported in the literature.

2.2. Steel mould materials

The discussion in the present section is focused on the following five steel mould materials (also known as mould steels in the industry): H13, P20, AISI 420 stainless steel, S136, and 18Ni-300 maraging steel. The term AISI is used to represent the American Iron and Steel Institute, and the naming of H13, P20, 420, and S136 follows the AISI classification system for tool steels. These five grades of steel mould materials were systematically discussed in the present section due to the presence of considerable research in academia and reports of its application in the industry [6,65–67]. It should be noted that the grades of steel mould materials discussed in the present section are not exhaustive, as there are other grades available depending on its application [68,69]. The chemical composition of the five steel mould materials is summarised in **Table 1**.

Table 1: Chemical composition of steel mould materials.

Steel Mould Material	Chemical Composition [wt.%]													
	C	Cr	Ni	Mn	Mo	Si	V	Cu	Co	Ti	Al	P	S	Fe
H13 [70]	0.45	5.36	–	0.43	1.62	0.94	1.10	–	–	–	–	–	–	Bal.
P20 [71]	0.40	1.95	–	0.83	0.33	0.45	–	0.02	–	–	–	–	–	Bal.
AISI 420 stainless steel [72]	0.30	12.80	–	0.72	–	0.79	–	–	–	–	–	0.012	0.008	Bal.
S136 [73]	0.29	13.55	–	0.98	–	0.96	0.4	–	–	–	–	0.010	–	Bal.
18-Ni 300 maraging steel [28]	0.02	0.20	18.50	0.08	5.20	0.01	–	–	9.00	0.62	0.07	0.020	–	Bal.

In the present section, the steel mould materials were categorised according to their precipitate strengthening elements. 18Ni-300 maraging steel has high Ni content of up to 18 wt. %, and is precipitate strengthened via Ni-based intermetallics [16,17]. The other four steel mould materials are precipitate strengthened via carbides [68,69]. The steel mould materials strengthened via carbide precipitation were further categorised into two subgroups. The first subgroup consists of conventional steel mould materials, which are H13 and P20. The second subgroup consists of steel mould materials with improved corrosion resistance, which are AISI 420 stainless steel and S136. H13 and P20 are classified as conventional steel mould materials due to their extensive use in the mould making industry. H13 is a type of hot work tool steel that is able to withstand thermal stresses at elevated temperatures while maintaining dimensional accuracy of the moulded product. P20 is a type of low carbon tool steel commonly used in mould making, with characteristics such as good machinability and ease of repair via welding. AISI 420 stainless steel and its equivalent grade, S136 both possess improved corrosion resistance due to its high Cr content of up to 13.5 wt. %. It is suitable for injection moulding of polymer products that require mirror surface finish, and is able to process polymers such as polycarbonate (PC) and polyvinyl chloride (PVC) [74]. The categorisation of steel mould materials introduced in the present section is applied in **Section 2.3** when discussing their microstructure evolution during metal AM processing and subsequent heat treatment.

Steel mould materials are usually chosen based on their achievable mechanical properties and intended application. In terms of mechanical properties, steel moulds are required to have high tensile strength ranging between 1500 to 2000 MPa after post-processing heat treatment [68,69]. This enables the mould to withstand the thermal and mechanical stresses induced during injection moulding. Moulds are also required to have high surface hardness, ranging between 50 to 54 HRC after post-processing heat treatment. This property is especially important for the production of transparent polymer products, as well as polymer products that require mirror surface finish. This is because any defect on the mould surface is directly replicated on the polymer product itself. **Table 2** provides a comparison of the mechanical properties of steel mould materials, categorised according to its processing condition. The modulus of elasticity is denoted by E, the 0.2% proof strength is $R_{p0.2}$, the yield strength is R_e, the ultimate tensile strength is R_m, and the elongation at fracture is A_{t}.

In terms of microstructure, a homogeneous microstructure is desirable for steel moulds as it leads to isotropic mechanical properties. A homogeneous microstructure also means that there are less non-metallic inclusions (e.g. sulphides and oxides) in the microstructure, leading to improved microcleanliness and better polishability [68,69] In conventional mould making, electroslag remelting was utilised to obtain a more homogeneous microstructure in moulds [75].

Steel mould materials are used for the fabrication of moulds for polymer injection moulding. Injection moulding is commonly known as one of the main manufacturing processes for mass production of polymer products. The geometry, contour and even the surface finish of polymer products are directly replicated from the mould itself. Injection moulded polymer products have a widespread application across various industries including automotive, medical, and electronics [76].

Table 2: A comparison for the mechanical properties of steel mould materials processed via conventional and metal AM technologies.

Steel Mould Material	Manufacturing Process	Condition	E [GPa]	$R_{p0.2}$ [MPa]	R_e [MPa]	R_m [MPa]	A_t [%]	Hardness [HRC]
H13	Conventional [77,78]	Heat-treated	210	–	1596	1930	12.0	50 (505 HV)
	SLM [78,79]	As-built	194	–	1073	1965	3.7	59 (667 HV)
		Stress relieved (SR), hot isostatic pressed (HIP), hardened and double tempered (HT) (HT: 1020 ℃ for 1.25 h , then 585 ℃ for 3 h)	191	–	1502	1743	6.6	54 (562 HV)
P20	Conventional [80]	Forged, hardened, and tempered	205	–	896	1030	15.0	32 (320 HV)
	SLM [71]	As-built	–	–	–	–	–	45–48 (440–480 HV)
		Tempered (550 ℃ / 2 h)	–	–	–	–	–	32–34 (320–340 HV)
AISI 420 stainless steel	Conventional [74]	Pre-hardened	214.5	890	–	1100	9.0	32 HRC
		Heat-treated	–	1540	–	1940	15.0	53 HRC
	SLM [72]	As-built	190	700	–	1050	2.5	55 HRC
		Tempered (315 ℃ / 2 h)	195	950	–	1520	6.3	53 HRC
S136	Conventional [73]	Casted	–	–	–	–	–	41 HRC
	SLM [81,82]	As-built (chemical composition #2, horizontal orientation)	–	–	–	1184.2	9.2	50 HRC
		As-built (chemical composition #2, vertical orientation)	–	–	–	1467.9	11.1	49 HRC
		Austenitised (1050 ℃ / 1 h)	–	–	–	–	–	54 HRC
18-Ni 300 maraging steel	Conventional [83]	Wrought	180	760–895	–	1000–1170	6.0 – 15.0	35 HRC
		Wrought and aged	190	1910–2020	–	1951–2041	11.0	54 HRC
	SLM [84]	As-built	–	–	915	1165	12.4	35–36 HRC
		Solution-aging treatment (SAT) (840 ℃ / 1 h, then 490 ℃ / 6 h)	–	–	1882	1943	5.6	52–54 HRC

Researchers have explored using metal AM technologies to fabricate steel moulds [19–21]. SLM is the most frequently used metal AM technology for said purpose. It was identified in literature that the use of optimised process parameters resulted in the fabrication of steel moulds with high relative density and reduced manufacturing defects (e.g. pores) [28,63,64]. **Table 3** provides a comparison of the maximum relative density of additively manufactured steel mould materials, tabulated according to the respective material and the optimised process parameters used during fabrication. The relative density is denoted as $\rho_{relative}$, the volumetric energy density is $E_{volumetric}$, the laser power is P, the scanning speed is v, the hatch spacing between scan tracks is h, and the layer thickness is t_{layer}.

Table 3: A comparison for the maximum relative density of additively manufactured steel mould materials and the corresponding optimised SLM process parameters (or in-process parameters) used to fabricate it.

Steel Mould Material	$\rho_{relative}$ [%]	$E_{volumetric}$ [J mm^{-3}]	Optimised Process Parameters			
			P [W]	v [mm s^{-1}]	h [mm]	t_{layer} [mm]
H13 [85]	99.20	106.25	170	400	0.10	0.04
P20 [71]	98.30	190.48	160	350	0.08	0.03
AISI 420 stainless steel [86]	99.95	159.09	140	550	0.08	0.02
S136 [73]	98.90	58.33	280	800	0.12	0.05
18-Ni 300 maraging steel [28]	99.80	71.43	300	700	0.12	0.05

2.2.1. Material of interest: 18Ni-300 maraging steel

Maraging steels are a special class of high-strength steels that are strengthened via precipitation hardening of Ni-based intermetallics [16,17]. Its main alloying element is nickel, while carbon is treated as an impurity element and is kept as low as commercially feasible. The term 'maraging' denotes the age hardening of martensite, and its low carbon content confers it a unique mix of improved hardenability, formability, strength, and toughness compared to other steels that are precipitation hardened via carbides. The 18Ni-300 grade of maraging steel has high nickel content (up to 18 wt. %), has been commercially optimised to provide specific strength levels (i.e. 2068 MPa or 300 ksi), and has applications in the aerospace and mould making industries.

Shown in **Figure 7** are the metastable and equilibrium phase diagrams for the iron-nickel binary system, where maraging steels are a part of [17]. **Figure 7**(a) shows the range of austenite reversion temperature and martensite formation temperature upon heating and cooling of the material. In **Figure 7**(b), the equilibrium phases for maraging steels with higher nickel content include austenite (γ) and ferrite (α). Martensite phase (α') is not included in **Figure 7**(b) as it is not an equilibrium phase and instead forms via rapid cooling. Following that, maraging steels are usually fully martensitic at room temperature because no other phase transformations were identified to occur during cooling. The range of temperature for martensite formation in maraging steels is usually between 200 ℃ to 300 ℃, and varies depending on nickel content (**Figure 7**(a)). The martensite phase in maraging steels has a body-centered cubic (BCC) crystal structure, a lath morphology, contains high dislocation density but no twinning. Besides that, retained austenite was identified to form in the heat-affected zones of welded maraging steel components due to non-uniform cooling.

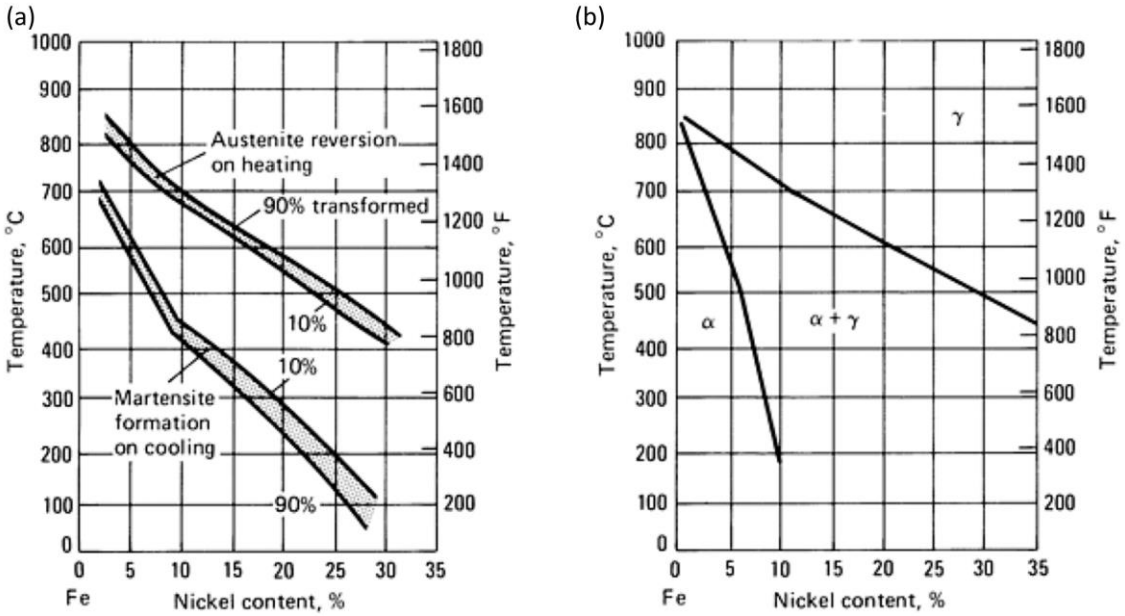

Figure 7: The (a) metastable and (b) equilibrium phase diagrams for the iron-nickel binary system [17].

Age hardening heat treatment of maraging steels is often conducted at temperatures ranging between 455 ℃ to 510 ℃ and durations ranging between 3 h to 9 h as it facilitates the precipitation of Ni-based intermetallics such as $\mathrm{Ni_3Ti}$ and $\mathrm{Ni_3Mo}$ [17]. Precipitation preferably occurs at dislocations within the material, and $\mathrm{Ni_3Mo}$ was identified to form first due to its better lattice fit with the martensite matrix. Prolonged age hardening at temperatures above 510 ℃ would result in austenite reversion and the formation of $\mathrm{Fe_2Mo}$ precipitates, which reduces the strength and hardness of the material.

Recently, researchers have conducted investigations on the microstructure and mechanical properties of 18Ni-300 maraging steel samples processed via metal AM technologies. Mutua et al. [28] investigated the influence of varying SLM process parameters (or in-process parameters) on the build quality of 18Ni-300 maraging steel samples, and devised a process map as shown in **Figure 8**. It was identified that the combined use of high laser power (P) and low scanning speed (v) resulted in burnt surfaces and shrinkage in the additively manufactured samples due to the excessive energy supplied during fabrication (**Figure 8**, Region VI). In contrast, the combined use of low P and high v resulted in incomplete fusion of powder material and balling in the samples due to insufficient energy supplied during fabrication (**Figure 8**, Region II). Following that, an optimal processing window which enabled the fabrication of samples with reduced manufacturing defects and good mechanical properties was identified (**Figure 8**, Region IV). The optimal SLM in-process parameters was identified as $P = 300\ \mathrm{W}, v = 700\ \mathrm{mm\ s^{-1}},\ h = 0.12\ mm, E_{volumtric} = 71.43\ \mathrm{J\ mm^{-3}}$, and a scan track overlap rate of 40 %. The layer thickness (t_{layer}) was reported as 0.05 mm. The samples fabricated via this set of process parameters have a relative density of 99.8 % and an average surface roughness of $35\ \mu\mathrm{m}$. The ultimate tensile strength, elongation at fracture, and hardness for the as-built samples were 1125 MPa, 10.38 %, and 330–403 HV respectively, and consisted of mainly martensite phase with traces of austenite. After solution-aging treatment (SAT, i.e. $820\ ℃\ \mathrm{for\ 1h, then}\ 460\ ℃\ \mathrm{for\ 5\ h}$), the ultimate tensile strength and hardness of samples had increased to 2033 MPa and 618 HV, while its elongation at fracture had decreased to 5.27 %.

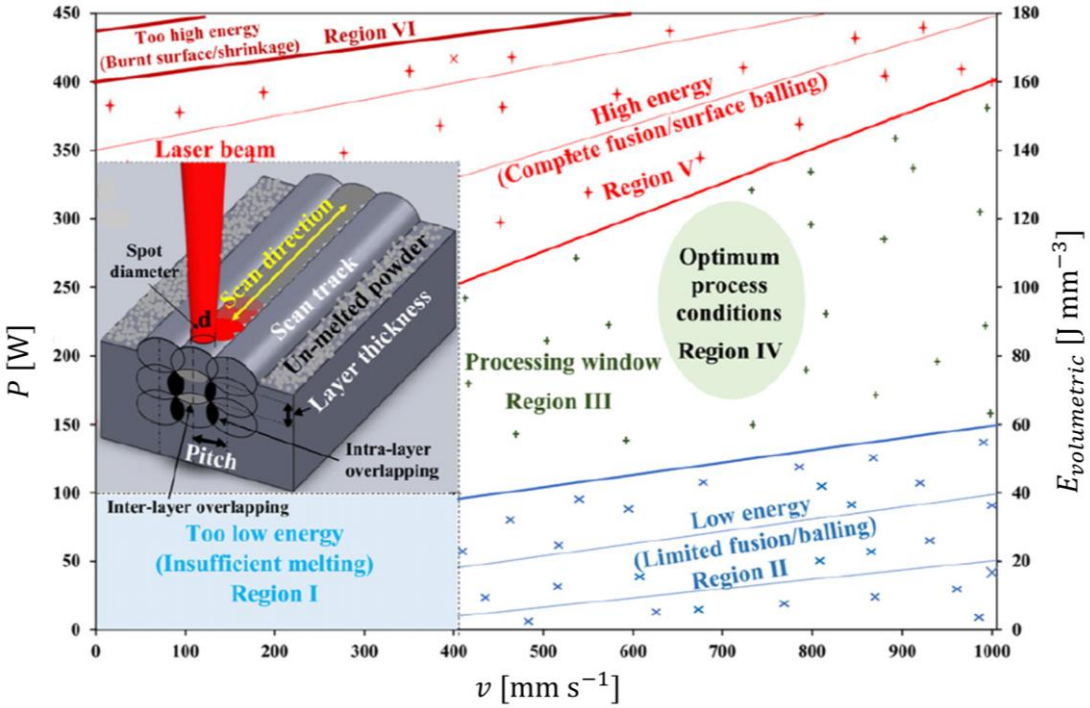

Figure 8: Process map for fabricating 18Ni-300 maraging steel samples via SLM [28].

Researchers also reported that SLM 18Ni-300 maraging steel test samples exhibited a heterogeneous microstructure and anisotropic mechanical properties [25,26,61]. Yao et al. [26] reported that the microstructure of as-built SLM 18Ni-300 maraging steel samples has a mix of equiaxed and columnar morphologies, and the grain orientations were random and do not exhibit a particular directionality (i.e. weak grain texture). It was also reported that its mechanical properties varied depending on the samples' build orientation. In particular, vertically built samples (i.e. 90 ° from horizontal) have an ultimate tensile strength, elongation at fracture, and hardness of 1038 MPa, 10.0 %, and 349 HV, respectively. On the other hand, the horizontally built samples (i.e. 0 ° from horizontal) recorded 1123 MPa, 12.0 %, and 398 HV, respectively. In addition, its mechanical properties were comparable with conventionally made samples (i.e. 981 MPa, 10 %, 382 HV). Bai et al. [61] identified that horizontally built samples have better tensile strength due to the difference in angle between the scan tracks and the samples' loading direction (**Figure 9**(a and b)). Bhardwaj and Shukla [25] identified that samples fabricated using an orthogonal scanning strategy (i.e. 90 ° rotation between subsequent build layers) have better tensile strength and reduced porosity due to better fusion between the scan tracks.

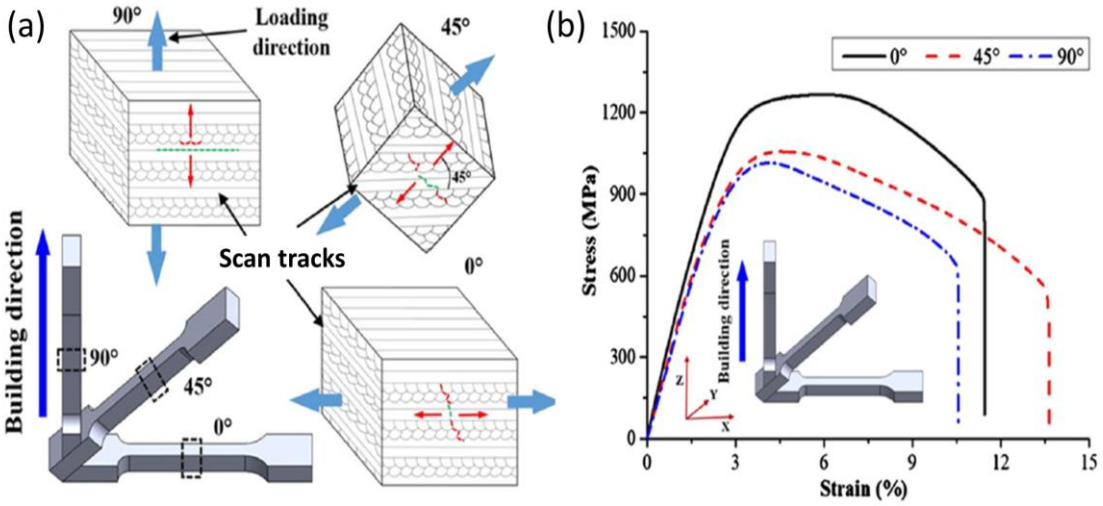

Figure 9: Influence of (a) build orientation and scanning pattern on (b) tensile strength of SLM 18Ni-300 maraging steel samples [61].

Following that, post-processing heat treatment is known to induce significant changes in the mechanical properties of SLM 18Ni-300 maraging steel [87,88]. Kučerová et al. [87] compared the mechanical properties of as-built, solution annealed, and age hardened SLM 18Ni-300 maraging steel samples. Solution annealing was conducted at 820 ℃ for 20 min, while age hardening was conducted at 490 ℃ for 6 h. The ultimate tensile strength, elongation at fracture, and hardness of as-built samples were reported as 1050 MPa, 8 %, and 371 HV, respectively. The microstructure of the as-built samples consisted of mainly martensite with a mix of equiaxed and columnar morphologies. Traces of retained austenite along the martensite grain boundaries were detected via EBSD. Solution annealing resulted in decreased ultimate tensile strength and hardness, accompanied with increased ductility as compared to the as-built sample (solution annealing: 980 MPa, 9 %, 328 HV). The equiaxed and columnar morphologies found in the microstructure of the as-built sample had disappeared and were replaced with elongated lath morphology. Complete austenite reversion was also reported. Age hardening resulted in increased ultimate tensile strength and hardness, while ductility decreased as compared to the as-built sample (age hardening: 1837 MPa, 4 %, 665 HV). The microstructure of age-hardened samples consisted of Ni_3Ti and Ni_3Mo nanoprecipitates that were distributed throughout the martensite matrix, and the equiaxed and columnar morphologies found in the as-built sample had disappeared. An increase in retained austenite volume fraction compared to the as-built sample was also reported.

Yin et al. [88] reported that the phase transformations and microstructure of SLM maraging steel were more sensitive to changes in aging temperature instead of aging duration. It was reported that age hardening the samples at 490 ℃ for 3 h was most optimal for obtaining samples with high ultimate tensile strength. The use of a lower or higher aging temperature than the one mentioned resulted in reduced ultimate tensile strength instead.

2.2.2. Implementation of metal AM technologies in the mould making industry

In the mould making industry, metal AM technologies have been applied for the fabrication of steel moulds [6,19–21]. By leveraging the capabilities of metal AM technologies, mould makers are able to fabricate steel moulds with complex geometries, as well as test multiple prototypes in rapid succession during the design stage. Vasco et al. [89] reported the use of additively manufactured steel moulds facilitated a more homogeneous surface temperature during injection moulding, in addition to faster cooling at thicker regions of the injection moulded polymer product. Furthermore, injection moulding defects such as warpage and sink marks in the injection moulded polymer product were greatly reduced.

Metal AM technologies (especially SLM) are able to additively manufacture steel moulds with conformal cooling channels built directly inside it, a feat that is hard to accomplish via conventional manufacturing technologies [19,90,91]. Conformal cooling channels are specifically designed to follow the contour of the injection moulded polymer product, thus providing increased cooling efficiency during injection moulding. A comparison between steel moulds that feature conventional straight-drilled cooling channels and additively manufactured conformal cooling channels is shown in **Figure 10**. Following that, the design of conformal cooling channels has received considerable attention due to the benefits it brings to injection moulding. Park et al. [90] utilised a combination of analytical formulas and computer-aided engineering (CAE) simulations to devise an optimal cooling channel design taking into consideration the complex features of the polymer product and cooling channel geometry.

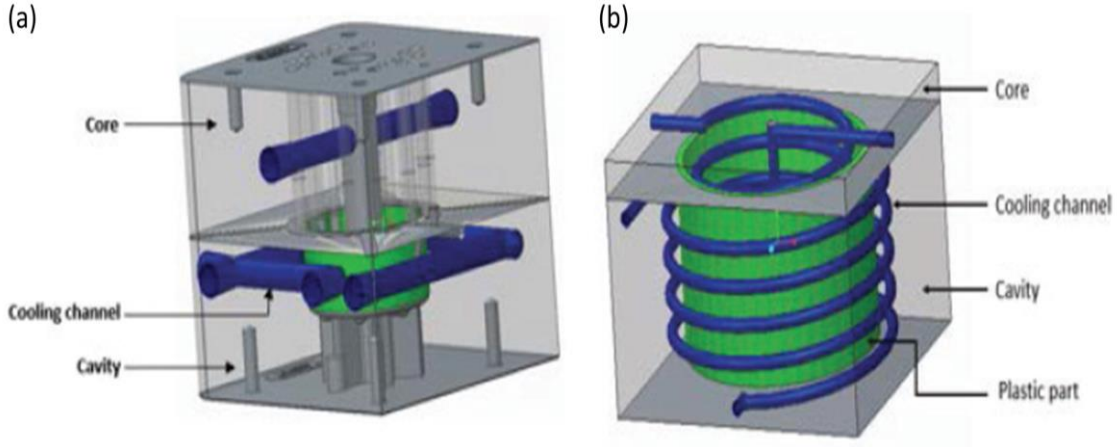

Figure 10: Comparison between steel moulds that feature (a) conventional straight-drilled cooling channels, and (b) additively manufactured conformal cooling channels [91].

Park and Dang [92] mentioned that the cooling stage occupied a large portion of the injection moulding cycle, and its reduction would result in increased process efficiency. It was reported that the use of conformally cooled steel moulds resulted in a 23 % reduction in cooling time as compared to steel moulds with conventional straight-drilled channels. Evens et al. [93] also reported that the use of conformally cooled steel moulds resulted in a 70 % reduction in injection moulding cycle time and the start-up losses during injection moulding were reduced. However, Mazur et al. [77] reported the

occurrence of residual stress in additively manufactured steel moulds, which resulted in reduced tensile and fatigue strength as compared to its conventionally made counterpart. A stress relieving heat treatment is required to minimise residual stress in additively manufactured moulds.

Recently, researchers have utilised SLM to additively manufacture conformally cooled 18Ni-300 maraging steel moulds [19–21]. Liu et al. [19] compared the cooling performance of additively manufactured conformal cooling channels with conventional straight-drilled cooling channels. The cooling channels were fabricated using 18Ni-300 maraging steel. The additively manufactured conformal cooling channels were identified to have a lower cooling performance compared to its conventionally made counterpart. This is due to it having a lower dimensional accuracy and increased surface roughness, which reduced coolant flow rate and heat conduction across the cooling channel's surface. It can be deduced that the use of optimal SLM in-process parameters and good cooling channel design are necessary for fabricating conformally cooled moulds with increased cooling efficiency.

2.3. Microstructure evolution in steel mould materials processed via metal AM technologies

A comprehensive understanding of the process-microstructure-properties relationships in steel mould materials processed via metal AM technologies is necessary for optimising metal AM process parameters and fabricating steel moulds with improved mechanical properties. In particular, the knowledge of the microstructure evolution provides key insights for explaining the interdependence between its process parameters and mechanical properties. Furthermore, metal AM processes feature complex grain solidification and growth phenomena, which should be taken into consideration when discussing microstructure evolution.

The steel mould materials of interest in the present section include: H13, P20, AISI 420 stainless steel, S136, and 18Ni-300 maraging steel. These five steel mould materials were previously introduced and discussed in **Section 2.2**. A few reviews have comprehensively analysed the microstructure and mechanical properties of additively manufactured H13 [65] and 18Ni-300 maraging steel [66,67,94]. Other reviews have included both H13 and 18Ni-300 maraging steel in a broader comparative analysis of various steel grades processed via metal AM technologies [95–97]. Following that, Cunha et al. [6] conducted a comparative analysis of the mechanical properties of additively manufactured H13, P20, and AISI 420 stainless steel. However, to the best of the author's knowledge and at the time of writing, no existing review has provided a comprehensive comparative analysis of the microstructure evolution and mechanical properties of these five steel mould materials processed via metal AM technologies.

In **Sections 2.3.1** to **2.3.4**, the microstructure evolution and mechanical properties of the five steel mould materials processed via metal AM technologies are analysed in detail. To begin, the grain solidification and growth phenomena that are characteristic of metal AM processes are introduced (**Section 2.3.1**). Next, in situ experimental techniques for characterising microstructure evolution in metal AM processes are presented (**Section 2.3.2**). The comparative analysis for the microstructure evolution in the five steel mould materials is presented in two categories, i.e. steel mould materials strengthened via precipitation of carbides (H13, P20, AISI 420, S136) and Ni-based intermetallics (18Ni-300) (**Sections 2.3.3** and **2.3.4**). The microstructure evolution of each steel mould material was further characterised into two stages, namely the as-built condition (Stage 1) and after post-processing heat treatment condition (Stage 2). Stage 1 focuses on the formation of the material's microstructure as it solidifies into the as-built condition. Stage 2 focuses on changes in the material's microstructure after post-processing heat treatment. It should be noted that the investigations discussed in **Sections 2.3.1** to **2.3.4** are not exhaustive, as this topic is currently being researched and new reports may emerge after the time of writing. A more detailed discussion of 18Ni-300 maraging steel is included in **Section 2.3.4**. This reflects the greater number of investigations and the increasing relevance of 18Ni-300 maraging steel in metal AM research, together with its central role in the present thesis.

The findings of the comparative analysis were published as a review paper [39]. It should be noted that the discussions presented in **Sections 2.3.1** to **2.3.4** may differ from the published version, as they have been updated to include more recent findings

in the literature. In addition, **Table 4** and **Table 5** in **Section 2.3.4** were not included in the review paper as they were developed after the review paper was published.

2.3.1. Grain solidification and growth in metal AM processes

Metal AM processes feature an interesting microstructure evolution phenomenon known as intrinsic heat treatment (IHT). IHT is caused by the transient reheating on the adjacent regions of the current scan track during fabrication This phenomenon is caused by the scanning motion of the heat source as it melts and solidifies the powder material. The heat from the melt pool is transferred towards its surroundings, causing a transient reheating effect on it. The influence of IHT on steel mould materials processed via metal AM technologies has been reported in the literature [70,84,98,99] and is schematically illustrated in **Figure 11**.

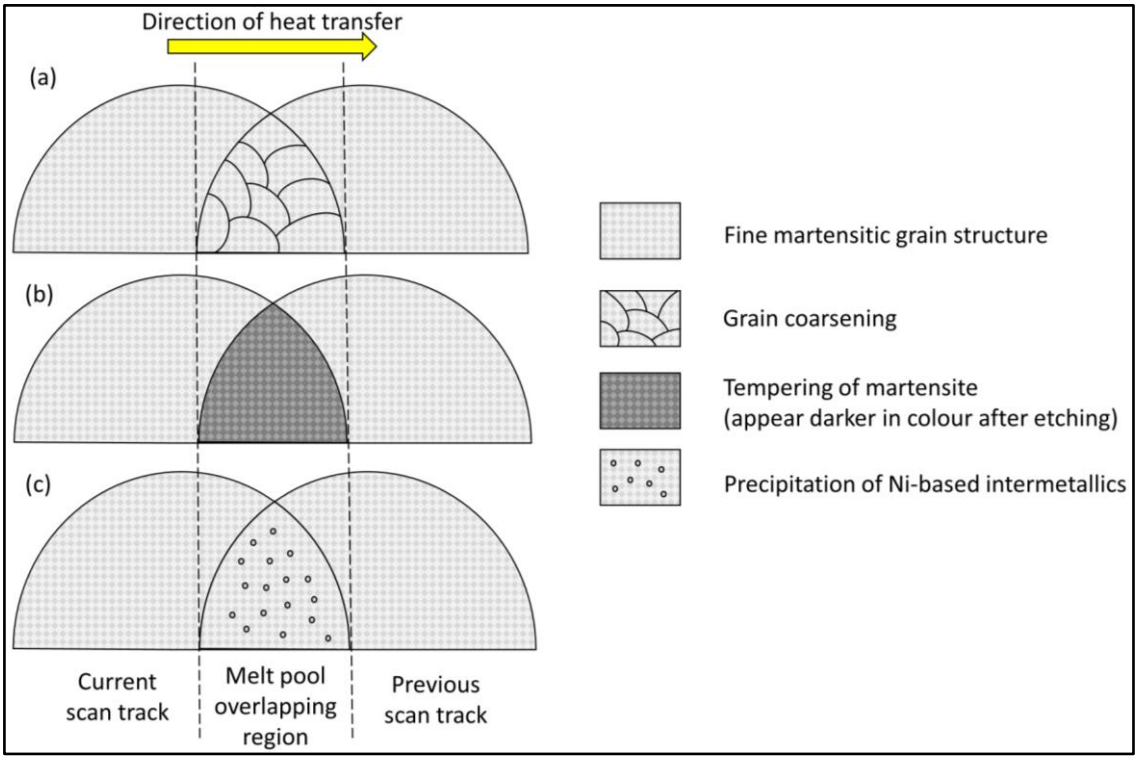

Figure 11: Illustration for the effects of IHT in steel mould materials: (a) grain coarsening in melt pool overlapping regions; (b) tempering of martensite in carbide strengthened steel mould materials; and (c) precipitation of Ni-based intermetallics in maraging steel.

Another interesting microstructure evolution phenomenon is the rapid solidification in metal AM processes. Rapid solidification occurs due to the high cooling rate and temperature gradient induced by the scanning motion of the heat source (e.g. laser beam) during fabrication. Metal AM processes (particularly SLM) feature high cooling rates ranging between $10^3\ \mathrm{K\,s^{-1}}$ to $10^6\ \mathrm{K\,s^{-1}}$ [31,100,101]. In contrast, cooling rates in conventional casting processes are much lower, ranging from $10\ \mathrm{K\,s^{-1}}$ to $10^2\ \mathrm{K\,s^{-1}}$ [100,102]. In terms of microstructure, finer grains are found in the additively manufactured metal components (AMMCs), while coarser grains are found in conventionally casted components. This is because the higher cooling rate in metal AM processes induced further grain refinement in the microstructure.

The temperature gradient induced by the scanning motion of the heat source resulted in directional solidification in AMMCs. Flemings [100] identified six different grain morphologies during the solidification process of directionally solidified alloys. Among them, the following three grain morphologies are commonly reported in AMMCs: equiaxed cellular grains, equiaxed dendrites, and columnar dendrites [84,98,103]. **Figure 12** schematically illustrates the relationship between temperature gradient and grain morphologies formed after rapid solidification in metal AM processes. During rapid solidification, columnar dendrites form in regions with a high temperature gradient. The growth of columnar dendrites is oriented according to the direction of temperature gradient during solidification. In addition, the scanning motion of the heat source introduced a certain level of agitation on the melt pool. As a result, equiaxed cellular grains form in regions with vigorous agitation and low temperature gradient. Equiaxed cellular grains are replaced by equiaxed dendrites at lower agitation levels.

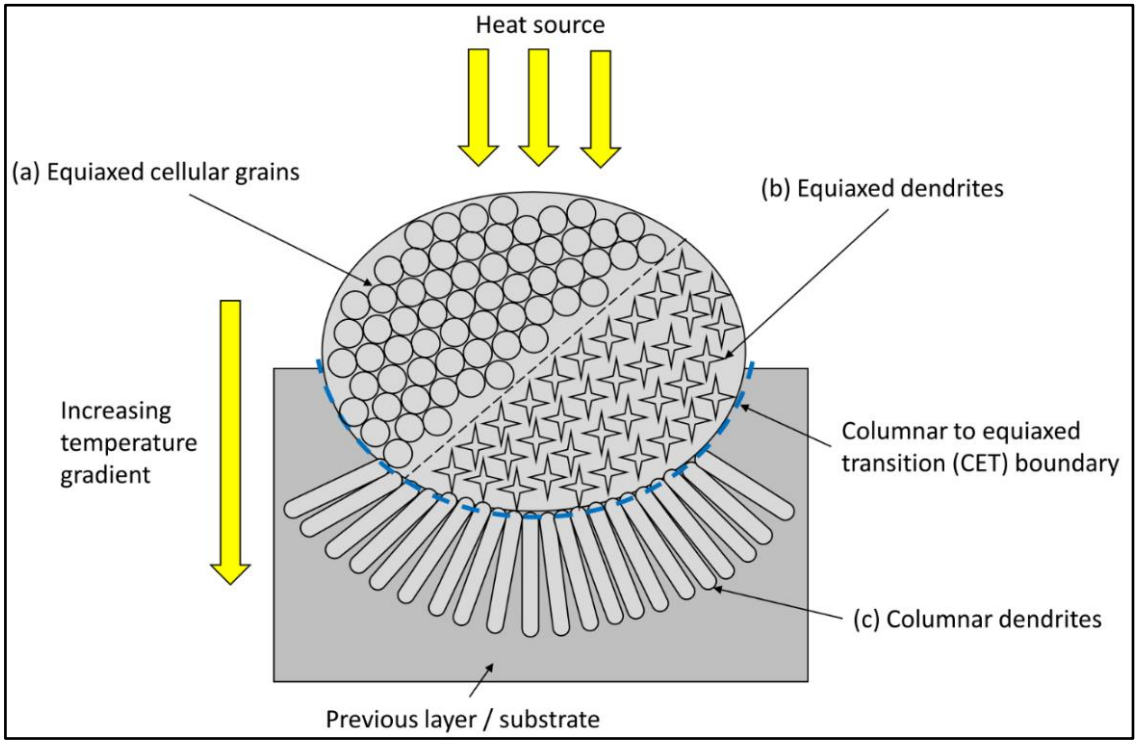

Figure 12: Illustration for the formation of different grain morphologies after rapid solidification in metal AM processes: (a) equiaxed cellular grains, (b) equiaxed dendrites, and (c) columnar dendrites.

Similarities were identified when comparing the solidification process and grain morphologies of AMMCs and welded components. The two main factors governing the formation of a particular grain morphology in both components were the local temperature gradient in the melt pool and the solidification growth rate of the grains [57,104]. Equiaxed grains would form in regions directly scanned by the heat source, where the temperature gradient was relatively low. In contrast, columnar grains would form in regions further away from the heat source, where the temperature gradient was higher. Columnar-to-equiaxed transition (CET) may occur depending on the ratio of local temperature gradient to solidification growth rate (G/R) in the melt pool. A lower G/R ratio promoted the formation of equiaxed grains, while a higher G/R ratio promoted the formation of columnar grains. The growth of columnar grains was aligned with the

direction of the local temperature gradient. The presence of columnar grains was identified as the cause of anisotropy in mechanical properties, which was undesirable in AMMCs and welded components.

2.3.2. In situ characterisation of microstructure evolution in metal AM processes

Conventional microstructure characterisation techniques such as scanning electron microscopy (SEM), electron backscatter diffraction (EBSD), and X-ray diffraction (XRD) are frequently utilised to investigate various aspects of the microstructure in metals, including grain morphology, crystallographic texture, and phase composition. A comparative analysis of the material's pre- and post-processing states is often conducted to infer the microstructure evolution induced by the metallurgical process, i.e. changes in grain morphology, texture, and phases. Although conventional microstructure characterisation techniques possess the spatial resolution to characterise the microstructure up to the nanometer scale, they lack the temporal resolution required to capture the transient dynamics of microstructure evolution in situ. A before-after comparison may not be sufficient to fully explain the changes in microstructure evolution that occurred during metal AM processes, particularly those associated with rapid solidification and grain growth.

In situ microstructure characterisation techniques allow researchers to study microstructure evolution in real-time during metal AM processes. Recently, a new microstructure characterisation technique termed dynamic transmission electron microscopy (DTEM) was developed to solve the problem of temporal resolution that was limiting conventional techniques [12,105–107]. DTEM enabled researchers to observe and study transient microstructure evolution phenomena such as rapid solidification of alloys in situ, with both spatial and temporal resolutions up to the nanometer and nanosecond scale, respectively. This was achieved by redesigning a conventional transmission electron microscope (TEM) to emit a large number of electrons in a short pulse, thus enabling microstructure evolution phenomena to be captured in real-time.

Two derivative techniques were devised from DTEM, which are single-shot mode and movie mode DTEM. McKeown et al. [105] explained that single-shot mode DTEM involved taking an image of the microstructure evolution phenomena at fixed time intervals. By analysing these images in sequence, new insights on microstructure evolution can be obtained. Movie mode DTEM improves on single-shot mode as it can capture images at user-defined time intervals. This was achieved by controlling the time intervals for the emission of electron pulses, resulting in enhanced temporal control during data collection. Recent findings have reported the successful application of single-shot mode [106] and movie mode DTEM [107] to study microstructure evolution in situ. McKeown et al. [12] utilised movie mode DTEM to study rapid solidification of hypoeutectic Al-Cu and Al-Si thin films (**Figure 13**). A pulsed laser was used to induce rapid solidification in the samples, and the results obtained were used to determine the solidification front velocities of both alloys.

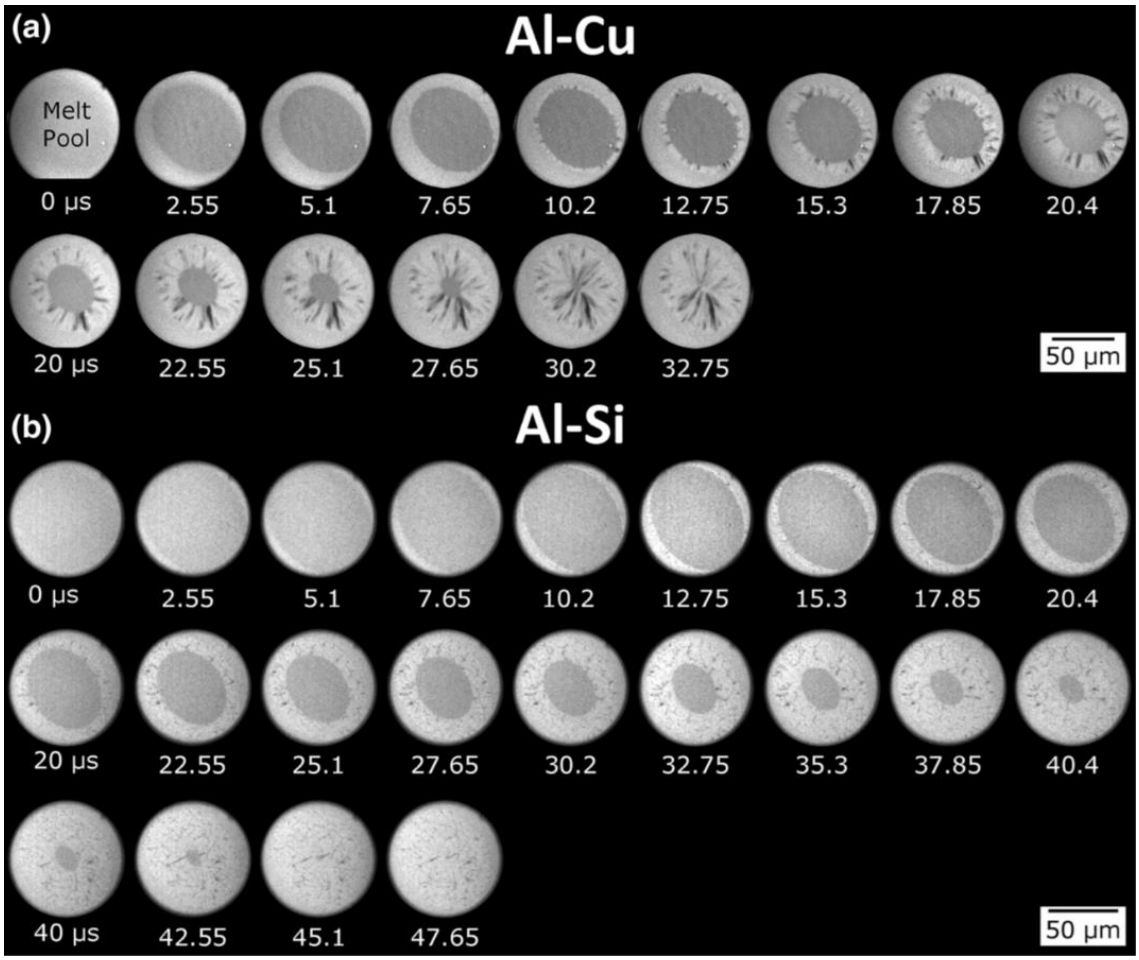

Figure 13: Rapid solidification of (a) Al-Cu and (b) Al-Si thin films captured via movie mode DTEM [12].

Besides DTEM, researchers also applied synchrotron X-ray diffraction to study and capture microstructure evolution in situ during metal AM processes [10,108]. Synchrotron X-ray is produced from high energy electrons which are accelerated via a synchrotron machine. Ultrafast in situ synchrotron X-ray imaging and diffraction techniques were developed by researchers to study the complex interaction between the heat source and the powder material during metal AM processes. Sun et al. [108] reported that this imaging technique has a minimum spatial resolution of 1 µm and a minimum temporal resolution of 100 ps.

Synchrotron X-ray diffraction have been successfully implemented for in situ investigations on pore formation mechanisms and melt pool dynamics in metal AM processes [109–111]. Hojjatzadeh et al. [109] investigated the dynamics of pore motion within the melt pool using in situ synchrotron X-ray imaging. **Figure 14** shows the formation of pores during SLM process captured using synchrotron X-ray imaging. It was identified that the movement of pores in the currently scanned region was governed by the thermocapillary force in the melt pool. This thermocapillary force was created as a result of the high temperature gradient between the heat source and melt pool boundary. It was concluded that the thermocapillary force aided in pore elimination, as the pores escaped from the melt pool by travelling along the direction of temperature gradient.

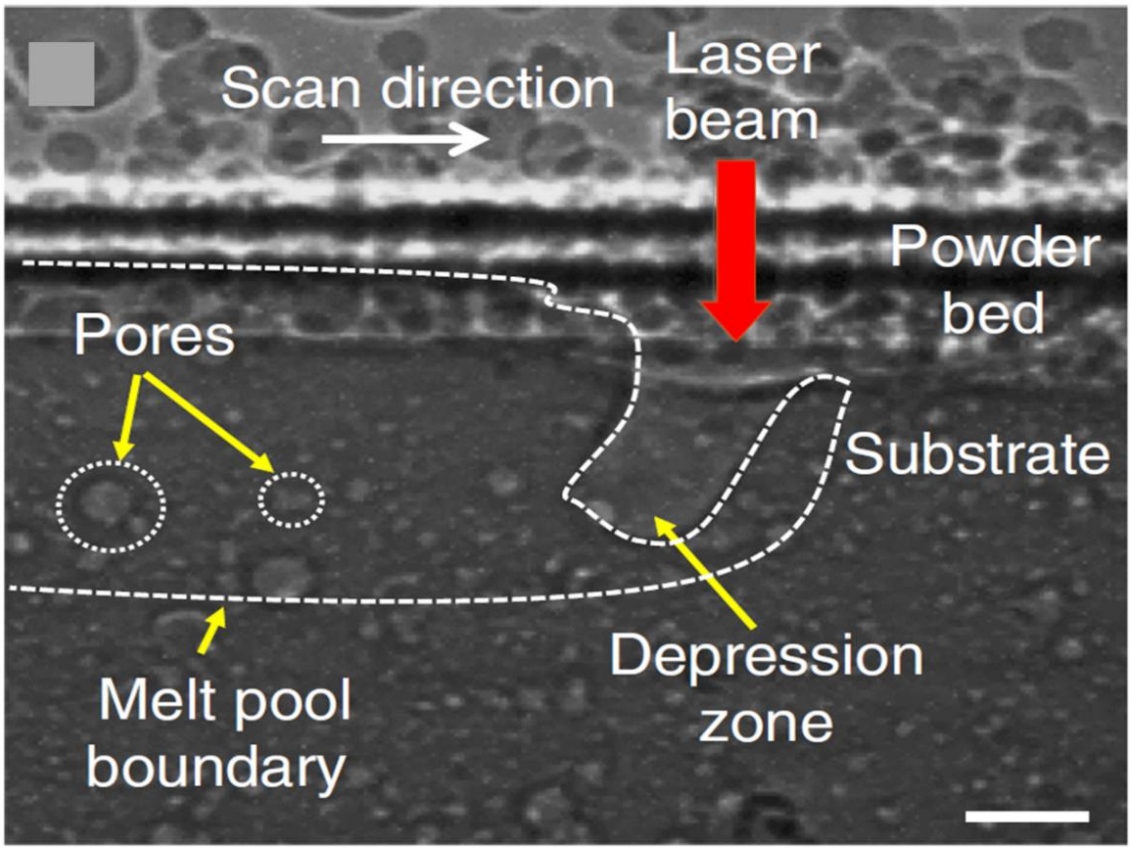

Figure 14: Formation of pores during SLM process captured using synchrotron X-ray technique, the scale bar in the figure is 50 μm [109].

2.3.3. Microstructure evolution in steel mould materials strengthened via carbide precipitation

2.3.3.1. Conventional steel mould materials : H13 and P20

Stage 1: As-built condition

The microstructure evolution in steel mould materials (i.e. H13, P20, AISI 420, S136) is characterised into two stages, namely the as-built condition (Stage 1) and after post-processing heat treatment condition (Stage 2). It should be noted that the investigations discussed in the present section are not exhaustive, as there exist several reports that addressed similar research themes and new reports may emerge after the time of writing. The relevant review papers may also be consulted for a more comprehensive perspective and as a supplement for the discussion in the present section [6,65].

Several researchers have investigated the microstructure and mechanical properties of additively manufactured H13 samples [70,79,85,103,112–119] and P20 samples [71,120]. Deirmina et al. [70] reported the occurrence of IHT in additively manufactured H13 samples. After etching, alternating rows of light and dark regions were observed in the microstructure (**Figure 15**(a)). The light regions were identified as untempered martensite, while the dark regions were identified as tempered martensite. It was deduced that in situ tempering (or intrinsic heat treatment, IHT) of martensite phase had occurred during the fabrication process. A higher magnification image for the heterogeneous distribution of cellular and columnar grains is shown in **Figure 15**(b). Silveira et al. [114] utilised synchrotron X-ray diffraction to investigate the phase transformations that occurred during the additive manufacturing of H13 samples. The occurrence of IHT during the fabrication process was also reported. Furthermore, in situ diffraction data and thermal histories revealed that IHT was characterised by a combination and repetition of five distinct phase transformations, i.e.: full melting, partial melting, full austenitisation, partial austenitisation, and in situ tempering.

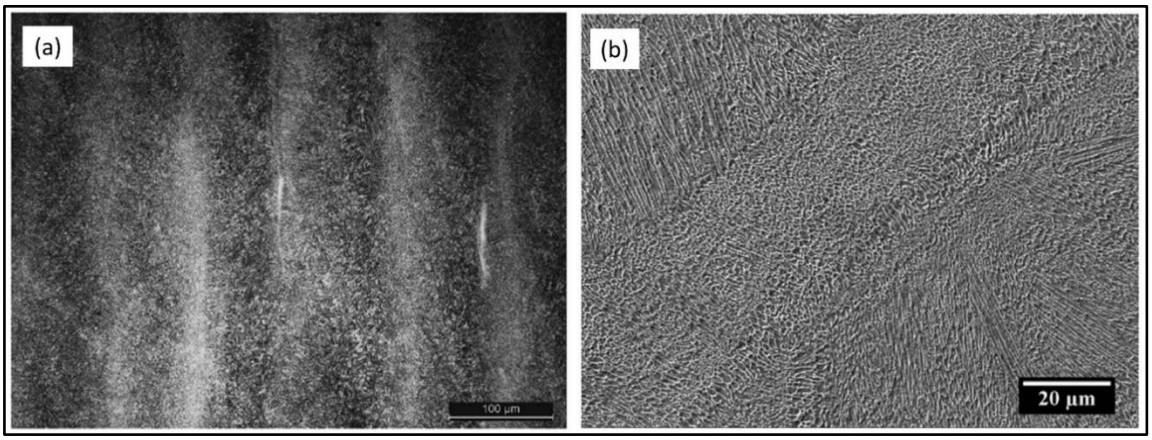

Figure 15: Microstructure of additively manufactured H13 samples in the as-built condition where (a) alternating rows of light and dark regions were observed. (b) A higher magnification image showing a heterogeneous microstructure [70].

Mazumder et al. [115] identified that the microstructure of additively manufactured H13 samples consisted of the following two grain morphologies: equiaxed dendrites and columnar dendrites. Equiaxed dendrites were found in immediate regions that were scanned by the heat source, and their growth was attributed to the uniform local temperature gradient in all directions. Columnar dendrites were found growing perpendicular to the region where equiaxed dendrites had formed. It was deduced that the growth of columnar dendrites was influenced by the direction of local temperature gradient during the solidification process. Chen et al. [103] reported that the formation of equiaxed or columnar morphologies was directly influenced by the SLM in-process parameters, i.e. laser power and scanning speed. Variations in these parameters led to localised variations in the temperature gradient, cooling rate, and solidification rate in the melt pool. Consequently, higher cooling rates promoted the formation of fine equiaxed grains, which exhibited greater localised hardness compared to columnar grains. Similar observations regarding the formation of equiaxed and columnar grain morphologies were also reported in other investigations [116–118].

Ren et al. [85] identified that the grain sizes found in additively manufactured H13 samples were smaller compared to those found in conventionally forged samples. The presence of smaller grains was attributed to the influence of high cooling rate during the metal AM process, which induced grain refinement in the microstructure. The phases found in additively manufactured H13 samples were identified to be martensite and retained austenite. Carbide precipitates were found in conventionally forged samples, but were absent in additively manufactured samples. It was deduced that the high cooling rate in metal AM process had suppressed the diffusion and precipitation of carbides. In terms of mechanical properties, the ultimate tensile strength and toughness obtained for additively manufactured samples were slightly lower compared to conventionally forged samples. This was attributed to the lower relative density (99.2 %) obtained for additively manufactured samples as compared to conventionally forged ones. The occurrence of grain refinement in additively manufactured H13 samples was also reported in other investigations [112,118,119].

Li et al. [71] investigated the microstructure of additively manufactured P20 samples. The phases found in as-built condition consisted of mainly martensite with traces of retained austenite. The microstructure consisted of alternating rows of fine and coarse lath grains. The rows of fine grains were identified to be the scanning tracks where a higher energy intensity resulted in the formation of said grains. The rows of coarse grains were identified to be the melt pool overlapping regions where grain coarsening occurred.

Stage 2: After post-processing heat treatment

Åsberg et al. [79] investigated the influence of post-processing heat treatment on additively manufactured H13 samples. The samples were subjected to the following post-processing heat treatment conditions. The first heat treatment condition was stress relief (SR) at $650\ ^{\circ}\mathrm{C}$ for $8\ \mathrm{h}$ to reduce residual stress. This second was hot isostatic pressing (HIP) at $1130\ ^{\circ}\mathrm{C}$ for $6\ \mathrm{h}$ and 100 MPa chamber pressure to reduce porosity in the samples. The third was hardening at $1020\ ^{\circ}\mathrm{C}$ for $1.25\ \mathrm{h}$, followed by double tempering at $585\ ^{\circ}\mathrm{C}$ for $3\ \mathrm{h}$ (HT) to improve hardness and strength. It was reported that after SR, the martensite phase found in as-

built condition decomposed into ferrite and carbide precipitates. The precipitates had formed a discontinuous network along prior austenite grain boundaries (**Figure 16**(a)), and were rich in Cr and Mo. After HT, tempered martensite was found in the microstructure and carbides were dispersed throughout the matrix. It was concluded that a combination of SR, HIP, and HT led to reduced porosity, as well as improved hardness and strength in additively manufactured H13 samples. Also, samples that had undergone SR, HIP, and HT have a more homogeneous microstructure as shown in **Figure 16**(b). Wang et al. [121] studied the influence of tempering at $500-560\ ^{\circ}\mathrm{C}$ for $2\ \mathrm{h}$ on conventional H13 samples. It was reported that double tempering resulted in a more thermodynamically stable and homogeneous microstructure compared to single tempering. This is because the second stage of tempering facilitated a more complete transformation of retained austenite into martensite and its subsequent tempering.

Hosseinlou et al. [113] also investigated the influence of post-processing heat treatment on additively manufactured H13 samples. It was identified that samples heat-treated via double tempering at $550\ ^{\circ}\mathrm{C}$ for $2\ \mathrm{h}$ exhibited higher ultimate tensile strength, higher hardness, and lower elongation at fracture compared to as-built condition (Double tempering: 2100 MPa, 665 HV, 7.6 % vs. As-built: 1900 MPa, 593 HV, 9.7 %). The mechanical properties of the additively manufactured and double tempered H13 samples were identified to be better than the conventionally wrought and tempered condition (conventional wrought: 1520 MPa, 548 HV, 7.4 %).

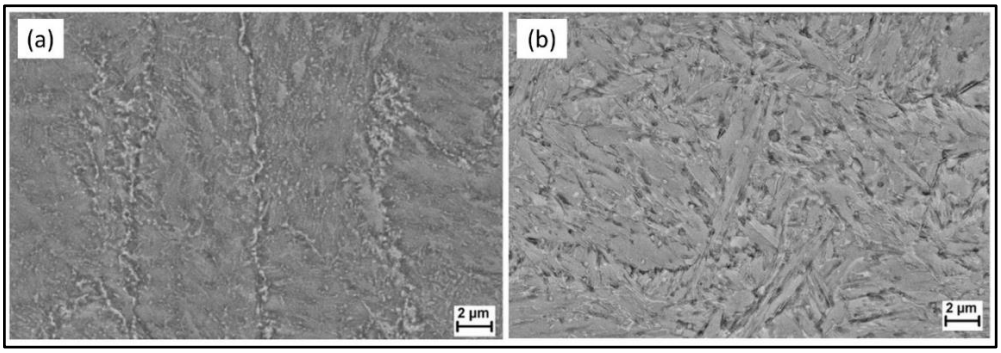

Figure 16: Microstructure of additively manufactured H13 samples after undergoing (a) SR and (b) a combination of SR, HIP, and HT [79].

Li et al. [71] investigated the effects of tempering on additively manufactured P20 samples. Carbide precipitates were identified between martensite laths, and consisted of mainly Cr and Si. As the tempering temperature was increased from 450 °C to 550 °C, the carbide precipitates grew larger and rounder in shape. An increase in corrosion resistance was observed in tempered P20 samples, while hardness remained similar to as-built condition.

Following that, Chen et al. [120] reported that tempering at $316-538\ ^{\circ}\mathrm{C}$ for 1 h destabilised the retained austenite in additively manufactured P20 samples, causing it to transform into martensite upon cooling. This transformation reduced the amount of retained austenite in the samples and significantly altered their residual stress state relative to the as-built condition. It was identified that the volumetric expansion associated with the austenite-to-martensite phase transformation would counteract the tensile residual stresses generated during the metal AM process, and may result in compressive residual stresses.

2.3.3.2. Steel mould materials with improved corrosion resistance: AISI 420 stainless steel and S136

Stage 1: As-built condition

Researchers have investigated using metal AM technologies to process AISI 420 stainless steel [72,86,98,122,123] and S136 [73,81,82]. Similar to **Section 2.3.3.1.**, it should be noted that the investigations discussed in the present section are not exhaustive. Sun et al. [98] observed a mix of columnar and cellular grains in additively manufactured AISI 420 samples. The phases found in as-built condition were identified as ferrite, lath martensite, and retained austenite. In addition, $M_{23}C_6$ carbides (M representing Fe and Cr) were found to be dispersed throughout the matrix. Tempering was not observed in as-built samples with continuous scan tracks. In contrast, when an idle time of 80 s was implemented between each scan track, tempered martensite was observed as dark bands in the melt pool overlapping regions. In addition, M_7C_3 carbides were found dispersed in the tempered martensite matrix. It was deduced that the idle time between scans allowed further cooling of the microstructure, while subsequent scans induced IHT in the scan tracks. This resulted in the decomposition of martensite into ferrite and M_7C_3 carbide precipitates, indicated by a higher volume of carbide precipitation and dark bands of tempered martensite. The occurrence of columnar and cellular grains was also reported by Zhao et al. [86].

Krakhmalev et al. [122] reported that IHT induced the diffusion of carbon atoms to the cellular boundaries in additively manufactured AISI 420 samples. However, the diffusion process had a interrupted character due to the transient reheating effect induced by IHT. Numerical simulations of the thermal history indicated that the temperatures reached during IHT were high enough to initiate carbon diffusion, but the diffusion distances were limited by the short cycle times. The selective diffusion of carbon atoms to the cellular boundaries resulted in local carbon enrichment, and promoted austenite reversion in those regions.

Wen et al. [73] investigated the microstructure of additively manufactured S136 samples and compared it with conventionally casted samples. The microstructure in as-built samples consisted of finely distributed equiaxed and columnar grains, while coarse grains were found in conventionally casted samples. Phases identified in additively manufactured samples consisted mainly of martensite with some retained austenite. No carbides were found in additively manufactured samples. In contrast, conventionally casted samples contained fully martensite phase, and carbides rich in C and Cr were dispersed throughout the martensite matrix. The variation in the results obtained was attributed to the significant difference in cooling rate between the two manufacturing processes. A similar observation regarding the microstructure of additively manufactured S136 was also reported by Zhou et al. [81].

Stage 2: After post-processing heat treatment

Nath et al. [72] investigated the influence of post-processing heat treatment on additively manufactured AISI 420 samples. The samples were subjected to tempering at 315 °C for 2 h. A relative density of over 99 % was reported for as-built and tempered samples. A comparison of the microstructure found in as-built condition and after

tempering is shown in **Figure 17.** In **Figure 17**(a), martensite laths were found to be dispersed in the microstructure of as-built samples. Tempering resulted in an increase in lath martensite, observed as needles with a darker shade in the microstructure as shown in **Figure 17**(b). However, no carbides were found in as-built condition and after tempering. It was deduced that carbide precipitation may have been inhibited by rapid solidification during the process. Tempering also resulted in improved yield strength, ultimate tensile strength, and elongation at fracture. However, no significant improvement in hardness and corrosion resistance were reported for tempered samples. After tempering, the tensile strength and elongation at fracture of the tempered samples increased compared to their as-built condition, while the hardness slightly decreased instead (Tempered: 1520 ± 30 MPa, 6.3 ± 0.2 %, 53 ± 1 HRC vs. As-built: 1050 ± 25 MPa, 2.5 ± 0.2 %, 55 ± 1 HRC). The mechanical properties of the tempered samples were also comparable with conventionally wrought condition (Wrought: 1625 ± 40 MPa, 7.0 ± 1.0%, 53 ± 2 HRC).

Alam et al. [123] conducted post-processing heat treatment on additively manufactured AISI 420 samples at 565 ℃ for 1 h. Heat treatment was reported to be effective in minimising the anisotropy in mechanical properties of samples fabricated using different build orientations. Anisotropy was attributed to the non-uniform heat dissipation during fabrication, which varied with the samples' build orientation and resulted in directional solidification.

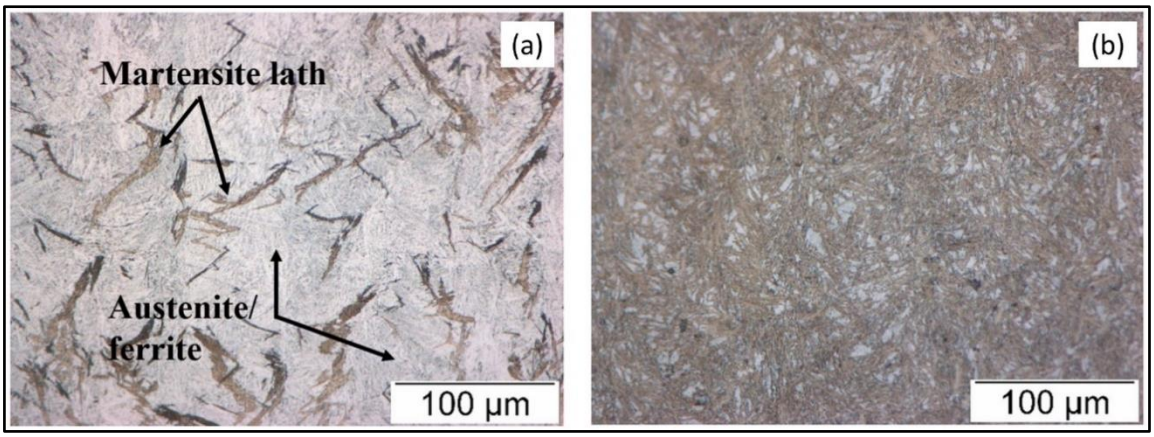

Figure 17: Microstructure of additively manufactured AISI 420 samples in the (a) as-built condition and (b) after tempering [72].

Ji et al. [82] investigated the effects of varying the austenitisation temperature on additively manufactured S136 samples. The samples were heated up to different austenitisation temperatures ranging from 980 °C to 1100 °C, and maintained for 1 h. The samples were then subjected to oil quenching. It was identified that the microstructure consisted of mainly martensite phase after quenching. In addition, carbides rich in C and Cr were found dispersed throughout the matrix. These carbides appeared as white particles in samples that were heat-treated at temperatures ranging between 980 °C to 1020 °C. However, no carbides were found when the austenitisation temperature was increased to 1100 °C. It was concluded that the carbides had dissolved in the matrix at higher austenitisation temperatures.

2.3.4. Microstructure evolution in steel mould materials strengthened via precipitation of Ni-based intermetallics

2.3.4.1 18Ni-300 maraging steel

Stage 1: As-built condition

The microstructure evolution in additively manufactured 18Ni-300 maraging steel is characterised into two stages similar to **Section 2.3.3**. Stage 1 is named the as-built condition, and Stage 2 is named the post-processing heat treatment condition. It should be noted that the investigations discussed in the present section are not exhaustive, as there exist several reports that addressed similar research themes and new reports may emerge after the time of writing. The relevant review papers may also be consulted for a more comprehensive perspective and as a supplement for the discussion in the present section [66,67,94].

Researchers have conducted investigations on the microstructure of additively manufactured 18Ni-300 maraging steel samples [20,24,64,84,99,124]. Tan et al. [84] reported that the microstructure consisted of fine, equiaxed cellular grains in immediate regions scanned by the heat source (**Figure 18**(a)). The formation of equiaxed cellular grains can be attributed to the equilibrium in interfacial energies and grain boundary angles in that region, resulting in an energetically stable crystalline structure. Coarse cellular grains were observed in melt pool overlapping regions, reflecting the influence of IHT during the fabrication process. Columnar dendrites were observed in areas further away from the scan track, and their growth was influenced by the direction of local temperature gradient during the fabrication process. The microstructure in as-built samples consisted of mainly martensite phase with traces of retained austenite. It was deduced that the high cooling rate in metal AM processes favoured the formation of martensite phase. The occurrence of cellular and columnar grains was also reported in other investigations [20,64].

The occurrence of IHT was reported by other researchers [24,99,124], where the induced precipitation of Ni-based intermetallics at high number densities (up to $1.2 \times 10^{25}\ \mathrm{m}^{-3}$) strengthened the martensite matrix and resulted in increased hardness in the fabricated samples. Following that, Jägle et al. [99] suggested that IHT may be harnessed to design SLM 18Ni-300 maraging steels that are precipitation-strengthened in situ, potentially eliminating the need for post-processing heat treatment.

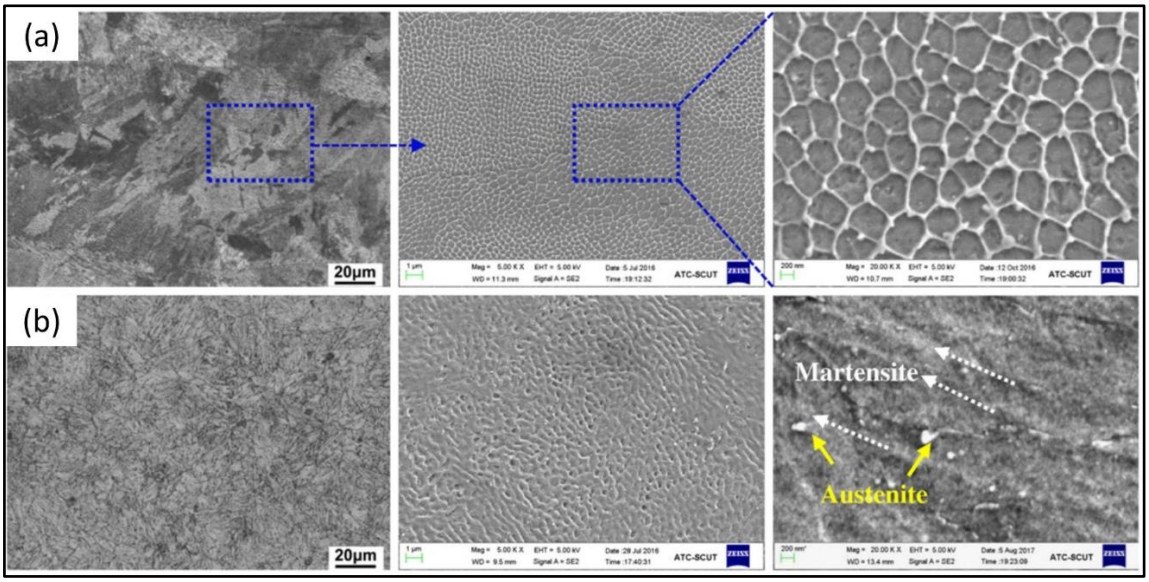

Figure 18: Microstructure of additively manufactured 18Ni-300 maraging steel samples in the (a) as-built condition and (b) after SAT [84].

Investigations on the relationship between the process parameters and mechanical properties of additively manufactured 18Ni-300 maraging steel samples were also conducted [18,22–28,61,63,64]. Mutua et al. [28] fabricated samples with a maximum relative density of 99.80 % using an optimised set of process parameters. The volume energy density for the optimised set of process parameters was reported as 71.43 $\mathrm{J\,mm^{-3}}$. It was concluded that less pores were found in samples with higher relative density. In addition, the building direction was found to influence the mechanical properties of additively manufactured samples. Samples with build orientation perpendicular to the loading direction (i.e. horizontally built samples) have higher ultimate tensile strength and elongation at fracture as compared to samples with build orientation parallel to the loading direction (i.e. vertically built samples). This observation was also reported by several other researchers [18,26,61]. However, Zhao et al. [27] reported the opposite where samples with build orientation parallel to the loading direction exhibited higher ultimate tensile strength instead. This difference was attributed to the variation in crystallographic texture between the samples.

The relative density of samples was also reported to be influenced by the scanning strategy used and the volumetric energy density of the process parameters used during fabrication [24,25]. Bhardwaj and Shukla [25] reported that the use of an orthogonal scanning strategy (i.e. zig-zag scanning pattern with 90 ° rotation for subsequent layers) was found to produce samples with better mechanical properties compared to a scanning strategy without rotation between subsequent layers. Hong et al. [24] reported that samples with near full density may be fabricated using SLM parameter configurations with volumetric energy density higher than 75.00 $\mathrm{J\,mm^{-3}}$. A maximum relative density of 99.86 % was reported for samples fabricated with a volumetric energy density of 93.03 $\mathrm{J\,mm^{-3}}$.

Zhao et al. [23] reported that the corrosion resistance of the samples was negatively affected by porosity. Pores formed due to incomplete fusion of powder material were more susceptible to corrosion, as their larger size promoted the penetration of corrosive media and accelerated material loss beyond the pore volume.

Subsequently, researchers have utilised statistical optimisation methods (e.g. RSM and ANOVA) [22,61,63,64] as well as post-processing heat treatment [23] to address the issue of porosity and fabricate samples with high relative density.

Following that, the in-process parameters for SLM 18Ni-300 maraging steel, together with the reported mechanical properties of conventionally and additively manufactured samples, are summarised in **Table 4**. It should be noted that the cited investigations are not exhaustive. A zig-zag scanning pattern was employed in all of the cited investigations during sample fabrication. The optimal SLM in-process parameters identified in **Chapter 3 Section 3.3** and the mechanical properties of samples fabricated by it are included in the first row of **Table 4** for comparison.

Table 4: The SLM in-process parameters and the resultant mechanical properties of conventionally and additively processed 18Ni-300 maraging steel, reported in the cited investigations. The $\rho_{relative}$ is the maximum achieved in the cited investigations. SLM: selective laser melting. AB: as-built condition.

Sample condition	SLM in-process parameters							$\rho_{relative}$ [%]	Mechanical properties		
	Build orientation	Rotation angle between scanning layers [°]	P [W]	v [mm s^{-1}]	h [mm]	t_{layer} [mm]	$E_{volumetric}$ [J mm^{-3}]		R_m [MPa]	A_t [%]	Hardness [HV]
SLM-AB [41] Optimal SLM config. from **Section 3.3** of present thesis.	Horizontal (0 °)	90	275.00	700.00	0.080	0.040	122.77	99.39	1218 ± 4	9.2 ± 1.0	365.0 ± 0.4
SLM-AB [61]	Horizontal (0 °) Diagonal (45 °) Vertical (90 °)	90	150.19	388.89	0.089	0.035	123.98	99.30	1262 ± 9 1055 ± 2 1023 ± 15	11.2 ± 1.6 13.2 ± 0.3 10.4 ± 0.3	346.4 ± 14.4 306.4 ± 11.1 291.4 ± 4.2
SLM-AB [18]	Horizontal (0 °) Vertical (90 °)	67	285.00	960.00	0.110	0.040	67.47	99.90	1165 ± 7 1085 ± 19	12.4 ± 0.1 11.3 ± 0.3	≈ 332 HV (34.8 ± 0.2 HRC) ≈ 351 HV (35.7 ± 1.1 HRC)
SLM-AB [26]	Horizontal (0 °) Vertical (90 °)	67	380.00	960.00	0.110	0.040	89.96	–	1123 ± 15 1038 ± 3	12.0 ± 0.3 10.0 ± 0.1	398.0 ± 6.0 349.0 ± 23.0
SLM-AB [25]	Horizontal (0 °)	0	285.00	960.00	0.110	0.040	67.47	99.30	1021 ± 28	19.0 ± 0.7	380.0 ± 7.0
	Horizontal (0 °)	90						99.62	1082 ± 62	17.5 ± 1.0	399.0 ± 4.0
SLM-AB [125]	–	90	160.00	400.00	0.070	0.030	190.48	99.19	≈ 1250	11.5	380.0
SLM-AB [64]	–	67	283.60	867.50	0.081	0.050	80.52	99.45	1245 ± 3	10.5 ± 0.5	N/A
SLM-AB [30]	–	67	300.00	1000.00	0.080	0.040	93.75	≈ 99.7	1128 ± 18	8.9 ± 0.1	N/A
SLM-AB [87]	Horizontal (0 °)	67	258.00	960.00	0.110	0.040	61.08	–	1050	8.0	371.0

SLM-AB [83]	–	Island scanning	100.00	150.00	0.112	0.030	198.41	≈ 99	1290 ± 114	13.3 ± 1.9	≈ 388 (39.9 ± 0.1 HRC)
SLM-AB [23]	–	–	200.00	600.00	0.105	0.030	105.82	> 99	1160	14.5	428.2
Conventional rolled bar [87]	–	–	–	–	–	–	–	–	981	10	323
Wrought [84]	–	–	–	–	–	–	–	–	1000–1170	6–15	≈345.5 (35 HRC)

Stage 2: After post-processing heat treatment

Researchers have conducted studies to investigate the influence of post-processing heat treatment on additively manufactured 18Ni-300 maraging steel [28–30,83,84,88,125,126]. Yin et al. [88] reported that the cellular structure found in as-built condition was no longer maintained after aging at 490 °C for 3 h. Instead, precipitation of Ni-based intermetallics was identified in aged samples. Ni_3Mo was identified to form first due to its lattice compatibility with martensite. Ni_3Ti was identified to form rapidly during aging due to the increased interaction between Ni and Ti. Ni_3Al formed as a result of Al replacing the remaining Ti in the matrix. Further aging at 590 °C for 3 h resulted in the decomposition of Ni_3Mo and the formation of Fe_2Mo instead. Austenite reversion was identified in samples that were subjected to aging at 590 °C for 3 h. Similar observations regarding precipitation of Ni-based intermetallics upon aging and austenite reversion after aging at similar temperatures and longer durations (i.e. $510–550$ °C, 3–6 h) were also reported by other researchers [29,30,126].

Tan et al. [84] reported that solution aging treatment (SAT) had significantly altered the mechanical properties of additively manufactured 18Ni-300 maraging steel samples. SAT involves solution annealing the samples at 840 °C for 1 h, followed by aging at 490 °C for 6 h. A comparison of the microstructure found in as-built condition and after SAT is shown in **Figure 18**. The cellular-shaped structure found in as-built condition (**Figure 18**(a)) was no longer maintained, and was replaced with martensite laths (**Figure 18**(b)). Austenite reversion was identified as white spots in the microstructure of SAT samples. In terms of mechanical properties, the ultimate tensile strength and hardness of the samples had increased significantly after SAT, while the elongation at fracture decreased instead (SAT: 1943 MPa, 52–54 HRC, 5.60 % vs. As-built: 1165 MPa, 35–36 HRC, 12.44 %). The significant increase in strength and hardness was attributed to the precipitation of Ni-based intermetallics during SAT. The reported mechanical properties were identified to be comparable with conventional wrought and aged condition (Wrought-aged: 1930–2050 MPa, 52 HRC, 5–7 %). Similar observations were also reported by other researchers [28,83,125].

Following that, the post-processing parameters for conventionally and additively processed 18Ni-300 maraging steel, along with their reported mechanical properties, are summarised in **Table 5**. It should be noted that the cited investigations are not exhaustive. The data in **Table 5** are organised according to the heat treatment conditions reported in literature, namely solution-aging treatment (SAT), direct aging treatment (DAT) and solution treatment (SOL). The mechanical properties of SAT samples obtained during the preliminary experiments in **Chapter 4 Section 4.3** are included in the first row of **Table 5** for comparison.

Table 5: The post-processing heat treatment parameters and the resultant mechanical properties of conventionally and additively processed 18Ni-300 maraging steel, reported in the cited investigations. SLM: Selective laser melting. SAT: Solution-aging treatment. DAT: Direct aging treatment. SOL: Solution treatment.

Sample condition	SLM process parameters							Mechanical properties		
	Build orientation	Rotation angle between scanning layers [°]	P [W]	v [mm s^{-1}]	h [mm]	t_{layer} [mm]	$E_{volumetric}$ [J mm^{-3}]	R_m [MPa]	A_t [%]	Hardness [HV]
SAT										
SLM-SAT [43] 840 °C / 1 h + 490 °C / 6 h Preliminary results from **Section 4.3** of present thesis.	Horizontal (0 °)	90	275.00	700.00	0.080	0.040	122.77	1910	6.5	584.7 ± 3.0
SLM-SAT [27] 820 °C / 1 h + 480 °C / 5 h	Horizontal (0 °)	67	200.00	600.00	0.105	0.030	105.82	2002 ± 50	7.6 ± 0.2	625.0 ± 11.0
	Diagonal (45 °)							1912 ± 28	5.6 ± 0.2	618.0 ± 15.0
	Vertical (90 °)							2075 ± 35	3.5 ± 0.3	630.0 ± 13.0
SLM-SAT [18] 840 °C / 1 h + 490 °C / 6 h	Horizontal (0 °)	67	285.00	960.00	0.110	0.040	67.47	1943 ± 8	5.6 ± 0.1	≈ 589 (53.5 ± 0.8 HRC)
	Vertical (90 °)							1898 ± 33	4.8 ± 0.2	≈ 549 (51.3 ± 0.9 HRC)
SLM-SAT [64] 850 °C / 1 h + 500 °C / 6 h	–	67	283.60	867.50	0.081	0.050	80.52	1915 ± 22	5.0 ± 0.5	–
DAT										
SLM-DAT [30] 440 °C / 3 h	Horizontal (0 °)	67	300.00	1000.00	0.080	0.040	93.75	1799 ± 8	4.6 ± 0.1	–

SLM-DAT [23] 480 ℃ / 2 h	–	–	200.00	600.00	0.105	0.030	105.82	1943	≈ 7.8	683.2
SLM-DAT [23] 480 ℃ / 5 h								2010	≈ 6.9	711.5
SLM-DAT [83] 480 ℃ / 5 h	–	–	100.00	150.00	0.112	0.030	198.41	2217 ± 73	1.6 ± 0.3	≈ 746 (58 ± 0.1 HRC)
SLM-DAT [30] 490 ℃ / 3 h	Horizontal (0 °)	67	300.00	1000.00	0.080	0.040	93.75	1906 ± 15	4.6 ± 0.1	–
SLM-DAT [87] 490 ℃ / 6 h	Horizontal (0 °)	67	258.00	960.00	0.110	0.040	61.08	1837	4.0	665.0
SLM-DAT [18] 490 ℃ / 6 h	Horizontal (0 °)	67	285.00	960.00	0.110	0.040	67.47	2014 ± 9	3.3 ± 0.1	≈ 649 (54.6 ± 0.8 HRC)
	Vertical (90 °)							1942 ± 31	2.8 ± 0.1	≈ 589 (52.9 ± 1.2 HRC)
SLM-DAT [125] 520 ℃ / 6 h Best config. among those studied.	–	90	160.00	400.00	0.070	0.030	190.48	2126	~7.3	653.9
SLM-DAT [30] 540 ℃ / 3 h	Horizontal (0 °)	67	300.00	1000.00	0.080	0.040	93.75	1797 ± 13	7.8 ± 0.2	–
Conventional rolled bar-DAT [87] 490 ℃ / 6 h	–	–	–	–	–	–	–	1877	6	655
SOL										
SLM-SOL [87] 820 ℃ / 0.33 h	Horizontal (0 °)	67	258.00	960.00	0.110	0.040	61.08	980	9.0	328.0
SLM-SOL [23] 820 ℃ / 1 h	–	–	200.00	600.00	0.105	0.030	105.82	1028	16.0	366.5

SLM-SOL [18] 840 ℃ / 1 h	Horizontal (0 °)	67	285.00	960.00	0.110	0.040	67.47	1025 ± 5	14.4 ± 0.4	≈ 292 (29.8 ± 1.3 HRC)
	Vertical (90 °)							983 ± 13	13.7 ± 0.7	≈ 271 (27.5 ± 0.4 HRC)
Conventional rolled bar-SOL [87] 820 ℃ / 0.33 h	–	–	–	–	–	–	–	930	11	339
Others										
Wrought-aged [84]	–	–	–	–	–	–	–	1930–2050	5–7	549 (52 HRC)
Casting [27]	–	–	–	–	–	–	–	2031 ± 29	8.0 ± 0.5	600 ± 20

2.4. Digital image correlation

Digital image correlation (DIC) is a non-contacting, image-based measuring technique for measuring the surface displacement and deformation of objects. Pan [127] explained that there are three main steps for the implementation of DIC, which include: the creation of a suitable speckle pattern on the object's surface, the acquisition of digital images of the object during loading, followed by surface displacement and strain calculations using image correlation algorithms. For speckle patterns, chemical etching may be used to reveal the microstructure of metals (i.e. natural patterns) which can be used as speckle patterns for DIC measurements [128,129]. Artificial speckle patterns where the size of speckles could be customised may also be created on the samples' surface to facilitate DIC measurements at higher spatial resolution [130]. Further details about the creation of artificial speckle patterns are discussed in **Section 2.4.1**.

DIC is compatible with a wide range of digital imaging devices including scanning electron microscope (SEM), optical microscope (OM), and charge-coupled device (CCD) cameras [127]. The temporal and spatial resolution of DIC measurements are directly dependent on the digital imaging devices used and the speckle pattern on the object's surface. **Figure 19** shows the working principle of the two commonly used DIC techniques, namely 2D-DIC and 3D-DIC (or stereo-DIC). In 2D-DIC, a single digital imaging device is used to capture images of a planar object's surface at selected timeframes (or loading states). In 3D-DIC, a pair (or multiple pairs) of digital imaging devices were used to achieve the same objective. 3D-DIC facilitates the 3D measurement of surface displacement and deformation of a planar or curved object. The digital imaging devices need to be calibrated properly before the start of DIC measurements to reduce measurement uncertainties and to avoid artefacts in digital images.

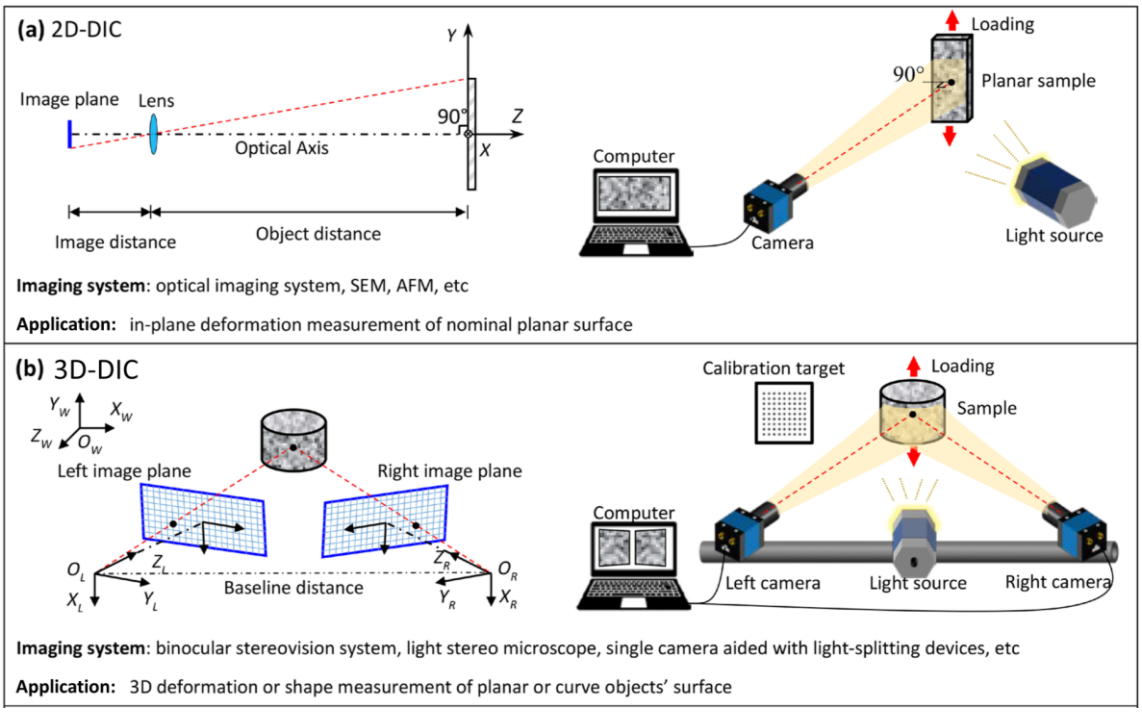

Figure 19: Working principle and applications for (a) 2D-DIC and (b) 3D-DIC [127].

Weidner and Biermann [131] explained that the image correlation algorithms in DIC function by first dividing a digital image into smaller regions (i.e. subsets), followed by comparing the greyscale intensity of the pixels in a reference subset with those found in the target subset. The displacement vector of a measurement point was determined when a similarity between the reference subset and target subset was identified. The degree of similarity between the subsets was determined by the type of image correlation algorithm used, namely the cross-correlation algorithm and the sum-of-squared differences algorithm. The cross-correlation algorithm searched for the maximisation of similarity in greyscale intensity between the subsets, whereas the sum-of-squared differences algorithm searched for the minimisation of the differences instead. Pan et al. [132] reported that the zero-normalised versions of the cross-correlation and sum-of-squared differences algorithms, which considered the global variation in greyscale intensity were reported to provide the most robust performance in the presence of noise and were less sensitive to variations in lighting conditions.

Stinville et al. [133] reported that DIC has an extensive application in various fields of research (**Figure 20**). Its application was directly dependent on the object or phenomena being studied, the digital imaging equipment used, in addition to the spatial and temporal resolution required for adequate characterisation and analysis. Optical imaging-based DIC (optical-DIC) has been applied to study the plastic deformation in conventionally and additively processed steels [134–136]. Recently, an increasing number of investigations have utilised SEM-based DIC (SEM-DIC) for the same purpose [137–142]. In particular, SEM-DIC enables the measurement of plastic strain localisation at higher spatial resolution compared to optical-DIC. Further discussion on the application of SEM-DIC is presented in **Section 2.5.1**.

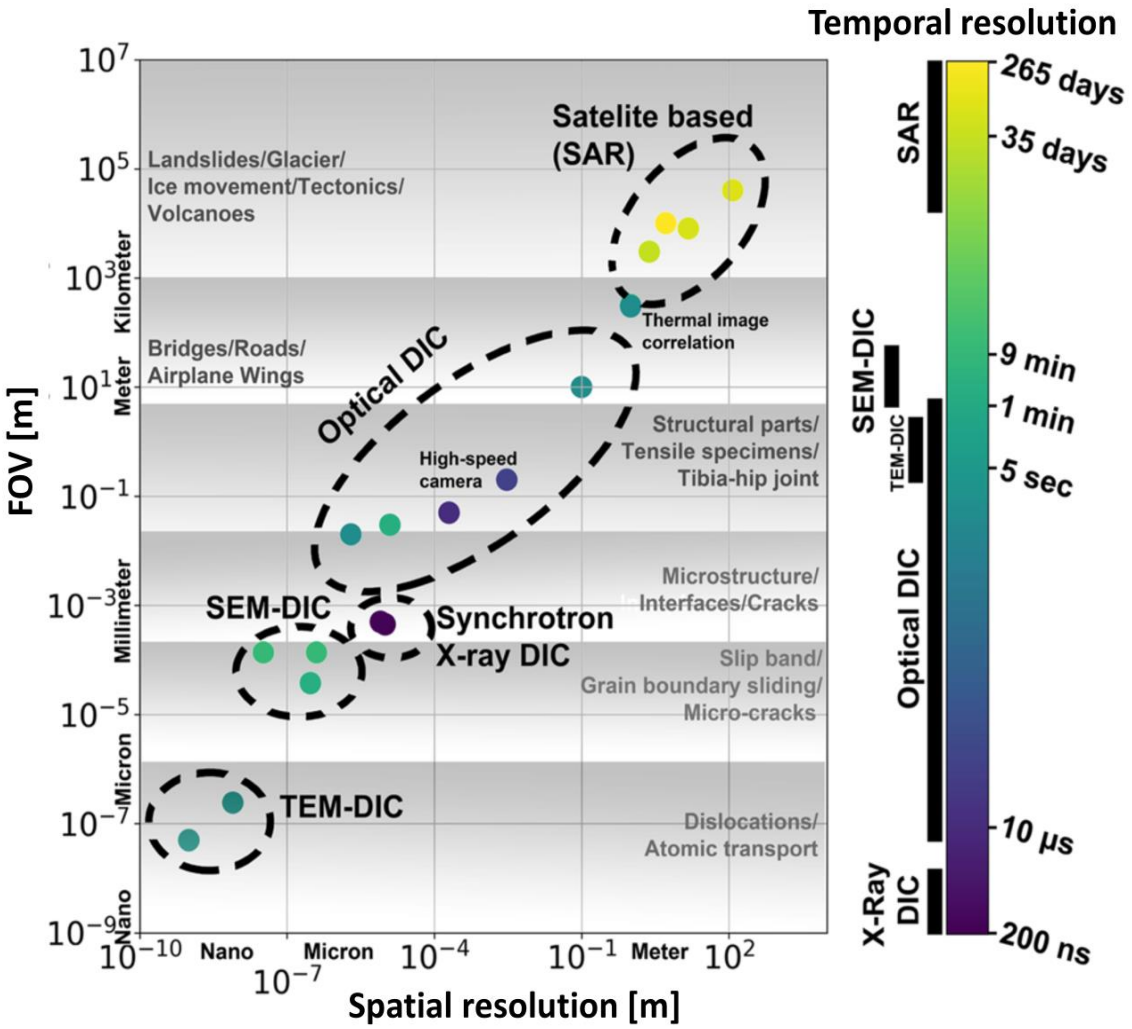

Figure 20: Application of DIC in various fields of research (visualised as coloured dots), grouped according to digital imaging devices (dashed ellipses), field of view (FOV), spatial resolution, and temporal resolution. SAR: Synthetic Aperture Radar [133].

2.4.1. Creation of artificial speckle patterns for DIC measurements

Dong and Pan [130] mentioned that the accuracy and precision of DIC measurements are directly influenced by the use of a suitable speckle pattern. The following factors were taken into consideration when choosing a suitable speckle pattern: the object or the phenomenon being studied, experiment conditions and digital imaging device used, the desired field of view and spatial resolution, as well as the speckle's creation method. A suitable speckle pattern should possess the following characteristics: have good contrast and good adherence with the surface of the test sample, in addition to being non-periodic (i.e. random) and does not exhibit directionality to facilitate full-field surface displacement and strain mapping in all directions. Reu [143] suggested that a suitable speckle pattern should have speckles that were at least 3 pixels in size to avoid aliasing effects (i.e. speckle edges were not well defined) when the speckle pattern was captured via digital imaging devices.

It was reported that naturally occurring patterns in a material's microstructure (e.g. grain boundaries and second phases in metals) may be used for DIC measurements

[130]. However, its application was restricted to the grain scale due to its limited spatial resolution and insufficient contrast with other microstructural features. Artificial speckle patterns with customisable speckle sizes are scalable to different spatial resolutions and can be created via a variety of methods. The commonly used methods for creating artificial speckle patterns include spray-painting or airbrushing [144], as well as gold nano-film remodelling [137,138]. Recently, Hoefnagels et al. [36] utilised magnetron sputtering to create sub-micron sized speckle patterns for studying the microscale plastic strain localisation near the fracture location of a polycrystalline Fe foil. This methodology was also applied in their subsequent work to study the strain partitioning in conventionally processed ferritic-pearlitic steel [139]. However, a suitable speckle pattern for studying the microscale plastic strain localisation in SLM 18Ni-300 maraging steel is yet to be developed.

2.5. Plastic deformation and strain localisation in metals

Plastic deformation in metals occur when it is loaded beyond its elastic limit, causing an irreversible change in shape. Continued loading would result in damage and failure, which is undesirable in engineering components. Weidner [145] explained that plastic deformation in metals is caused by a multitude of loading conditions, including uniaxial tension or compression, cyclic loading (i.e. fatigue), multiaxial loading, impact loading, and thermal loading. Plastic strain localisation phenomena that occur at the macroscopic scale include necking and propagation of Lüders bands. Necking is often observed in metals subjected to tensile loading, where a continuous reduction in cross-sectional area and high stress concentration around that area can be identified as the deformation progressed. Lüders bands would form on the onset of plastic deformation in metals subjected to tensile loading, and would propagate along the entire gauge length of the test sample as the deformation progressed. The formation of Lüders bands was reported to be influenced by the geometry of test samples. In particular, Lüders bands would initiate preferably at the shoulder regions of test samples with rectangular cross-sections due to the increased stress concentration around that region.

The plastic strain localisation phenomena that occur at the microscale include the activation of deformation mechanisms such as dislocation slip and deformation twinning. This resulted in the formation of microscopic slip bands, deformation bands, and persistent slip bands on the material's surface [145]. Micrographs of these phenomena are shown in **Figure 21**. Slip bands occur due to the activation of slip systems during plastic deformation, and are restricted to the grain size of the metal. Primary and secondary slip bands can be distinguished depending on the crystallographic orientation and resolved shear strain of individual grains. Primary slip bands and secondary slip bands can be distinguished according to the resolved shear strain of individual grains. Deformation bands occur due to deformation twinning within individual grains, identified as regions with deviating stain state as compared to its surroundings and are often accompanied by variation in orientation or dislocation density. Plastic strain localisations that arise due to cyclic loading are known as persistent slip bands, and are named as such due to its repeated occurrence at the same location of the test sample after repolishing and continued cyclic loading. The occurrence of microscale plastic strain localisation was identified to be directly influenced by the material's chemical composition, crystal structure, stacking fault energy, grain size and orientation, loading conditions, as well as temperature.

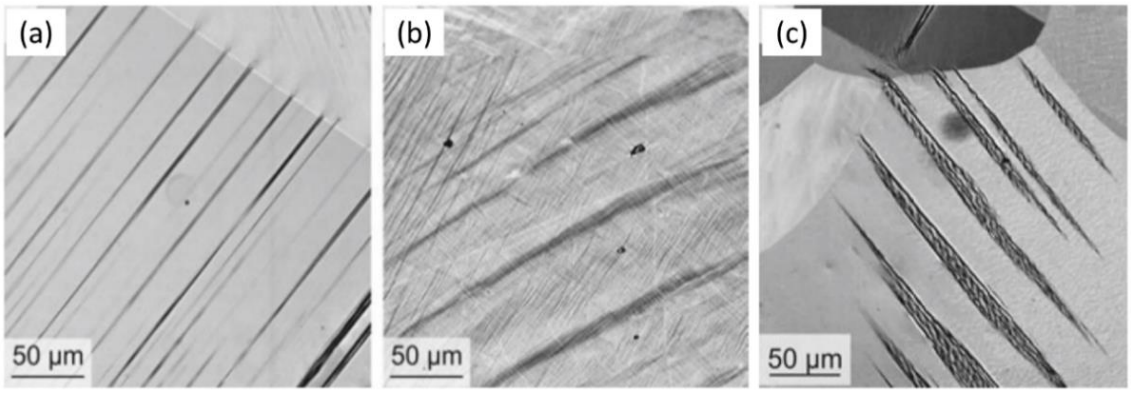

Figure 21: Microscale plastic strain localisation in metals, where (a) shows slip bands in polycrystalline nickel under tensile loading, (b) shows deformation bands in polycrystalline steel under tensile loading, and (c) shows persistent slip bands in polycrystalline nickel cyclically deformed at a plastic strain amplitude of 5×10^{-4} up to 30,000 cycles [145].

2.5.1. Application of SEM-DIC in investigations on the microscale plastic strain localisation in steels

Recently, SEM-DIC has been implemented together with EBSD in challenging investigations to uncover the plastic deformation mechanisms, microscale plastic strain localisation, and active slip systems in steels. This methodology enables researchers to characterise the microscale plastic strain localisation in steels in relation to its microstructure with nanoscale spatial resolution. Stinville et al. [146] highlighted the importance of SEM-DIC for experimental quantification of microscale plastic strain localisation in steels and other metals [137–139,147], identification of active slip and twinning systems during deformation [38,148–150], in addition to numerical verification of crystal plasticity simulations [151–154].

Polatidis et. al. [138] utilised SEM-DIC to investigate the interplay between plastic deformation mechanisms in conventionally processed austenitic AISI 304 stainless steel subjected to uniaxial and equibiaxial loading. For uniaxial loading, microscale plastic strain localisation was initially dominated by slip in the $(\bar{1}\bar{1}1)[01\bar{1}]$ slip system, and the formation of strong $< 111 >$ grain texture. Subsequent deformation resulted in twinning, and martensitic phase transformation was retarded due to the lack of intersecting slip systems. For equibiaxial loading, slip occurs in $(1\bar{1}1)[0\bar{1}\bar{1}]$ and $(\bar{1}11)[01\bar{1}]$ slip systems, and strong $< 110 >$ grain texture was identified. Subsequent deformation resulted in earlier martensitic phase transformation at the intersections of slip systems. It was deduced that the activation of multiple slip planes and their intersections created more nucleation sites for martensitic phase transformation. The preferred deformation mechanism was identified to be influenced by the loading conditions and grain texture.

Vermeij and Hoefnagels [139] utilised SEM-DIC to investigate the microscale plastic strain localisation and damage in conventionally processed ferritic-pearlitic steel. The evolution of microscale plastic strain localisation was characterised using global Von Mises surface strain at $\overline{\varepsilon_{vM}} = 0.07, 0.12, 0.36$ (**Figure 22**). During uniaxial tensile loading, strain partitioning between ferrite and pearlite phases arose due to the differences in

microhardness between them. Initially, microscale plastic strain localisation was identified in ferrite phase due to it being the softer phase, while the hard cementite lamellae of the pearlite phase hindered plastic deformation of the pearlite phase. Subsequent deformation led to the build-up of stress concentration in the ferrite phase, ultimately resulting in brittle facture in the cementite lamellae of the pearlite phase.

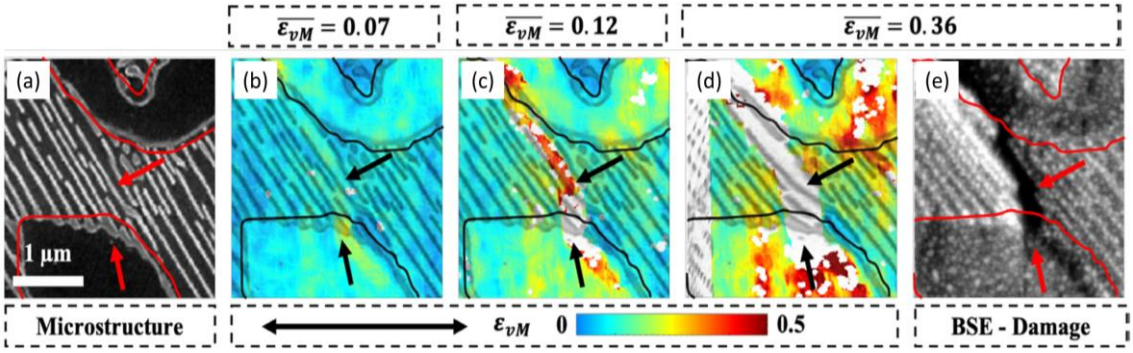

Figure 22: Evolution of microscale plastic strain localisation and damage in ferritic-pearlitic steel captured via SEM-DIC, with (a) showing the pearlite phase with bright cementite lamellae, (b, c, d) showing localised and global Von Mises surface strain (ε_{vM} and $\overline{\varepsilon_{vM}}$) obtained from SEM-DIC, and (e) showing crack in the pearlite phase. The ferrite grain boundaries are drawn as red or black lines, and tensile loading occurs along the horizontal axis [139].

Recently, researchers have utilised SEM-DIC to investigate the microscale plastic strain localisation in additively processed (i.e. SLM) 316L stainless steel [140–142]. Bean et al. [140] reported that dislocation slip, deformation twinning, and martensitic phase transformation may be active concurrently at different stages during the plastic deformation of SLM 316L stainless steel. SEM-DIC analysis revealed that plastic strain localisation occurred heterogeneously due to the non-uniform distribution of rapid solidification-induced cellular structures and the high density of low-angle grain boundaries (LAGBs) throughout the sample. Strengthening in SLM 316L stainless steel was due to the cellular structures acting as forest-type dislocation obstacles during plastic deformation. Furthermore, An et al. [141] reported that the intrinsic arrangement of dislocations in the cellular structures acted as dislocation sources during plastic deformation. This resulted in the formation of slip bands with extremely fine band spacing (35.0 ± 5.0 nm). Hu et al. [142] studied the plastic strain localisation in SLM 316L stainless steel via SEM-DIC and crystal plasticity simulations. It was reported that plastic strain localisation was more concentrated in grains smaller than 50 µm^2 due to the presence of residual stress after SLM fabrication. The contribution of residual stress to plastic strain localisation was less significant compared to the deformation incompatibility between neighbouring grains.

Recent investigations have applied SEM-DIC to investigate the microscale plastic strain localisation in conventionally processed 304 stainless steel [138], conventionally processed ferritic-pearlitic steel [139], as well as additively processed (i.e. SLM) 316L stainless steel [140]. At the time of writing, the microscale plastic strain localisation in SLM 18Ni-300 maraging steel is yet to be elucidated in the literature.

2.6. Summary and identified gaps in current literature

The advent of metal AM technologies such as selective laser melting (SLM), electron beam melting (EBM), and directed energy deposition (DED) have revolutionised current manufacturing practices [44]. In particular, SLM has been applied in the medical, aerospace, automotive, and mould making industries for the fabrication of engineering components [3–6]**.**

In the mould making industry, researchers and mould makers have utilised SLM to fabricate 18Ni-300 maraging steel moulds with conformal cooling channels [20,21,90]. Conformal cooling channels provide increased cooling efficiency over conventional straight-drilled cooling channels due to its design which follows the contour of the injection moulded component. However, it was reported in literature that the widespread application of SLM for mould making was hindered by issues found in additively manufactured moulds. In particular, the 18Ni-300 maraging steel moulds possessed a heterogeneous microstructure and exhibited anisotropic mechanical properties [25,26,61]. Furthermore, the lack of process optimisation led to the fabrication of steel moulds with manufacturing defects, resulting in inferior mechanical properties as compared to conventionally made moulds [19,23]. A deeper understanding of the process-microstructure-properties relationships in SLM 18Ni-300 maraging steel is needed to fabricate steel moulds with high relative density and mechanical properties that are comparable with conventionally made moulds.

Following that, the identified research gaps in current literature are summarised in the following:

1. In **Section 2.1.2**, it was identified that the heterogeneous microstructure and anisotropic mechanical properties in SLM 18Ni-300 maraging steel and other additively processed steel mould materials were influenced by the rapid solidification phenomenon during the SLM process [70,84,98,99]. However, the influence of SLM process parameters (or in-process parameters) on their microstructure evolution and mechanical properties have not been comprehensively analysed in the literature. This research gap is addressed in **Section 2.3**.
2. In **Section 2.1.3**, statistical optimisation methods such as analysis of variance (ANOVA) have been utilised to optimise SLM in-process parameters for fabricating 18Ni-300 maraging steel samples [28,63,64]. However, these studies were limited to single-response optimisation, e.g. focusing on either relative density or hardness [63]. A comprehensive optimisation methodology incorporating the multi-response optimisation of several mechanical properties for SLM 18Ni-300 maraging steel is yet to be reported in the literature. This research gap is addressed in **Chapter 3 Section 3.3**. Supplementary experiments were conducted to investigate the influence of SLM in-process parameters and porosity on the fabricated samples, with the aim of obtaining a deeper understanding on the process-microstructure-properties relationships in SLM 18Ni-300 maraging steel. The findings are presented in **Chapter 3 Section 3.2** and **3.4**.
3. In **Section 2.4.1**, researchers have reported using scanning electron microscope-based digital image correlation (termed SEM-DIC) to investigate the microscale plastic strain localisation in steels [131]. The spatial resolution of SEM-DIC

measurements was directly dependent on the speckle pattern and digital imaging device used. Literature suggested using magnetron sputtering to create sub-micron sized speckle patterns for SEM-DIC investigations [36]. However, a suitable speckle pattern for SEM-DIC investigations of microscale plastic strain localisation in SLM 18Ni-300 maraging steel is yet to be developed. This research gap is addressed in **Chapter 4 Section 4.2**.

4. In **Section 2.5.1**, it was identified that the occurrence of microscale plastic strain localisation in SLM 316L stainless steel (i.e. dislocation slip and deformation twinning) was found to be directly influenced by the rapid solidification-induced cellular structures in the material [140]. However, the influence of microstructural heterogeneity (i.e. variations in grain size and crystallographic texture) on the microscale plastic strain localisation in SLM 18Ni-300 maraging steel is yet to be elucidated in current literature. This research gap is addressed in **Chapter 4 Section 4.3**.

3. Influence of SLM in-process parameters on microstructure and mechanical properties of SLM 18Ni-300 maraging steel

3.1 Introduction

The occurrence of microstructural heterogeneity and mechanical anisotropy has been reported in SLM 18Ni-300 maraging steel moulds [25,26,61]. Both microstructural heterogeneity and mechanical anisotropy were attributed to the complex laser-powder interactions inherent to the SLM process [13]. In particular, the formation of equiaxed and columnar grains led to microstructural heterogeneity in the as-built samples. In addition, the presence of columnar grains and pronounced crystallographic texture resulted in mechanical anisotropy due to the directional solidification of the microstructure. The complex laser-powder interactions in SLM process also resulted in manufacturing defects such as pores and cracks (**Figure 4**, [14]). The issues found in additively manufactured metal components (AMMCs) were further discussed in **Chapter 2 Section 2.1.2**.

In **Chapter 2 Section 2.1.3**, researchers have utilised statistical optimisation methods to determine optimal processing conditions for fabricating SLM 18Ni-300 maraging steel samples with reduced manufacturing defects and mechanical properties comparable with their conventionally made counterparts [28,63,64]. However, statistical optimisation methods such as response surface methodology (RSM) and analysis of variance (ANOVA) were applied to varying extents across the cited investigations [28,63,64], indicating a lack of standardisation. In particular, the Taguchi methods such as orthogonal arrays were not employed in the design of experiments of the cited investigations, and ANOVA was not applied by Mutua et al. [28] to analyse the statistical variance in the experimental results obtained. Furthermore, the cited investigations were limited to single-response optimisation, i.e. the optimisation of one response variable at a time. A more comprehensive optimisation methodology incorporating the multi-response optimisation of several response variables would be desirable, as it allows for the simultaneous optimisation of several mechanical properties via the use of a suitable set of SLM process parameters (or in-process parameters). Subsequently, statistical optimisation methods alone are unable to provide an in-depth understanding of the process-microstructure-properties relationships in SLM 18Ni-300 maraging steel. Additional experimental investigations are necessary to obtain further insights and to adequately address the issues related to microstructural heterogeneity and mechanical anisotropy in the fabricated samples.

In the present chapter, a combined statistical optimisation methodology incorporating Taguchi methods and grey relational analysis (GRA) was implemented to determine suitable SLM in-process parameters for fabricating SLM 18Ni-300 maraging steel samples with reduced manufacturing defects and mechanical properties comparable with conventionally made condition. Supplementary experiments were also conducted to obtain further insights of the process-microstructure-properties relationships in said material and to support the statistical findings obtained via the combined statistical optimisation methodology. RSM was not employed in the combined statistical optimisation methodology due to its inherent limitation to single-objective optimisation.

Following that, the objectives of the experimental investigations in the present chapter include:

1. To investigate the influence of SLM in-process parameters on the microstructure and mechanical properties of SLM 18Ni-300 maraging steel (**Section 3.2**). The investigated SLM in-process parameters include: laser power (P), scanning speed (v), and hatch spacing (h). The build quality of additively manufactured individual scan tracks and fully built samples was evaluated to obtain further insights on the influence of SLM in-process parameters.
2. To identify the order of influence of SLM in-process parameters (i.e. $p, v, \text{and } h$) on a particular mechanical property using Taguchi methods, specifically orthogonal arrays, signal-to-noise ratios (SNRs), and ANOVA (**Section 3.3**).
3. To determine optimal SLM in-process parameters (i.e. combination of $p, v, \text{and } h$) for the multi-response optimisation of several mechanical properties using GRA. Mechanical properties to be optimised include: ultimate tensile strength (R_m), elongation at fracture (A_t), hardness, and impact energy (KV_2) (**Section 3.3**).
4. To investigate the influence of porosity on the macroscale plastic strain localisation and fracture in samples subjected to uniaxial tensile loading using optical imaging-based digital image correlation (optical-DIC) (**Section 3.4**).

The experimental findings in the present chapter were discussed in **Sections 3.2** to **3.4**, and collectively summarised in **Section 3.5**. The experimental findings were subsequently published in two peer-reviewed papers [40,41]. The contents in the present chapter may differ slightly from the published version, as they were reorganised to align with the structure of the present thesis.

3.2. Experiments on additively manufactured individual scan tracks and fully built samples

3.2.1. Experimental methodology

The SLM process features a multitude of in-process parameters, which can be grouped into four categories: laser related, scan related, powder related, and temperature related [31,32]. The following three SLM process parameters (or in-process parameters) were selected for the present investigation: laser power (P), scanning speed (v), and the hatch spacing between scan tracks (h). These three SLM in-process parameters were selected due to their direct contribution towards the amount of laser energy transferred to the metal powder, and were determined based on the equation for volumetric energy density ($E_{volumetric}$). Layer thickness (t_{layer}) was not included in the present investigation, because the inclusion of another parameter would have significantly increased the time and cost required to conduct additional experimental runs, with the risk that they may not yield additional meaningful results.

The amount of laser energy transferred to the metal powder during the SLM process can be expressed in terms of the linear energy density (E_{linear}) and volumetric energy density ($E_{volumetric}$) as shown in **Equations (1)** and **(2)**, respectively [31]:

$$E_{linear} = \frac{P}{v} \quad \textbf{(1)}$$

$$E_{volumetric} = \frac{P}{v \times h \times t_{layer}} \quad \textbf{(2)}$$

The layer thickness is denoted as t_{layer} in **Equation (2)**. In particular, E_{linear} is used to calculate the amount laser energy transferred per unit length of a scan track, while $E_{volumetric}$ is used to calculate the amount of laser energy transferred per unit volume to the melt pool during fabrication.

Two different approaches were used to investigate the influence of SLM in-process parameters. For the first approach, the influence of P and v were investigated by evaluating the build quality of additively manufactured individual scan tracks. An additively manufactured scan track with good build quality is expected to be free of manufacturing defects and possess a uniform shape due to the complete melting and fusion of powder material. Six SLM parameter configurations were chosen, as shown in **Table 6**. The optimal SLM processing conditions suggested by Mutua et al. [28] was used as reference when selecting the SLM parameter configurations for the present investigation. Six individual scan tracks (representing configurations A-1 to A-6) were deposited 1 mm apart from each other on the top surface of a 18Ni-300 maraging steel substrate block using an EOS M290 metal 3D printer (**Figure 23**). The build quality of each individual scan track was evaluated by examining its cross-section via Leica DM2500 M optical microscope. The cross-section of individual scan tracks were polished using standard metallography techniques and chemically etched using 8 % Nital solution to reveal its microstructure and melt pool boundaries. The results are presented and discussed in **Section 3.2.2**.

Table 6: The SLM in-process parameter configurations used to fabricate individual scan tracks.

Config.	P [W]	v [mm s^{-1}]	E_{linear} [J m^{-1}]
A-1	150	700	214.29
A-2	200	700	285.71
A-3	250	700	357.14
A-4	300	700	428.57
A-5	300	800	375.00
A-6	300	900	333.33

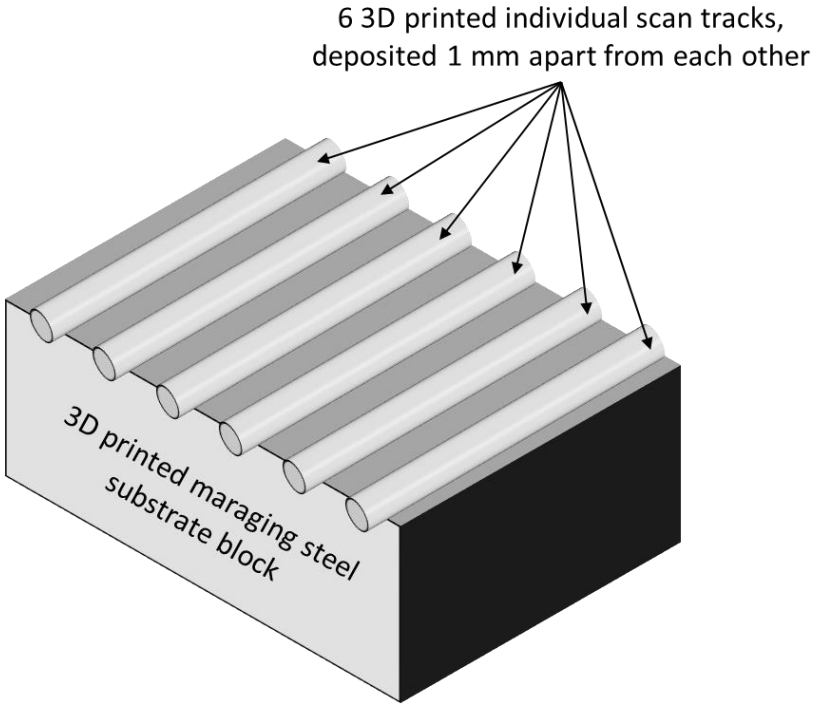

Figure 23: Schematic showing the additively manufactured individual scan tracks.

For the second approach, the influence of v and h were investigated by studying the relative density of fully built cube samples and the mechanical properties of tensile test samples. Another six SLM parameter configurations were selected for fabricating the samples, as shown in **Table 7**. An orthogonal scanning strategy featuring a zig-zag scanning pattern with 90 ° rotation for subsequent layers was used to 3D print samples with high relative density [25]. The P and t_{layer} was set to 300 W and 0.03 mm respectively. The base plate was preheated to 100 ℃. The 18Ni-300 maraging steel powder used in the present investigation was produced via gas atomisation. The powder particles have an average particle size of 33 μm, and its chemical composition is shown in **Table 8**.

Table 7: The SLM in-process parameter configurations and the mechanical properties of fully built samples. The P and t_{layer} was fixed at 300 W and 0.03 mm, respectively. The maximum value of each property was highlighted using bold text. R_m: Ultimate tensile strength. $R_{p0.2}$: 0.2 % proof strength. E: Modulus of elasticity. A_{t}: Elongation at fracture. $\rho_{relative}$: Relative density.

Config.	SLM in-process parameters				Mechanical properties				$\rho_{relative}$ [%]
	v [mm s^{-1}]	h [mm]	E_{linear} [J m^{-1}]	$E_{volumetric}$ [J mm^{-3}]	R_m [MPa]	$R_{p0.2}$ [MPa]	E [GPa]	A_{t} [%]	
B-1	700	0.08	**428.57**	**178.57**	1203	1101	167	**10.2**	97.66
B-2	700	0.10	**428.57**	142.86	**1204**	**1104**	162	8.3	**99.71**
B-3	800	0.08	375.00	156.25	1187	1090	164	8.4	96.69
B-4	800	0.10	375.00	125.00	1191	1067	**172**	6.8	98.78
B-5	900	0.08	333.00	138.89	1200	1093	170	8.1	96.31
B-6	900	0.10	333.33	111.11	1169	1048	163	7.9	96.85
Conventional wrought condition [83]					1000-1170	760-895	180	6-15	–

Table 8: Chemical composition of 18Ni-300 maraging steel powder used in the present investigation.

Element [wt. %]	Ni	Co	Mo	Ti	Al	Si	C	S	P	Fe
	17.9	9.1	5.04	0.81	0.11	0.02	0.007	0.002	0.001	Bal.

Relative density tests were conducted for cube samples according to ISO 3369 standard, and the relative density of each cube sample was calculated via Archimedes' principle as shown in **Equation (3)**:

$$\rho_{relative} = \left(\frac{m_{air}\rho_{water}}{m_{submerged}}\right)\left(\frac{1}{\rho_{MS}}\right) \text{ x } 100\ \% \qquad \textbf{(3)}$$

The relative density is denoted as $\rho_{relative}$, the density of distilled water is ρ_{water}, taken as 0.997 g cm^{-3} at 25 °C (as defined in ISO 3369), and the theoretical full density of 18Ni-300 maraging steel is ρ_{MS}, taken as 8.1 g cm^{-3} [18]. The mass of samples when weighed in air is m_{air}, the mass of displaced liquid when the samples are submerged in water is $m_{submerged}$. Cube samples measuring 10 mm in length were fabricated for all six configurations in **Table 7**. The build quality of cube samples were evaluated by examining its cross-section using the Leica DM2500 M optical microscope. The results are presented and discussed in **Section 3.2.3**.

Subsequently, tensile tests were conducted using a WDW-50 universal tensile test machine according to ISO 6892-1 standard at room temperature, and the cross-head separation rate was set to 0.5 mm min^{-1}. The tensile test samples fabricated for the six configurations in **Table 7** have a gauge length of 20 mm and a rectangular cross-

section measuring 5 mm in width and 2 mm in thickness. The mechanical properties of interest include ultimate tensile strength (R_m), 0.2 % proof strength ($R_{p0.2}$), modulus of elasticity (E), and elongation at fracture (A_t). The results are presented in **Table 7** and discussed together with the build quality of cube samples in **Section 3.2.3**.

3.2.2. Build quality of additively manufactured individual scan tracks

Shown in **Figure 24** are the cross-sections of the six individual scan tracks fabricated using configurations A-1 to A-6, arranged according to increasing E_{linear}. Higher E_{linear} was achieved by using a higher P or lower v during fabrication. Incomplete melting of powder particles was observed in **Figure 24**(a and c), while pores were observed in **Figure 24**(d and e). Furthermore, a gap was observed in **Figure 24**(b) indicating incomplete fusion between the scan track and the substrate surface. However, no manufacturing defects were observed in **Figure 24**(f).

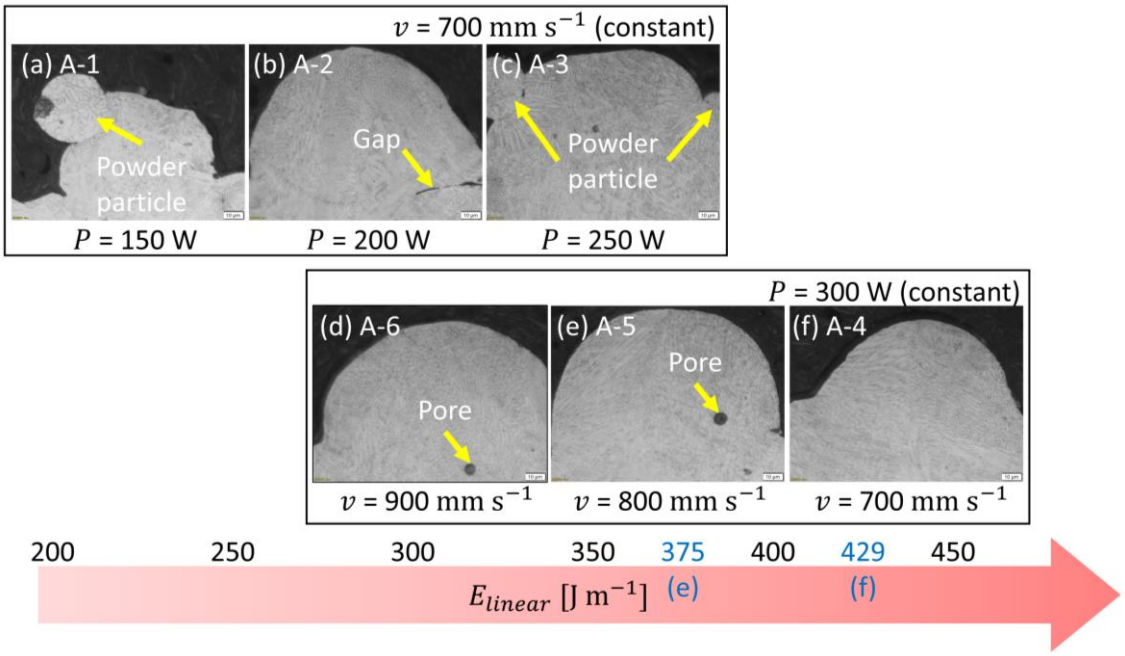

Figure 24: The influence of (a-c) increasing P and (d-f) reducing v on the build quality of additively manufactured individual scan tracks. The micrographs for the cross-section of individual scan tracks are arranged according to increasing E_{linear}. The E_{linear} for (e) and (f) are indicated using blue text. The configuration numbers from **Table 6** are included in the figure.

It can be deduced that the occurrence of manufacturing defects was due to the lower E_{linear} during the SLM process, particularly the usage of configurations with $E_{\text{linear}} \leq 375.00$ J m^{-1} (**Figure 24**(a-e)). It can be deduced that the lower laser energy supplied (150 – 250 W) during the SLM process resulted in the incomplete melting and fusion of adjacent powder particles (**Figure 24**(a-c)). In contrast, a more uniform melt pool shape can be observed when the laser power was increased to 300 W (**Figure 24**(d-f)). Zhang et al. [9] explained that the use of lower laser energy resulted in a smaller melt pool, due to the energy supplied being insufficient to cause complete melting of adjacent powder particles and create enough overlap between them.

Besides that, the use of higher scanning speeds (800 – 900 $\mathrm{mm\ s^{-1}}$) resulted in pores forming in the microstructure after solidification (**Figure 24**(d-e)). Zhang et al. [9] explained that the melt pool would experience rapid cooling during solidification, and the dissolved gas particles were unable to escape the melt pool in time before solidification had completed.

It can be concluded that configuration A-4 is better compared to the other configurations in **Table 6**. This is because the higher E_{linear} of this configuration (428.57 $\mathrm{J\ m^{-1}}$) resulted in complete melting and fusion of the adjacent powder particles, the creation of a more uniform melt pool shape, as well as reduced occurrence of manufacturing defects.

3.2.3. Build quality and mechanical properties of fully built samples

Shown in **Figure 25** are the cross-sections of the cube samples fabricated via configurations B-1 to B-6, arranged according to its corresponding $E_{volumetric}$ and $\rho_{relative}$. **Figure 25**(d) shows a zoomed-in image of the microstructure where multiple rows of semi-ellipses were observed after chemical etching. The semi-ellipses were identified as the cross-sections of individual melt pools, and similar patterns were observed in **Figure 25**(a-g). This characteristic pattern was created as a result of the scanning strategy used during the SLM process, and was consistent with those reported in current literature [84,99]. During the SLM process, the laser would selectively melt regions of the powder bed according to the predefined scanning pattern, resulting in the formation of scan tracks with elliptical shaped melt pools as its cross-section. The shape of the melt pools would follow the shape of the laser spot used during the process. This process was repeated layer-by-layer until the sample was fully built, and the repeated scanning of the laser was reported to induce intrinsic heat treatment in the overlapping regions of the scan tracks [84,99].

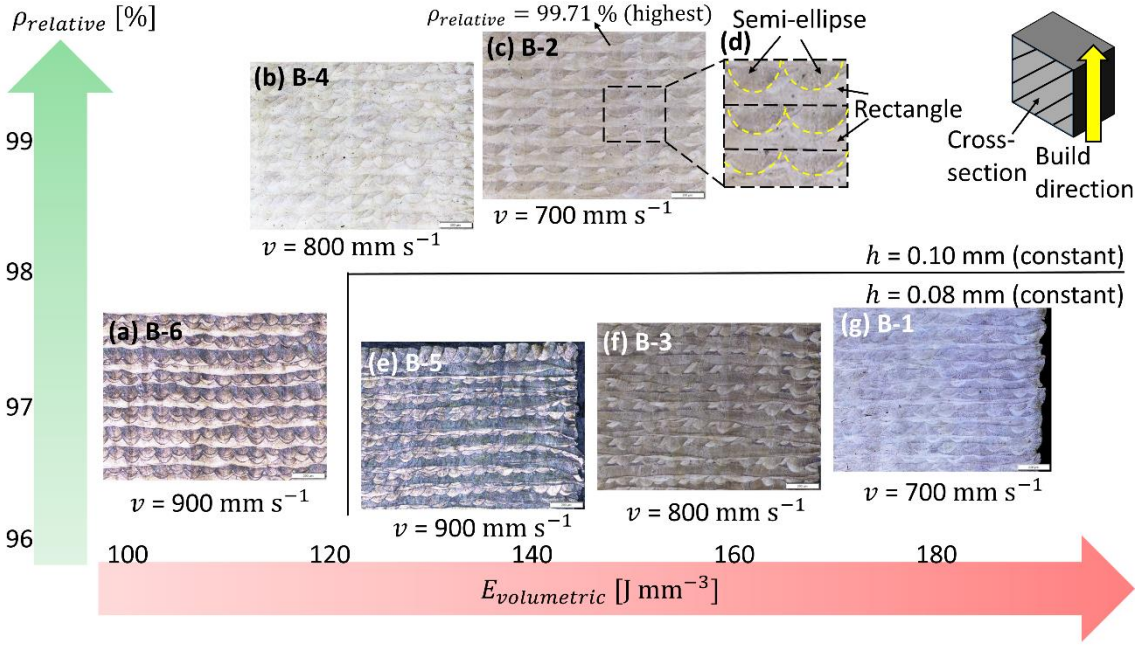

Figure 25: The influence of manipulating v and h on the $\rho_{relative}$ of cube samples. The results are organised into two sets based on a constant h: (a-d) 0.10 mm and (e-g) 0.08

mm. The micrographs for the cross-section of cube samples are arranged according to its corresponding $\rho_{relative}$ and $E_{volumetric}$. The configuration numbers from **Table 7** are included in the figure.

In terms of the build quality of the cube samples, it was identified that the $\rho_{relative}$ had increased as the v was decreased from 900 $\mathrm{mm\,s^{-1}}$ to 700 $\mathrm{mm\,s^{-1}}$ (**Figure 25**(a-c and e-g)). According to **Equation (1)**, a higher E_{linear} can be obtained by using a lower v. As such, the resultant microstructure would contain less manufacturing defects, resulting in increased $\rho_{relative}$ in the cube samples.

It could be deduced that configurations with higher $E_{volumetric}$ would produce samples with higher $\rho_{relative}$. According to **Equation (2)**, a higher $E_{volumetric}$ can be obtained by using a smaller h. The use of a smaller h would lead to increased overlap between the scan tracks, resulting in better bonding between them and reduced porosity. However, the trends for h, $E_{volumetric}$, and $\rho_{relative}$ were identified as different from expected. In particular, $\rho_{relative}$ increased with increasing h (**Figure 25**(a vs. e, b vs. f, c vs. g)). Furthermore, configuration B-2 had produced samples with the highest $\rho_{relative}$ although its $E_{volumetric}$ was lower compared to configurations B-1 and B-3 (**Figure 25**(c vs. f and g)).

Thus, a more correct deduction would be there exists an optimal processing window where the careful selection of SLM parameters would result in the fabrication of samples with high relative density and good mechanical properties. Mutua et al. [28] had identified an optimal processing window for SLM 18Ni-300 maraging steel, which is shown in **Figure 8** (**Chapter 2 Section 2.2.1**). The occurrences of manufacturing defects in SLM 18Ni-300 maraging steel can be greatly reduced by selecting parameters that lie within the optimum processing window.

The mechanical properties of tensile test samples fabricated via config. B-1 to B-6 are tabulated in **Table 7**. The ultimate tensile strength is denoted as R_m, the 0.2 % proof strength is $R_{p0.2}$, the modulus of elasticity is E, and the elongation at fracture is A_t. In particular, the tensile test samples fabricated via configuration B-2 (P = 300 W, v = 700 $\mathrm{mm\,s^{-1}}$, h = 0.100 mm) possessed higher R_m, $R_{p0.2}$ and $\rho_{relative}$ as compared to the other six configurations. Furthermore, the samples fabricated via configuration B-1 and B-4 were identified as having the highest A_t and E respectively among the six configurations. Besides that, the samples fabricated via configurations B-1 to B-6 were identified to have higher $R_m$and $R_{p0.2}$ as compared to conventional wrought condition ($R_m = 1000 - 1170$ MPa, $R_{p0.2} = 760 - 895$ MPa) [83].

3.3. Statistical analysis and optimisation using Taguchi methods and grey relational analysis (GRA)

3.3.1. Experimental methodology

A combined statistical optimisation methodology featuring Taguchi methods and grey relational analysis (GRA) was utilised in the present investigation. The Taguchi methods enable the statistical identification of the most influential SLM process parameter (or in-process parameter) on a particular mechanical property. Following that, GRA was used in the determination of optimal SLM in-process parameters for the multi-response optimisation of the mechanical properties studied in the present investigation. The SLM in-process parameters chosen for the present investigation include laser power (P), scanning speed (v), and hatch spacing (h). A total of four levels were assigned to each SLM in-process parameter as shown in **Table 9**. A $\mathrm{L}_{16}(4^3)$ Taguchi orthogonal array was used to determine the sixteen SLM parameter configurations for the present investigation (**Table 10**). Taguchi orthogonal arrays provide a cost-effective method for obtaining statistically meaningful results with a reduced number of configurations as compared to a full factorial design of experiments [34]. The inclusion of higher scanning speeds instead of lower ones (e.g. 1000 $\mathrm{mm\ s^{-1}}$ instead of 600 $\mathrm{mm\ s^{-1}}$) in **Table 9** was to allow for a clearer comparison of process outcomes and to facilitate the best-worst comparative analysis among the fabricated samples (**Section 3.4**).

An EOS M290 metal 3D printer was used to fabricate all samples studied in the present investigation. The laser spot diameter was fixed at 100 µm, and the base plate was preheated to 100 ℃. An orthogonal scanning strategy consisting of a zig-zag scanning pattern with 90 ° rotation for each subsequent layer was selected for fabricating samples with high relative density [25]. The 18Ni-300 maraging steel powder used for the fabrication of samples have an average particle size of 33 µm, and its chemical composition is shown in **Table 8** (**Section 3.2.1**).

Table 9: The SLM in-process parameters studied in the present investigation.

SLM in-process parameters	Level 1	Level 2	Level 3	Level 4
P [W]	250	275	300	325
v [mm s^{-1}]	700	800	900	1000
h [mm]	0.07	0.08	0.09	0.10

The mechanical properties chosen for optimisation in the present investigation include ultimate tensile strength (R_m), elongation at fracture (A_t), Vickers hardness, and Charpy impact energy (KV_2). The optimization of both R_m and KV_2 is essential for fabricating SLM 18Ni-300 maraging steel moulds that possess high core strength and impact toughness. Larger A_t is desirable because it increases the ductility of the material. Lastly, a high Vickers hardness is important because it provides better polishability as well as resistance to surface indentation during the mould's operation [68,69].

The samples used for mechanical tests were additively manufactured in the form of individual blocks, and machined to the specified dimensions using electrical discharge machining (EDM). The samples were not fabricated to their final dimensions using SLM

to prevent accumulation of residual stress after fabrication. Sample preparation was done following standard metallography procedures. Grinding was done using P240 to P2000 silicon carbide grinding papers until a flat and level surface was obtained. Polishing was done using $1\ \mu m$ diamond suspension, followed by final polish using $0.05\ \mu m$ colloidal silica to obtain a smooth and mirror-like surface finish. The results obtained from mechanical tests were reported in terms of the arithmetic mean of three repeated readings for each SLM parameter configuration. The measurement uncertainty in repeated readings was quantified using standard error and presented together with the results in **Figure 26** (**Section 3.3.3**).

Table 10: The 16 SLM parameter configurations determined via Taguchi orthogonal array $(L_{16}4^3)$. The t_{layer} was fixed at 0.04 mm during fabrication.

Config.	P [W]	v [mm s^{-1}]	h [mm]	E_{linear} [J m^{-1}]	$E_{volumetric}$ [J mm^{-3}]
1	250	700	0.07	357.14	127.55
2	250	800	0.08	312.50	97.66
3	250	900	0.09	277.78	77.16
4	250	1000	0.10	250.00	62.50
5	275	700	0.08	392.86	122.77
6	275	800	0.07	343.75	122.77
7	275	900	0.10	305.56	76.39
8	275	1000	0.09	275.00	76.39
9	300	700	0.09	428.57	119.05
10	300	800	0.10	375.00	93.75
11	300	900	0.07	333.33	119.05
12	300	1000	0.08	300.00	93.75
13	325	700	0.10	464.29	116.07
14	325	800	0.09	406.25	112.85
15	325	900	0.08	361.11	112.85
16	325	1000	0.07	325.00	116.07

Tensile tests were conducted at room temperature according to ISO 6892-1 standard using a WDW-50 universal tensile test machine. A cross-head separation rate of $0.5\ \mathrm{mm\ min^{-1}}$ was used for the test. Two samples were fabricated for each SLM parameter configuration. Each sample has a gauge length of 20 mm and a rectangular cross-section measuring 5mm in width and 2mm in thickness.

Hardness tests were conducted using a 430 SVA Vickers hardness tester with an applied load of 49.03 N (HV 5). The test was conducted at room temperature in accordance with ISO 6507-1 standard. An additively manufactured rectangular metal piece with a base area of 8 mm by 8 mm and a thickness of 2 mm was used for the hardness test of each SLM parameter configuration. A total of six indents were made on the top surface of each metal piece.

Impact tests were conducted according to ISO 148-1 standard using a PIT 750 metal pendulum impact tester. Three samples were additively manufactured for each SLM parameter configuration with dimensions as specified in the standard (i.e. 55 mm by 10 mm by 10 mm). A V-shaped notch measuring 2 mm in depth was made on each

sample, and a striker with 2 mm radius was used during the test. A total of three readings were recorded for each SLM parameter configuration, and the results were presented in terms of the energy absorbed by the V-notch test samples (KV_2). The results for mechanical tests are presented and discussed in **Section 3.3.3**.

3.3.2. Statistical optimisation methods

3.3.2.1. Taguchi methods: SNR and ANOVA

The Taguchi methods were developed by Dr. Genichi Taguchi to improve the quality of manufactured products and to optimise manufacturing processes via statistical analysis. This methodology offers a systematic way for investigating complex problems where multiple factors (i.e. process parameters) are involved, and is particularly useful for determining the main contributing factors that influence a particular response (i.e. mechanical property). In Taguchi methods, the experiment data are analysed in two phases: the signal-to-noise ratio (SNR, η), and the analysis of variance (ANOVA)[34].

The first phase of the analysis involves the conversion of experimental data into SNR. One of the following quality characteristics is chosen for the conversion: higher is better, lower is better, or nominal is best. The equations for converting experimental data into SNR are shown in **Equation (4)** [34,155]:

$$\text{SNR}, \eta = \begin{cases} -10 \log\left(\frac{1}{r}\sum_{i=1}^{r}\frac{1}{y_i^2}\right) & \text{Higher is better} \\ -10 \log\left(\frac{1}{r}\sum_{i=1}^{r} y_i^2\right) & \text{Lower is better} \\ -10 \log\left(\frac{1}{r}\sum_{i=1}^{r}(y_i - y_0)^2\right) & \text{Nominal is best} \end{cases} \quad \textbf{(4)}$$

where r is the number of readings, y_i is the response obtained for that particular configuration, and y_0 is the reference response. In the present investigation, the higher is better quality characteristic was chosen in order to obtain better mechanical properties.

Next, a response table was used to determine the order of influence of each SLM process parameter on a particular response. the mean SNR for each parameter level was calculated using **Equation (5)** [34,155]:

$$\text{Mean SNR} = \frac{1}{N}\sum_{i=1}^{N}\eta_i \quad \textbf{(5)}$$

where N denotes the number of occurrences of that parameter level in the Taguchi orthogonal array. Following that, the main effects plot was generated for each response using the values from the response table. The main effects plot provides a graphical interpretation for the deviation in the results obtained as compared to the mean value, as well as a visual identification for the optimal SLM parameter configuration for a particular response.

The second phase of the analysis involves the use of ANOVA to evaluate the variability in the results obtained, and to determine the percentage contribution of each factor on a particular response. ANOVA is commonly used to determine the source of variance and to gauge the confidence level of the data obtained. The formulas used for

ANOVA calculations are shown in **Table 11**. The F-ratio (also known as variance ratio) is used to evaluate the significance of a particular factor on the response studied by comparing it with the critical F-ratio obtained from standard F-tables [34]. A factor is considered as having a significant influence on the response if the F-ratio obtained from ANOVA calculations is larger than the critical F-ratio. The results are presented and discussed in **Section 3.3.4**.

Table 11: Table of formulae for ANOVA [34,155].

Responses	Factors	DOF, f	Sum of squares, S	Variance, V	F-ratio, F	Percentage contribution, C (%)
Mechanical property, e.g. R_m	P	$f_P = L_P - 1$	$S_P = \left[\sum_{j=1}^{L} \frac{1}{N_j}\left(\sum_{i=1}^{N} \eta_{Pij}\right)^2\right] - S_m$	$V_P = \frac{S_P}{f_p}$	$F_P = \frac{V_P}{V_e}$	$C_P = \frac{S_P}{S_T}\ x\ 100$
	v	$f_v = L_v - 1$	$S_v = \left[\sum_{j=1}^{L} \frac{1}{N_j}\left(\sum_{i=1}^{N} \eta_{vij}\right)^2\right] - S_m$	$V_v = \frac{S_v}{f_v}$	$F_v = \frac{V_v}{V_e}$	$C_v = \frac{S_v}{S_T}\ x\ 100$
	h	$f_h = L_h - 1$	$S_h = \left[\sum_{j=1}^{L} \frac{1}{N_j}\left(\sum_{i=1}^{N} \eta_{hij}\right)^2\right] - S_m$	$V_h = \frac{S_h}{f_h}$	$F_h = \frac{V_h}{V_e}$	$C_h = \frac{S_h}{S_T}\ x\ 100$
	Error, e	$f_e = f_{Total} - f_p - f_v - f_h$	$S_e = S_T - S_P - S_v - S_h$	$V_e = \frac{S_e}{f_e}$	$F_P = \frac{V_e}{V_e} = 1$	$C_e = \frac{S_e}{S_T}\ x\ 100$
	Total, T	$f_T = n - 1$	$S_T = \sum_{i=1}^{n} \eta_i^2 - S_m$	–	–	$C_P + C_v + C_h + C_e = 100\ \%$
	Mean sum of squares, S_m	–	$S_m = \frac{1}{n}(\sum_{i=1}^{n} \eta_i)^2$	–	–	–

n : Total no. of SLM parameter configurations in Taguchi orthogonal array, i.e. 16 for the present investigation.
N : No. of occurrences of that parameter level in the Taguchi orthogonal array, i.e. 4 for each parameter level.
L : No. of levels for each parameter, i.e. 4.
η : signal-to-noise ratio for that response.

3.3.2.2. Grey relational analysis (GRA)

Grey relational analysis (GRA, also known as grey incidence analysis, GIA) was developed by Prof. Julong Deng as a means to study control systems that contain partially known and unknown information (i.e. grey systems). The objective of GRA is to understand the relationship between the input and output of a particular system via the systematic analysis of the existing connections between them [35]. In the present investigation, GRA is utilised to determine optimal SLM in-process parameters for the multi-response optimisation of several mechanical properties.

The three main steps in GRA include the normalization of the results obtained, followed by the calculation of grey relational coefficient (GRC) and the subsequent determination of the grey relational grade (GRG) [35,155]. First, the results obtained for each SLM parameter configuration were converted into normalized values ranging from 0 to 1 using one of the following normalisation methods: higher is better, lower is better, or nominal is best. The equations for the three normalisation methods are shown in **Equation (6)** [35,155]:

$$x_{ij} = \begin{cases} \dfrac{y_{ij} - \min y_{ij}}{\max y_{ij} - \min y_{ij}} & \text{Higher is better} \\ \dfrac{\max y_{ij} - y_{ij}}{\max y_{ij} - \min y_{ij}} & \text{Lower is better} \\ \dfrac{\left|y_{ij} - y_0\right|}{\max\left(\max y_{ij} - y_0,\ y_0 - \min y_{ij}\right)} & \text{Nominal is best} \end{cases} \quad \textbf{(6)}$$

where x_{ij} and y_{ij} denote the normalised value and the result obtained for the i-th SLM parameter configuration and the j-th response, respectively. The smallest and largest value of y_{ij} were denoted in terms of $\min y_{ij}$ and $\max y_{ij}$, respectively. In the present investigation, the higher is better normalization method was chosen to obtain better mechanical properties.

Second, the GRC was calculated using **Equation (7)** [35,155]:

$$\text{GRC, } \gamma_{GRC}(x_{0j}, x_{ij}) = \frac{\Delta_{min} + \xi\Delta_{max}}{\Delta_{ij} + \xi\Delta_{max}} \quad \textbf{(7)}$$

where $\Delta_{ij} = \left|x_{0j} - x_{ij}\right|$ was used to denote the absolute difference between the ideal (or reference) condition and the results obtained. The smallest and largest value of Δ_{ij} were denoted using Δ_{min} and Δ_{max}, respectively. In the present investigation, the ideal condition is $x_{0j} = 1$, and the distinguishing coefficient is $\xi = 0.5$.

Third, the GRG was determined using **Equation (8)** [35,155]:

$$\text{GRG, } \Gamma(x_0, x_i) = \sum_{j=1}^{4} \omega_j\, \gamma(x_{0j}, x_{ij}) \quad \textbf{(8)}$$

where ω_j is the weightage for the j-th response. The GRG can be interpreted as the combined performance grade for all four responses studied. Following that, the optimal processing conditions for the multi-response optimisation of mechanical properties was determined with the use of a response table. In the present investigation, a higher weightage of $\omega_j = 0.35$ was assigned to both R_m and KV_2, while a lower weightage of $\omega_j = 0.15$ was assigned to both A and Vickers hardness. Both R_m and KV_2 were given

a higher weightage because the optimisation of these two mechanical properties would allow SLM 18Ni-300 maraging steel moulds to withstand higher stresses and impact loads during operation. The results are presented and discussed in **Section 3.3.5**.

3.3.3. Results from mechanical tests

The results obtained from mechanical tests are shown in **Figure 26**. The mechanical properties for conventional wrought 18Ni-300 maraging steel were also included for comparison [17]. It should be noted that the tensile properties (i.e. R_m and A_t) reported in the present investigation were calculated using the load-displacement curves obtained during experiments, and an extensometer was used to measure the displacement of the samples. Following that, it was identified that the majority of SLM parameter configurations studied in **Table 10** produced samples with mechanical properties that were higher than conventional wrought condition. In particular, 14 out of 16 SLM parameter configurations produced samples with higher R_m, 15 out of 16 exhibited higher A_t, and all 16 exhibited higher Vickers hardness compared to conventional wrought condition.

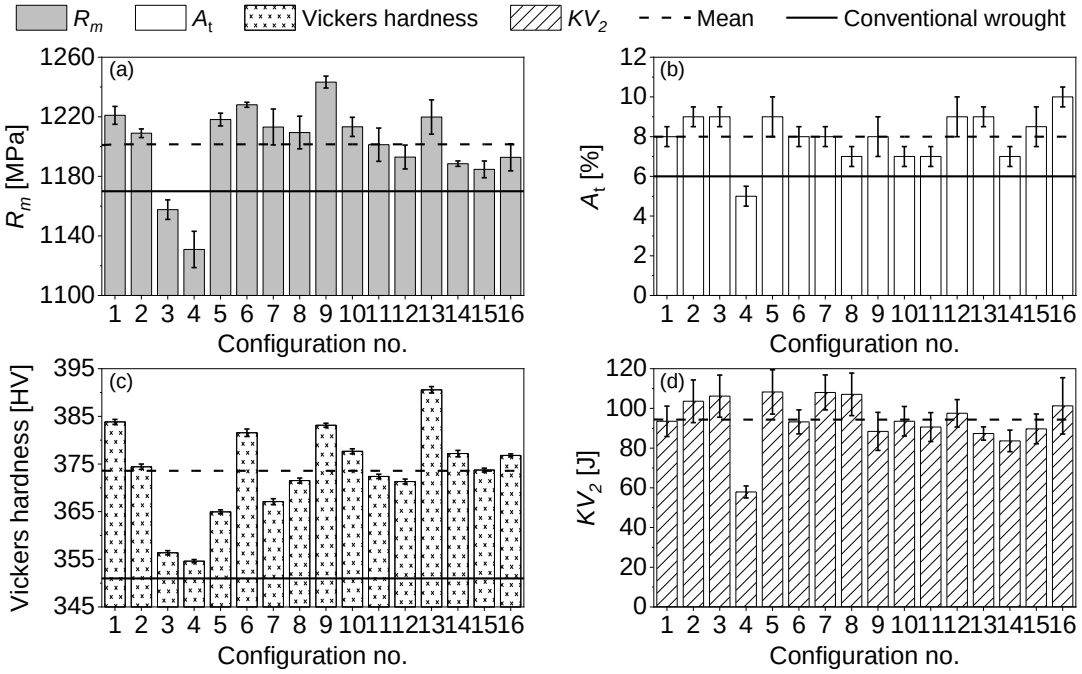

Figure 26: The results obtained from mechanical tests. The mechanical properties for conventional wrought 18Ni-300 maraging steel were taken from literature [17]. R_m: Ultimate tensile strength. A_t: Elongation at fracture. KV_2: Charpy impact energy.

The samples produced using SLM parameter configuration no. 3 had a lower value of R_m but a higher value of A_t and Vickers hardness as compared to conventional wrought condition. Configuration no. 4 was identified as the worst overall due to the samples produced using this configuration having lower mechanical properties as compared to the samples produced using other configurations and standard wrought condition. This can be attributed to configuration no. 4 having the lowest laser energy input (i.e. $E_{linear} = 250.00\ \mathrm{J\ m^{-1}}$ and $E_{volumetric} = 62.50\ \mathrm{J\ mm^{-3}}$) among the

sixteen configurations shown in **Table 10**. This implies that less laser energy was transferred to the metal powder during SLM process, resulting in the incomplete melting of powder particles. Consequently, these additively manufactured samples exhibited lower mechanical properties due to the weaker bonding between the powder particles after solidification.

When comparing SLM parameter configurations that have identical values of $E_{volumetric}$, it can be deduced that configurations with a higher value of E_{linear} produced samples with better mechanical properties. For example, the values of R_m and KV_2 for configuration no. 7 and no. 8 ($E_{volumetric} = 76.39\ \mathrm{J\,mm^{-3}}$) were identified to increase as the E_{linear} was increased. A similar trend was also identified in the A_t for configuration no. 5 and no. 6 ($E_{volumetric} = 122.77\ \mathrm{J\,mm^{-3}}$), as well as the Vickers hardness for configuration no. 10 and no. 12 ($E_{volumetric} = 93.75\ \mathrm{J\,mm^{-3}}$).

To infer, sufficient E_{linear} is needed to fully melt the metal powder and create a uniform melt pool. The use of sufficient E_{linear} led to increased interlayer bonding between adjacent melt pools (and scan tracks), resulting in better mechanical properties. From **Equation (1),** a higher value of E_{linear} can be achieved by either increasing P or decreasing v. Sun et al. [31] explained that the use of a higher value of E_{linear} led to an increase in the melt pool's temperature and a decrease in the melt pool's viscosity, enabling the melt pool to spread more properly on the formerly processed layer. Following that, the use of excessively high E_{linear} resulted in the formation of manufacturing defects such as balling instead [28].

Besides that, it can be deduced that the use of a smaller h resulted in a higher value of A_t and KV_2. This is because the use of smaller h resulted in increased overlap between the scan tracks, which is beneficial for fabricating samples with high relative density. For example, the A_t and KV_2 for configuration no. 15 was higher compared to configuration no. 14. A similar trend was also observed when comparing the A_t and KV_2 for configuration no. 16 and no. 13.

According to the literature [18,83,156], the impact energy for selective laser melted 18Ni-300 maraging steel was found to be in the range of 24–68 J. It was also mentioned that the impact test was conducted in accordance with ASTM E23, and the values were reported in terms of energy difference. However, the impact energy for conventional wrought condition was not reported. The impact energy data found in literature was not included in **Figure 26**(d) due to the differences in test standards (ISO vs. ASTM) and reported values (KV_2 vs. energy difference).

3.3.4. The order of influence of SLM in-process parameters

The experiment results shown in **Figure 26** were converted into signal-to-noise ratio (SNR) and tabulated in **Table 12**. The SNR for each SLM parameter configuration was then used to generate the response table and main effects plot as shown in **Table 13** and **Figure 27**, respectively. The optimal SLM in-process parameters and its order of influence were found to differ according to the response to be optimised, i.e. there is no absolute best. The SLM in-process parameters for optimising R_m was $P = 275\ \mathrm{W}, v = 700\ \mathrm{mm\ s^{-1}}, h = 0.07\ \mathrm{mm}$. The SLM in-process parameters for optimising A_t, Vickers hardness, and KV_2 were different from those for R_m (A_t: $325\ \mathrm{W}, 700\ \mathrm{mm\ s^{-1}}, 0.08\ \mathrm{mm}$ vs. Vickers hardness: $325\ \mathrm{W}, 700\ \mathrm{mm\ s^{-1}}, 0.07\ \mathrm{mm}$ vs. KV_2: $275\ \mathrm{W}, 900\ \mathrm{mm\ s^{-1}}, 0.08\ \mathrm{mm}$). The order of influence of SLM in-process parameters was identified by comparing the rankings for $P, v, \mathrm{and}\ h$ for each response shown in **Table 13**. In particular, v was identified to have the largest influence on R_m, h was identified to have the largest influence on A, and P was identified to have the largest influence on KV_2. Also, both P and v were identified to have an equal level of influence on Vickers hardness.

Table 12: The signal-to-noise ratio (SNR) for all four responses studied in the present investigation.

Config.	Taguchi orthogonal array (levels)			SNR (Criterion: higher-is-better)			
	P	v	h	R_m	A_t	Vickers hardness	KV_2
1	1	1	1	61.73	17.76	51.7	39.1
2	1	2	2	61.65	19.04	51.5	39.8
3	1	3	3	61.27	19.21	51.0	40.1
4	1	4	4	61.07	13.82	51.0	35.2
5	2	1	2	61.71	18.95	51.2	40.2
6	2	2	1	61.78	17.65	51.6	39.2
7	2	3	4	61.68	18.15	51.3	40.4
8	2	4	3	61.65	17.30	51.4	40.1
9	3	1	3	61.89	18.20	51.7	38.4
10	3	2	4	61.68	16.91	51.5	39.2
11	3	3	1	61.59	16.67	51.4	38.9
12	3	4	2	61.53	18.15	51.4	39.6
13	4	1	4	61.72	18.69	51.8	38.8
14	4	2	3	61.50	16.83	51.5	38.3
15	4	3	2	61.47	18.38	51.5	38.7
16	4	4	1	61.53	20.10	51.5	39.2

Table 13: Response table calculated using mean SNR. The optimal processing conditions and highest ranking were highlighted using bold text.

Response	Factor	Mean SNR				Difference (max. – min.)	Rank
		Level 1	Level 2	Level 3	Level 4		
R_m	P	61.43	**61.71**	61.67	61.56	0.28	2
	v	**61.77**	61.65	61.50	61.44	0.32	**1**
	h	**61.66**	61.59	61.58	61.54	0.12	3
A_t	P	17.46	18.01	17.48	**18.50**	1.04	3
	v	**18.40**	17.61	18.10	17.34	1.06	2
	h	18.05	**18.63**	17.89	16.90	1.74	**1**
Vickers hardness	P	51.3	51.4	51.5	**51.6**	0.3	**1**
	v	**51.6**	51.5	51.3	51.3	0.3	**1**
	h	**51.6**	51.4	51.4	51.4	0.2	2
KV_2	P	38.5	**40.0**	39.0	38.8	1.4	**1**
	v	39.1	39.1	**39.5**	38.5	1.0	3
	h	39.1	**39.6**	39.2	38.4	1.2	2

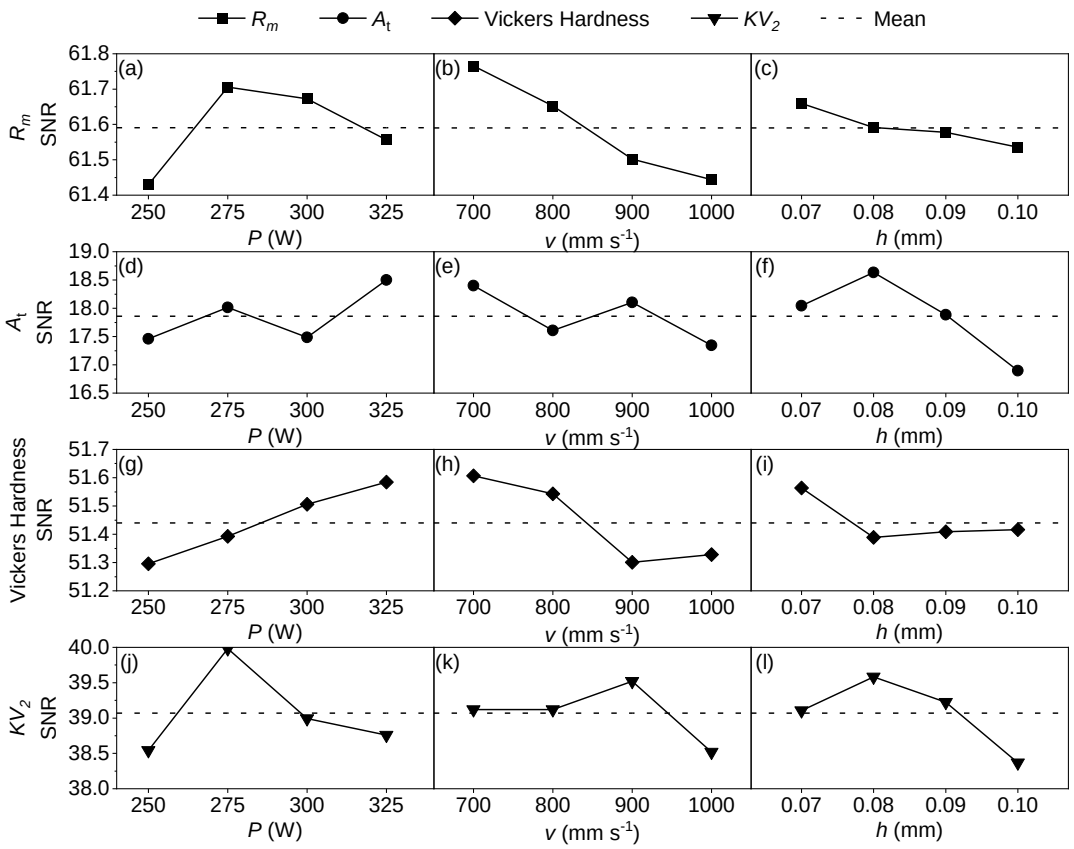

Figure 27: Main effects plots for all four responses: (a–c) for R_m, (d–f) for A_t, (g–i) for Vickers Hardness, and (j–l) for KV_2. SNR: signal-to-noise ratio.

For the second phase of Taguchi analysis, the SNR was used as input for ANOVA calculations, and the results are shown in **Table 14**. The ANOVA results indicated that v have a higher percentage contribution on R_m and Vickers hardness (41.79 % and 37.4 %, respectively). In contrast, the error term has a higher percentage contribution on A_t and KV_2 instead (61.27 % and 55.8 %, respectively). The reason is that the results obtained for configuration no. 4 exhibited the largest deviation from the mean value as compared to the other configurations (**Figure 26**(a-d)). These results can be interpreted as outlying values which contributed a larger variance towards the current pool of data, thus resulting in a larger variance for the error term in ANOVA calculations. In addition, the error term has a larger degree of freedom (DOF = 6) as compared to each SLM process parameter (DOF = 3), indicating a larger degree of error between experiments. Following that, the F-ratio for v was identified to be larger than the F-ratio given in the F-tables (3.78 > 3.2888). This means that within a confidence level of 90 %, R_m was found to be sensitive towards the changes in v. However, this statement does not apply to the other responses as the F-ratio for v was smaller. The F-ratio for P and h were also found to be smaller than the given F-ratio of 3.2888, i.e. all four responses may be less sensitive to the individual changes of these two SLM in-process parameters.

Table 14: ANOVA for all 4 responses. F-ratio for 90% confidence level is $F_{0.10}(3,6) = 3.2888$ [34].

Response	Factor	DOF	Sum of squares	Variance	F-ratio	Percentage contribution (%)
R_m	P	3	0.19	0.06	2.79	30.90
	v	3	0.26	0.09	3.78	41.79
	h	3	0.03	0.01	0.47	5.18
	Error	6	0.13	0.02	1.00	22.12
	Total	15	0.61			100.00
A_t	P	3	2.94	0.98	0.31	9.54
	v	3	2.73	0.91	0.29	8.89
	h	3	6.25	2.08	0.66	20.31
	Error	6	18.85	3.14	1.00	61.27
	Total	15	30.76			100.00
Vickers hardness	P	3	0.2	0.1	1.9	25.7
	v	3	0.3	0.1	2.8	37.4
	h	3	0.1	0.0	0.8	10.3
	Error	6	0.2	0.0	1.0	26.6
	Total	15	0.8			100.0
KV_2	P	3	4.9	1.6	0.8	21.4
	v	3	2.0	0.7	0.3	9.0
	h	3	3.1	1.0	0.5	13.8
	Error	6	12.7	2.1	1.0	55.8
	Total	15	22.7			100.0

3.3.5. Optimal SLM in-process parameters for multi-response optimisation of mechanical properties

Next, GRA was conducted using the results shown in **Figure 26** as input. The results are shown in **Table 15**. The GRG for each SLM parameter configuration was then used to generate the response table shown in **Table 16**. The optimal SLM in-process parameters for the multi-response optimisation of all four mechanical properties was identified as $275\ \mathrm{W}, 700\ \mathrm{mm\ s^{-1}}, 0.08\ \mathrm{mm}$ and happened to coincide with configuration no. 5 in **Table 10**. In terms of order of influence, P was identified to have the largest influence on all four responses studied in the present investigation, followed by v and h (**Table 16**). Furthermore, P and v exhibited similar levels of influence on the investigated mechanical properties (0.14 > 0.13).

Table 15: Results from grey relational analysis (GRA). R_m: Ultimate tensile strength. A_t: Elongation at fracture. KV_2: Charpy impact energy.

Config.	Normalization (Method: higher-is-better)				GRC				GRG	Rank
	R_m	A_t	Vickers hardness	KV_2	R_m	A_t	Vickers hardness	KV_2		
1	0.80	0.56	0.81	0.71	0.72	0.53	0.7	0.6	0.66	9
2	0.69	0.76	0.55	0.91	0.62	0.68	0.5	0.8	0.69	5
3	0.24	0.82	0.05	0.96	0.40	0.73	0.3	0.9	0.62	10
4	0.00	0.00	0.00	0.00	0.33	0.33	0.3	0.3	0.33	16
5	0.78	0.80	0.29	1.00	0.69	0.72	0.4	1.0	0.76	1
6	0.86	0.54	0.75	0.70	0.79	0.52	0.7	0.6	0.67	8
7	0.73	0.61	0.35	1.00	0.65	0.56	0.4	1.0	0.72	3
8	0.70	0.47	0.47	0.98	0.62	0.49	0.5	1.0	0.70	4
9	1.00	0.64	0.79	0.61	1.00	0.58	0.7	0.6	0.74	2
10	0.73	0.40	0.64	0.71	0.65	0.46	0.6	0.6	0.61	11
11	0.63	0.38	0.49	0.65	0.57	0.45	0.5	0.6	0.55	13
12	0.55	0.73	0.46	0.79	0.53	0.65	0.5	0.7	0.60	12
13	0.79	0.71	1.00	0.58	0.71	0.63	1.0	0.5	0.68	7
14	0.51	0.38	0.63	0.51	0.51	0.45	0.6	0.5	0.51	15
15	0.48	0.68	0.53	0.63	0.49	0.61	0.5	0.6	0.54	14
16	0.55	1.00	0.62	0.86	0.53	1.00	0.6	0.8	0.69	6

Table 16: Response table calculated using mean GRG. The optimal processing conditions and highest ranking were highlighted using bold text.

SLM process parameter	Mean GRG				Difference (max. – min.)	Rank
	Level 1	Level 2	Level 3	Level 4		
P	0.58	**0.71**	0.62	0.61	0.14	**1**
v	**0.71**	0.62	0.61	0.58	0.13	2
h	0.64	**0.65**	0.64	0.59	0.06	3

The results obtained from **Table 13** and **Table 16** were further summarised in **Table 17** to provide a direct comparison between them. The overall order of influence for each SLM process parameter can be interpreted as $P \approx v > h$, where the influence of P and v are approximately equal to each other, and the influence of h was found to be less significant. This implies that the interaction effects between SLM in-process parameters should also be factored into consideration in order to fabricate samples with reduced manufacturing defects and good mechanical properties. Mutua et al. [28] reported that different combinations of P and v resulted in the formation of different microstructures. For example, a combination of low P and low v (i.e. low E_{linear}) resulted in the incomplete melting of powder particles, which led to poor mechanical properties as well as increased porosity. In contrast, a combination of excessively high P and low v (i.e. high E_{linear}) resulted in a burnt surface due to the excessive energy input.

Table 17: Summary of results obtained from statistical analysis.

Method	Response	Optimal processing conditions					Order of influence (largest > smallest)
		P [W]	v [mm s^{-1}]	h [mm]	E_{linear} [J m^{-1}]	$E_{volumetric}$ [J mm^{-3}]	
Taguchi methods - S/N Ratio	R_m	275	700	0.07	392.86	140.31	$v > P > h$ (0.32 > 0.28 > 0.12)
	A	325	700	0.08	464.29	145.09	$h > v > P$ (1.74 > 1.06 > 1.04)
	Vickers hardness	325	700	0.08	464.29	145.09	$v = P > h$ (0.3 = 0.3 > 0.2)
	KV_2	275	900	0.08	305.56	95.49	$P > h > v$ (1.4 > 1.2 > 1.0)
GRA (Config. 5)	Optimized for all responses	275	700	0.08	392.86	122.77	$P > v > h$ (0.14 > 0.13 > 0.06)

When comparing the optimal SLM in-process parameters for each response, it was identified that the SLM in-process parameter level that has the most number of occurrences was $P = 275\ \text{W}, v = 700\ \text{mm s}^{-1}, h = 0.08\ \text{mm}$ and was identical to configuration no. 5. Also, it was identified that the E_{linear} and $E_{volumetric}$ for configuration no. 5 was not the highest among the five optimal processing conditions listed in **Table 17**. This implies that the multi-response optimisation of all four mechanical properties studied in the present investigation can be achieved with a lower E_{linear} and $E_{volumetric}$.

In summary, the results obtained from statistical analysis suggested configuration no. 5 ($P = 275\ \text{W}, v = 700\ \text{mm s}^{-1}, h = 0.08\ \text{mm}, t_{layer} = 0.04\ \text{mm}, E_{linear} = 392.86\ \text{J m}^{-1}, E_{volumetric} = 122.77\ \text{J mm}^{-3}$) as the most optimal among the sixteen configurations studied in **Table 10** for the multi-response optimisation of the investigated mechanical properties. On the other hand, configuration no. 4 ($P = 250\ \text{W}, v = 1000\ \text{mm s}^{-1}, h = 0.10\ \text{mm}, t_{layer} = 0.04\ \text{mm}, E_{linear} =$

$250.00\ \mathrm{J\ m^{-1}}, E_{volumetric} = 62.50\ \mathrm{J\ mm^{-3}}$) was identified as the worst among the sixteen configurations studied due to it producing additively manufactured samples with the worst mechanical properties overall. The findings were identified to be consistent with those reported in the literature [28,63,64]. In particular, configuration no. 5 was identified to fall within the optimal processing window reported by Mutua et al. [28]. The process map showing the optimal processing window is shown in **Figure 8** (**Chapter 2 Section 2.2.1**).

3.4. Influence of porosity on the macroscale plastic strain localisation and fracture

3.4.1. Experimental methodology

Fracture in engineering components occur when the applied load exceeds the maximum load bearing capacity of the material. Knowledge about the material's plastic deformation behaviour and fracture mechanisms would aid researchers in tailoring the material's mechanical properties, in addition to helping engineers obtain more accurate predictions of fracture in said components. Porosity was identified as the main cause of fracture in SLM 18Ni-300 maraging steel samples [22–24]. However, its influence on the plastic deformation behaviour of said material is yet to be fully documented.

In the present investigation, the macroscale uniaxial tensile deformation behaviour of selective laser melted 18Ni-300 maraging steel is elucidated via investigations on its plastic strain localisation phenomena and fracture mechanisms. A 3D-DIC (or optical-DIC) system was used in the present investigation, and its working principle is illustrated in **Figure 28**. Two charge-coupled device (CCD) cameras were mounted in line with a light source, and an image acquisition rate of 1 image per second was used to capture digital images of the gauge section during tensile tests.

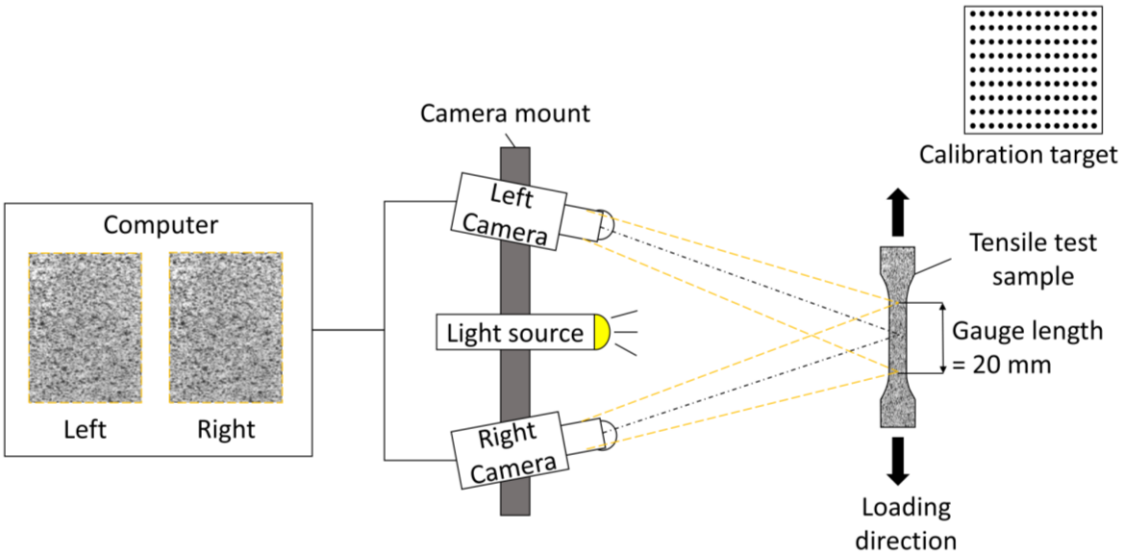

Figure 28: Schematic for the working principle of optical-DIC system used in the present investigation.

Tensile samples fabricated using SLM parameter configurations no. 4 and no. 5 (**Table 10**) were utilised in the present investigation to study the influence of porosity. These two configurations were chosen due to them being the best (no. 5) and worst (no. 4) configurations as identified in statistical analysis (**Section 3.3.5**). The tensile test samples were polished to obtain a mirror-like surface, then spray-painted with black paint to create a layer of black speckles on its surface. These speckles play an important role during testing and optical-DIC data acquisition, as the cameras will track the changes in the position of these speckles during testing. Following that, the digital images were post-processed using VIC 3D software to generate strain distribution maps for the surface of test samples. The y-direction (vertical) engineering surface strain

experienced by the test samples were characterised in terms of ε_{yy}, and calculated using **Equation (9)** [157]:

$$\varepsilon_{yy} = \sqrt{1 + 2E_{yy}} - 1 \quad \textbf{(9)}$$

where E_{yy} is the Lagrange strain tensor in the y-direction (vertical). This method of calculating ε_{yy} was utilised because the tensile test samples were loaded in the y-direction (vertical), and is less sensitive to rigid body motion. The results for macroscale plastic strain localisation are presented and discussed in **Section 3.4.2**.

To ensure the accuracy of the optical-DIC system, both CCD cameras were calibrated using a calibration target at different calibration angles before tensile tests were conducted. Particular care was taken to avoid accidentally moving the CCD cameras and the camera mount during testing. It should be noted that the camera mount features a locking mechanism to lock the mount itself and the CCD cameras in place after calibration was completed.

Micrographs for the fracture surface of tensile test samples were captured using the ZEISS Sigma 500 scanning electron microscope (SEM). These micrographs were then used to analyse the fracture mechanisms of selective laser melted 18Ni-300 maraging steel. The fractography analysis is presented and discussed in **Section 3.4.3**.

3.4.2. Evolution of macroscale plastic strain localisation captured via optical-DIC

Presented in **Figure 29** is a comparison for the evolution in macroscale plastic strain localisation in tensile test samples fabricated using SLM parameter configuration no. 4 (worst) and no. 5 (best), captured via optical-DIC. The loading duration during tensile test was indicated in the horizontal axis to allow for the real-time characterisation of macroscale plastic strain localisation in the two samples. The y-direction engineering surface strain experienced by the test samples were characterised in terms of ε_{yy} and presented in **Figure 29** as contour plots.

It was identified that the transition from elastic deformation to plastic deformation in both samples occurred at approximately the same time (**Figure 29**(a)(ii) vs (b)(ii)). However, the duration of plastic deformation in configuration no. 4 was identified to be twice as short as compared to configuration no. 5 (**Figure 29**(a)(ii-iv) vs. (b)(ii-iv)), loading duration = 112 s vs. 251 s). This difference can be attributed to the solidification conditions during SLM process. The use of optimal processing conditions (i.e. configuration no. 5) led to better solidification conditions as the laser energy transferred was sufficient to completely melt the powder particles and create better bonding between the melt pools, resulting in better mechanical properties.

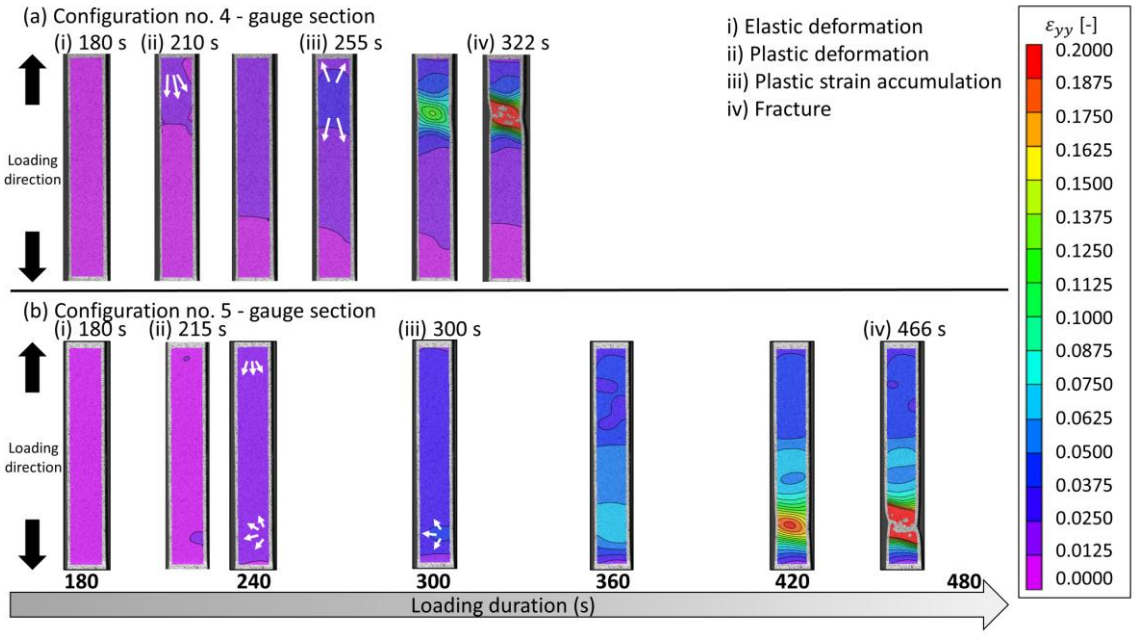

Figure 29: Evolution of the macroscale plastic strain localisation in SLM 18Ni-300 maraging steel tensile test samples fabricated via (a) SLM parameter configuration no. 4 and (b) no. 5.

After progressing to plastic deformation, regions of significantly higher strain accumulation (leading to plastic strain localisation) started to appear and gradually expanded until it covered the whole gauge length. In configuration no. 4, it was identified that the accumulation of plastic strain was more focused around the top region of the gauge length (**Figure 29**(a)(iii)). In configuration no. 5, the accumulation of plastic strain was more uniformly distributed along the whole gauge length before transitioning to be more focused around the bottom region (**Figure 29**(b)(iii)). These regions of high plastic strain accumulation would later become the location of fracture for the respective samples.

It can be deduced that subsequent plastic deformation resulted in the formation and propagation of Lüders bands [145] in selective laser melted 18Ni-300 maraging steel. In **Figure 29**, both samples entered plastic deformation at around the same time (**Figure 29**(a)(ii) vs **Figure 29**(b)(ii), loading duration = 180 s). Lüders bands started to form as the samples were deformed beyond the yield limit of the material, and propagated until it covered the entire gauge section. For configuration no. 4, Lüders bands formed near the top of the gauge section and propagated downwards, while the opposite was observed for configuration no. 5 (**Figure 29**(a)(iii) vs. **Figure 29**(b)(iii)). The location of fracture in both samples were found to coincide with the location where the Lüders bands had initially formed (**Figure 29**(a-b)(iv)).

3.4.3. Fracture

The fracture surface of tensile test samples produced using SLM parameter configuration no. 4 and no. 5 are shown in **Figure 30** and **Figure 31**, respectively. In comparison, it was identified that configuration no. 4 has increased porosity at the fracture surface as compared to configuration no. 5 (**Figure 30**(a) vs. **Figure 31**(a)). At higher magnifications, microvoids (or dimples) were found to be dispersed around the pore perimeter, while the pore surface exhibited a smooth, layered texture (**Figure 30**(b-c) and **Figure 31**(b-d)). The hollowed region shown in **Figure 30**(d) contained unmelted powder particles and melt pools with non-uniform shape, an indication of insufficient laser energy input and poor solidification conditions. The fracture mechanism for both samples was identified as ductile fracture as significant necking can be observed around the location of fracture (**Figure 29**(a)(iv) and **Figure 29**(b)(iv)). It was deduced that the difference in location of fracture can be attributed to the distribution of pores along the gauge length, and fracture tends to occur at regions with increased porosity.

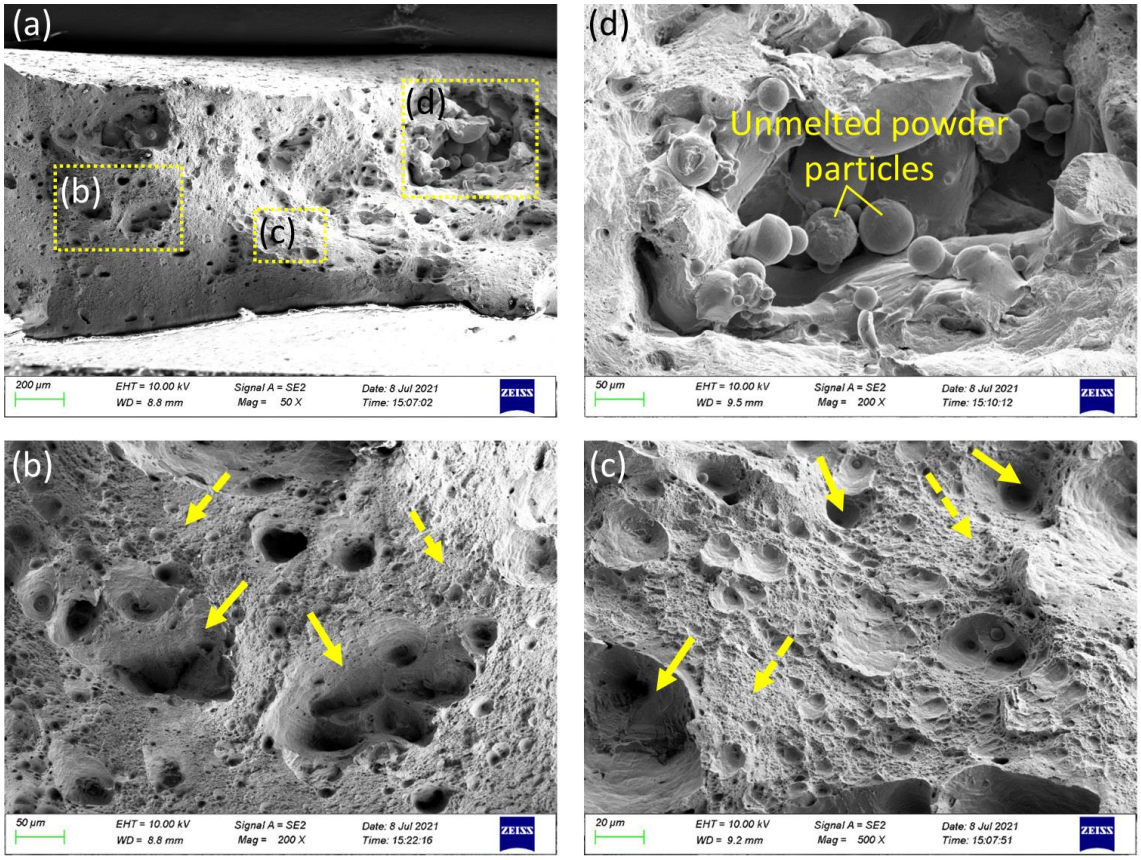

Figure 30: Fracture micrographs for samples fabricated using SLM parameter configuration no. 4: (a) fracture location, (b-d) higher magnification micrographs of fracture location. Solid arrows: pores. Dashed arrows: microvoid coalescence.

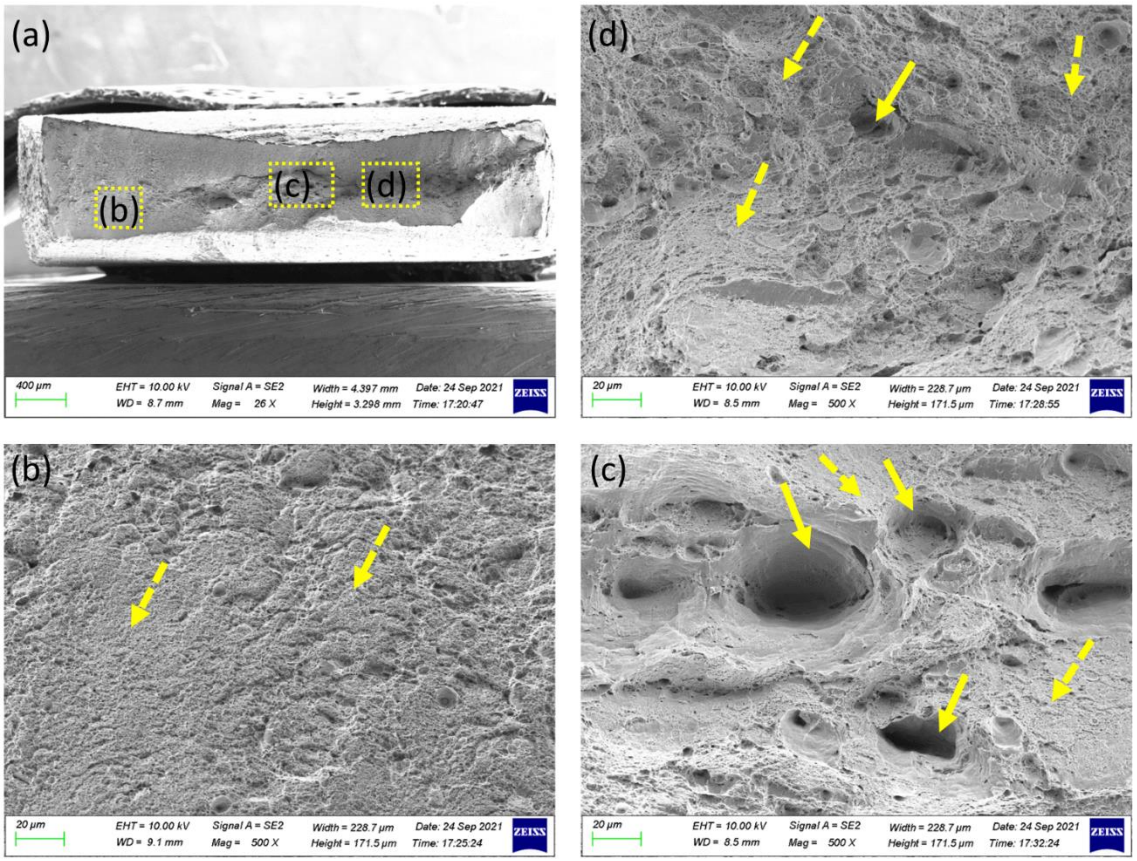

Figure 31: Fracture micrographs for samples fabricated using SLM parameter configuration no. 5: (a) fracture location, (b-d) higher magnification micrographs of fracture location. Solid arrows: pores. Dashed arrows: microvoid coalescence.

The pores were found to play a significant role in reducing the tensile strength of the sample, due to it serving as crack initiation sites during plastic deformation. The relative density of samples fabricated via configuration no. 4 and no. 5 were measured as 98.88 % and 99.39 %, respectively. Samples with increased porosity and reduced relative density (i.e. configuration no. 4) has a higher chance to have multiple crack initiation sites, leading towards an earlier fracture (**Figure 29**(a)). Cao et al. [158] reported that the pore perimeter exhibited high stress concentrations during tensile loading, and cracks started to form around the pore perimeter when the local strength of that region exceeds the fracture strength of the material. It was also reported that regions with larger pores and increased porosity resulted in higher stress concentrations.

Following that, it can be deduced that crack propagation had occurred via microvoid coalescence around the pore perimeter. Haidemenopoulos [159] explained that after crack initiation had occurred, further plastic deformation resulted in the formation and growth of microvoids. The individual microvoids will coalesce together to form larger regions of microvoids around the pore perimeter, ultimately resulting in fracture at that particular region.

3.5. Summary

Experimental investigations and statistical optimisation were employed to investigate the influence of SLM process parameters (or in-process parameters) on the microstructure and mechanical properties of SLM 18Ni-300 maraging steel. The following three SLM in-process parameters were selected for investigation: laser power (P), scanning speed (v), and hatch spacing (h). The findings were summarised in the following paragraphs.

In **Section 3.2**, it was identified that the occurrence of manufacturing defects in additively manufactured scan tracks and fully built samples could be reduced via the use of SLM parameter configurations with $E_{linear} > 375.00\ \mathrm{J\ m^{-1}}$ (**Figure 24**). The use of higher P during the SLM process resulted in the complete melting and fusion of metal powder, in addition to better bonding between adjacent melt pools. Configuration B-2 from **Table 7** ($P = 300\ \mathrm{W}, v = 700\ \mathrm{mm\ s^{-1}}, h = 0.10\ \mathrm{mm}, t_{layer} = 0.03\ \mathrm{mm}, E_{linear} = 428.57\ \mathrm{J\ m^{-1}}, E_{volumetric} = 142.86\ \mathrm{J\ mm^{-3}}$) produced samples with the highest relative density and good mechanical properties ($\rho_{relative} = 99.71\ \%, R_m = 1204\ \mathrm{MPa}, A_t = 8.3\ \%$). The mechanical properties of the fabricated samples were also comparable with conventional wrought condition ($R_m = 1000 - 1170\ \mathrm{MPa}, A_t = 6 - 15\ \%$). The use of lower v or smaller h was found to produce samples with higher $\rho_{relative}$.

In **Section 3.3**, the optimal SLM in-process parameters for the multi-response optimisation of ultimate tensile strength (R_m), elongation at fracture (A_t), Vickers hardness, and impact toughness (KV_2) was identified as configuration no. 5 from **Table 10** ($P = 275\ \mathrm{W}, v = 700\ \mathrm{mm\ s^{-1}}, h = 0.08\ \mathrm{mm}, t_{layer} = 0.04\ \mathrm{mm}, E_{linear} = 392.86\ \mathrm{J\ m^{-1}}, E_{volumetric} = 122.77\ \mathrm{J\ mm^{-3}}$). The achieved mechanical properties of samples fabricated via configuration no. 5 are: $R_m = 1218\ \mathrm{MPa}$, $A_t = 9.2\ \%$, $\mathrm{hardness} = 365.0\ \mathrm{HV}$, and $KV_2 = 108.3\ \mathrm{J}$. Besides that, configuration no. 4 ($P = 250\ \mathrm{W}, v = 1000\ \mathrm{mm\ s^{-1}}, h = 0.10\ \mathrm{mm}, t_{layer} = 0.04\ \mathrm{mm}, E_{linear} = 250.00\ \mathrm{J\ m^{-1}}, E_{volumetric} = 62.50\ \mathrm{J\ mm^{-3}}$) was identified as the worst among the sixteen configurations in **Table 10**. This can be attributed to it having the lowest E_{linear} and $E_{volumetric}$ among the configurations studied, resulting in insufficient laser energy during SLM fabrication and inferior mechanical properties in the samples fabricated via it. The order of influence of SLM parameters was identified as $P \approx v > h$, where the influence of P and v were approximately equal on all four investigated mechanical properties and the influence of h was less significant (**Table 17**). There exists an optimal processing window where the careful selection of SLM parameters resulted in the fabrication of samples with high $\rho_{relative}$ and mechanical properties comparable with conventional wrought condition. The optimal SLM in-process parameters was identified to differ according to the mechanical property to be optimised. The findings were identified to be consistent with those reported in the literature [28,63,64].

In **Section 3.4**, a best-worst comparison was carried out to quantitatively and qualitatively explain the influence of porosity on the macroscale plastic strain localisation and fracture in SLM 18Ni-300 maraging steel. Tensile test samples fabricated via configurations no. 4 (worst) and no. 5 (best) in **Table 10** were used for comparison. Quantitative analysis via optical-DIC revealed that tensile test samples fabricated using configuration no. 5 were able to withstand plastic deformation for more than twice the duration as compared to configuration no. 4 before fracturing (**Figure 29**). Qualitative

analysis indicated the propagation of Lüders bands and occurrence of necking in the samples fabricated via both configurations. The location of fracture coincided with the location where the Lüders bands had initially formed. Furthermore, the location of fracture was found to be influenced by the sample's geometry as well as porosity. This is because during tensile loading, the shoulder regions of the tensile samples experienced larger strain accumulation, whereas regions with increased porosity were more prone to crack initiation and propagation. The fracture mechanism for both configurations was identified as ductile fracture, as significant necking was observed near the location of fracture (**Figure 29**). Fracture occurred via crack initiation around the pore perimeter, and subsequent propagation via microvoid coalescence (SLM config. no. 4: **Figure 30**, no. 5: **Figure 31**).

4. Influence of microstructural heterogeneity on microscale plastic strain localisation in SLM 18Ni-300 maraging steel

4.1. Introduction

Research on the plastic deformation mechanisms and microscale plastic strain localisation in metals provide fundamental insights into its mechanical behaviour and directly influence its application in the industry. Engineering components are often subjected to various loading conditions during operation, such as uniaxial tension and compression, multiaxial loading, as well as cyclic loading (or fatigue). These complex loading conditions give rise to plastic strain localisation in the component, ultimately resulting in failure during operation. Further discussion about the plastic deformation mechanisms (e.g. dislocation slip, deformation twinning) and plastic strain localisation in metals are included in **Chapter 2 Section 2.5**.

In **Chapter 2 Section 2.5.1**, researchers have utilised scanning electron microscope-based digital image correlation (SEM-DIC) to investigate the microscale plastic strain localisation in SLM 316L stainless steel [140–142]. Bean et al. [140] reported that plastic strain localisation in SLM 316L stainless steel occurred heterogeneously due to the non-uniform distribution of cellular structures that formed during rapid solidification in the SLM process. The cellular structures acted as forest-type dislocation obstacles during plastic deformation, thus contributing to the strengthening of said material. However, the plastic strain localisation in SLM 18Ni-300 maraging steel is yet to be elucidated in the literature due to lack of investigations on this topic. Given said material's application for mould making and fabrication of aerospace components [16,17], knowledge about its microscale plastic strain localisation behaviour is essential for the numerical predictions of damage and failure in engineering components made using said material.

In **Chapter 2 Section 2.4.1**, it was reported that the spatial resolution of SEM-DIC measurements was directly influenced by the speckle pattern and digital imaging device used [130]. Furthermore, a suitable speckle pattern should have good contrast and good adherence with the surface of test samples, in addition to being randomly distributed to facilitate full-field surface displacement and strain mapping in all directions. Hoefnagels et al. [36] suggested using magnetron sputtering to deposit submicron-sized speckle patterns on the surface of test samples for SEM-DIC investigations of a polycrystalline Fe foil. Magnetron sputtering is a type of physical vapour deposition process that utilises plasma (i.e. ionised argon gas) to bombard the sputter target, followed by the ejection of sputtered atoms and their subsequent deposition on the surface of test samples. However, the methodology for creating suitable speckle patterns for SEM-DIC measurements of SLM 18Ni-300 maraging steel is yet to be developed or reported in the literature.

In the present chapter, uniaxial in situ tensile experiments were conducted inside the SEM to investigate the influence of microstructural heterogeneity on the plastic strain localisation in SLM 18Ni-300 maraging steel. The microstructural heterogeneity (i.e. variations in grain size and crystallographic texture) was characterised using EBSD, and the plastic strain localisation phenomena was characterised via SEM-DIC. Two sample conditions were investigated, namely the as-built (AB) condition and the solution-aging treatment (SAT) condition. The magnetron sputtering methodology

suggested by Hoefnagels et al. [36] was adapted and developed for creating sub-micron sized speckle patterns for SEM-DIC investigations in the present chapter. Following that, the obtained EBSD and SEM-DIC datasets need to be digitally aligned to facilitate slip system identification in the selected grains of AB and SAT samples. Custom MATLAB scripts developed by Vermeij et al. [37,38] were adapted and developed for digitally aligning the EBSD and SEM-DIC datasets. Further details regarding the experimental methodology for SEM-DIC investigations of microscale plastic strain localisation, along with the adapted procedures are presented in **Section 4.3.1**.

Following that, the objectives of the experimental investigations in the present chapter include:

1. To investigate the influence of magnetron sputtering parameters on speckle characteristics and determine suitable sputtering parameters for depositing sub-micron sized speckle patterns on the samples' surface for SEM-DIC investigations of SLM 18Ni-300 maraging steel (**Section 4.2.1**). The investigated parameters include: sputter current ($I_{sputter}$), sputter duration ($t_{sputter}$), and chamber pressure during sputtering ($P_{sputter}$).
2. To evaluate the capability of the developed speckle patterns for characterising microscale plastic strain localisation in said material (**Section 4.2.2**). The findings for **Section 4.2.1** and **4.2.2** are then summarised (**Section 4.2.3**).
3. To investigate the microstructural heterogeneity (i.e. variations in grain size and crystallographic texture) in SLM 18Ni-300 maraging steel using EBSD (**Section 4.3.2**). Characterisation was done for both as-built (AB) and solution-aging treatment (SAT) samples.
4. To investigate the localised evolution of microscale plastic strain localisation in AB and SAT samples using SEM-DIC (**Section 4.3.3**).
5. To investigate the changes in microscale plastic strain localisation before and after post-processing heat treatment in the selected grains of AB and SAT samples (**Section 4.3.4**). Digital alignment of EBSD and SEM-DIC datasets was performed to correlate plastic strain localisation with microstructural heterogeneity in selected grains.
6. To investigate and identify the deformation mechanism(s) and active slip system(s) in selected grains of AB and SAT samples (**Section 4.3.5**). The findings for **Section 4.3.2** to **4.3.5** are then comparatively analysed and discussed in detail (**Section 4.3.6**).

The findings of the present chapter are collectively summarised in **Section 4.4**, and published in two peer-reviewed papers [42,43]. The contents in the present chapter may differ from the published version, as they were reorganised to align with the structure of the present thesis. Also, certain content in the published version (e.g. Schmid factor distribution of all the grains in AB and SAT samples) was not included in the present chapter as the insights provided were less impactful to the central discussion of the present chapter.

4.2. Development of speckle patterns for SEM-DIC investigations of microscale plastic strain localisation

4.2.1. Influence of magnetron sputtering parameters on speckle characteristics

4.2.1.1. Experimental methodology

Hoefnagels et al. [36] have reported the successful application of magnetron sputtering for creating sub-micron sized speckle patterns on the surface of polycrystalline Fe foil for studying the microscale plastic strain localisation near the sample's fracture location via SEM-DIC. It was also reported that this method was scalable and robust for creating artificial speckle patterns of varying speckle sizes and can be fine-tuned to suit the desired application. However, the methodology for creating suitable speckle patterns for studying the microscale plastic strain localisation of SLM 18Ni-300 maraging steel via SEM-DIC is yet to be developed or reported in the literature. Furthermore, an adequate understanding of the influence of magnetron sputtering parameters is needed to fine-tune its parameters and deposit suitable speckle patterns for the SEM-DIC investigations in the present chapter.

Following that, the influence of the following three main magnetron sputtering parameters were investigated: sputter current ($I_{sputter}$), sputter duration ($t_{sputter}$), and chamber pressure during sputtering ($P_{sputter}$). For the design of experiments, a Taguchi $L_4(2^3)$ orthogonal array consisting of four parameter configurations was utilised (**Table 18**). Taguchi orthogonal arrays provide a cost-effective method for the design of experiments because each parameter can be evaluated independently of each other without the need of a full factorial design [34]. The speckle patterns deposited via magnetron sputtering were quantitatively evaluated by fitting the speckle size distribution histogram of a particular speckle pattern to a Gaussian distribution profile to determine its average speckle size and standard deviation.

Table 18: Taguchi $L_4(2^3)$ orthogonal array for magnetron sputtering parameter configurations studied in the present investigation.

Config.	$I_{sputter}$ [mA]	$t_{sputter}$ [s]	$P_{sputter}$ [Pa]
1	75	240	3
2	75	480	5
3	55	240	5
4	55	480	3

Subsequently, the most suitable speckle pattern was selected for the SEM-DIC of SLM 18Ni-300 maraging steel. The following selection criteria were used for determining the most suitable speckle pattern: average speckle size, uniformity in speckle size, and spatial distribution of speckles. A suitable speckle pattern would possess the following characteristics: (i) have an average speckle size that was at least 3 pixels in size when captured using the intended SEM image resolution and field of view (FOV), (ii) the individual speckles were relatively uniform in size (i.e. low standard deviation) so that speckle edge sharpness is retained and have good contrast with the test sample's

surface, in addition to (ii) having a dense spatial distribution for the full-field mapping of SEM-DIC measurements.

Selective laser melting (SLM) was used to fabricate the 18Ni-300 maraging steel samples for in situ uniaxial tensile tests. The SLM parameters used during the fabrication of test samples include a laser power of 275 W, scanning speed of 700 $\mathrm{mm\ s^{-1}}$, hatch spacing of 0.08 mm, and layer thickness of 0.04 mm. This set of SLM parameters was optimised in **Chapter 3 Section 3.3** (**Table 10**, SLM config. no. 5, [41]) to obtain high relative density (> 99 %) and good mechanical properties. Sample preparation involved grinding and polishing the surface of test samples until smooth and mirror-like. Final polishing was done using 0.05 $\mu\mathrm{m}$ colloidal silica. Subsequently, speckle patterns were deposited on the surface of test samples via magnetron sputtering (**Figure 32**).

A direct current magnetron sputtering machine was utilised in the present investigation (**Figure 32**), manufactured by Zhengzhou Ketan Instrument Equipment Co. Ltd. It has a relatively small size (i.e. can be placed on the table) as well as several customisable features, such as the option to change the sputter current, sputter duration, rotation speed and height of the sputter platform, in addition to controlling the chamber pressure during sputtering. Argon gas was used during the sputtering process.

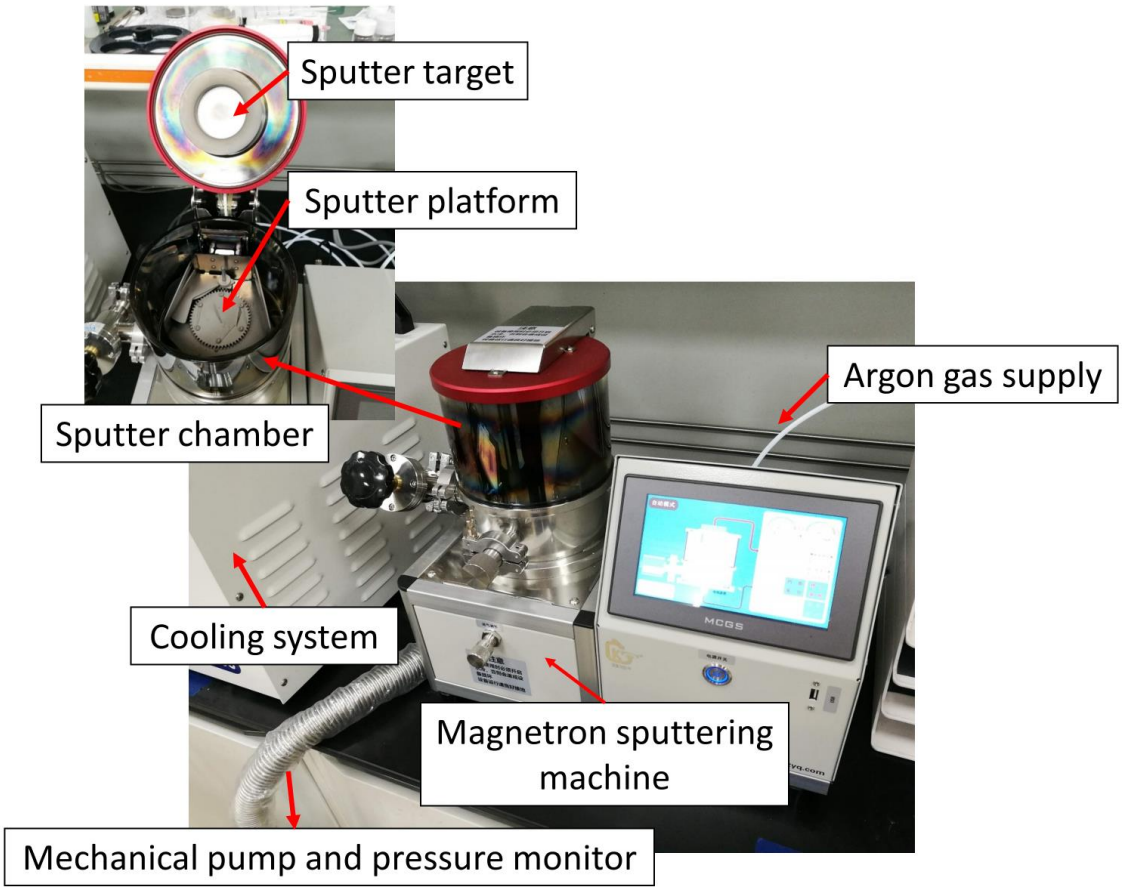

Figure 32: Direct current magnetron sputtering machine.

Testing was conducted inside the Zeiss Sigma 500 SEM using an IBTC-300SL in situ tensile machine manufactured by CARE Measurement and Control Co. Ltd. The samples were deformed to predefined deformation steps via displacement control, where the samples exhibited significant plastic deformation (3 % global strain). DIC images of selected deformation steps were captured in situ via SEM using specific imaging parameters (**Table 19**), and subsequently analysed via Vic 2D DIC software to generate strain distribution maps.

Table 19: SEM imaging parameters and Vic 2D analysis parameters used in the present investigation.

SEM	
Image resolution [px × px]	3072 × 2304
Field of view, FOV [µm × µm]	45.73 × 34.30
Pixel size [nm px^{-1}] (Divide field of view by image resolution)	14.89
Vic 2D DIC software	
Subset size	49
Step size	2
Correlation algorithm	Normalised squared differences

The strain distribution was characterised in terms of von Mises surface strain, ε_{vM}. The equation for ε_{vM} (**Equation (10)**) was formulated via considerations for principal plain strain and only considers the surface strain of the test sample [157]:

$$\varepsilon_{vM} = \frac{2}{3}\sqrt{\varepsilon_1^2 - \varepsilon_1\varepsilon_2 + \varepsilon_2^2} \quad \textbf{(10)}$$

4.2.1.2. Results and discussion

Several trends were identified when comparing the speckle patterns deposited using different magnetron sputtering parameter configurations (**Figure 33**). All four speckle patterns exhibited island growth mode (or Volmer-Weber growth mode) [160]. The individual speckles were first deposited on the sample's surface as islands, and grew into clusters and agglomerated as the sputtering continued. However, the speckle pattern deposited via configuration 3 (**Figure 33**(c)) was too sparsely distributed and not suitable for SEM-DIC. The magnified image of individual speckles and the speckle size distribution histogram were included in the inset of each speckle pattern. The values for average speckle size and standard distribution for each speckle pattern were denoted as Mean and SD (**Figure 33**(a-d)). Speckle patterns deposited using configuration 1 (**Figure 33**(a)) had the smallest average speckle size and a more uniform size distribution (i.e. Mean = 71.45 nm, SD = 16.85 nm) as compared to the other three speckle patterns.

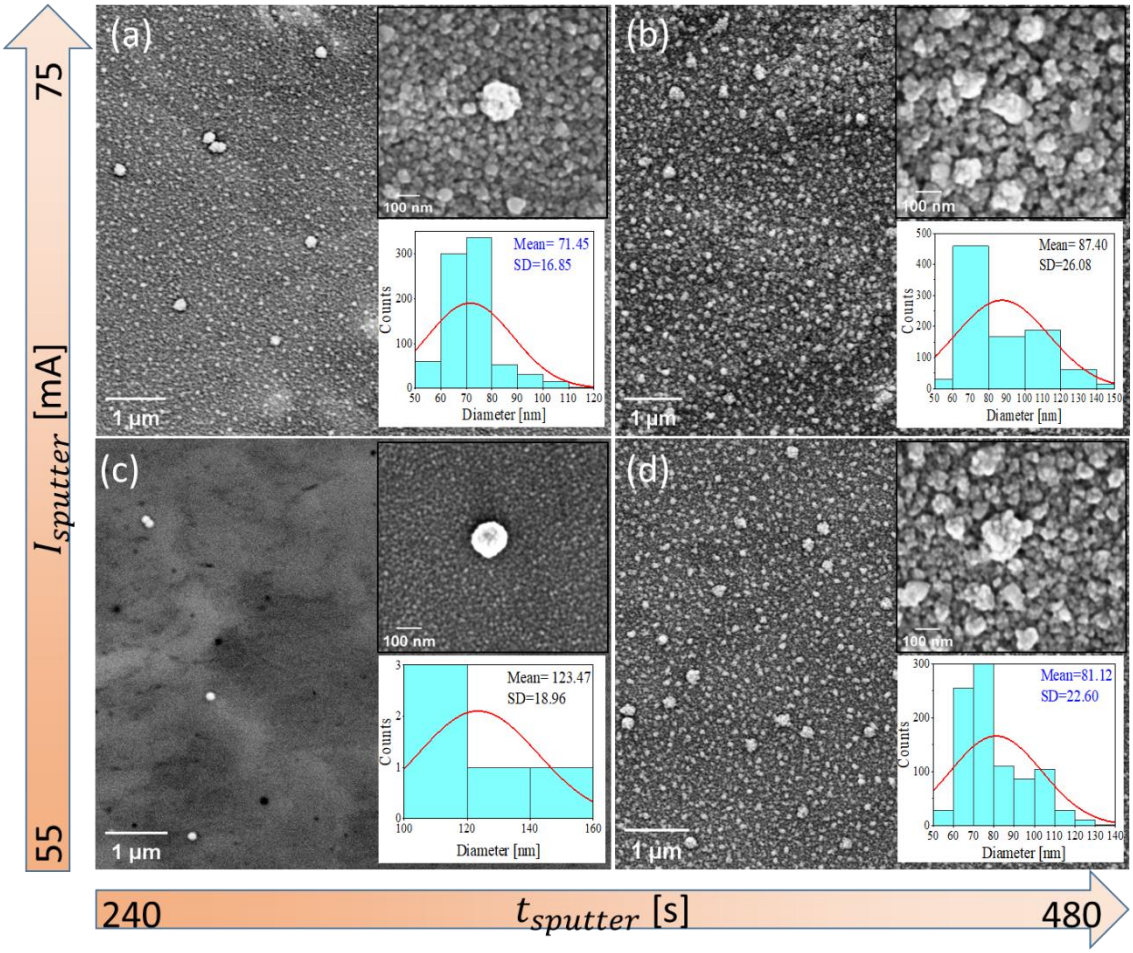

Figure 33: Speckle patterns deposited using the four magnetron sputtering configurations listed in **Table 18**, where (a), (b), (c) and (d) represents configurations 1, 2, 3 and 4 respectively. The magnified image of individual speckles and the speckle size distribution histogram are shown in the inset for each speckle pattern. Configurations that utilised a chamber pressure of 3 Pa during sputtering were indicated using blue text.

The increase in sputter current from 55 mA to 75 mA resulted in increased ejection and deposition of sputtered atoms (**Figure 33**(c vs. a)), and the speckles grew larger and less uniform in size (**Figure 33**(d vs. b)). This is because the use of a higher sputter current caused the argon plasma to bombard the sputter target with increased energy, resulting in increased sputter deposition rate [161]. In contrast, the use of a lower sputter current resulted in the deposition of a sparse and porous speckle pattern, where the white dots were the speckles and the black dots were regions where the deposition of sputtered atoms was not dense enough (**Figure 33**(c)). This is because the sputtered atoms do not have sufficient kinetic energy during its transport from sputter target to test sample [161], and thus were unable to form the desired speckle pattern.

When the sputter duration was increased from 240 s to 480 s, the speckles grew larger and less uniform in size (**Figure 33**(a vs. b)), and significant agglomeration was identified (**Figure 33**(c vs. d)). During sputtering, the sputtered atoms first adhered to the surface of the test samples and formed individual islands (also known as a population of single adatoms) [160]. As the sputtering process continued, agglomeration occurred around these individual adatoms to form clusters which continued to grow in size and become more stable (i.e. do not decay back into individual atoms).

Decreasing the chamber pressure from 5 Pa to 3 Pa during sputtering resulted in the deposition of smaller and more uniformly sized speckles (**Figure 33**(c vs. a), **Figure 33**(b vs. d)). The use of lower chamber pressure during sputtering resulted in reduced particle scattering (i.e. reduced collisions between sputtered atoms and argon plasma), and the sputtered atoms retained more kinetic energy during its transport from sputter target to the test sample [162]. Following that, the influences of the three magnetron sputtering parameters were summarised in **Table 20**, which provided a guideline for fine-tuning magnetron sputtering configurations to obtain the desired speckle patterns.

Table 20: Influence of magnetron sputtering parameters on speckle characteristics.

Magnetron sputtering parameters	Resultant speckle characteristics		
	Average speckle size (Mean)	Uniformity in speckle size (SD)	Spatial distribution of speckles
Increasing sputter current, $I_{sputter}$	Increased	Less uniform	More dense
Increasing sputter duration, $t_{sputter}$	Increased	Less uniform	More dense
Decreasing chamber pressure, $P_{sputter}$	Decreased	More uniform	More dense

4.2.2. Application of the developed speckle patterns in SEM-DIC investigations

Magnetron sputtering configuration 1 ($I_{sputter} = 75$ mA, $t_{sputter} = 240$ s, $P_{sputter} = 3$ Pa) was selected for SEM-DIC because the speckles deposited via this configuration were smaller and more uniformly shaped when compared to the other three configurations (**Figure 33**(a vs. b-d)). A pixel size of 14.89 nm px^{-1} (or approx. 15 nm px^{-1}) and a strain resolution of 71.45 nm (or approx. 71 nm) was achieved, i.e. each speckle was approximately 5 pixels and was sufficient to avoid aliasing effects when captured via SEM.

In situ tensile experiments were conducted to evaluate the capability of this speckle pattern for characterising the strain distribution and slip bands in SLM 18Ni-300 maraging steel samples subjected to uniaxial tensile loading (**Figure 34**). This speckle pattern was identified to have good contrast with the surface of the test sample, and the grain morphology was still visible after the speckle pattern was applied (**Figure 34**(a)). Subsequent deformation resulted in cracks forming on the surface of the test sample (**Figure 34**(b)). Despite that, the speckle pattern continued to adhere to the surface of the test sample, indicating good adherence as well as enabling continued tracking of SEM-DIC measurements.

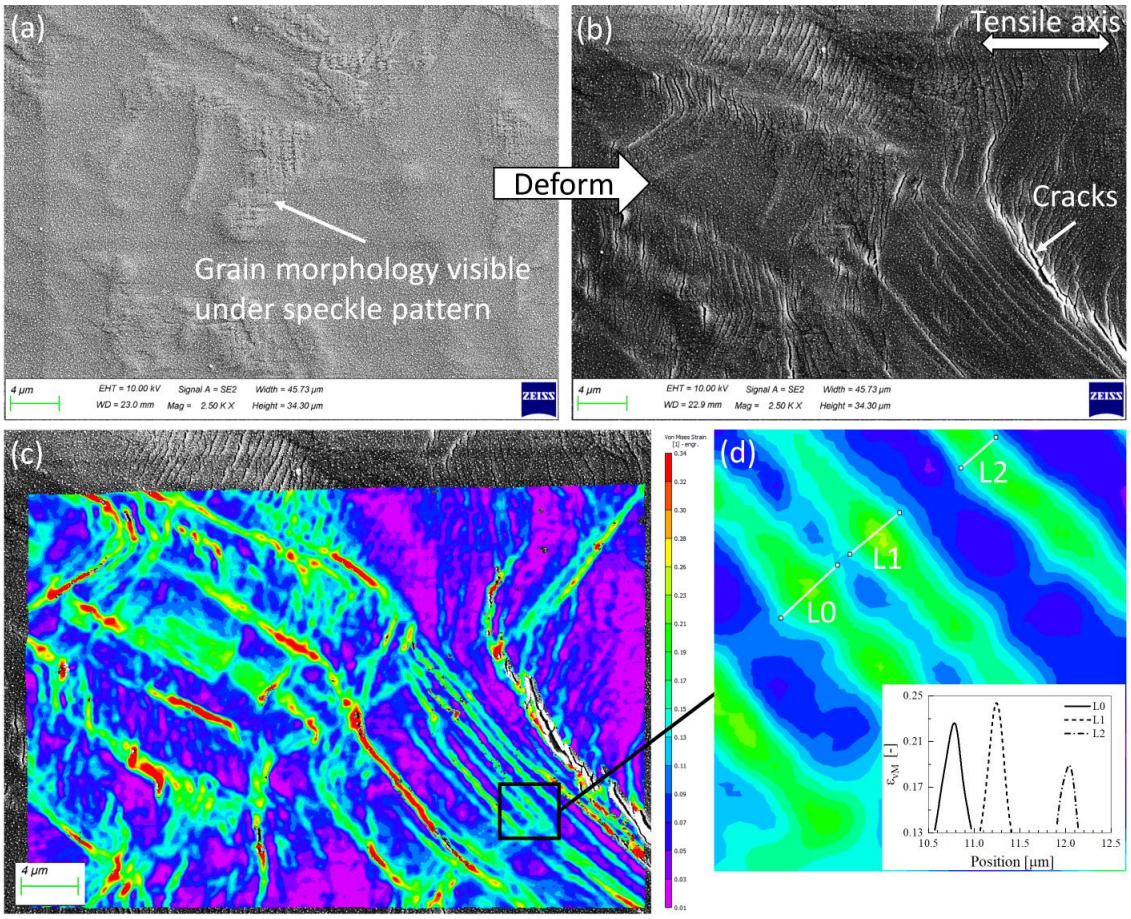

Figure 34: Application of speckle pattern deposited via magnetron sputtering configuration 1 for SEM-DIC of SLM 18Ni-300 maraging steel: (a) shows the initial condition with no loading, (b) shows the last deformation step, (c) shows the DIC strain

distribution map overlaid on last deformation step, and (d) shows the width and amplitude of three slip bands measured via SEM-DIC.

Slip bands were identified from SEM-DIC measurements of the last deformation step, which were presented in terms of von Mises strain, ε_{vM} (**Figure 34**(c-d)). In particular, slip bands were clearly observed when $\varepsilon_{vM} \geq 0.19$, and were aligned with the location of cracks (**Figure 34**(c)). A closer inspection of three slip bands revealed their strain amplitudes were in the range of $0.19 \geq \varepsilon_{vM} \geq 0.24$, while their widths were in the range of 0.24 – 0.40 μm (or 240 – 400 nm, **Figure 34**(d)).

4.2.3. Summary

The influence of magnetron sputtering parameters, i.e. sputter current ($I_{sputter}$), sputter duration ($t_{sputter}$), and chamber pressure during sputtering ($P_{sputter}$) on the resultant speckle characteristics were investigated using a $L_4(2^3)$ Taguchi orthogonal array with four parameter configurations. In **Figure 33** and **Table 20**, it was identified that increasing $I_{sputter}$ resulted in increased average speckle size and denser spatial distribution of speckles due to the bombardment of argon plasma with higher energy. Increasing $t_{sputter}$ resulted in significant agglomeration due to the formation of clusters around the previous speckles as the sputtering process continued, which may reduce speckle edge sharpness. The use of a lower $P_{sputter}$ led to reduced collisions between sputtered atoms and argon plasma, resulting in the deposition of smaller and more uniformly sized speckles. The deposition of speckle patterns was identified to follow island growth mode (or Volmer-Weber growth mode).

Among the four magnetron sputtering configurations studied, configuration 1 ($I_{sputter} = 75\ \mathrm{mA}, t_{sputter} = 240\ \mathrm{s}, P_{sputter} = 3\ \mathrm{Pa}$) was identified as the most suitable for SEM-DIC of SLM 18Ni-300 maraging steel subjected to uniaxial tensile loading. A pixel size of approximately 15 $\mathrm{nm\ px^{-1}}$ and a strain resolution of approximately 71 nm were achieved using this speckle pattern. Slip bands were successfully characterised via SEM-DIC strain distribution maps. Individual slip bands were identified to have von Mises surface strain amplitudes (ε_{vM}) ranging between 0.19–0.24 and widths ranging between 240–400 nm.

Following that, it was identified in subsequent experiments that a larger FOV and higher image resolution are needed to investigate the microscale plastic strain localisation in SLM 18Ni-300 maraging steel. This is to accommodate for more grains within the FOV and higher resolution of SEM-DIC measurements. Further experiments and fine-tuning of magnetron sputtering parameters were conducted to identify suitable parameter configurations that meet the experimental requirements. In particular, a speckle pattern with smaller average speckle size is desirable for SEM-DIC measurements at higher image resolution (i.e. up to $4096\ \mathrm{px} \times 3072\ \mathrm{px}$). The speckles should also be relatively uniform in size and densely distributed throughout the entire FOV.

Subsequently, the magnetron sputtering parameters were fine-tuned with reference to **Table 20**, using configuration 1 ($I_{sputter} = 75\ \mathrm{mA}, t_{sputter} = 240\ \mathrm{s}, P_{sputter} = 3\ \mathrm{Pa}$) as the starting configuration. The $I_{sputter}$ was increased from 75 mA to 95 mA and $t_{sputter}$ was increased from 240 s to 360 s to deposit a speckle pattern with a larger average speckle size and denser distribution throughout a larger FOV. The $P_{sputter}$ was increased slightly from 3 Pa to 4 Pa for creating speckles with a larger average size, and the uniformity in speckle size and dense distribution throughout the FOV was visually inspected and confirmed using SEM micrographs. Thus, a new set of magnetron sputtering parameters was identified, i.e. $I_{sputter} = 95\ \mathrm{mA}, t_{sputter} = 360\ \mathrm{s}, P_{sputter} = 4\ \mathrm{Pa}$. A pixel size of 55.30 $\mathrm{nm\ px^{-1}}$ was achieved using this speckle pattern, and the speckle pattern deposited via this new configuration is shown in **Figure 36**(d) in **Section 4.3.1.3**.

4.3. SEM-DIC investigations of microscale plastic strain localisation

4.3.1. Experimental methodology

4.3.1.1. Material processing and sample fabrication

SEM-DIC investigations of microscale plastic strain localisation have been conducted to obtain essential insights on the process-microstructure-properties relationships in steels. Bean et al. [140] conducted SEM-DIC investigations on SLM 316L stainless steel, and identified that the microscale plastic strain localisation occurred heterogeneously due to the non-uniform distribution of rapid solidification-induced cellular structures throughout the sample. Also, it was reported that dislocation slip, deformation twinning, and martensitic phase transformation may be active concurrently at different stages during plastic deformation. However, the plastic strain localisation in SLM 18Ni-300 maraging steel is yet to be elucidated in the literature due to lack of investigations on this topic.

Following that, SEM-DIC investigations were conducted in the present investigation to elucidate the microscale plastic strain localisation in SLM 18Ni-300 maraging steel. Two sample conditions were investigated, namely the as-built (AB) condition and the solution-aging treatment (SAT) condition. The experimental methodology is explained in **Section 4.3.1**, the experimental findings are reported and analysed in **Sections 4.3.2** to **4.3.5**, and a comparative analysis between AB and SAT samples together with an in-depth discussion of microscale plastic strain localisation in relation to microstructural heterogeneity are included in **Section 4.3.6**.

In the present investigation, the 18Ni-300 maraging steel powder used for the fabrication of samples was produced via argon gas atomisation. The size of powder particles was identified to be between 15 µm and 53 µm, and its chemical composition is shown in **Table 21**. The metal powder used for the fabrication of samples in the present investigation is the same material as the one used in the **Chapter 3** (**Table 21** vs. **Table 8**). The differences in powder particle size and chemical composition was due to the use of different batches of metal powder during fabrication.

Table 21: Chemical composition of 18Ni-300 maraging steel studied in the present investigation.

Element [wt. %]	Ni	Co	Mo	Ti	Al	Fe
	17.00 – 19.00	8.50 – 10.00	4.50 – 5.20	0.60 – 0.80	0.05 – 0.15	Bal.

The in situ tensile samples used in the present investigation were fabricated in a nitrogen-filled atmosphere using an EOS M290 metal 3D printer, and the SLM parameters are shown in **Table 22**. The SLM parameters used for fabricating in situ tensile samples were identical to the best configuration identified in the statistical optimisation experiment in **Chapter 3 Section 3.3** (**Table 10**, SLM config. no. 5, [41]). This SLM parameter configuration was optimised for fabricating samples with high relative density (> 99 %) and mechanical properties that were comparable with conventionally made condition. The samples were fabricated in the form of individual metal blocks (50

mm × 15 mm × 6 mm) and subsequently machined to the final dimensions using electrical discharge machining (EDM) (**Figure 35**(a)). The samples were not fabricated to their final dimensions using SLM to minimise the effects of residual stress after fabrication. An orthogonal scanning strategy was used during SLM fabrication where each layer was scanned in a zig-zag pattern and subsequent layers were rotated by 90 ° (**Figure 35**(b)). Chemical etching using 8 % Nital was done to reveal the microstructure morphology in AB and SAT samples (**Figure 35**(c)). The etched microstructure was captured via optical microscope.

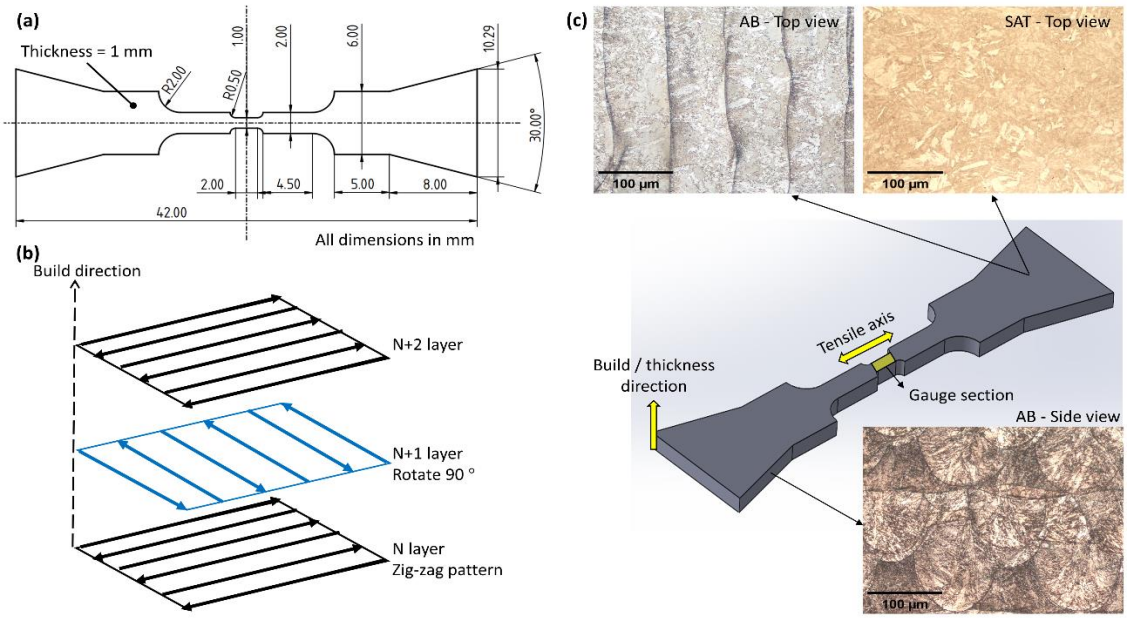

Figure 35: Fabrication of in situ tensile samples. (a) The dimensions of samples used in the present investigation. (b) The orthogonal scanning strategy used to fabricate the samples. (c) Chemically etched microstructure of SLM 18Ni-300 maraging steel.

Table 22: SLM parameters used for the fabrication of in situ tensile samples, obtained via statistical optimisation (**Chapter 3 Section 3.3 Table 10**, SLM config. no. 5, [41]).

Parameter	Value
Laser power [W]	275
Scan speed [mm s^{-1}]	700
Hatch spacing [mm]	0.08
Layer thickness [mm]	0.04
Base plate preheat temperature [°C]	100
Scanning strategy	Orthogonal, **Figure 35**(b)
Relative density [%]	> 99

For post-processing heat treatment, the solution-aging treatment (SAT) plan was used to heat treat the in situ tensile samples and obtain mechanical properties that were comparable with conventional wrought and aged condition. The samples were first heat-treated at 840 ℃ for 1 h, followed by 490 ℃ for 6 h. The furnace was heated at 8 ℃ min^{-1} until it reached the desired temperature and maintained for 10 min to ensure uniform chamber temperature before the start of heat treatment. Heat treatment was conducted in an argon atmosphere and the samples were cooled in air after the duration. It should be noted that the individual metal blocks were subjected to heat treatment before they were machined to the final dimensions using EDM. This was done to ensure dimensional accuracy and to avoid warping and residual stress in the in situ tensile samples after heat treatment. The SAT plan was determined based on the differential scanning calorimetry (DSC) analysis presented by Tan et al. [18]. The SAT plan was suggested for heat treating SLM 18Ni-300 maraging steel samples to obtain mechanical properties that were comparable with conventional wrought and aged condition. The phase transformations in 18Ni-300 maraging steel were identified to occur at two temperature ranges. The formation of Ni-based intermetallics due to precipitation hardening in the material corresponded to the DSC curve's exothermic peak between 387 ℃ and 485 ℃. The dissolution of Ni-based intermetallics in the martensite matrix and recrystallisation corresponded to the DSC curve's endothermic peak between 724 ℃ and 832 ℃. The temperatures of 490 ℃ and 840 ℃ in the SAT plan were selected to allow for the complete transformation of phases.

4.3.1.2. Sample preparation and microstructure characterisation

Common metallography procedures were utilised to prepare the samples for microstructure characterisation via EBSD. The samples were ground using P240 to P2000 silicon carbide grinding papers until a flat and level surface was obtained. Polishing was done using 1 μm diamond suspension followed by final polish using 0.05 μm colloidal silica to obtain a mirror-like surface finish. Before polishing, Vickers hardness indents were made on the sample's surface around the region of interest (ROI) to facilitate in situ data acquisition from the same location on the sample [134,135]. The Vickers hardness indents were made using a 430 SVA Vickers hardness tester with a load of 2.94 N (HV 0.3) and 10 s dwell time. The shape and location of the Vickers indents served as reference points for locating the same ROI during EBSD scanning, in situ tensile experiments, and SEM-DIC measurements. Following that, the samples were subjected to vibration polishing for 1 h in 0.05 μm colloidal silica to prepare for EBSD scanning. EBSD was conducted using Zeiss Sigma 500 SEM equipped with a Symmetry S2 EBSD detector from Oxford Instruments. The EBSD scanning parameters are summarised in **Table 23**.

Table 23: SEM parameters and image resolution used during data acquisition and after alignment.

Dataset	EBSD	SEM-Microstructure	SEM-DIC	Aligned dataset
SEM detector	EBSD	Secondary electron (SE2)	Secondary electron (SE2)	–
Accelerating voltage [kV]	20	20	20	–
Working distance [mm]	12	10	23	–
Aperture [µm]	60	60	60	–
SEM magnification [-]	$1000\times$	$1000\times$	$1000\times$	–
Beam dwell time [$\mu s\ px^{-1}$]	8000.00	3.20	3.20	–
SEM stage tilt [°]	70.0	0.0	0.0	–
Field of View [$\mu m\ \times\ \mu m$]	114.25×85.65	114.30×85.75	112.60×84.30	114.25×85.65
Resolution [$px \times px$]	750×563	4096×3072	2038×1526	2286×1714
Pixel Size [$nm\ px^{-1}$]	150.00	27.91	55.30	50.00

The microstructural heterogeneity (i.e. variations in grain size and crystallographic texture) in AB and SAT samples was characterised using MTEX [163,164]. MTEX is an open-source MATLAB toolbox used for analysing the crystallographic texture of metals using EBSD data as input. A grain misorientation threshold angle of $2°$ was used during the grain reconstruction for the EBSD datasets of both AB and SAT samples. In particular, all grain boundaries with a misorientation angle $\geq 2°$ were included during grain reconstruction. The grain boundaries were further filtered into two ranges representing the low-angle and high-angle grain boundaries, i.e. LAGBs $= 2°–15°$, HAGBs $> 15°$. The EBSD datasets were then used to generate the various figures for characterising microstructural heterogeneity, including: inverse pole figure (IPF) maps, grain size distribution, phase composition maps, and kernel average misorientation (KAM) maps. It should be noted that the grain boundaries along the outer edges of the grains have a misorientation angle ranging between $2°–62°$, and the majority of them were HAGBs ($> 15°$). These grain boundaries were defined as outer grain boundaries when plotting the related microstructure maps in the present investigation.

Following that, the KAM maps provided a measure for the orientation gradients (i.e. internal misorientations) within individual grains. KAM was calculated using **Equation (11)** as shown below [165]:

$$KAM_{(i,j)} = \frac{1}{|N(i,j)|} \sum_{(k,l)\in N(i,j)} \omega(o_{i,j}, o_{k,l}) \quad \textbf{(11)}$$

where $o_{i,j}$ denotes the orientations at pixel position (i,j) obtained from EBSD datasets, $o_{k,l}$ denotes the orientations of the neighbouring pixel position (k,l), $\omega(o_{i,j}, o_{k,l})$ denotes the misorientation angle between $o_{i,j}$ and $o_{k,l}$, $N(i,j)$ denotes the set of all neighboring pixel positions, and $|N(i,j)|$ denotes the number of elements in $N(i,j)$. The selection of $N(i,j)$ is crucial for computing KAM. The KAM maps in the present investigation were generated using the third nearest neighbours for each pixel position, and only pixel positions belonging to the same grain were considered.

4.3.1.3. Magnetron sputtering, in situ tensile experiments, and microscale SEM-DIC

Prior to conducting in situ tensile experiments, submicron-sized speckle patterns need to be created on the in situ tensile samples' surface to facilitate the tracking of surface displacements and strain via SEM-DIC. Hoefnagels et. al. [36] suggested the use of magnetron sputtering as a scalable and robust method for depositing sub-micron sized speckle patterns on the samples' surface. For the present investigation, a KT-Z1650PVD direct current magnetron sputtering machine manufactured by Zhengzhou Ketan Instrument and Equipment Co. Ltd. was used to deposit the speckle patterns (**Figure 36**(a and b)). Magnetron sputtering is a physical vapour deposition process which utilises argon plasma to bombard a sputter target, resulting in the ejection of sputtered atoms and subsequent deposition on the samples' surface (**Figure 36**(c)). The deposition of sub-micron sized speckle pattern on the samples' surface is shown together with the Vickers indent (**Figure 36**(d) and zoomed-in image at top right). The magnetron sputtering parameters used include a sputtering current of 95 mA, a sputter duration of 360 s, and the chamber pressure was maintained at around 4 Pa during sputtering. These parameters were fine-tuned based on the experimental findings reported in **Section 4.2** [42]. The material used for the sputter target was an Indium-Tin solder alloy with low melting temperature, $\mathrm{In_{52}Sn_{48}}$.

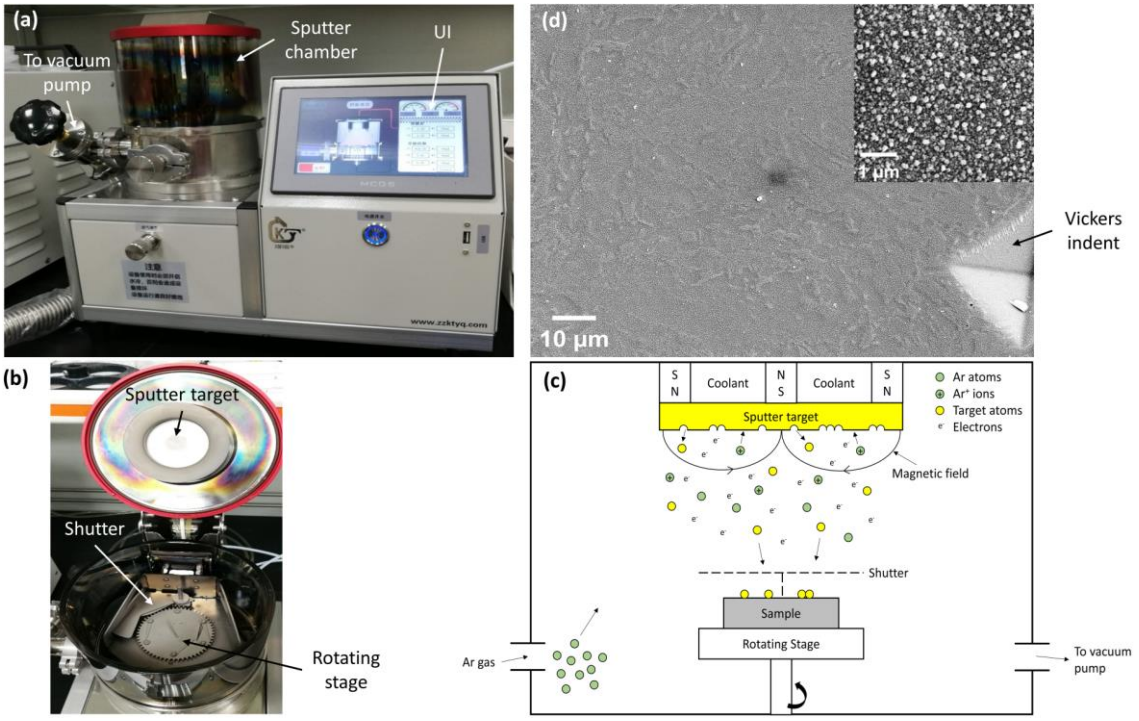

Figure 36: Deposition of submicron-sized speckles on the surface of in situ tensile samples via magnetron sputtering. (a) The magnetron sputtering machine used in the present investigation. (b) The inside of the sputter chamber shown in (a). (c) Schematic for the working principle of magnetron sputtering. (d) Speckle pattern deposited on the samples' region of interest (ROI), marked with Vickers indent. Inset shows the submicron-sized speckles.

In situ tensile experiments were conducted inside the Zeiss Sigma 500 SEM using an IBTC-300SL in situ tensile test stage manufactured by CARE Measurement and Control Co. Ltd. A preload of 50 N was applied to secure the samples on the in situ tensile test stage and prevent slipping during experiments. The samples were subjected to uniaxial tension at a constant displacement rate of 0.003 $\mathrm{mm\,s^{-1}}$. Each sample condition (AB and SAT) was tested twice for repeatability. Note that the in situ tensile experiments were not conducted until completed fracture (i.e. separation into two pieces) had occurred in the sample.

SEM-DIC images were captured at fixed displacement intervals of 0.025 mm. The SEM scanning parameters are summarized in **Table 23**. A SEM magnification of 1000× and beam dwell time of 3.2 $\mathrm{\mu m\ px^{-1}}$ were utilised to minimise the effects of image drift between SEM scans. The field of view (FOV) and resolution of SEM-DIC images were decided after considering the grain characteristics (i.e. average grain size and quantity within the ROI) and speckle pattern (i.e. average speckle size and distribution within the ROI) produced via magnetron sputtering. The shape and location of the Vickers indents served as absolute reference points for locating the same ROI after each displacement interval (**Figure 36**(d)). The effective surface strain, ε_{eff} occurring within the ROI on the sample during plastic deformation was calculated via **Equation (12)** [38]:

$$\varepsilon_{eff} = \sqrt{\frac{1}{2}\left(H_{xx} - H_{yy}\right)^2 + \frac{1}{2}\left(H_{xy} + H_{yx}\right)^2} \quad \textbf{(12)}$$

where $H_{xx}, H_{yy}, H_{xy}, H_{yx}$ denote the in-plane displacement gradient tensor components in the axial and shear directions. Note that this is a 2D approximation for the surface strain occurring on the sample, and that the deformation is fully plastic. Calculations for ε_{eff} was done using the Vic 2D DIC software by Correlated Solutions, Inc. A subset size of 35, a step size of 2, and the normalised squared differences correlation algorithm were used during calculations.

4.3.1.4. Dataset alignment

The EBSD dataset requires post-processing to align it with the SEM-DIC dataset before further analysis can be done. This is due to the 70 ° stage tilt that was inherent during EBSD scanning, causing the EBSD dataset to be tilted. The alignment of datasets from different sources (i.e. EBSD and SEM-DIC) to a common grid would facilitate the precise characterisation of microscale plastic strain localisation and active slip systems in relation to the microstructural heterogeneity of SLM 18Ni-300 maraging steel. The dataset alignment methodology used in the present investigation is illustrated in **Figure 37**.

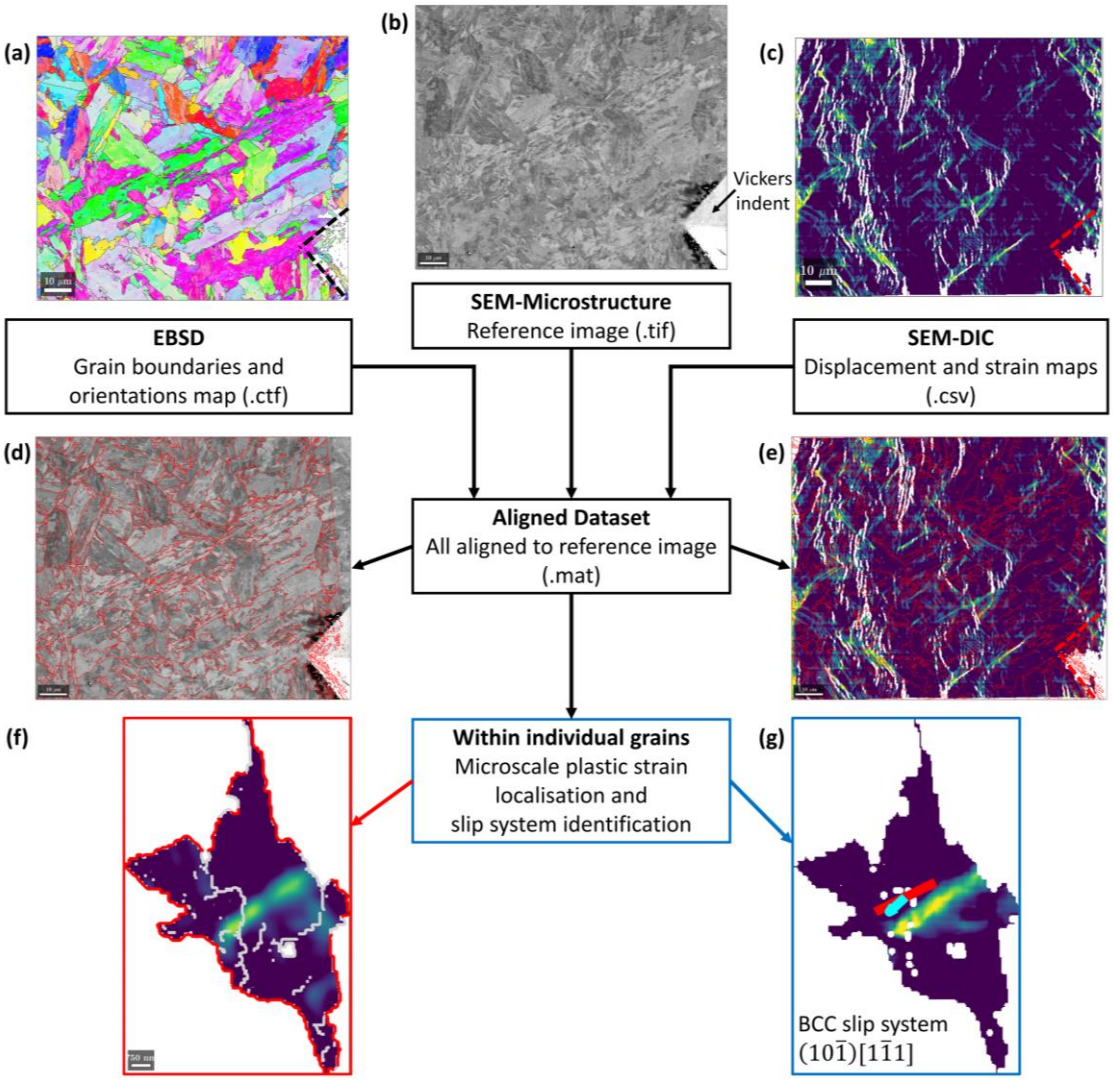

Figure 37: Dataset alignment methodology used to align datasets from different sources to a common grid. (a) EBSD dataset. (b) Reference image of the microstructure (SEM-Microstructure). (c) SEM-DIC dataset. Aligned dataset showing the (d) reference image and (e) SEM-DIC image with the outer grain boundaries outlined in red. (f) Characterisation of microscale plastic strain localisation within a grain, with the low-angle and high-angle grain boundaries (LAGBs and HAGBs) outlined in light grey and red. (g) Active slip system for said grain, with slip plane and slip direction indicated using red and cyan lines. The Vickers indent marks were used for aligning the datasets together,

and were outlined using dashed black or red lines. The dataset shown in the present figure is for SAT sample.

The dataset alignment methodology suggested by Vermeij et al. [37] was adapted and developed in the present investigation to correct tilting in the EBSD dataset and digitally align it and the SEM-DIC dataset to a common grid (**Figure 37**). The alignment was done using custom MATLAB scripts based on those written by Vermeij et al. The EBSD and SEM-DIC datasets were aligned to a common grid using the SEM image of the microstructure as the reference image (**Figure 37**(a-c)). The working principle of the alignment methodology involved calculating the misalignments (i.e. differences in x- and y-coordinates) between the selected points in the dataset to be aligned (i.e. EBSD or SEM-DIC) and the reference image. The misalignments were then used to fit a 2D polynomial displacement field and align the datasets to a common grid. A second-order polynomial function with 12 degrees of freedom was used to align the EBSD dataset to the reference image, while a first-order polynomial function with 6 degrees of freedom was used to align the SEM-DIC dataset. The selected points used for calculating the misalignments between datasets include the grain boundaries from the EBSD dataset, Vickers indent marks, and the outline dimensions of the datasets. The same methodology was applied for aligning the datasets for both AB and SAT samples. The aligned AB and SAT datasets containing both EBSD grain information and SEM-DIC strain maps were saved as separate MATLAB .mat files (**Figure 37**(d, e)), which were then used to generate the figures for analysing the microscale plastic strain localisation and active slip systems in the investigated grains (**Figure 37**(f, g), grain from SAT sample). The identification of active slip systems in the grains of both samples was done using a separate set of MATLAB scripts, and its methodology was further explained in **Section 4.3.1.5.**

4.3.1.5. Slip system identification

According to the literature, martensite is the dominant phase in 18Ni-300 maraging steel, and has a BCC crystal lattice [17]. The main deformation mechanism in BCC crystal was reported as dislocation slip, and slip occurred in the closed-packed planes and along the closed-packed directions [145,166]. There are a total of 48 independent slip systems in the BCC crystal, including 12 slip systems in the $\{110\}\langle\bar{1}11\rangle$ family (i.e. 6 non-parallel $\{110\}$ planes each containing 2 $\langle\bar{1}11\rangle$ slip directions), 12 slip systems in the $\{112\}\langle11\bar{1}\rangle$ family, and 24 slip systems in the $\{123\}\langle11\bar{1}\rangle$ family.

Slip system identification was done to determine the active slip systems in the grains of SLM 18Ni-300 maraging steel during plastic deformation. The Slip Systems based Local Identification of Plasticity (SSLIP) methodology suggested by Vermeij et al. [38] was adapted and developed in the present investigation to identify the active slip systems within the investigated grains. The working principle of SSLIP involved matching the in-plane displacement gradient tensor components calculated via SEM-DIC measurements with the localised slip systems of each grain calculated from EBSD grain information. Following that, the slip activity fields for each considered slip system in the investigated grains were generated using custom MATLAB scripts. The slip activity in the individual slip systems was characterised in terms of slip magnitude, γ. The slip activity was generated by numerically solving the constrained optimisation problem where the total slip magnitude over all slip systems was minimised. It was assumed that the 2D slip kinematics were sufficiently described via the minimisation of the sum of 3D slip magnitude. Also, it was assumed that the in-plane deformation behaviour of the investigated grains, described by their in-plane displacement gradient tensor components, were consistent with the combined active slip system kinematics in those grains.

Following that, the active slip systems within the investigated grains of SLM 18Ni-300 maraging steel were analysed using Schmid factor to determine the primary slip system for those grains. The Schmid factor is used to denote the orientation of a single crystal's slip system (i.e. slip plane normal and slip direction) in relation to the direction of applied load [145,167]. Slip initiation would occur more easily in slip systems with a higher Schmid factor, due to them being favourably oriented for easier dislocation motion (i.e. $45\ °$ with respect to the direction of applied load). The primary slip system is defined as the slip system with the highest Schmid factor (max. 0.5) among the evaluated slip systems. When calculating the Schmid factor, it is assumed that only uniaxial tensile loading is present and the grains are approximated as single crystals. Calculations for the Schmid factor were done using MTEX [168].

4.3.2. Microstructural heterogeneity captured via EBSD

The findings of the present investigation are analysed in **Sections 4.3.2** to **4.3.5**. In **Section 4.3.2,** the microstructural heterogeneity (i.e. variations in grain size and crystallographic texture) in SLM 18Ni-300 maraging steel was characterised via EBSD. Comparisons of the crystallographic texture (i.e. overall grain orientation distribution), grain size, phase composition, and the variation in low-angle and high-angle grain boundaries (LAGBs and HAGBs) between AB and SAT samples are presented. In **Section 4.3.3**, the evolution of plastic strain localisation in both samples was analysed via SEM-DIC. In **Section 4.3.4**, a microscale analysis of the evolution of plastic strain localisation within the selected grains of both samples was conducted by digitally aligning the EBSD and SEM-DIC datasets to a common grid. The alignment methodology used in the present investigation was adapted from Vermeij et al. [37]. In **Section 4.3.5**, the active slip systems within the selected grains of both samples were analysed using the SSLIP methodology adapted from Vermeij et al. [38].

The microstructural heterogeneity in SLM 18Ni-300 maraging steel was characterised via EBSD as shown in **Figure 38**. Note that the results shown in **Figure 38** are localised to the ROI itself. A total of 10599 and 2686 grains were identified in the ROI of AB and SAT samples, respectively. Analysis of microstructural heterogeneity was done taking into consideration all grains within the selected ROI. **Figure 38**(a and b) show the microstructure for the ROI in AB and SAT samples in the form of inverse pole figure (IPF) maps. The grains found in AB and SAT samples both exhibited a heterogeneous nature, i.e. have varying sizes, shapes and orientations. In particular, the microstructure found in AB sample included a mix of fine equiaxed grains as well as columnar grains of varying lengths and sizes (**Figure 38**(a)). In contrast, the microstructure found in SAT sample was significantly larger, more elongated and had varying degrees of inclination (**Figure 38**(b)). The spatial distribution of grains for both samples was random throughout the whole ROI. **Figure 38**(c and d) show the IPF density plots for **Figure 38**(a and b), respectively. The grains found in the AB sample were predominantly oriented along the $[001]$ direction. In contrast, the grains in the SAT sample were predominantly oriented close to the $[\bar{1}12]$ direction, followed by a smaller fraction oriented along the $[011]$ direction.

Following that, **Figure 38**(e) shows the grain size distribution of grains found in **Figure 38**(a and b). The grains were sorted according to different ranges of grain diameter and plotted against the area fraction of grains for that range (i.e. the sum of all area fractions for all ranges is 1). This facilitated the quantitative comparison between the grains found in AB and SAT samples. The grains found in AB sample (red columns) were generally smaller in diameter and more uniform in size. The majority of AB grains have a diameter of less than 5 μm and occupied an area fraction of 0.52 (i.e. 52 % of the total grain area in the ROI for AB sample). In contrast, the grains found in SAT sample (blue columns) were spread out across different ranges of diameters and less uniform in size. The majority of grains were between $5\ \mu m$ and $10\ \mu m$ in diameter and occupied an area fraction of 0.22 (i.e. 22 % of the total grain area for SAT sample).

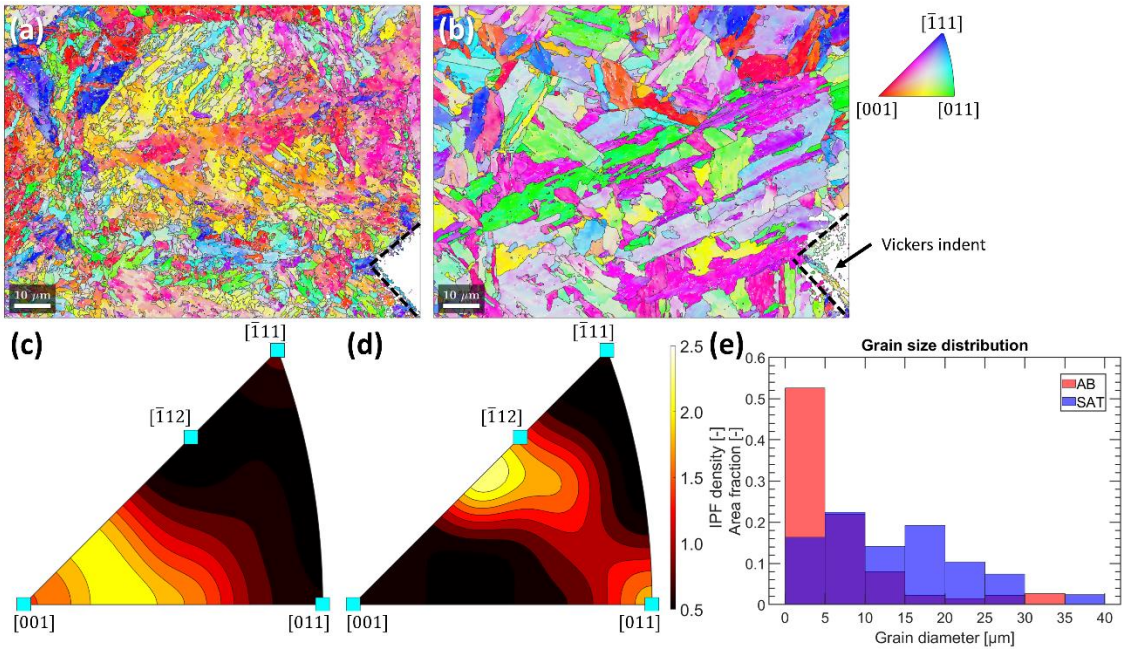

Figure 38: Crystallographic texture and grain size distribution in the ROI of AB and SAT samples. The IPF maps for (a) AB and (b) SAT samples, respectively. The outer grain boundaries are outlined using solid black lines, while Vickers indent marks are outlined using dashed black lines. The Z-direction colour key for IPF maps is shown at the top right. The orientation distribution of grains in the (c) AB and (d) SAT samples was presented as IPF density plots. The grain size distribution histogram (e) for AB and SAT samples. The purple columns in (e) represent the overlap between the AB and SAT datasets.

The phase composition for the ROI in AB sand SAT samples are shown in **Figure 39**(a and b), respectively. Note that the results shown in **Figure 39** are localised to the ROI itself. A comparison for the phase composition and percentage of grain boundary lengths in the ROI of AB and SAT samples are tabulated in **Table 24**. Martensite (Fe-BCC) is the dominant phase in both ROI for AB and SAT samples, followed by traces of austenite (Fe-FCC) and precipitates (Ni_3Ti). The SAT sample has a slightly higher martensite content compared to the AB sample, while the opposite was identified for austenite content (**Table 24**, 99.97 % vs. 99.91 %; 0.01 % vs. 0.02 %). The precipitate content in SAT sample was slightly lower compared to the AB sample (**Table 24**, 0.02 % vs. 0.07 %). The changes in phase composition is due to the phase transformation and precipitation of Ni_3Ti intermetallics that occurred during the second stage of the SAT heat treatment plan. However, its effects were less pronounced in the SAT sample. This may be due to experimental or measurement uncertainties, such as the quality of surface finish after vibration polishing and the quality of EBSD patterns during data acquisition.

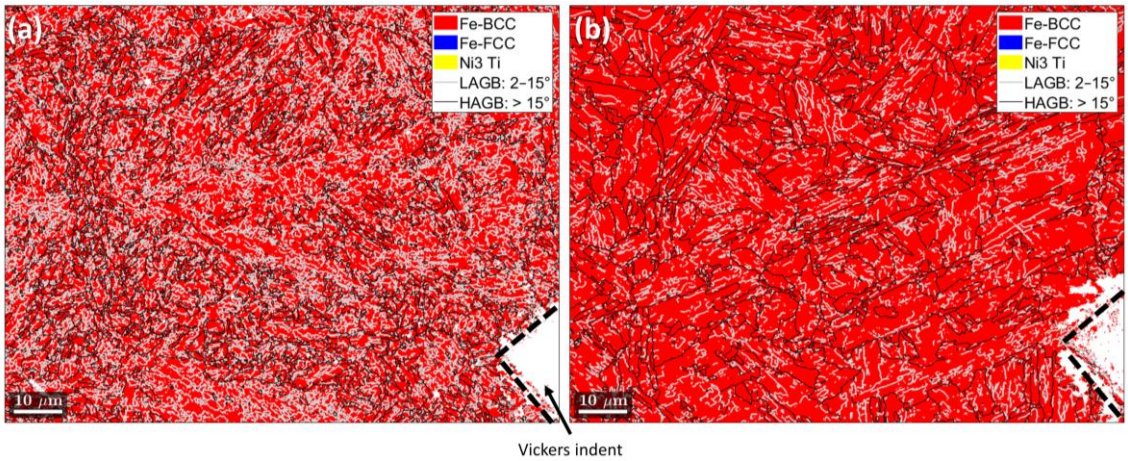

Figure 39: Phase composition in the ROI of (a) AB and (b) SAT samples. The LAGBs and HAGBs are outlined using solid light grey and black lines, respectively. The Vickers indent marks are outlined using dashed black lines.

Table 24: Comparison for the phase composition and percentage of grain boundary lengths in the ROI of AB and SAT samples.

Microstructural features	Sample Condition	
	AB	SAT
Phase composition		
Martensite, Fe-BCC [%]	99.91	99.97
Austenite, Fe-FCC [%]	0.02	0.01
Ni-based intermetallic, Ni_3Ti [%]	0.07	0.02
Percentage of grain boundary lengths		
Percentage of LAGBs $(2\,°–15\,°)$[%]	64.01	53.28
Percentage of HAGBs $(>15\,°)$ [%]	35.99	46.72

Following that, the percentage of grain boundary lengths was calculated by taking the summation of a particular type of grain boundary (i.e. summation of LAGBs or HAGBs) within the ROI and dividing it by the total sum of all grain boundaries within said ROI (**Equations (13) and (14)**) :

$$\text{Percentage of LAGBs} = \frac{\text{Total length of LAGBs}}{\text{Total length of LAGBs} + \text{Total length of HAGBs}} \times 100\,\% \quad \textbf{(13)}$$

$$\text{Percentage of HAGBs} = \frac{\text{Total length of HAGBs}}{\text{Total length of LAGBs} + \text{Total length of HAGBs}} \times 100\,\% \quad \textbf{(14)}$$

The AB and SAT samples both had a higher percentage of LAGBs compared to HAGBs (**Table 24**, AB: 64.01 % vs. 35.99 %, SAT: 53.28 % vs. 46.72 %). The percentage of LAGBs and HAGBs were altered after heat treatment. The SAT sample exhibited a lower percentage of LAGBs and a higher percentage of HAGBs compared to the AB sample (**Table 24**, LAGBs: 53.28 % vs. 64.01 %, HAGBs: 46.72 % vs. 35.99 %). This may be attributed to the recrystallisation and formation of more larger and elongated grains in the SAT sample after heat treatment.

The KAM maps for AB and SAT samples and their corresponding frequency distribution are shown in **Figure 40**(a-c), respectively. A misorientation threshold angle of 5 ° was used during plotting. It was identified that 65.4 % of AB grains have KAM values between 0 ° and 2 °, with 50.4 % of them concentrated between 1 ° and 2 °. The SAT grains exhibited a similar trend to the AB grains, where 81.2 % of them have KAM values between 0 ° and 2 °, with 41.0 % of them concentrated between 0 ° and 1 °. It can be deduced that the occurrence of internal misorientations in SAT grains was directly influenced by the heat treatment process itself. In particular, recrystallisation significantly reduced the KAM in SAT grains, resulting in the formation of a more homogeneous microstructure.

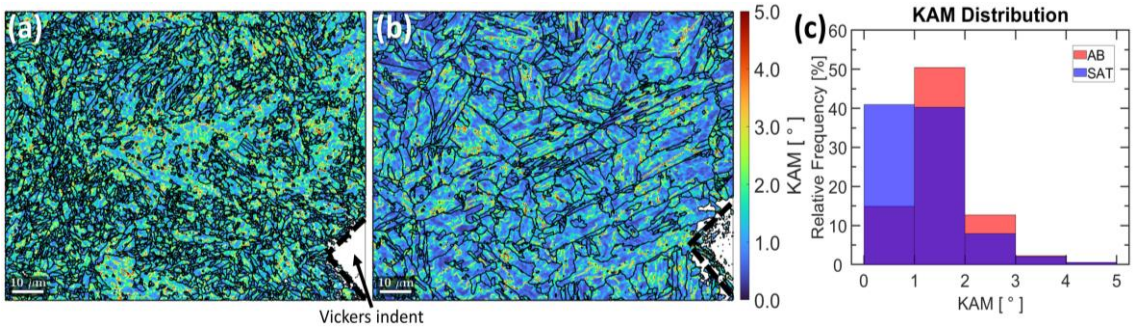

Figure 40: KAM maps for the grains in (a) AB and (b) SAT samples, together with their (c) frequency distribution. The outer grain boundaries are outlined using solid black lines, while Vickers indent marks are outlined using dashed black lines. The purple columns in (c) represent the overlap between the AB and SAT datasets.

4.3.3. Evolution of microscale plastic strain localisation captured via SEM-DIC

In situ uniaxial tensile experiments were conducted inside the SEM to investigate the evolution of microscale plastic strain localisation in SLM 18Ni-300 maraging steel. Two sample conditions were investigated, namely the as-built (AB) and solution-aging treatment (SAT) conditions. The results are shown in **Figure 41**. The nominal stress-strain ($\sigma - \varepsilon_{xx}$) curves for AB and SAT samples are shown in **Figure 41**(a). The jagged appearance of both curves is due to the pausing of the experiment to acquire SEM-DIC images at selected deformation stages. Plastic deformation in AB sample was identified to progress differently compared to the SAT sample. When the AB sample was deformed beyond the elastic limit ($\varepsilon_{xx} \geq 0.030$), it maintained a relatively constant stress state until necking occurred. In contrast, significant strain hardening was identified in the SAT sample as the deformation progressed. The ultimate tensile strength for AB and SAT samples were calculated to be 1161 MPa and 1915 MPa, respectively. Significant necking and microcracks were observed in the gauge region and within the ROI of AB sample, as shown in **Figure 41**(b and c). A similar phenomenon was identified in SAT sample, but the propagation of microcracks occurred more rapidly compared to AB sample.

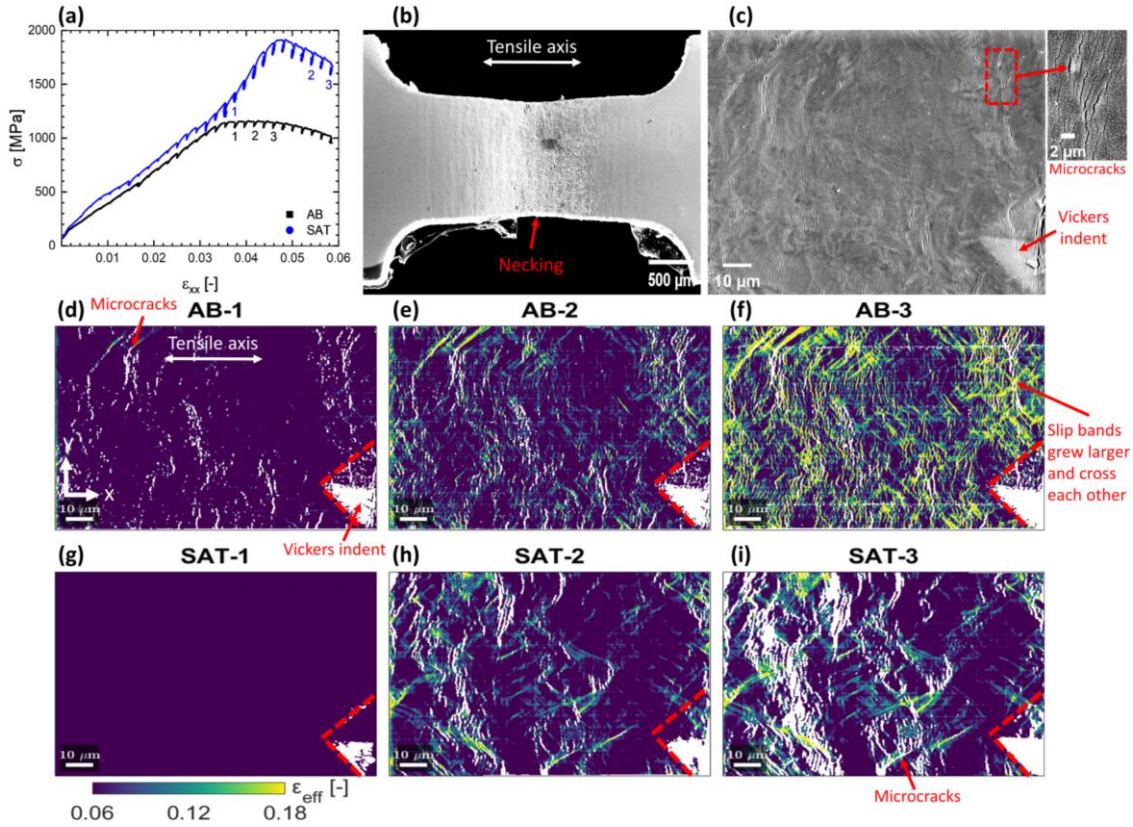

Figure 41: Evolution of plastic strain localisation in AB and SAT samples. (a) The nominal stress-strain curve for AB and SAT samples, together with the deformation stages of interest (i.e. AB-1 to AB-3, SAT-1 to SAT-3). (b) Necking in the gauge section of AB sample after deformation to $\varepsilon_{xx} = 0.058$. (c) Microcracks in AB sample's ROI after deformation to $\varepsilon_{xx} = 0.046$, with zoomed-in image shown at top right. (d-f) Strain accumulation in AB sample's ROI, characterised in terms of effective surface strain (ε_{eff}). The deformation stages AB-1 to AB-3 correspond to $\varepsilon_{xx} = 0.038$, 0.042 and 0.046 ,

respectively. (g-i) Strain accumulation in SAT sample's ROI. The deformation stages SAT-1 to SAT-3 correspond to $\varepsilon_{xx} = 0.038,\ 0.054 \text{ and } 0.058$, respectively. The Vickers indent marks are outlined using dashed red lines. The coordinate axes used during SEM-DIC analysis is shown in (d).

The evolution of microscale plastic strain localisation in AB and SAT samples was captured via SEM-DIC, and the formation of localised slip bands leading to cracks in the ROI of both samples was shown in **Figure 41**(d-i). Three deformation stages were selected for both AB and SAT samples, indicated as AB-1 to AB-3 and SAT-1 to SAT-3. The deformation stages AB-1 to AB-3 corresponded to $\varepsilon_{xx} = 0.038,\ 0.042 \text{ and } 0.046$, while SAT-1 to SAT-3 corresponded to $\varepsilon_{xx} = 0.038,\ 0.054 \text{ and } 0.058$, respectively. The deformation stages AB-1 and SAT-1 (both at $\varepsilon_{xx} = 0.038$) were selected to represent the onset of plastic deformation for the AB and SAT samples, as well as to illustrate the difference in plastic strain localisation between the two samples at the same nominal strain. The other deformation stages (i.e. AB-2, AB-3, SAT-2, SAT-3) were selected to illustrate the plastic strain localisation in AB and SAT samples after significant strain accumulation had occurred. The magnitude of slip bands was characterised via ε_{eff}, and the colour bar range for ε_{eff} was set to between 0.06 and 0.18. This was done to filter out some of the noise found in ε_{eff} datasets (i.e. excessively high strains and strains due to SEM scanning artefacts), display all the ε_{eff} datasets using a uniform colour map scale, and retain sufficient detail for providing an accurate representation of the plastic strain localisation phenomena. In doing so, some of the strains experienced by the material (i.e. $\varepsilon_{eff} \leq 0.06$) were inadvertently filtered out.

Plastic strain localisation in AB samples involve the formation of localised slip bands throughout the ROI, which increased in quantity and intensity as the deformation progressed (yellow lines in **Figure 41**(d-f)). The slip bands would grow longer and larger in size, and would cross other slip bands as the deformation progressed. A similar situation was also identified in the SAT sample (**Figure 41**(g-i)). However, the quantity and magnitude of slip bands in the SAT sample was less compared to those found in AB sample. Continued deformation of both samples led to the formation of microcracks at the location of slip bands as the localised stress concentration exceeded the load bearing capacity of the material. These microcracks are shown in the zoomed-in image of **Figure 41**(c), and appeared as white lines in the ε_{eff} maps shown in **Figure 41**(d-f, h, and i). Microcracks were found in AB sample after being deformed to $\varepsilon_{xx} = 0.038$, while none were found in SAT sample when it was deformed to the same ε_{xx} (**Figure 41**(d) vs. **Figure 41**(g)). For both samples, the cracks were found to increase in quantity and size as the deformation progressed.

4.3.4. Alignment of EBSD and SEM-DIC datasets for microscale analysis

4.3.4.1. Microstructural heterogeneity in selected grains

The EBSD and SEM-DIC datasets for AB and SAT samples shown in **Figure 38**(a and b) and **Figure 41**(d-i) were aligned to a common grid using the alignment method shown in **Figure 37** (**Section 4.3.1.4**). This enabled the localised mapping of surface strain during tensile loading to the microstructure of SLM 18Ni-300 maraging steel, in addition to facilitating the analysis of microscale plastic strain localisation within individual grains. Shown in **Figure 42**(a and b) are the aligned EBSD datasets for AB and SAT samples, respectively. The aligned SEM-DIC datasets for AB-2 and SAT-2 deformation stages are shown in **Figure 42**(c and d), respectively.

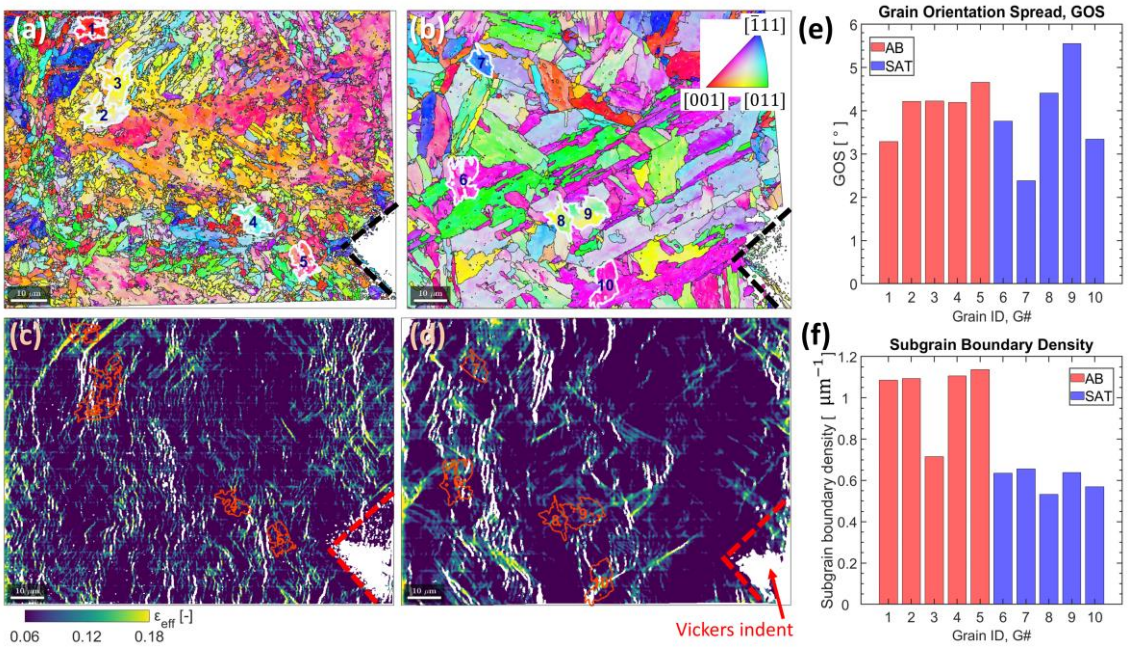

Figure 42: The aligned EBSD and SEM-DIC datasets. The aligned IPF maps for the ROI of (a) AB and (b) SAT samples, together with the grains of interest. The aligned ε_{eff} maps for deformation stages (c) AB-2 and (d) SAT-2 (ε_{xx} = 0.042 and 0.054, respectively), together with the grains of interest. The (e) grain orientation spread and (f) subgrain boundary density for the grains of interest. The grains of interest are assigned a Grain ID of G1 to G5 for AB grains, and G6 to G10 for SAT grains. The outer grain boundaries in (a-b) are outlined using solid black lines. Vickers indent marks used for aligning the datasets in (a-d) are outlined using dashed black or red lines. The length of the scale bars in (a-d) is 10 μm.

A selection criteria was devised to filter out the grains of interest for investigating its plastic strain localisation phenomena. The selected grains should preferably be of similar size and exhibit significant strain accumulation. To fine-tune the filtering process, only grains that contained increased internal misorientation and a higher density of LAGBs were selected. The grain orientation spread (GOS) was used to identify grains with increased internal misorientation [169]. GOS provided an indicator for the deviation in internal misorientation in each grain in comparison to the grain's mean orientation. A grain with a higher GOS value has a larger deviation in internal misorientation compared to other grains. Note that GOS is different compared to KAM

in that GOS computes the deviation in internal misorientation on a grain-by-grain basis, while KAM computes it on a pixel-by-pixel basis [165]. GOS was used as the selection criteria instead of KAM because KAM was more susceptible to noise during EBSD data acquisition and the kernel size used during plotting [170]. Following that, the subgrain boundary density was used to identify grains with a higher density of LAGBs [171]. The subgrain boundary density was calculated using **Equation (15)** [172]:

$$\text{Subgrain boundary density} = \frac{\text{Total length of LAGBs within a grain}}{\text{Grain area}} \quad \textbf{(15)}$$

In summary, the grains were chosen according to the following selection criteria: grains that have a grain area between $30\ \mu m^2$ and $100\ \mu m^2$, exhibited significant strain accumulation (i.e. ε_{eff} higher than 0.12), has a GOS value higher than $2\ °$, and has a subgrain boundary density higher than $0.5\ \mu m^{-1}$. It was identified that significant strain activity preferentially occurred within grains with higher GOS and higher subgrain boundary density.

The grains of interest were highlighted in **Figure 42**(a-d). The grains of interest were assigned a Grain ID of G1 to G5 for AB grains, and G6 to G10 for SAT grains. The GOS values and subgrain boundary density for G1 to G10 are shown in **Figure 42**(e, f), respectively. In **Figure 42**(e), the selected AB grains have GOS values between 3.3 ° and 4.7 °, while the selected SAT grains have values between 2.4 ° and 5.6 °. In **Figure 42**(f), the selected AB grains have subgrain boundary densities between 0.72 μm^{-1} and 1.14 μm^{-1}, while the selected SAT grains have values between 0.53 μm^{-1} and 0.66 μm^{-1}. The selected AB grains exhibited less variation in GOS between individual grains and contained a higher subgrain boundary density when compared to the selected SAT grains (**Figure 42**(e and f), G1 to G5 vs. G6 to G10). Less variation in GOS between individual grains implied that the AB grains were more homogeneous due to decreased internal misorientation between the grains. Individual grains with higher subgrain boundary density contained more LAGBs, which strengthened them by impeding dislocation motion.

4.3.4.2. Evolution of microscale plastic strain localisation in selected grains

The evolution of microscale plastic strain localisation within G1 to G5 of AB sample is shown in two deformation stages, AB-2 and AB-3 (**Figure 43**(a-e and f-j), $\varepsilon_{xx} = 0.042 \text{ and } 0.046$, respectively). The magnitude of slip bands was characterised via ε_{eff} (yellow regions). The white regions within the grains were caused by the formation of microcracks in that region, resulting in DIC correlation failure when calculating the changes in displacement. It can be deduced that the plastic strain localisation in G1 to G5 was more discrete and exhibited higher magnitudes. Increased strain accumulation was observed in G1 and G2, but was less pronounced in G3 to G5 (**Figure 43**(a and b) vs. (c-e)). Subsequent deformation to AB-3 resulted in increased quantity of slip bands in G1 to G5. In G1, the slip band that formed in the middle of the grain grew in size and magnitude (**Figure 43**(f vs. a)). In G2 to G5, the quantity of slip bands within the grains had increased significantly, and extended length-wise throughout the investigated grains (**Figure 43**(g-j vs. b-e)).

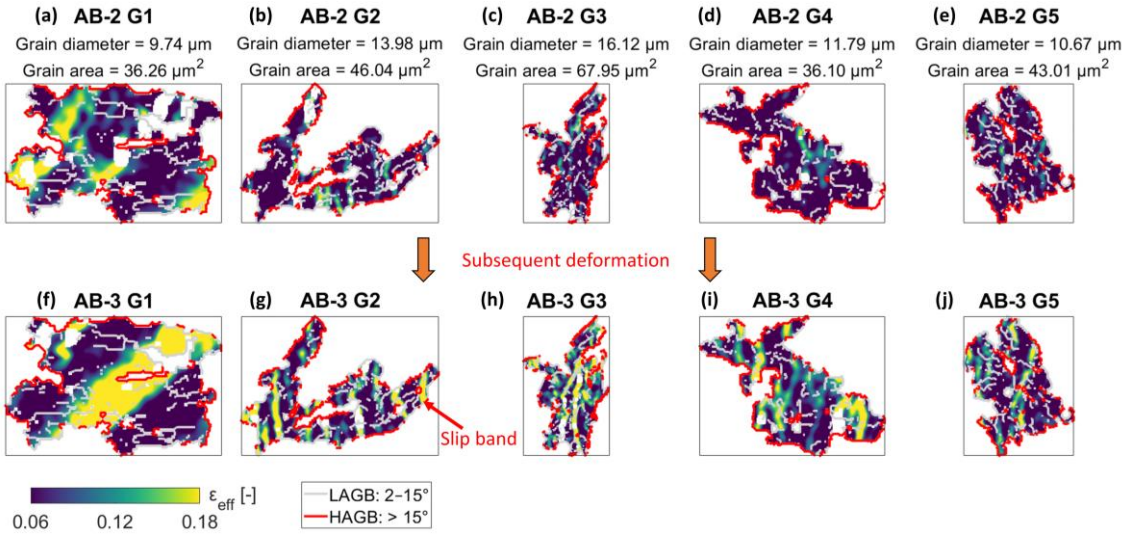

Figure 43: Evolution of plastic strain localisation in selected AB grains, with the LAGBs and HAGBs outlined in light grey and red respectively. (a-e) Strain accumulation within the grains at deformation stage AB-2 ($\varepsilon_{xx} = 0.042$). (f-j) Strain accumulation in said grains after subsequent deformation to AB-3 ($\varepsilon_{xx} = 0.046$).

The evolution of microscale plastic strain localisation within G6 to G10 is shown in two deformation stages, SAT-2 and SAT-3 (**Figure 44**(a-e and f-j) $\varepsilon_{xx} = 0.054 \text{ and } 0.058$, respectively). After deforming the sample to SAT-2, slip bands with varying intensities were observed in G6 to G10 (**Figure 44**(a-e)). It can be deduced that the plastic strain localisation in G6 to G10 was more diffuse and exhibited lower magnitudes compared to those experienced by G1 to G5 (**Figure 44** vs. **Figure 43**). Subsequent deformation to SAT-3 resulted in increased strain accumulation in the grains, indicated by the increased magnitude of slip bands (**Figure 44**(f-j)). Subsequent deformation also resulted in the formation of more microscracks and its subsequent propagation, indicated by extended white regions within the grains (**Figure 44**(f, g, and j) vs. (a, b, and e)).

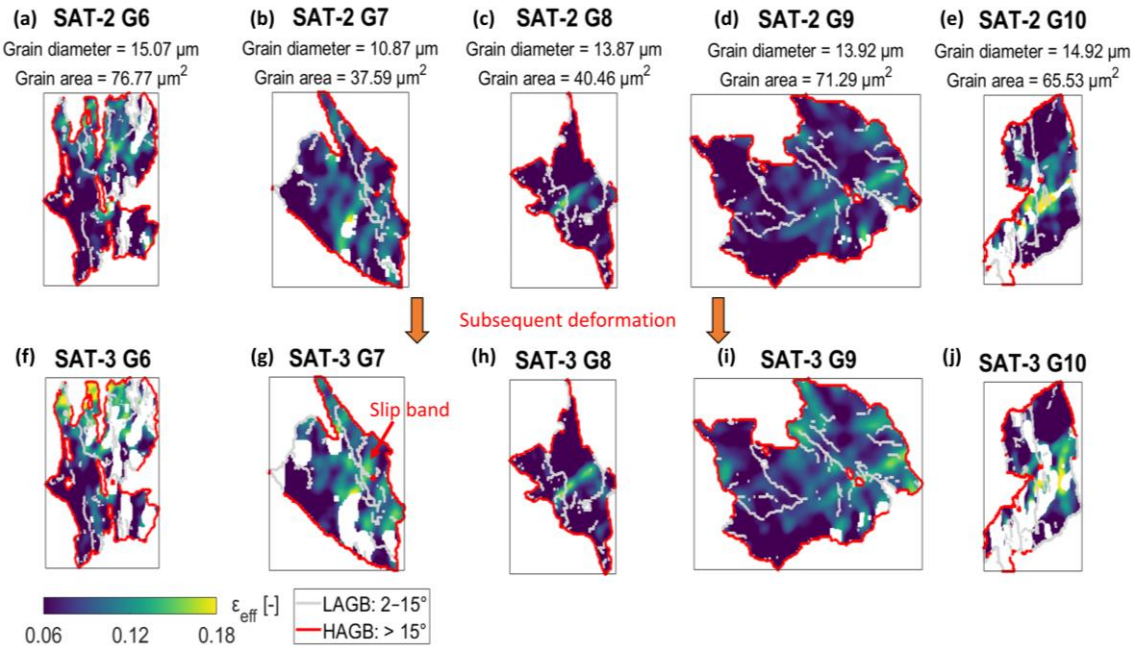

Figure 44: Evolution of plastic strain localisation in selected SAT grains, with the LAGBs and HAGBs outlined in light grey and red respectively. (a-e) Strain accumulation within the grains at deformation stage SAT-2 ($\varepsilon_{xx} = 0.054$). (f-j) Strain accumulation in said grains after subsequent deformation to SAT-3 ($\varepsilon_{xx} = 0.058$).

4.3.5. Slip system identification for selected grains

The following deformation stages and grains were selected for slip identification, i.e. AB-3 for G2 ($\varepsilon_{xx} = 0.046$) and SAT-3 for G8 ($\varepsilon_{xx} = 0.058$). G2 and G8 were selected due to them having a similar grain diameter and grain area (AB-3 G2: **Figure 43**(g), SAT-3 G8: **Figure 44**(h)). The SSLIP methodology suggested by Vermeij et al. [38] was adapted and developed to identify the active slip systems in G2 and G8. Further details regarding the SSLIP methodology are presented in **Section 4.3.1.5**. The x-direction and y-direction in-plane displacement fields (i.e. U_x and V_y) for the selected grains were measured via SEM-DIC, and were subsequently used as input to calculate the in-plane displacement gradient tensor components and effective surface strain in G2 and G8 ($H_{xx}, H_{xy}, H_{yx}, H_{yy}$, and ε_{eff}). The data obtained were then correlated with the investigated grain's localised slip systems determined from EBSD grain information to identify the active slip systems in G2 and G8. In the present investigation, the slip activity in the active slip systems was characterised in terms of slip magnitude, γ. The colour bar range for γ was set to between 0.06 and 0.18 to provide consistent visual comparison across all γ fields and ε_{eff} fields.

The following assumptions were made during the analysis (also mentioned in **Section 4.3.1.5**): The martensite phase in maraging steel has a BCC crystal structure [17], and deforms via the 48 independent slip systems as reported in the literature [145,166]. The 48 BCC slip systems include 12 slip systems in the $\{110\}\langle\bar{1}11\rangle$ family, 12 slip systems in the $\{112\}\langle11\bar{1}\rangle$ family, and 24 slip systems in the $\{123\}\langle11\bar{1}\rangle$ family. A 2D approximation was utilised when calculating $H_{xx}, H_{xy}, H_{yx}, H_{yy}$, and ε_{eff} . It was assumed that the in-plane deformation behaviour of the investigated grains, denoted as H_{xx}, H_{xy}, H_{yx}, and H_{yy} in the present investigation, were consistent with the combined active slip system kinematics within those grains. The grains were approximated as single crystals during the analysis, and the results presented were highly localised to the investigated grains.

The strain distribution in G2 of AB sample is shown in **Figure 45**. During uniaxial tensile loading, the displacement in G2 was not uniform in the x- and y- directions (**Figure 45**(a and b)). The displacement values varied in magnitude across G2, with the left side of the grain exhibiting greater leftward and downward displacement (**Figure 45**(a and b), colour gradient in the grain). The white regions in G2 were due to correlation failure during SEM-DIC analysis, and were filtered out during plotting.

The spatial variations in x - and y - displacements gave rise to in-plane displacement gradients in the axial and shear directions, which were illustrated in tensor form in the present investigation (**Figure 45**(c-f)). In particular, both H_{xx} and H_{yx} tensor components exhibited near-vertical bands of positive strain across G2, with H_{xx} exhibiting greater magnitudes compared to H_{yx} (**Figure 45**(c and d), dashed red arrows). In contrast, both H_{xy} and H_{yy} tensor components exhibited near-horizontal bands of alternating positive and negative strain (**Figure 45**(e and f). The magnitudes of the H_{xx}, H_{xy}, H_{yx}, and H_{yy} tensor components indicated that tensile strain was more concentrated along the x-direction, with lower magnitudes in the yx-direction. This was coupled with lower magnitudes of compressive strain along the y- and xy-directions. The combined in-plane deformation behaviour in G2 was illustrated using ε_{eff} (**Figure 45**(g)). It can be deduced that the tensile strain in H_{xx} was the dominant component among the four in-plane displacement gradient tensor components in G2.

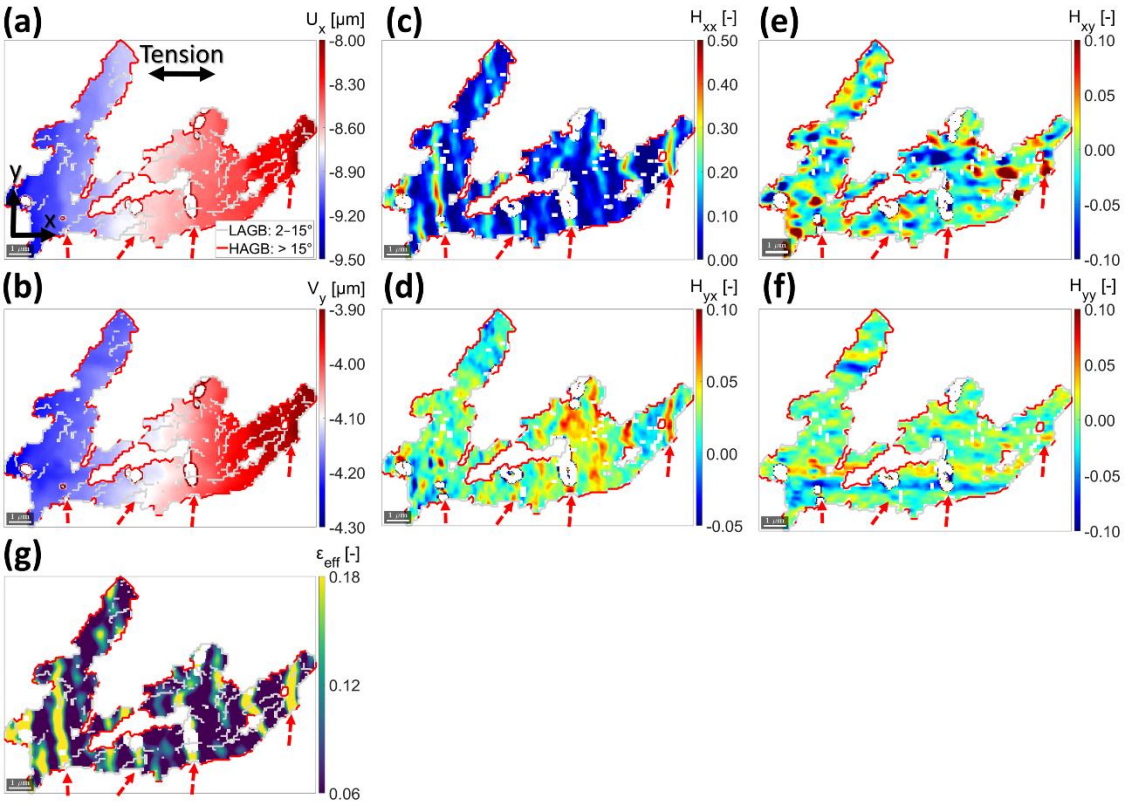

Figure 45: Heterogeneous strain distribution in G2 of AB sample at deformation stage AB-3 ($\varepsilon_{xx} = 0.046$). (a) The x-direction displacement field, U_x. (b) The y-direction displacement field, V_y. (c-f) The in-plane displacement gradient tensor components, H_{xx}, H_{yx}, H_{xy}, and H_{yy}. (g) The effective surface strain field, ε_{eff}. The coordinate axes used during SEM-DIC analysis is shown in (a). The locations of slip bands in (a-g) are indicated using dashed red arrows, and the length of the scale bars is 1 µm.

Shown in **Figure 46**(a-c) are the IPF, KAM, and ε_{eff} maps for G2 of AB sample, respectively. Internal misorientations (i.e. variations in IPF colour within the grain) were identified in G2 and were partially separated via LAGBs (**Figure 46**(a)). Regions with increased KAM provided an indication of the orientation gradients within G2 (**Figure 46**(b)). A misorientation threshold angle of 2 ° was used when plotting the KAM map for G2. The regions of increased strain accumulation (ε_{eff}) in G2 intersected with the regions of internal misorientation and increased KAM (**Figure 46**(c vs. a and b), dashed red arrows).

The active slip systems in G2 at deformation stage AB-3 are shown in **Figure 46**(d-h), and characterised in terms of slip magnitude (γ). Plastic deformation resulted in the simultaneous activation of 5 out of 48 BCC slip systems in G2. Slip activity was more concentrated in the $\{110\}\langle\bar{1}11\rangle$ family of slip systems as compared to the other two families, where 3 out of 12 slip systems were active (**Figure 46**(d-f vs. g and h)). Following that, slip systems with a Schmid factor higher than 0.40 exhibited higher slip magnitude and more discrete slip activity (**Figure 46**(d, g, and h vs. e and f)). The regions of increased slip activity intersected with regions of internal misorientation and increased KAM (**Figure 46**(d-h vs. a and b), dashed red arrows). The primary slip system in G2 was identified as $(\bar{2}1\bar{3})[\bar{1}11]$, with a Schmid factor of 0.46 (**Figure 46**(h)).

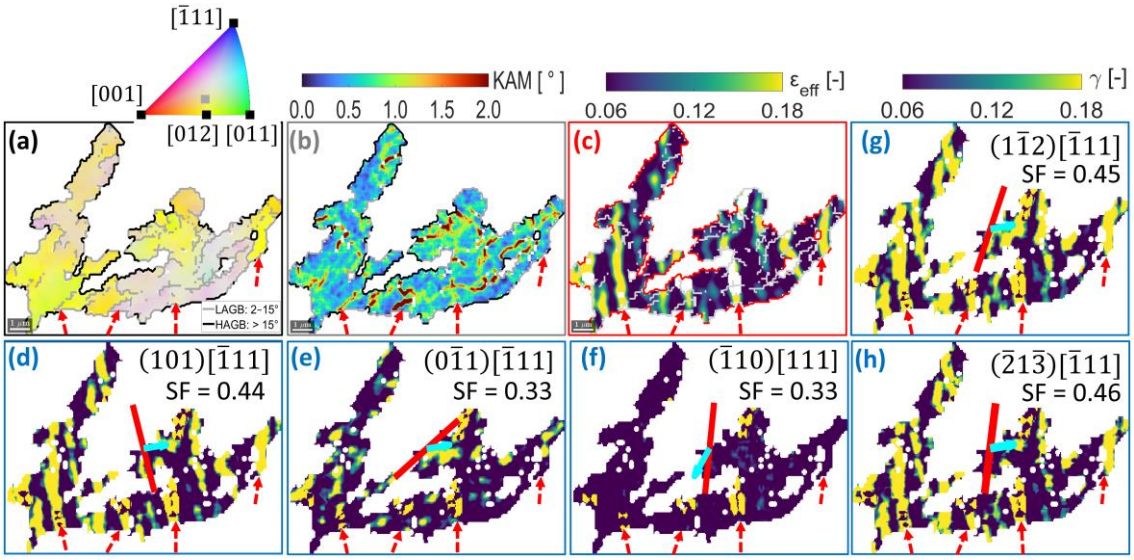

Figure 46: The active slip systems in G2 of AB sample at deformation stage AB-3 ($\varepsilon_{xx} = 0.046$), identified via SSLIP. (a) The IPF map for G2. (b) The KAM map for G2. (c) The ε_{eff} map for G2. The LAGBs are outlined in dark or light grey, while the HAGBs are outlined in black or red. The IPF colour key above (a) shows the mean orientation of G2 (grey square). The length of the scale bars in (a-c) is 1 μm. A total of 5 BCC slip systems were active, including (d-f) from the $\{110\}\langle\bar{1}11\rangle$ family, (g) from the $\{112\}\langle11\bar{1}\rangle$ family, and (h) from the $\{123\}\langle11\bar{1}\rangle$ family. The slip plane and slip direction for each slip system were indicated using solid red and cyan lines, respectively. The slip activity was indicated using dashed red arrows. ε_{eff}: Effective surface strain. γ: Slip magnitude. SF: Schmid factor.

The combined active slip system kinematics in G2 was found to reflect the in-plane deformation behaviour in said grain. Discrete slip bands were identified in the active slip systems and were reflected in the H_{xx} and H_{yx} tensor components, in addition to the ε_{eff} field (**Figure 46**(d-h) vs. **Figure 45**(c, d, and g), red dashed red arrows). However, the regions of compressive strain in the H_{xy} *and* H_{yy} tensor components had lower magnitudes and were less noticeable in the active slip systems. This may be due to the lower γ values (i.e. $\gamma < 0.06$) being inadvertently filtered out during plotting.

The strain distribution in G8 of SAT sample is shown in **Figure 47**. Similar to G2, G8 also exhibited greater leftward and downward displacement (**Figure 47**(a and b) vs. **Figure 45**(a and b)). However, the displacement of G8 in the negative x-direction was less compared to G2 (**Figure 47**(a) vs. **Figure 45**(a)). Following that, the strain distribution in the H_{xx}, H_{yx}, H_{xy}, and H_{yy} tensor components exhibited several differences compared to G2. All four tensor components exhibited significant tensile or compressive strain around the centre region of G8 (**Figure 47**(c-f), dashed red arrows). This was coupled with a lower magnitude of tensile strain extending from the top-left region towards the centre of G8. In particular, both H_{xx} and H_{yx} components exhibited tensile strain around the centre and top-left regions in G8 (**Figure 47**(c and d), dashed red arrows). In contrast, both H_{xy} and H_{yy} components exhibited compressive strain around the centre of G8, and tensile strain in the top-left region (**Figure 47**(e and f), dashed red arrows). Furthermore, the strain in G8 was more evenly distributed in both

axial and shear directions compared to G2 (**Figure 47**(c-f) vs. **Figure 45**(c-f)). The combined in-plane deformation behaviour in G8 was illustrated using ε_{eff} (**Figure 45**(g)). It can be deduced that the tensile strain in H_{xx} was the dominant component among the four in-plane displacement gradient tensor components in G8.

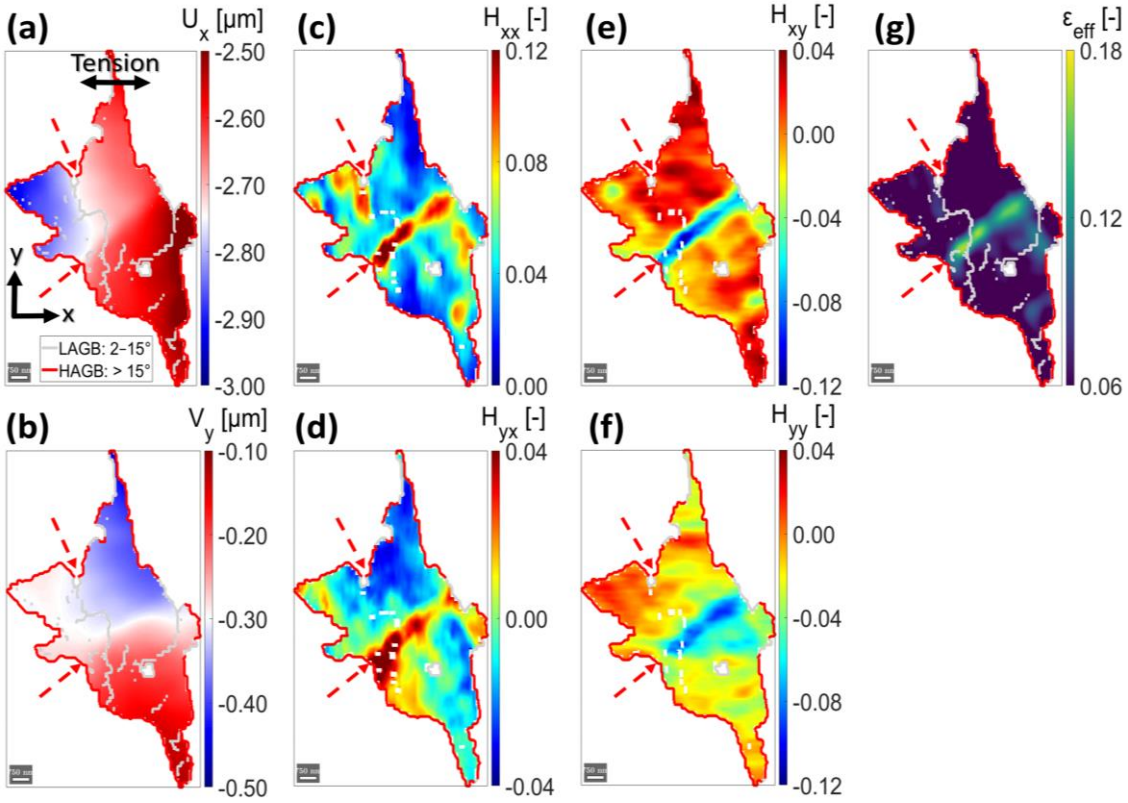

Figure 47: Heterogeneous strain distribution in G8 of SAT sample at deformation stage SAT-3 ($\varepsilon_{xx} = 0.058$). (a) The x-direction displacement field, U_x. (b) The y-direction displacement field, V_y. (c-f) The in-plane displacement gradient tensor components, $H_{xx}, H_{yx}, H_{xy}, \text{and } H_{yy}$. (g) The effective surface strain field, ε_{eff}. The coordinate axes used during SEM-DIC analysis is shown in (a). The locations of slip bands in (a-g) are indicated using dashed red arrows, and the length of the scale bars is 0.75 µm.

The IPF, KAM, and ε_{eff} maps for G8 of SAT sample are shown in **Figure 48**(a-c), respectively. Internal misorientations (i.e. variations in IPF colour within the grain) were identified in G8 and were partially separated by LAGBs, similar to those found in G2 (**Figure 48**(a) vs. **Figure 46**(a)). The orientation gradients within G8 were indicated via regions of increased KAM (**Figure 48**(b)). A misorientation threshold angle of 2 ° was used when plotting the KAM map for G8. The regions of strain accumulation (ε_{eff}) in G8 intersected with the regions of internal misorientation and increased KAM ((**Figure 48**(c vs. a and b)). The strain accumulation in G8 was more concentrated around the middle region of the grain, and was more diffuse compared to those found in G2 (**Figure 48**(c) vs. **Figure 46**(c), dashed red arrows).

The active slip systems in G8 at deformation stage SAT-3 are shown in **Figure 48**(d-l), and characterised in terms of slip magnitude (γ). Plastic deformation resulted in the simultaneous activation of 9 out of 48 BCC slip systems in G8. The slip activity in G8 was more dispersed between the active slip systems as compared to those found in G2 (**Figure 48**(d-l) vs. **Figure 46**(d-h)). In particular, each of the 3 slip system families had

3 slip systems that were active during plastic deformation (**Figure 48**(d-f, g-i, and j-l)). The slip activity in several slip systems was concentrated around the middle region of the grain, while others were dispersed instead (**Figure 48**(f, i, and l vs. d-e, g-h, and j-k)). In addition, the slip activity intersected with the regions of internal misorientation and increased KAM (**Figure 48**(d-l vs. a and b), dashed red arrows). The primary slip system in G8 was identified as $(0\bar{1}1)[111]$, with a Schmid factor of 0.47 (**Figure 48**(d)).

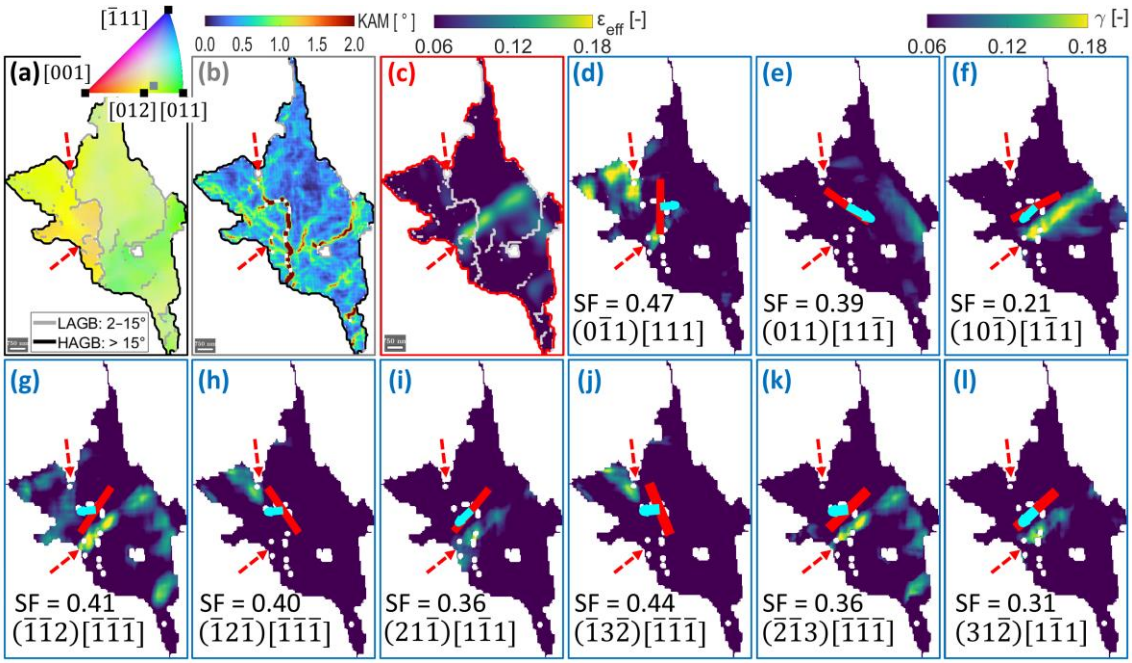

Figure 48: The active slip systems in G8 of SAT sample at deformation stage SAT-3 ($\varepsilon_{xx} = 0.058$), identified via SSLIP. (a) The IPF map for G8. (b) The KAM map for G8. (c) The ε_{eff} map for G8. The LAGBs are outlined in dark or light grey, while the HAGBs are outlined in black or red. The IPF colour key above (a) shows the mean orientation of G8 (grey square). The length of the scale bars in (a-c) is 0.75 μm. A total of 9 BCC slip systems were active, including (d-f) from the $\{110\}\langle\bar{1}11\rangle$ family, (g-i) from the $\{112\}\langle11\bar{1}\rangle$ family, and (j-l) from the $\{123\}\langle11\bar{1}\rangle$ family. The slip plane and slip direction for each slip system were indicated using solid red and cyan lines, respectively. The slip activity was indicated using dashed red arrows. ε_{eff}: Effective surface strain. γ: Slip magnitude. SF: Schmid factor.

The combined active slip system kinematics in G8 was found to reflect the in-plane deformation behaviour in that grain, similar to G2. The region of tensile (or compressive) strain around the centre of G8 reflected the slip activity exhibited by the following 6 active slip systems: $(0\bar{1}1)[111]$, $(10\bar{1})[1\bar{1}1]$, $(\bar{1}\bar{1}2)[\bar{1}\bar{1}\bar{1}]$, $(21\bar{1})[1\bar{1}1]$, $(\bar{2}\bar{1}3)[\bar{1}\bar{1}\bar{1}]$, and $(31\bar{2})[1\bar{1}1]$ (**Figure 48**(d, f, g, i, k, and l) vs. **Figure 47**(c-g), dashed red arrows). In addition, the region of tensile strain around the top-left region in G8 reflected the slip activity exhibited by the following 4 active slip systems: $(0\bar{1}1)[111]$, $(\bar{1}\bar{1}2)[\bar{1}\bar{1}\bar{1}]$, $(\bar{1}2\bar{1})[\bar{1}\bar{1}\bar{1}]$, and $(\bar{1}3\bar{2})[\bar{1}\bar{1}\bar{1}]$ (**Figure 48**(d, g, h, and j) vs. **Figure 47**(c-g), dashed red arrows). Discrete slip was identified in the centre region of G8, while diffuse slip was identified in the other regions of G8. Thus, it can be deduced that the strain exhibited in the $H_{xx}, H_{xy}, H_{yx}, \text{and } H_{yy}$ tensor components was due to the combined effect of slip activity in the active slip systems.

4.3.6. Discussion

4.3.6.1. Microstructural heterogeneity in the as-built (AB) sample and its evolution after solution-aging treatment (SAT)

The experimental findings reported in **Sections 4.3.2** to **4.3.5** are collectively analysed and discussed in the present section. The heterogeneous distribution of equiaxed and columnar grains of varying sizes and orientations in the AB sample of SLM 18Ni-300 maraging steel can be attributed to rapid solidification during the SLM process (**Figure 38**(a)). Researchers reported that the rapid solidification phenomenon in SLM process shared several similarities with conventional welding [57,104]. Grain growth was initiated by epitaxial growth along the edges of the melt pool (or scan track), followed by competitive growth towards its centre. The formation of certain grain morphologies (i.e. equiaxed or columnar) were governed by several factors including the temperature gradient, solidification rate, undercooling, and solute diffusion coefficient of the melt pool. Columnar grains would form along the edges of the melt pool due to higher temperature gradient in that region, and were oriented in the direction of said temperature gradient after solidification. Equiaxed grains would form nearer to the centre of the melt pool, where temperature gradient was more uniform. It can be deduced that the heterogeneity in the microstructure of AB sample was caused by the competitive growth between the equaixed and columnar grains.

The influence of post-processing heat treatment on SLM 18Ni-300 maraging steel has been investigated extensively in the literature [29,84,126]. The microstructure found in the SAT sample was larger and more elongated compared to those found in the AB sample due to the occurrence of grain coarsening and recrystallisation during the first stage of the SAT plan (**Figure 38**(a, b, and e), SAT: 840 ℃, $1\mathrm{h}$). Furthermore, heat treatment also significantly altered the crystallographic texture in SAT sample. The majority of the grains in SAT sample were oriented close to the $[\bar{1}12]$ direction, while the majority of the grains in AB samples were oriented along the $[001]$ direction. (**Figure 38** (d vs. c)). Kučerová et al. [29] reported that grain coarsening and austenite reversion occurred when the material was subjected to solution annealing at 820 ℃ for 1 h. The mix of equiaxed and columnar grains found in the AB sample was replaced by grains with larger and more elongated morphology after heat treatment. Increasing the heat treatment temperature and duration resulted in increased grain coarsening and austenite reversion. Following that, the second stage of the SAT plan (490 ℃ $\mathrm{for}\ 6\mathrm{h}$) led to the precipitation of Ni-based intermetallics in the material. Allam et al. [126] reported that aging at 510 ℃ for 6 h resulted in increased nucleation sites for the precipitation of $\mathrm{Ni_3Ti}$ intermetallics. As the heat treatment progressed, the Co element diffused out of the precipitates and was replaced by segregation of Mo element due to the solubility of both elements in the martensite matrix. Increasing the heat treatment duration resulted in the formation of $\mathrm{Fe_7Mo_6}$ intermetallics.

The changes in microstructure after post-processing heat treatment had a direct influence on the resultant mechanical properties of SLM 18Ni-300 maraging steel. Tan et al. [84] reported that the SAT samples exhibited higher ultimate tensile strength but lower elongation at fracture compared to the AB samples (AB: 1165 MPa, 12.44 % vs. SAT: 1943 MPa, 5.6 %). The ultimate tensile strength for the AB and SAT samples investigated in the present investigation exhibited a similar trend to those reported in literature, and was comparable to conventionally made samples (**Figure 41**(a); AB: 1161

MPa vs. wrought: 1000 MPa; SAT: 1915 MPa vs. wrought-aged: 1930 MPa). The significant increase in ultimate tensile strength after post-processing heat treatment is attributed to precipitation hardening of Ni-based intermetallics. In particular, the Ni_3Ti intermetallic have a needle-shaped morphology, with diameters ranging between 6 nm and 10 nm, and lengths ranging between 15 nm and 45 nm [84]. Precipitation hardening also resulted in the formation of Ti- and Al-based intermetallics. They have a spherical morphology, and have diameters ranging between 50 and 60 nm. These precipitates strengthened the martensite matrix by impeding dislocation motion during plastic deformation.

4.3.6.2. Microscale plastic strain localisation in SLM 18Ni-300 maraging steel

Extensive research was conducted to elucidate the microscale plastic strain localisation in steels [137–142] (**Chapter 2 Section 2.5.1**). However, the microscale plastic strain localisation in SLM 18Ni-300 maraging steel is yet to be fully explored in current literature. Through the present investigation, the microscale plastic strain localisation in SLM 18Ni-300 maraging steel was identified to be directly influenced by the material's microstructure and exhibited significant microstructural heterogeneity. According to the research findings presented in **Sections 4.3.2** to **4.3.5**, it can be deduced that the main deformation mechanism for SLM 18Ni-300 maraging steel was dislocation slip. Although transformation induced plasticity was reported in literature [173,174], it was not identified in the current investigation due to relatively low austenite content in the ROI (**Figure 39**, **Section 4.3.2**).

Figure 49 schematically illustrates the plastic strain localisation in SLM 18Ni-300 maraging steel. The role of Ni-based intermetallics in impeding dislocation motion during plastic strain localisation in AB and SAT samples is presented together for comparison. The microstructural heterogeneity in AB and SAT samples is characterised using SEM micrographs showing their chemically etched microstructures (**Figure 49**(a vs. d)). The grain boundaries in both samples are traced and enlarged for comparison (**Figure 49**(b, c, e, and f)). The distribution of Ni-based intermetallics and dislocations are also indicated in the schematics. A detailed discussion of the interactions between the microstructural heterogeneity in AB and SAT samples, Ni-based intermetallics, and dislocations during plastic strain localisation are included in the following paragraphs. Subsection titles were included for easier navigation, namely: '*In AB sample*', '*In SAT sample*', and '*In selected grains of AB and SAT samples'*.

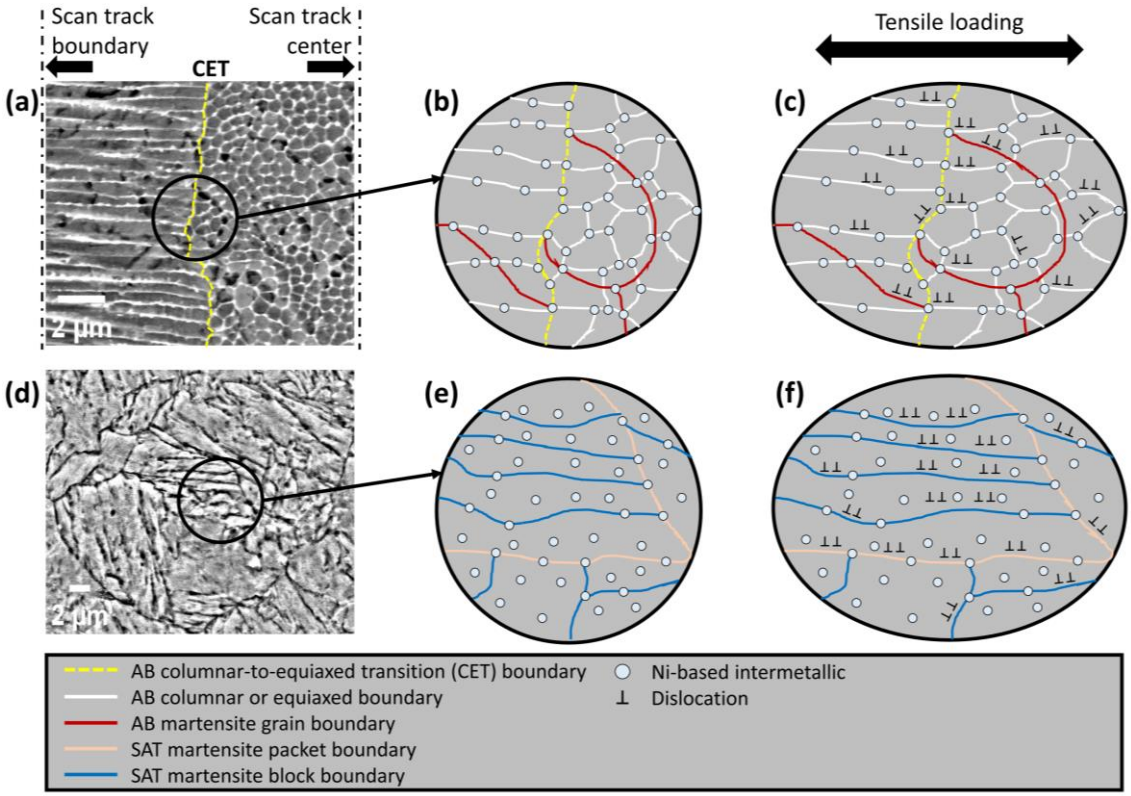

Figure 49: Schematic showing the role of Ni-based intermetallics in impeding dislocation motion during the plastic strain localisation of SLM 18Ni-300 maraging steel. (a) SEM image showing the chemically etched microstructure of the AB sample. (b) Segregation of Ni-based intermetallics along grain boundaries after SLM fabrication. (c) The Ni-based intermetallics impeding dislocation motion in the AB sample. In comparison, (d) SEM image showing the chemically etched microstructure of the SAT sample. (e) Dissolution of Ni-based intermetallics throughout the martensite matrix after SAT. (f) The Ni-based intermetallics impeding dislocation motion in the SAT sample. AB: As-built. SAT: Solution-aging treatment.

In AB sample

The AB sample demonstrated the ability to withstand increasing plastic strain whilst maintaining a relatively constant stress state (**Figure 41**(a), AB curve). This could be attributed to the microstructure of AB sample itself, which contained a heterogeneous mix of equiaxed grains, columnar grains, and Ni-based intermetallics throughout the investigated ROI (**Figure 38**(a ,c, e) and **Figure 39**(a)).

The chemically etched microstructure of AB sample revealed that the columnar and equiaxed grains were separated by the columnar-to-equiaxed transition (CET) boundary. The martensite grain boundaries were identified to intersect the columnar and equiaxed grain boundaries (**Figure 49**(a)). Precipitation of Ni-based intermetallics was identified along the columnar and equiaxed grain boundaries and schematically illustrated (**Figure 49**(b)). Mei et al. [30] reported that the columnar and equiaxed grain boundaries consisted of dislocation tangles and did not form a sharp interface like those exhibited by the martensite grain boundaries. The occurrence of the CET boundary and

transition from columnar to equiaxed grain growth was influenced by the localised temperature gradient and solidification rate in the scan tracks [57,104].

It can be deduced that the relatively small size, uniform shape, and large quantity of equiaxed grains and Ni-based intermetallics formed a network that resisted deformation in all directions. The interactions between the equiaxed grains in AB sample, Ni-based intermetallics, and dislocations during uniaxial tensile loading were schematically illustrated (**Figure 49**(c)). Plastic deformation in AB sample occurs via dislocation slip, and new dislocations would pile-up along the grain boundaries resulting in grain boundary strengthening. Further dislocation motion was impeded by the pre-existing dislocations as well as the Ni-based intermetallics. Strain hardening was not identified in the AB sample as the deformation progressed (**Figure 41**(d-f)). Instead, subsequent deformation resulted in the formation of discrete slip bands with increasing magnitude and quantity, and microcracks would form at regions with increased slip activity. These microcracks would coalesce together and propagate further to cover the whole gauge section (**Figure 41**(b and c)), eventually resulting in ductile fracture (i.e. fracture occurs after significant plastic deformation) [28,41,87].

In SAT sample

The microscale plastic strain localisation in SAT sample differs from the AB sample due to it experiencing strain hardening with increasing plastic strain (**Figure 41**(a), SAT curve). After post-processing heat treatment, the microstructure in SAT sample had undergone recrystallisation and grain coarsening, resulting in the formation of larger and more elongated grains (**Figure 38**(b, d, e) and **Figure 39**(b)). Heat treatment significantly altered the crystallographic texture of SAT sample, resulting in the grains being predominantly oriented close to the $[\bar{1}12]$ direction, in addition to an increase in HAGBs and a decrease in LAGBs compared to the AB sample (**Figure 38**(d) vs. **Figure 38**(c), **Table 24**). The higher percentage of HAGBs in the grains of SAT sample may suggest increased resistance to slip transfer between adjacent grains, which is to be validated in future investigations. Agius et al. [175] reported that the slip transfer between adjacent grains in 316L stainless steel was influenced by the misorientation angle of the grain boundaries, and that slip transfer was impeded at the HAGBs.

Furthermore, heat treatment was identified to influence the KAM in the grains of SAT sample. The KAM in SAT sample decreased compared to the AB sample (**Figure 40**(a-c)). In particular, the majority of SAT grains have a KAM between 0 ° and 1 °, while the majority of AB grains have a KAM between 1 ° and 2 °. Thus, it can be deduced that the grains in SAT sample were more homogeneous compared to the grains found in AB sample, due to their lower KAM values. Heat treatment also resulted in the precipitation of Ni-based intermetallics throughout the martensite matrix, especially along the grain boundaries [30,124]. The boundaries of martensite packets and blocks in the SAT sample were clearly visible after chemical etching (**Figure 49**(d)). These microstructure characteristics were schematically illustrated (**Figure 49**(e)).

It can be deduced that strain hardening in the SAT sample is directly influenced by the presence of densely distributed Ni-based intermetallics which impeded dislocation motion. The interactions between the elongated grains in SAT sample, Ni-based intermetallics, and dislocations during uniaxial tensile loading were schematically illustrated (**Figure 49**(f)). Plastic deformation in SAT sample occurs via dislocation slip,

and new dislocations would pile-up along the grain boundaries (similar to AB sample). As the deformation progressed, the Ni-based intermetallics along the grain boundaries and in the martensite matrix impeded further dislocation motion. The interaction between Ni-based intermetallics and dislocations was identified to follow the Orowan bowing mechanism [18,176]. The Orowan bowing mechanism describes the motion of the dislocations as they bow (or loop) around the Ni-based intermetallics when the applied load exceeded the resisting force from the Ni-based intermetallics. This resulted in strain hardening of the SAT sample, as a greater load is required for the dislocations to move past these Ni-based intermetallics. Subsequent deformation beyond the ultimate tensile strength of the SAT sample resulted in the formation of slip bands and microcracks (**Figure 41**(a, g-i), SAT sample). The slip bands were more diffuse and exhibited lower ε_{eff}, while the microcracks were larger compared to the AB sample, indicating the SAT sample's reduced ability to sustain plastic deformation. Fracture in SAT sample occurred via rapid crack propagation. The fracture mode was identified as brittle fracture, and consisted of shallow dimples and quasi-cleavage fracture surfaces [28,84,87].

In selected grains of AB and SAT samples

Plastic strain localisation in the selected AB grains feature discrete slip bands with high strain accumulation (**Figure 43**, regions with high ε_{eff} in G1 to G5). Subsequent deformation resulted in the slip bands growing larger in magnitude, size, and quantity, eventually covering the whole grain. The identification of active slip systems in G2 of AB sample revealed highly localised slip activity that occurred along the LAGBs that separated the internal misorientations within the grain (**Figure 46**(a vs. d-h), dashed red arrows). The regions of increased slip activity also intersected with the regions of increased KAM (**Figure 46**(b vs. d-h), dashed red arrows). It can be deduced that regions of internal misorientation within individual grains were prone to plastic strain localisation and exhibited increased slip activity during uniaxial tensile loading. A total of 5 out of 48 BCC slip systems were active simultaneously during the plastic deformation of G2. Slip activity was more pronounced in slip systems with a Schmid factor higher than 0.40 (**Figure 46**(d, g, and h), regions with high γ). The primary slip system in G2 was identified as $(\bar{2}1\bar{3})[\bar{1}11]$, with a Schmid factor of 0.46 (**Figure 46**(h)).

In contrast, plastic strain localisation in the selected SAT grains was more diffuse compared to those found in AB grains (**Figure 44** G6 to G10 vs. **Figure 43** G1 to G5). The slip bands in SAT grains also exhibited varying strain magnitudes (**Figure 44**, regions with varying ε_{eff} in G6 to G10). Subsequent deformation resulted in increased strain magnitude of slip bands. The identification of active slip systems in G8 of SAT sample revealed a total of 9 out of 48 BCC slip systems were active simultaneously during plastic deformation, almost double compared to those identified in G2 of AB sample (**Figure 48**(d-l) vs. **Figure 46**(d-h), 9 vs. 5). The slip activity in G8 was identified to be more diffuse between the active slip systems and within the grain itself (**Figure 48**(d-l), regions with varying γ). In addition, the slip activity in the active slip systems was aligned with its respective slip planes, and intersected with the regions of internal misorientation and increased KAM within the grain (**Figure 48**(a-b vs. d-l), dashed red arrows). The primary slip system in G8 was identified as $(0\bar{1}1)[111]$, with a Schmid factor of 0.47 (**Figure 48**(d)).

To summarise, the plastic strain localisation in SLM 18Ni-300 maraging steel (both AB and SAT samples) involved the simultaneous activation of 5 or more independent slip systems within individual grains. According to literature [145,167], the plastic deformation of individual grains in polycrystalline metals required the activation of at least 5 independent slip systems to maintain three-dimensional geometrical compatibility between neighbouring grains. In particular, the activation of the primary slip system (i.e. slip system with the highest Schmid factor) in a particular grain has to be compensated by the activation of secondary and tertiary slip systems as said grain adapted to the deformation of neighbouring grains. Following that, slip in SLM 18Ni-300 maraging steel (both AB and SAT samples) preferentially occurred in slip systems with a Schmid factor higher than 0.40. Furthermore, slip preferentially occurred within grains with increased internal misorientation, and intersected regions of increased KAM. Subsequently, it can be deduced that grains with higher GOS and higher subgrain boundary density were more resistant towards deformation. The increased internal misorientation and higher quantity of LAGBs within these grains impeded dislocation motion, resulting in dislocation strengthening of the material.

Furthermore, comparison between the in-plane displacement gradient tensors and active slip systems for G2 and G8 revealed complex slip behaviour including discrete slip, diffuse slip, and possible indication of cross-slip (or overlapping slip). The combined kinematics of the active slip systems were reflected in the in-plane deformation gradient tensors of both grains. In particular, G2 of AB sample exhibited discrete slip in all of the active slip systems and significant tensile strain in the x-direction during uniaxial tensile loading (**Figure 46**(d-h) vs. **Figure 45**(c, d, and g), dashed red arrows). In contrast, G8 of SAT sample exhibited discrete slip and diffuse slip, coupled with significant tensile strain in the x-direction during uniaxial tensile loading (**Figure 48**(d-l) vs. **Figure 47**(c-g), dashed red arrows). Following that, the slip bands in the top-left region of G8 may extend and potentially intersect the discrete slip band in the centre region of G8 with subsequent plastic deformation. This may suggest the occurrence of cross-slip, which is to be validated in future investigations. The occurrence of discrete slip, diffuse slip, and cross-slip was reported by Vermeij et al. [38]. In particular, cross-slip was identified in a BCC single crystal ferrite sample extracted from a dual-phase steel, and was suggested to be an important mechanism near highly active dislocation sources in the sample.

4.4. Summary

The influence of microstructural heterogeneity (i.e. variations in grain size and crystallographic texture) on the microscale plastic strain localisation in SLM 18Ni-300 maraging steel was investigated via EBSD, in situ tensile experiments, and scanning electron microscope-based digital image correlation (SEM-DIC). Two sample conditions were investigated, namely the as-built (AB) and solution-aging treatment (SAT) conditions. The interplay between microstructural heterogeneity, Ni-based intermetallics, and the impediment of dislocation motion in both samples were analysed and discussed in detail.

The influence of microstructural heterogeneity on the microscale plastic strain localisation in AB and SAT samples were comparatively analysed (**Sections 4.3.2** to **4.3.6**). The AB sample demonstrated the ability to withstand increasing plastic strain whilst maintaining a relatively constant stress state (**Figure 41**(a, d-f)). The rapid solidification during SLM process resulted in the formation of large quantities of relatively small, uniformly shaped equiaxed grains that were densely distributed throughout the sample (**Figure 38**(a and e)). These grains formed a network that resisted deformation in all directions, resulting in grain boundary strengthening (**Figure 49**(a-c)). In contrast, the SAT sample experienced strain hardening with increasing plastic strain (**Figure 41**(a, g-i)). After post-processing heat treatment, the grains in SAT sample had undergone recrystallisation and formed larger and more elongated grains compared to the AB sample (**Figure 38**(b and e)). Post-processing heat treatment also resulted in precipitation of Ni-based intermetallics throughout the martensite matrix. These Ni-based intermetallics impeded dislocation motion, resulting in strain hardening (**Figure 49**(d-f)).

The main deformation mechanism for SLM 18Ni-300 maraging steel was identified as dislocation slip. Localised surface strain distribution maps (ε_{eff} maps) of the selected grains revealed the formation of slip bands that increased in ε_{eff} magnitude and quantity as the deformation progressed (AB sample: **Figure 43**, G1 to G5, SAT sample: **Figure 44**, G6 to G10). The slip bands in the AB grains were more discrete and exhibited a higher ε_{eff} magnitude compared to those found in SAT grains. The occurrence of slip bands in the selected grains of both samples was directly influenced by the presence of localised misorientations within those grains. Slip preferentially occurred in grains with increased internal misorientation and higher density of low-angle grain boundaries (LAGBs). The slip bands were also identified to intersect regions with increased kernel average misorientation (KAM). Further deformation resulted in the formation of microcracks at regions with high ε_{eff}.

Slip system identification for selected grains, i.e. G2 from AB sample and G8 from SAT sample was conducted. It was revealed that plastic deformation resulted in the simultaneous activation of five or more slip systems within those grains, and was deduced to help maintain three-dimensional geometrical compatibility between adjacent grains during deformation. Slip activity in G2 was more discrete and focused in the $(101)[\bar{1}11]$, $(1\bar{1}2)[\bar{1}11]$, and $(\bar{2}1\bar{3})[\bar{1}11]$ slip systems (**Figure 46**(d-h)). In contrast, slip activity in G8 was more dispersed (or diffuse) between several slip systems (**Figure 48**(d-l)). For both grains, slip activity was more pronounced in slip systems with Schmid factor larger than 0.4. The slip system with the highest Schmid factor in G2 and G8 were identified as $(\bar{2}1\bar{3})[\bar{1}11]$ and $(0\bar{1}1)[111]$ respectively (Schmid factor of 0.46 and 0.47,

respectively). Comparison between the in-plane displacement gradient tensors and active slip systems for both grains revealed the possibility of cross-slip, i.e. the overlapping of discrete and diffuse slip activities in the grains (AB-G2: **Figure 45**(c-f) vs. **Figure 46**(d-h), SAT-G8: **Figure 47**(c-f) vs. **Figure 48**(d-l)). The combined kinematics of the active slip systems were reflected in the in-plane deformation behaviour for both grains.

5. Conclusions and suggestions for future research directions

5.1. Conclusions

The 18Ni-300 maraging steel is a grade of high-strength steel that is strengthened via precipitation hardening of Ni-based intermetallics, and has applications in the additive manufacturing of steel moulds for injection moulding as well as aerospace components. Literature reported that the microstructure of selective laser melted (SLM) 18Ni-300 maraging steel moulds exhibited significant microstructural heterogeneity and mechanical anisotropy (**Chapter 2 Section 2.1** and **2.2**). The use of unoptimised SLM process parameters (or in-process parameters) further introduced manufacturing defects such as pores and cracks in the additively manufactured steel moulds, resulting in inferior mechanical properties compared to their conventionally made counterparts. Thus, it is essential to obtain a fundamental understanding of the process-microstructure-properties relationships in SLM 18Ni-300 maraging steel in order to optimise SLM in-process parameters and additively manufacture 18Ni-300 maraging steel moulds with mechanical properties that meet industry expectations. The findings of the present thesis are summarised in the following paragraphs.

An extensive literature review facilitated a novel comparative analysis of how SLM in-process parameters influence the microstructure evolution and mechanical properties in SLM 18Ni-300 maraging steel and four other additively processed steel mould materials (i.e. H13, P20, AISI 420 stainless steel, and S136). In doing so, it also addressed the lack of comparative studies in this area (**Chapter 2 Section 2.3**). The rapid solidification during SLM process induced microstructural heterogeneity in all five steel mould materials, leading to the formation of grains with varying sizes, morphologies (i.e. equiaxed and columnar), and crystallographic textures. Laser scanning further induced intrinsic heat treatment (IHT), leading to in situ precipitation hardening in SLM 18N-300 maraging steel and martensite tempering in the other four steel mould materials. The formation of equiaxed or columnar grains in as-built samples was influenced by the local temperature gradient and solidification growth rate within the melt pool, and the microstructure was significantly altered after post-processing heat treatment. Solution-aging treatment (SAT: 840 ℃ for 1 h, then 490 ℃ for 6 h) was recommended for post-processing heat treatment of SLM 18Ni-300 maraging steel moulds to obtain mechanical properties comparable to conventionally wrought and aged condition. These insights provide the foundational background for the subsequent experimental findings in the present thesis.

Experimental investigations were conducted to obtain further insights on the influence of SLM in-process parameters on the microstructure and mechanical properties of SLM 18Ni-300 maraging steel (**Chapter 3**). Laser power (P), scanning speed (v), and hatch spacing (h) were selected for investigation due to their direct contribution to laser energy input, which was mathematically expressed using linear (E_{linear}) and volumetric ($E_{volumetric}$) energy densities (**Chapter 3 Section 3.2**). It was concluded that the use of SLM parameter configurations (or SLM configs. for short) with $E_{linear} > 375.00$ J m^{-1} produced scan tracks with reduced manufacturing defects. Among the six SLM configs. studied in **Table 7**, SLM config. B-2 ($P = 300$ W, $v = 700$ mm s^{-1}, $h = 0.10$ mm, $t_{layer} = 0.03$ mm, $E_{linear} = 428.57$ J m^{-1}, $E_{volumetric} = 142.86$ J mm^{-3})

produced fully built samples with the highest relative density and ultimate tensile strength ($\rho_{relative} = 99.71\ \%, R_m = 1204\ \text{MPa}$). It was concluded that: (i) increasing P resulted in complete melting and fusion of metal powder, (ii) reducing v resulted in reduced melt pool instability and manufacturing defects, and (iii) reducing h resulted in increased overlap between scan tracks and relative density of samples. However, the use of SLM configs. with excessively high E_{linear} and $E_{volumetric}$ is not recommended as it resulted in increased manufacturing defects and were detrimental to the samples' mechanical properties. The experimental findings were also consistent with those reported in the literature.

A combined statistical optimisation methodology was utilised for the multi-response optimisation of mechanical properties in SLM 18Ni-300 maraging steel (**Chapter 3 Section 3.3**). In particular, Taguchi methods were used to investigate the order of influence of $P, v, \text{and}\ h$. Grey relational analysis (GRA) was then utilised to determine the optimal SLM config. for multi-response optimisation. This methodology extends beyond conventional single-response optimisation studies as it provides a more comprehensive optimisation framework, and enables the simultaneous optimisation of ultimate tensile strength (R_m), elongation at fracture (A_t), Vickers hardness, and impact toughness (KV_2). It was concluded that both $P\ \text{and}\ v$ had an approximately equal influence on the investigated mechanical properties, while the influence of h was less significant (i.e. $P \approx v > h$). Among the 16 SLM configs. studied in **Table 10**, SLM config. no. 5 $\left(P = 275\ \text{W}, v = 700\ \text{mm s}^{-1}, h = 0.08\ \text{mm}, t_{layer} = 0.04\ \text{mm},\ E_{linear} = 392.86\ \text{J m}^{-1}, E_{volumetric} = 122.77\ \text{J mm}^{-3}\right)$ was identified as the most optimal. The mechanical properties of samples fabricated via SLM config. no. 5 were also comparable with conventional wrought condition ($\text{SLM config. no. 5: } R_m = 1218\ \text{MPa},\ A_\text{t} = 9.2\ \%,\ \text{Vickers hardness} = 365.0\ \text{HV vs. conventional wrought: } R_m = 1000 - 1170\ \text{MPa}, A_\text{t} = 6 - 15\ \%, \text{Vickers hardness} = 345.5\ \text{HV}$). On the other hand, SLM config. no. 4 was identified as the worst among the 16 SLM configs. studied due to it having the lowest E_{linear} and $E_{volumetric}$, resulting in inferior mechanical properties in the fabricated samples.

The influence of porosity on the evolution of macroscale plastic strain localisation and fracture in SLM 18Ni-300 maraging steel subjected to uniaxial tensile loading was quantitatively and qualitatively investigated via optical-DIC (**Chapter 3 Section 3.4**). A best-worst comparison between samples fabricated using SLM config. no. 5 (best) and no. 4 (worst) (**Table 10**) was conducted. Quantitative analysis revealed that samples fabricated via SLM config. no. 5 sustained plastic deformation for more than twice the duration before fracturing compared to those of config. no. 4. Qualitative analysis indicated the occurrence of macroscale plastic strain localisation phenomena including the propagation of Lüders bands and necking in both samples. Fracture occurred at the location where Lüders bands had initially formed, and was influenced by sample geometry and porosity. The fracture mechanism for both samples was identified as ductile fracture, characterised by crack initiation around the pore perimeter and subsequent propagation via microvoid coalescence.

Scanning electron microscope-based digital image correlation (SEM-DIC) investigations were conducted to elucidate the microscale plastic strain localisation in SLM 18Ni-300 maraging steel in relation to its microstructural heterogeneity (**Chapter 4**). Sub-micron sized speckle patterns were created via magnetron sputtering (**Chapter 4 Section 4.2**). This methodology facilitated high-resolution strain measurements via

SEM-DIC, and addressed the lack of established speckle creation methodology for said material. The influence of sputter current ($I_{sputter}$), sputter duration ($t_{sputter}$), and chamber pressure during sputtering ($P_{sputter}$) on the resultant speckle characteristics were systematically investigated to determine suitable sputtering parameters. It was concluded that: (i) increasing $I_{sputter}$ resulted in increased average speckle size due to the increased plasma bombardment, (ii) increasing $t_{sputter}$ resulted in significant speckle agglomeration via cluster formation (Volmer-Weber growth), and (iii) reducing $P_{sputter}$ resulted in the deposition of smaller and more uniformly sized speckles due to reduced atom-plasma collisions. A suitable set of magnetron sputtering parameters ($I_{sputter} = 95\ \mathrm{mA}, t_{sputter} = 360\ \mathrm{s}, P_{sputter} = 4\ \mathrm{Pa}$) was identified for SEM-DIC investigations in the present thesis after fine-tuning the sputtering parameters.

The influence of microstructural heterogeneity (i.e. variations in grain size and crystallographic texture) on the evolution of microscale plastic strain localisation in SLM 18Ni-300 maraging steel was investigated via EBSD, in situ uniaxial tensile experiments, and SEM-DIC (**Chapter 4 Section 4.3**). Custom MATLAB scripts were utilised to digitally align and overlay the EBSD and SEM-DIC datasets together. This methodology facilitated a novel grain-to-grain comparison of the microscale plastic strain localisation between SLM as-built (AB) and the solution-aging treatment (SAT) samples at sub-micron scale spatial resolution, and addressed the lack of SEM-DIC investigations specific to said material. It was concluded that the AB sample sustained increasing plastic strain while maintaining a relatively constant stress state during loading. The presence of densely distributed, small, and equiaxed grains induced during rapid solidification in SLM process formed a network that resisted deformation in all directions, resulting in grain boundary strengthening. In contrast, post-processing heat treatment resulted in the formation of larger and more elongated grains in the SAT sample, and induced the precipitation of Ni-based intermetallics throughout the sample's microstructure. The Ni-based intermetallics impeded dislocation motion during plastic deformation, resulting in strain hardening. These findings demonstrate that microscale plastic strain localisation in SLM 18Ni-300 maraging steel (both AB and SAT samples) is driven by the interplay between microstructural heterogeneity, Ni-based intermetallics, and the impediment of dislocation motion.

In addition, custom MATLAB scripts were utilised to identify and analyse the plastic deformation mechanisms and active slip systems within individual grains of SLM 18Ni-300 maraging steel (**Chapter 4 Section 4.3.5** and **4.3.6**). G2 from AB sample and G8 from SAT sample were selected for further analysis due to their similar grain size. The main deformation mechanism was identified as dislocation slip, and its occurrence was directly influenced by the presence of internal misorientations in both grains. Slip preferentially occurred in grains with increased internal misorientation and higher density of low-angle grain boundaries (LAGBs), and intersected regions with increased kernel average misorientation (KAM). Slip systems with a Schmid factor higher than 0.4 exhibited pronounced slip activity, and it was deduced that the simultaneous activation of five or more slip systems helped maintain geometrical compatibility between adjacent grains during deformation. Furthermore, complex slip behaviour including discrete slip, diffuse slip, and possible cross-slip (or overlapping slip) were identified. The combined kinematics of the active slip systems were reflected in the in-plane deformation behaviour of both grains. These findings provide novel grain-level insights into the role of internal misorientations on slip activity in SLM 18Ni-300 maraging steel.

5.2. Suggestions for future research directions

5.2.1. Numerical modelling of microstructure evolution

In the present research, it was concluded that the microstructure evolution phenomena (i.e. laser-powder interactions, rapid solidification, and intrinsic heat treatment) in SLM process induced the formation of microstructural heterogeneity (i.e. variation in grain size and crystallographic texture) in SLM 18Ni-300 maraging steel. Furthermore, the microstructure evolution phenomena that occurred during post-processing heat treatment (i.e. austenite reversion, precipitation hardening, grain coarsening) significantly altered the material's microstructure and mechanical properties. Several investigations were conducted to experimentally characterise the influence of SLM process parameters (or in-process parameters) and post-processing heat treatment on SLM 18Ni-300 maraging steel [28–30,84,125,126]. However, numerical modelling of the microstructure evolution phenomena during the SLM process and post-processing heat treatment is yet to be fully explored.

The numerical modelling of microstructure evolution in SLM 18Ni-300 maraging steel facilitates the numerical prediction of microstructure during the SLM process and post-processing heat treatment. Potential applications include tailoring the material's microstructure to obtain isotropic mechanical properties or enhanced functionality. The use of coupled thermal-microstructure numerical models to fully characterise the microstructure evolution was reviewed [177]. For example, Narayama Samy et al. [178] utilised finite element method and phase-field modelling (FEM-PFM) to investigate the grain nucleation and growth in SLM ferritic stainless steel. The competing influence of localised temperature gradient and the presence of TiN particles on grain nucleation and growth was numerically characterised and validated via experiments. However, the application of FEM-PFM to numerically predict grain nucleation and growth in SLM 18Ni-300 maraging steel is yet to be fully explored in current literature.

5.2.2. Plastic strain localisation under complex loading conditions

Engineering components are often subjected to complex loading conditions such as multiaxial tension and compression, cyclic loading (i.e. fatigue), as well as thermal loading throughout its service life. The application of these loading conditions give rise to plastic strain localisation and damage in engineering components, reducing its service life. The application of scanning electron microscope-based digital image correlation (SEM-DIC) for the experimental characterisation of microscale plastic strain localisation in metals subjected to various loading conditions was reviewed [146,179]. For example, Hsu et al. [180] utilised SEM-DIC and synchrotron X-ray diffraction (XRD) to investigate the microscale plastic strain localisation in NiTi subjected to tensile loading with varying load paths. The relationship between the material's grain texture, stress-induced martensitic transformation phenomenon, and heterogeneous strain accommodation at the microscale was experimentally revealed. However, the microscale plastic strain localisation in SLM 18Ni-300 maraging steel subjected to multiaxial loading and fatigue is yet to be elucidated. The experimental insights would contribute to a more comprehensive understanding of the process-microstructure-properties relationships in SLM 18Ni-300 maraging steel.

References

[1] M. Attaran, The rise of 3-D printing: The advantages of additive manufacturing over traditional manufacturing, Bus. Horiz. 60 (2017) 677–688. https://doi.org/10.1016/j.bushor.2017.05.011.

[2] U. Aziz, M. McAfee, I. Manolakis, N. Timmons, D. Tormey, A Review of Optimization of Additively Manufactured 316/316L Stainless Steel Process Parameters, Post-Processing Strategies, and Defect Mitigation, Materials (Basel). 18 (2025) 2870. https://doi.org/10.3390/ma18122870.

[3] M. Lowther, S. Louth, A. Davey, A. Hussain, P. Ginestra, L. Carter, N. Eisenstein, L. Grover, S. Cox, Clinical, industrial, and research perspectives on powder bed fusion additively manufactured metal implants, Addit. Manuf. 28 (2019) 565–584. https://doi.org/10.1016/j.addma.2019.05.033.

[4] B. Blakey-Milner, P. Gradl, G. Snedden, M. Brooks, J. Pitot, E. Lopez, M. Leary, F. Berto, A. du Plessis, Metal additive manufacturing in aerospace: A review, Mater. Des. 209 (2021) 110008. https://doi.org/10.1016/j.matdes.2021.110008.

[5] B. Sarzyński, L. Śnieżek, K. Grzelak, Metal Additive Manufacturing (MAM) Applications in Production of Vehicle Parts and Components—A Review, Metals (Basel). 14 (2024) 195. https://doi.org/10.3390/met14020195.

[6] Â. Cunha, A. Marques, M.R. Silva, F. Bartolomeu, F.S. Silva, M. Gasik, B. Trindade, Ó. Carvalho, Laser powder bed fusion of the steels used in the plastic injection mould industry: a review of the influence of processing parameters on the final properties, Int. J. Adv. Manuf. Technol. 121 (2022) 4255–4287. https://doi.org/10.1007/s00170-022-09588-0.

[7] Electro Optical Systems (EOS) GmbH, Sogeti High Tech Additive Manufacturing for the New Airbus A350 XWB, (2018) 1–4. https://www.eos.info/industries/customer-success-stories/airbus-a350-xwb-3d-printed-cable-mount (accessed September 30, 2025).

[8] Electro Optical Systems (EOS) GmbH, Using Additive Manufacturing for Conformal Cooling, (2018) 1–4. https://www.eos.info/industries/customer-success-stories/innomia-automotive-3d-printed-cooling-channels (accessed September 30, 2025).

[9] B. Zhang, Y. Li, Q. Bai, Defect Formation Mechanisms in Selective Laser Melting: A Review, Chinese J. Mech. Eng. 30 (2017) 515–527. https://doi.org/10.1007/s10033-017-0121-5.

[10] C. Ioannidou, H.-H. König, N. Semjatov, U. Ackelid, P. Staron, C. Körner, P. Hedström, G. Lindwall, In-situ synchrotron X-ray analysis of metal Additive Manufacturing: Current state, opportunities and challenges, Mater. Des. 219 (2022) 110790. https://doi.org/10.1016/j.matdes.2022.110790.

[11] G. Yang, Y. Xie, S. Zhao, L. Qin, X. Wang, B. Wu, Quality Control: Internal Defects Formation Mechanism of Selective Laser Melting Based on Laser-powder-melt Pool Interaction: A Review, Chinese J. Mech. Eng. Addit. Manuf. Front. 1 (2022) 100037. https://doi.org/10.1016/j.cjmeam.2022.100037.

[12] J.T. McKeown, K. Zweiacker, C. Liu, D.R. Coughlin, A.J. Clarke, J.K. Baldwin, J.W. Gibbs, J.D. Roehling, S.D. Imhoff, P.J. Gibbs, D. Tourret, J.M.K. Wiezorek, G.H. Campbell, Time-Resolved In Situ Measurements During Rapid Alloy Solidification: Experimental Insight for Additive Manufacturing, JOM. 68 (2016)

985–999. https://doi.org/10.1007/s11837-015-1793-x.
[13] Y. Kok, X.P. Tan, P. Wang, M.L.S. Nai, N.H. Loh, E. Liu, S.B. Tor, Anisotropy and heterogeneity of microstructure and mechanical properties in metal additive manufacturing: A critical review, Mater. Des. 139 (2018) 565–586. https://doi.org/10.1016/j.matdes.2017.11.021.
[14] T. DebRoy, H.L. Wei, J.S. Zuback, T. Mukherjee, J.W. Elmer, J.O. Milewski, A.M. Beese, A. Wilson-Heid, A. De, W. Zhang, Additive manufacturing of metallic components – Process, structure and properties, Prog. Mater. Sci. 92 (2018) 112–224. https://doi.org/10.1016/j.pmatsci.2017.10.001.
[15] N. Sanaei, A. Fatemi, Defects in additive manufactured metals and their effect on fatigue performance: A state-of-the-art review, Prog. Mater. Sci. 117 (2021) 100724. https://doi.org/10.1016/j.pmatsci.2020.100724.
[16] W. Sha, Z. Guo, 1. Introduction to maraging steels, in: Maraging Steels Model. Microstruct. Prop. Appl., Elsevier, 2009: pp. 1–16. https://doi.org/10.1533/9781845696931.1.
[17] K. Rohrbach, M. Schmidt, Maraging Steels, in: ASM Handbook Committee (Ed.), ASM Handbook, Vol. 1 Prop. Sel. Irons, Steels, High-Performance Alloy., ASM International, 1990: pp. 793–800. https://doi.org/10.31399/asm.hb.v01.a0001043.
[18] C. Tan, K. Zhou, M. Kuang, W. Ma, T. Kuang, Microstructural characterization and properties of selective laser melted maraging steel with different build directions, Sci. Technol. Adv. Mater. 19 (2018) 746–758. https://doi.org/10.1080/14686996.2018.1527645.
[19] C. Liu, Z. Cai, Y. Dai, N. Huang, F. Xu, C. Lao, Experimental comparison of the flow rate and cooling performance of internal cooling channels fabricated via selective laser melting and conventional drilling process, Int. J. Adv. Manuf. Technol. 96 (2018) 2757–2767. https://doi.org/10.1007/s00170-018-1799-y.
[20] Y. Bai, Y. Yang, Z. Xiao, D. Wang, Selective laser melting of maraging steel: mechanical properties development and its application in mold, Rapid Prototyp. J. 24 (2018) 623–629. https://doi.org/10.1108/RPJ-05-2017-0104.
[21] M. Moshiri, D. Loaldi, F. Zanini, D. Sgaravato, S. Carmignato, G. Tosello, Analysis of an as-built metal additively manufactured tool cavity insert performance and advantages for plastic injection moulding, J. Manuf. Process. 61 (2021) 369–382. https://doi.org/10.1016/j.jmapro.2020.11.035.
[22] A.G. Demir, B. Previtali, Investigation of remelting and preheating in SLM of 18Ni300 maraging steel as corrective and preventive measures for porosity reduction, Int. J. Adv. Manuf. Technol. 93 (2017) 2697–2709. https://doi.org/10.1007/s00170-017-0697-z.
[23] Z. Zhao, C. Dong, D. Kong, L. Wang, X. Ni, L. Zhang, W. Wu, L. Zhu, X. Li, Influence of pore defects on the mechanical property and corrosion behavior of SLM 18Ni300 maraging steel, Mater. Charact. 182 (2021) 111514. https://doi.org/10.1016/j.matchar.2021.111514.
[24] S.H. Hong, S.Y. Ha, G. Song, J. Cho, K.B. Kim, H.J. Park, G.C. Kang, J.M. Park, Correlation between micro-to-macro mechanical properties and processing parameters on additive manufactured 18Ni-300 maraging steels, J. Alloys Compd. 960 (2023) 171031. https://doi.org/10.1016/j.jallcom.2023.171031.
[25] T. Bhardwaj, M. Shukla, Effect of laser scanning strategies on texture, physical

and mechanical properties of laser sintered maraging steel, Mater. Sci. Eng. A. 734 (2018) 102–109. https://doi.org/10.1016/j.msea.2018.07.089.
[26] Y. Yao, K. Wang, X. Wang, L. Li, W. Cai, S. Kelly, N. Esparragoza, M. Rosser, F. Yan, Microstructural heterogeneity and mechanical anisotropy of 18Ni-330 maraging steel fabricated by selective laser melting: The effect of build orientation and height, J. Mater. Res. 35 (2020) 2065–2076. https://doi.org/10.1557/jmr.2020.126.
[27] Z. Zhao, L. Wang, D. Kong, P. Liu, X. He, X. Ni, L. Zhang, C. Dong, Texture dependence on the mechanical properties of 18Ni300 maraging steel fabricated by laser powder bed fusion, Mater. Charact. 189 (2022) 111938. https://doi.org/10.1016/j.matchar.2022.111938.
[28] J. Mutua, S. Nakata, T. Onda, Z.-C. Chen, Optimization of selective laser melting parameters and influence of post heat treatment on microstructure and mechanical properties of maraging steel, Mater. Des. 139 (2018) 486–497. https://doi.org/10.1016/j.matdes.2017.11.042.
[29] L. Kučerová, K. Burdová, Š. Jeníček, I. Chena, Effect of solution annealing and precipitation hardening at 250 °C–550 °C on microstructure and mechanical properties of additively manufactured 1.2709 maraging steel, Mater. Sci. Eng. A. 814 (2021) 141195. https://doi.org/10.1016/j.msea.2021.141195.
[30] X. Mei, Y. Yan, H. Fu, X. Gao, S. Huang, L. Qiao, Effect of aging temperature on microstructure evolution and strengthening behavior of L-PBF 18Ni(300) maraging steel, Addit. Manuf. 58 (2022) 103071. https://doi.org/10.1016/j.addma.2022.103071.
[31] S. Sun, M. Brandt, M. Easton, 2 Powder bed fusion processes: An overview, in: Laser Addit. Manuf. Mater. Des. Technol. Appl., Elsevier, 2017: pp. 55–77. https://doi.org/10.1016/B978-0-08-100433-3.00002-6.
[32] N.T. Aboulkhair, M. Simonelli, L. Parry, I. Ashcroft, C. Tuck, R. Hague, 3D printing of Aluminium alloys: Additive Manufacturing of Aluminium alloys using selective laser melting, Prog. Mater. Sci. 106 (2019) 100578. https://doi.org/10.1016/j.pmatsci.2019.100578.
[33] D.O. Kazmer, Structural System Design, in: Inject. Mold Des. Eng., 2nd ed., Carl Hanser Verlag GmbH & Co. KG, München, 2016: pp. 381–428. https://doi.org/10.3139/9781569905715.012.
[34] R.K. Roy, 6 Analysis of Variance (ANOVA), in: A Prim. Taguchi Method, 2nd ed., Society of Manufacturing Engineers, 2010: pp. 129–183.
[35] S. Liu, Y. Yang, J. Forrest, 5 Grey Incidence Analysis Models, in: Grey Data Anal. Methods, Model. Appl., Springer Singapore, Singapore, 2017: pp. 67–103. https://doi.org/10.1007/978-981-10-1841-1_5.
[36] J.P.M. Hoefnagels, M.P.F.H.L. van Maris, T. Vermeij, One-step deposition of nano-to-micron-scalable, high-quality digital image correlation patterns for high-strain in-situ multi-microscopy testing, Strain. 55 (2019) e12330. https://doi.org/10.1111/str.12330.
[37] T. Vermeij, J.A.C. Verstijnen, T.J.J. Ramirez y Cantador, B. Blaysat, J. Neggers, J.P.M. Hoefnagels, A Nanomechanical Testing Framework Yielding Front & Rear-Sided, High-Resolution, Microstructure-Correlated SEM-DIC Strain Fields, Exp. Mech. 62 (2022) 1625–1646. https://doi.org/10.1007/s11340-022-00884-0.
[38] T. Vermeij, R.H.J. Peerlings, M.G.D. Geers, J.P.M. Hoefnagels, Automated

identification of slip system activity fields from digital image correlation data, Acta Mater. 243 (2023) 118502. https://doi.org/10.1016/j.actamat.2022.118502.
[39] W.K. Law, K.C. Wong, H. Wang, Z. Sun, C.S. Lim, Microstructure Evolution in Additively Manufactured Steel Molds: A Review, J. Mater. Eng. Perform. 30 (2021) 6389–6405. https://doi.org/10.1007/s11665-021-05948-1.
[40] W.K. Law, Z.Y. Wu, K.C. Wong, H.L. Wang, Z.Z. Sun, C.S. Lim, Investigation of the Influence of Selective Laser Melting Process Parameters on the Microstructure and Mechanical Properties of 18Ni-300 Maraging Steel, Key Eng. Mater. 913 (2022) 259–264. https://doi.org/10.4028/p-2tysi2.
[41] W.K. Law, Z. Wu, C. Song, H. Wang, K.-C. Wong, C.S. Lim, Z. Sun, Optimization of Selective Laser Melting Process Parameters Via Taguchi's Methods and Gray Relational Analysis for 3D Printing of 18Ni-300 Maraging Steel, Steel Res. Int. 94 (2023). https://doi.org/10.1002/srin.202200203.
[42] W.K. Law, H.L. Wang, C.H. Song, C.S. Lim, Z.Z. Sun, K.C. Wong, Influence of Magnetron Sputtering Parameters on Speckle Characteristics for Application in Microscale DIC of Maraging Steel, Mater. Sci. Forum. 1154 (2025) 37–42. https://doi.org/10.4028/p-Ht69Dm.
[43] W.K. Law, H. Wang, C. Song, K.-C. Wong, C.S. Lim, Z. Sun, Influence of microstructural heterogeneity on the plastic strain localisation in selective laser melted 18Ni-300 maraging steel, Int. J. Plast. 191 (2025) 104400. https://doi.org/10.1016/j.ijplas.2025.104400.
[44] F. Alifui-Segbaya, I.F. Ituarte, S. Hasanov, A. Gupta, I. Fidan, Opportunities and Limitations of Additive Manufacturing, in: E. Pei, A. Bernard, D. Gu, C. Klahn, M. Monzón, M. Petersen, T. Sun (Eds.), Springer Handb. Addit. Manuf., 2023: pp. 125–143. https://doi.org/10.1007/978-3-031-20752-5_9.
[45] P. Ahangar, M.E. Cooke, M.H. Weber, D.H. Rosenzweig, Current Biomedical Applications of 3D Printing and Additive Manufacturing, Appl. Sci. 9 (2019) 1713. https://doi.org/10.3390/app9081713.
[46] J.L. Dávila, P.I. Neto, P.Y. Noritomi, R.T. Coelho, J.V.L. da Silva, Hybrid manufacturing: a review of the synergy between directed energy deposition and subtractive processes, Int. J. Adv. Manuf. Technol. 110 (2020) 3377–3390. https://doi.org/10.1007/s00170-020-06062-7.
[47] C.Y. Yap, C.K. Chua, Z.L. Dong, Z.H. Liu, D.Q. Zhang, L.E. Loh, S.L. Sing, Review of selective laser melting: Materials and applications, Appl. Phys. Rev. 2 (2015) 041101. https://doi.org/10.1063/1.4935926.
[48] W.E. Frazier, Metal Additive Manufacturing: A Review, J. Mater. Eng. Perform. 23 (2014) 1917–1928. https://doi.org/10.1007/s11665-014-0958-z.
[49] D. Omidvarkarjan, R. Rosenbauer, C. Klahn, M. Meboldt, Implementation of Additive Manufacturing in Industry, in: E. Pei, A. Bernard, D. Gu, C. Klahn, M. Monzón, M. Petersen, T. Sun (Eds.), Springer Handb. Addit. Manuf., 2023: pp. 55–71. https://doi.org/10.1007/978-3-031-20752-5_4.
[50] E.J. Hurst, 3D Printing in Healthcare: Emerging Applications, J. Hosp. Librariansh. 16 (2016) 255–267. https://doi.org/10.1080/15323269.2016.1188042.
[51] M. Salmi, Additive Manufacturing Processes in Medical Applications, Materials (Basel). 14 (2021) 191. https://doi.org/10.3390/ma14010191.
[52] C. Tan, F. Weng, S. Sui, Y. Chew, G. Bi, Progress and perspectives in laser additive

manufacturing of key aeroengine materials, Int. J. Mach. Tools Manuf. 170 (2021) 103804. https://doi.org/10.1016/j.ijmachtools.2021.103804.
[53] Electro Optical Systems (EOS) GmbH, Future Ariane Propulsion Module Simplified, (2019) 1–3. https://www.eos.info/industries/customer-success-stories/aerospace-additive-manufacturing-for-ariane-injection-nozzles (accessed September 30, 2025).
[54] National Aeronautics and Space Administration (NASA), Successful NASA Rocket Fuel Pump Tests Pave Way for 3-D Printed Demonstrator Engine, (2015). https://www.nasa.gov/technology/manufacturing-materials-3-d-printing/successful-nasa-rocket-fuel-pump-tests-pave-way-for-3-d-printed-demonstrator-engine/ (accessed September 30, 2025).
[55] Electro Optical Systems (EOS) GmbH, Young Engineers Choose Additive Manufacturing to Tap the Full Potential of the Part, (2012) 1–4. https://www.eos.info/industries/customer-success-stories/formula-student-automotive-topology-optimized-steering-stub-axle (accessed September 30, 2025).
[56] Z. Chen, C. Han, M. Gao, S.Y. Kandukuri, K. Zhou, A review on qualification and certification for metal additive manufacturing, Virtual Phys. Prototyp. 17 (2022) 382–405. https://doi.org/10.1080/17452759.2021.2018938.
[57] X. Zhang, C.J. Yocom, B. Mao, Y. Liao, Microstructure evolution during selective laser melting of metallic materials: A review, J. Laser Appl. 31 (2019) 031201. https://doi.org/10.2351/1.5085206.
[58] J.P. Kruth, L. Froyen, J. Van Vaerenbergh, P. Mercelis, M. Rombouts, B. Lauwers, Selective laser melting of iron-based powder, J. Mater. Process. Technol. 149 (2004) 616–622. https://doi.org/10.1016/j.jmatprotec.2003.11.051.
[59] M. Rombouts, J.P. Kruth, L. Froyen, P. Mercelis, Fundamentals of Selective Laser Melting of alloyed steel powders, CIRP Ann. 55 (2006) 187–192. https://doi.org/10.1016/S0007-8506(07)60395-3.
[60] K.C. Mills, B.J. Keene, R.F. Brooks, A. Shirali, Marangoni effects in welding, Philos. Trans. R. Soc. London. Ser. A Math. Phys. Eng. Sci. 356 (1998) 911–925. https://doi.org/10.1098/rsta.1998.0196.
[61] Y. Bai, Y.J. Lee, C. Li, H. Wang, Densification Behavior and Influence of Building Direction on High Anisotropy in Selective Laser Melting of High-Strength 18Ni-Co-Mo-Ti Maraging Steel, Metall. Mater. Trans. A. 51 (2020) 5861–5879. https://doi.org/10.1007/s11661-020-05978-9.
[62] D.C. Montgomery, 11 Response Surface Methods and Designs, in: Des. Anal. Exp., 10th ed., 2019: pp. 408–476. https://www.wiley.com/en-us/Design+and+Analysis+of+Experiments%2C+10th+Edition-p-9781119492443.
[63] D.F.S. Ferreira, G. Miranda, F.J. Oliveira, J.M. Oliveira, Predictive models for an optimized fabrication of 18Ni300 maraging steel for moulding and tooling by Selective Laser Melting, J. Manuf. Process. 70 (2021) 46–54. https://doi.org/10.1016/j.jmapro.2021.07.066.
[64] Z. Mao, X. Lu, H. Yang, X. Niu, L. Zhang, X. Xie, Processing optimization, microstructure, mechanical properties and nanoprecipitation behavior of 18Ni300 maraging steel in selective laser melting, Mater. Sci. Eng. A. 830 (2022) 142334. https://doi.org/10.1016/j.msea.2021.142334.
[65] N. Omidi, P. Farhadipour, L. Baali, K. Bensalem, N. Barka, M. Jahazi, A

Comprehensive Review of Additively Manufactured H13 Tool Steel Applicable in the Injection Mold Industry: Applications, Designs, Microstructure, Mechanical Properties, JOM. 75 (2023) 4457–4469. https://doi.org/10.1007/s11837-023-05735-4.
[66] C. Tan, K. Zhou, W. Ma, D. Zeng, 激光增材制造成型马氏体时效钢研究进展 Research Progress of Laser Additive Manufacturing of Maraging Steels, Acta Metall. Sin. 56 (2020) 36–52. https://doi.org/10.11900/0412.1961.2019.00129.
[67] B.S. Rao, T.B. Rao, Effect of Process Parameters on Powder Bed Fusion Maraging Steel 300: A Review, Lasers Manuf. Mater. Process. 9 (2022) 338–375. https://doi.org/10.1007/s40516-022-00182-6.
[68] G. Roberts, G. Krauss, R. Kennedy, Chapter 15: Mold Steels, in: Tool Steels, 5th ed., ASM International, 1998: pp. 291–304. https://doi.org/10.31399/asm.tb.ts5.t65900291.
[69] R.A. Mesquita, Chapter 6: Plastic Mold Tool Steels, in: Tool Steels Prop. Perform., CRC Press, 2016: pp. 187–216. https://doi.org/10.1201/9781315181516.
[70] F. Deirmina, N. Peghini, B. AlMangour, D. Grzesiak, M. Pellizzari, Heat treatment and properties of a hot work tool steel fabricated by additive manufacturing, Mater. Sci. Eng. A. 753 (2019) 109–121. https://doi.org/10.1016/j.msea.2019.03.027.
[71] H.X. Li, H.L. Qi, C.H. Song, Y.L. Li, M. Yan, Selective laser melting of P20 mould steel: investigation on the resultant microstructure, high-temperature hardness and corrosion resistance, Powder Metall. 61 (2018) 21–27. https://doi.org/10.1080/00325899.2017.1368965.
[72] S.D. Nath, H. Irrinki, G. Gupta, M. Kearns, O. Gulsoy, S. Atre, Microstructure-property relationships of 420 stainless steel fabricated by laser-powder bed fusion, Powder Technol. 343 (2019) 738–746. https://doi.org/10.1016/j.powtec.2018.11.075.
[73] S.-F. Wen, X.-T. Ji, Y. Zhou, C.-J. Han, Q.-S. Wei, Y.-S. Shi, Corrosion Behavior of the S136 Mold Steel Fabricated by Selective Laser Melting, Chinese J. Mech. Eng. 31 (2018) 108. https://doi.org/10.1186/s10033-018-0312-8.
[74] International Mold Steel, S-Star 420 ESR Stainless Steel for Plastic Molds, MatWeb. (n.d.). http://www.matweb.com/search/datasheet.aspx?matguid=1d44d407531c458799b92f3776bb651f (accessed September 30, 2025).
[75] X. Wang, G. Li, Y. Liu, Y. Cao, F. Wang, Q. Wang, Investigation of Primary Carbides in a Commercial-Sized Electroslag Remelting Ingot of H13 Steel, Metals (Basel). 9 (2019) 1247. https://doi.org/10.3390/met9121247.
[76] Midstate Mold, Everyday Items Made in the Plastic Injection Molding Process, (2017). https://www.midstatemold.com/everyday-items-plastic-injection/ (accessed September 30, 2025).
[77] M. Mazur, P. Brincat, M. Leary, M. Brandt, Numerical and experimental evaluation of a conformally cooled H13 steel injection mould manufactured with selective laser melting, Int. J. Adv. Manuf. Technol. 93 (2017) 881–900. https://doi.org/10.1007/s00170-017-0426-7.
[78] R. Mertens, B. Vrancken, N. Holmstock, Y. Kinds, J.-P. Kruth, J. Van Humbeeck, Influence of Powder Bed Preheating on Microstructure and Mechanical

Properties of H13 Tool Steel SLM Parts, Phys. Procedia. 83 (2016) 882–890. https://doi.org/10.1016/j.phpro.2016.08.092.
[79] M. Åsberg, G. Fredriksson, S. Hatami, W. Fredriksson, P. Krakhmalev, Influence of post treatment on microstructure, porosity and mechanical properties of additive manufactured H13 tool steel, Mater. Sci. Eng. A. 742 (2019) 584–589. https://doi.org/10.1016/j.msea.2018.08.046.
[80] Schmolz + Bickenbach, P-20 High Hardness Plastic Mold Steel, MatWeb. (n.d.). http://www.matweb.com/search/DataSheet.aspx?MatGUID=ed034a5881774162a0f2e4ce26188efb (accessed September 30, 2025).
[81] Y. Zhou, L. Duan, X. Ji, S. Wen, Q. Wei, F. Ye, Y. Shi, Comparisons on microstructure, mechanical and corrosion resistant property of S136 mold steel processed by selective laser melting from two pre-alloy powders with trace element differences, Opt. Laser Technol. 108 (2018) 81–89. https://doi.org/10.1016/j.optlastec.2018.06.057.
[82] X. Ji, S. Wen, Q. Wei, Y. Zhou, Z. Chen, 淬火处理对激光选区熔化成形S136组织与性能的影响 (Effect of quenching treatment on performance of S136 steel fabricated via selective laser melting), J. ZheJiang Univ. (Engineering Sci. 53 (2019) 664–670. https://doi.org/10.3785/j.issn.1008-973X.2019.04.007.
[83] K. Kempen, E. Yasa, L. Thijs, J.-P. Kruth, J. Van Humbeeck, Microstructure and mechanical properties of Selective Laser Melted 18Ni-300 steel, Phys. Procedia. 12 (2011) 255–263. https://doi.org/10.1016/j.phpro.2011.03.033.
[84] C. Tan, K. Zhou, W. Ma, P. Zhang, M. Liu, T. Kuang, Microstructural evolution, nanoprecipitation behavior and mechanical properties of selective laser melted high-performance grade 300 maraging steel, Mater. Des. 134 (2017) 23–34. https://doi.org/10.1016/j.matdes.2017.08.026.
[85] B. Ren, D. Lu, R. Zhou, Z. Li, J. Guan, Preparation and mechanical properties of selective laser melted H13 steel, J. Mater. Res. 34 (2019) 1415–1425. https://doi.org/10.1557/jmr.2019.10.
[86] X. Zhao, Q. Wei, B. Song, Y. Liu, X. Luo, S. Wen, Y. Shi, Fabrication and Characterization of AISI 420 Stainless Steel Using Selective Laser Melting, Mater. Manuf. Process. 30 (2015) 1283–1289. https://doi.org/10.1080/10426914.2015.1026351.
[87] L. Kučerová, I. Zetková, A. Jandová, M. Bystrianský, Microstructural characterisation and in-situ straining of additive-manufactured X3NiCoMoTi 18-9-5 maraging steel, Mater. Sci. Eng. A. 750 (2019) 70–80. https://doi.org/10.1016/j.msea.2019.02.041.
[88] S. Yin, C. Chen, X. Yan, X. Feng, R. Jenkins, P. O'Reilly, M. Liu, H. Li, R. Lupoi, The influence of aging temperature and aging time on the mechanical and tribological properties of selective laser melted maraging 18Ni-300 steel, Addit. Manuf. 22 (2018) 592–600. https://doi.org/https://doi.org/10.1016/j.addma.2018.06.005.
[89] J. Vasco, F.M. Barreiros, A. Nabais, N. Reis, Additive manufacturing applied to injection moulding: technical and economic impact, Rapid Prototyp. J. 25 (2019) 1241–1249. https://doi.org/10.1108/RPJ-07-2018-0179.
[90] H.-S. Park, X.-P. Dang, D.-S. Nguyen, S. Kumar, Design of Advanced Injection Mold to Increase Cooling Efficiency, Int. J. Precis. Eng. Manuf. Technol. 7 (2020) 319–328. https://doi.org/10.1007/s40684-019-00041-4.

[91] S.A. Jahan, T. Wu, Y. Zhang, J. Zhang, A. Tovar, H. Elmounayri, Thermo-mechanical Design Optimization of Conformal Cooling Channels using Design of Experiments Approach, Procedia Manuf. 10 (2017) 898–911. https://doi.org/10.1016/j.promfg.2017.07.078.
[92] H.-S. Park, X.-P. Dang, Development of a Smart Plastic Injection Mold with Conformal Cooling Channels, Procedia Manuf. 10 (2017) 48–59. https://doi.org/10.1016/j.promfg.2017.07.020.
[93] T. Evens, W. Six, J. De Keyzer, F. Desplentere, A. Van Bael, Experimental analysis of conformal cooling in SLM produced injection moulds: Effects on process and product quality, in: AIP Conf. Proc., 2019: p. 070017. https://doi.org/10.1063/1.5084861.
[94] L. Guo, L. Zhang, J. Andersson, O. Ojo, Additive manufacturing of 18% nickel maraging steels: Defect, structure and mechanical properties: A review, J. Mater. Sci. Technol. 120 (2022) 227–252. https://doi.org/10.1016/j.jmst.2021.10.056.
[95] P. Bajaj, A. Hariharan, A. Kini, P. Kürnsteiner, D. Raabe, E.A. Jägle, Steels in additive manufacturing: A review of their microstructure and properties, Mater. Sci. Eng. A. 772 (2020) 138633. https://doi.org/https://doi.org/10.1016/j.msea.2019.138633.
[96] K. Li, T. Yang, N. Gong, J. Wu, X. Wu, D.Z. Zhang, L.E. Murr, Additive manufacturing of ultra-high strength steels: A review, J. Alloys Compd. 965 (2023) 171390. https://doi.org/10.1016/j.jallcom.2023.171390.
[97] M.S. Kenevisi, F.S. Gobber, P. Fino, M. Lombardi, F. Bondioli, S. Biamino, D. Ugues, Tool steels and their additive manufacturing for fabrication and repair via PBF and DED processes: techniques, challenges, and applications, Mater. Des. 258 (2025) 114639. https://doi.org/10.1016/j.matdes.2025.114639.
[98] S. Sun, D. Fabijanic, C. Barr, Q. Liu, K. Walker, N. Matthews, N. Orchowski, M. Easton, M. Brandt, In-situ quench and tempering for microstructure control and enhanced mechanical properties of laser cladded AISI 420 stainless steel powder on 300M steel substrates, Surf. Coatings Technol. 333 (2018) 210–219. https://doi.org/10.1016/j.surfcoat.2017.10.080.
[99] E.A. Jägle, Z. Sheng, P. Kürnsteiner, S. Ocylok, A. Weisheit, D. Raabe, Comparison of Maraging Steel Micro- and Nanostructure Produced Conventionally and by Laser Additive Manufacturing, Materials (Basel). 10 (2017) 8. https://doi.org/10.3390/ma10010008.
[100] M.C. Flemings, Solidification Processing, in: Mater. Sci. Technol., Wiley, Weinheim, Germany, 2006: pp. 1–56. https://doi.org/10.1002/9783527603978.mst0173.
[101] A. Abdali, S. Hossein Nedjad, H. Hamed Zargari, A. Saboori, M. Yildiz, Predictive tools for the cooling rate-dependent microstructure evolution of AISI 316L stainless steel in additive manufacturing, J. Mater. Res. Technol. 29 (2024) 5530–5538. https://doi.org/10.1016/j.jmrt.2024.03.008.
[102] S.W. Xu, K. Oh-ishi, S. Kamado, H. Takahashi, T. Homma, Effects of different cooling rates during two casting processes on the microstructures and mechanical properties of extruded Mg–Al–Ca–Mn alloy, Mater. Sci. Eng. A. 542 (2012) 71–78. https://doi.org/10.1016/j.msea.2012.02.034.
[103] Y. Chen, H. Chen, J. Chen, J. Xiong, Y. Wu, S. Dong, Numerical and experimental

investigation on thermal behavior and microstructure during selective laser melting of high strength steel, J. Manuf. Process. 57 (2020) 533–542. https://doi.org/10.1016/j.jmapro.2020.06.041.
[104] S. Kou, 6 Basic Solidification Concepts, in: Weld. Metall., Wiley, 2002: pp. 143–169. https://doi.org/10.1002/0471434027.
[105] J.T. McKeown, A.J. Clarke, J.M.K. Wiezorek, Imaging transient solidification behavior, MRS Bull. 45 (2020) 916–926. https://doi.org/10.1557/mrs.2020.273.
[106] T. LaGrange, M.R. Armstrong, K. Boyden, C.G. Brown, G.H. Campbell, J.D. Colvin, W.J. DeHope, A.M. Frank, D.J. Gibson, F. V. Hartemann, J.S. Kim, W.E. King, B.J. Pyke, B.W. Reed, M.D. Shirk, R.M. Shuttlesworth, B.C. Stuart, B.R. Torralva, N.D. Browning, Single-shot dynamic transmission electron microscopy, Appl. Phys. Lett. 89 (2006) 044105. https://doi.org/10.1063/1.2236263.
[107] T. LaGrange, B.W. Reed, D.J. Masiel, Movie-mode dynamic electron microscopy, MRS Bull. 40 (2015) 22–28. https://doi.org/10.1557/mrs.2014.282.
[108] T. Sun, W. Tan, L. Chen, A. Rollett, In situ / operando synchrotron x-ray studies of metal additive manufacturing, MRS Bull. 45 (2020) 927–933. https://doi.org/10.1557/mrs.2020.275.
[109] S.M.H. Hojjatzadeh, N.D. Parab, W. Yan, Q. Guo, L. Xiong, C. Zhao, M. Qu, L.I. Escano, X. Xiao, K. Fezzaa, W. Everhart, T. Sun, L. Chen, Pore elimination mechanisms during 3D printing of metals, Nat. Commun. 10 (2019) 3088. https://doi.org/10.1038/s41467-019-10973-9.
[110] A. Bobel, L.G. Hector, I. Chelladurai, A.K. Sachdev, T. Brown, W.A. Poling, R. Kubic, B. Gould, C. Zhao, N. Parab, A. Greco, T. Sun, In situ synchrotron X-ray imaging of 4140 steel laser powder bed fusion, Materialia. 6 (2019) 100306. https://doi.org/10.1016/j.mtla.2019.100306.
[111] Y. Li, J. Yu, S. Li, S. Wang, Y. Ren, K. Yang, Y.-D. Wang, The influence of post-aging treatment on the microstructure and micromechanical behaviors of additively manufactured maraging steel investigated by in situ high-energy X-ray diffraction, J. Mater. Sci. Technol. 200 (2024) 1–12. https://doi.org/10.1016/j.jmst.2024.02.044.
[112] J. Deng, G. Wang, H. Qi, H. Ma, Z. Huang, Excellent isotropic mechanical properties of electron beam melted H13 tool steel: Process optimization and microstructural control, J. Mater. Process. Technol. 343 (2025) 118980. https://doi.org/10.1016/j.jmatprotec.2025.118980.
[113] H. Hosseinlou, M. Shakeri, A.W. Abdelghany, M. Jaskari, A. Järvenpää, A. Hamada, Tailoring microstructure and mechanical properties of additively manufactured H13 tool Steel: Influence of build orientation and tempering treatments, Mater. Sci. Eng. A. 942 (2025) 148708. https://doi.org/10.1016/j.msea.2025.148708.
[114] A.C. de F. Silveira, R. Fechte-Heinen, J. Epp, Microstructure evolution during laser-directed energy deposition of tool steel by in situ synchrotron X-ray diffraction, Addit. Manuf. 63 (2023) 103408. https://doi.org/10.1016/j.addma.2023.103408.
[115] J. Mazumder, A. Schifferer, J. Choi, Direct materials deposition: designed macro and microstructure, Mater. Res. Innov. 3 (1999) 118–131. https://doi.org/10.1007/s100190050137.
[116] H. Zong, N. Kang, M. El Mansori, Characterizations of the anisotropic features of

the phase, texture and deformation behavior of laser powder bed fusion-processed H13 steel, Mater. Charact. 228 (2025) 115403. https://doi.org/10.1016/j.matchar.2025.115403.
[117] X. Yang, Z. Zhang, M. Huang, C. Song, H. Qi, H. Tang, In-depth evaluation of grain morphology, nanoprecipitate dynamics, and tensile properties in SEBM H13 steel, Mater. Today Commun. 43 (2025) 111664. https://doi.org/10.1016/j.mtcomm.2025.111664.
[118] F. Lei, T. Wen, F. Yang, J. Wang, J. Fu, H. Yang, J. Wang, J. Ruan, S. Ji, Microstructures and Mechanical Properties of H13 Tool Steel Fabricated by Selective Laser Melting, Materials (Basel). 15 (2022) 2686. https://doi.org/10.3390/ma15072686.
[119] E.B. Fonseca, A.H.G. Gabriel, J.A. Ávila, R.F. Vaz, D.B. Valim, I.G. Cano, É.S.N. Lopes, Fracture toughness and wear resistance of heat-treated H13 tool steel processed by laser powder bed fusion, Addit. Manuf. 78 (2023) 103862. https://doi.org/10.1016/j.addma.2023.103862.
[120] J.-Y. Chen, K. Conlon, L. Xue, R. Rogge, Experimental study of residual stresses in laser clad AISI P20 tool steel on pre-hardened wrought P20 substrate, Mater. Sci. Eng. A. 527 (2010) 7265–7273. https://doi.org/10.1016/j.msea.2010.07.098.
[121] Y. Wang, X. Ren, Z. Hou, A. Jiang, J. Zhao, Z. Liu, Optimization of Heat Treatment Process and Strengthening–Toughening and Mechanism for H13 Steel, Metals (Basel). 15 (2025) 1101. https://doi.org/10.3390/met15101101.
[122] P. Krakhmalev, I. Yadroitsava, G. Fredriksson, I. Yadroitsev, In situ heat treatment in selective laser melted martensitic AISI 420 stainless steels, Mater. Des. 87 (2015) 380–385. https://doi.org/10.1016/j.matdes.2015.08.045.
[123] M.K. Alam, M. Mehdi, R.J. Urbanic, A. Edrisy, Mechanical behavior of additive manufactured AISI 420 martensitic stainless steel, Mater. Sci. Eng. A. 773 (2020) 138815. https://doi.org/10.1016/j.msea.2019.138815.
[124] P. Kürnsteiner, M.B. Wilms, A. Weisheit, P. Barriobero-Vila, E.A. Jägle, D. Raabe, Massive nanoprecipitation in an Fe-19Ni- x Al maraging steel triggered by the intrinsic heat treatment during laser metal deposition, Acta Mater. 129 (2017) 52–60. https://doi.org/10.1016/j.actamat.2017.02.069.
[125] Y. Bai, D. Wang, Y. Yang, H. Wang, Effect of heat treatment on the microstructure and mechanical properties of maraging steel by selective laser melting, Mater. Sci. Eng. A. 760 (2019) 105–117. https://doi.org/10.1016/j.msea.2019.05.115.
[126] T. Allam, K.G. Pradeep, P. Köhnen, A. Marshal, J.H. Schleifenbaum, C. Haase, Tailoring the nanostructure of laser powder bed fusion additively manufactured maraging steel, Addit. Manuf. 36 (2020) 101561. https://doi.org/10.1016/j.addma.2020.101561.
[127] B. Pan, Digital image correlation for surface deformation measurement: historical developments, recent advances and future goals, Meas. Sci. Technol. 29 (2018) 082001. https://doi.org/10.1088/1361-6501/aac55b.
[128] J. Kang, Y. Ososkov, J. Embury, D. Wilkinson, Digital image correlation studies for microscopic strain distribution and damage in dual phase steels, Scr. Mater. 56 (2007) 999–1002. https://doi.org/10.1016/j.scriptamat.2007.01.031.
[129] H. Ghadbeigi, C. Pinna, S. Celotto, J.R. Yates, Local plastic strain evolution in a high strength dual-phase steel, Mater. Sci. Eng. A. 527 (2010) 5026–5032.

https://doi.org/10.1016/j.msea.2010.04.052.
[130] Y.L. Dong, B. Pan, A Review of Speckle Pattern Fabrication and Assessment for Digital Image Correlation, Exp. Mech. 57 (2017) 1161–1181. https://doi.org/10.1007/s11340-017-0283-1.
[131] A. Weidner, H. Biermann, Review on Strain Localization Phenomena Studied by High-Resolution Digital Image Correlation, Adv. Eng. Mater. 23 (2021). https://doi.org/10.1002/adem.202001409.
[132] B. Pan, K. Qian, H. Xie, A. Asundi, Two-dimensional digital image correlation for in-plane displacement and strain measurement: a review, Meas. Sci. Technol. 20 (2009) 062001. https://doi.org/10.1088/0957-0233/20/6/062001.
[133] J.C. Stinville, T. Francis, A.T. Polonsky, C.J. Torbet, M.A. Charpagne, Z. Chen, G.H. Balbus, F. Bourdin, V. Valle, P.G. Callahan, M.P. Echlin, T.M. Pollock, Time-Resolved Digital Image Correlation in the Scanning Electron Microscope for Analysis of Time-Dependent Mechanisms, Exp. Mech. 61 (2021) 331–348. https://doi.org/10.1007/s11340-020-00632-2.
[134] J.D. Carroll, W. Abuzaid, J. Lambros, H. Sehitoglu, An experimental methodology to relate local strain to microstructural texture, Rev. Sci. Instrum. 81 (2010). https://doi.org/10.1063/1.3474902.
[135] R.B. Vieira, H. Sehitoglu, J. Lambros, Representative volume elements for plasticity and creep measured from high-resolution microscale strain fields, Acta Mater. 214 (2021) 117021. https://doi.org/10.1016/j.actamat.2021.117021.
[136] L. Sun, F. Jiang, R. Huang, D. Yuan, C. Guo, J. Wang, Anisotropic mechanical properties and deformation behavior of low-carbon high-strength steel component fabricated by wire and arc additive manufacturing, Mater. Sci. Eng. A. 787 (2020) 139514. https://doi.org/10.1016/j.msea.2020.139514.
[137] F. Di Gioacchino, J. Quinta da Fonseca, An experimental study of the polycrystalline plasticity of austenitic stainless steel, Int. J. Plast. 74 (2015) 92–109. https://doi.org/10.1016/j.ijplas.2015.05.012.
[138] E. Polatidis, M. Šmíd, W.-N. Hsu, M. Kubenova, J. Capek, T. Panzner, H. Van Swygenhoven, The interplay between deformation mechanisms in austenitic 304 steel during uniaxial and equibiaxial loading, Mater. Sci. Eng. A. 764 (2019) 138222. https://doi.org/10.1016/j.msea.2019.138222.
[139] T. Vermeij, J.P.M. Hoefnagels, Plasticity, localization, and damage in ferritic-pearlitic steel studied by nanoscale digital image correlation, Scr. Mater. 208 (2022) 114327. https://doi.org/10.1016/j.scriptamat.2021.114327.
[140] C. Bean, F. Wang, M.A. Charpagne, P. Villechaise, V. Valle, S.R. Agnew, D.S. Gianola, T.M. Pollock, J.C. Stinville, Heterogeneous slip localization in an additively manufactured 316L stainless steel, Int. J. Plast. 159 (2022) 103436. https://doi.org/10.1016/j.ijplas.2022.103436.
[141] D. An, Y. Zhou, X. Liu, H. Wang, S. Li, Y. Xiao, R. Li, X. Li, X. Han, J. Chen, Exploring structural origins responsible for the exceptional mechanical property of additively manufactured 316L stainless steel via in-situ and comparative investigations, Int. J. Plast. 170 (2023) 103769. https://doi.org/10.1016/j.ijplas.2023.103769.
[142] D. Hu, Z. Guo, N. Grilli, A. Tay, Z. Lu, W. Yan, Understanding the strain localization in additively manufactured materials: Micro-scale tensile tests and crystal plasticity modeling, Int. J. Plast. 177 (2024) 103981.

https://doi.org/10.1016/j.ijplas.2024.103981.
[143] P. Reu, All about Speckles: Aliasing, Exp. Tech. 38 (2014) 1–3. https://doi.org/10.1111/ext.12111.
[144] Y. Dong, H. Kakisawa, Y. Kagawa, Development of microscale pattern for digital image correlation up to 1400°C, Opt. Lasers Eng. 68 (2015) 7–15. https://doi.org/10.1016/j.optlaseng.2014.12.003.
[145] A. Weidner, 2 Plastic Deformation and Strain Localizations, in: Deform. Process. TRIP/TWIP Steels, 2020: pp. 7–45. https://doi.org/10.1007/978-3-030-37149-4_2.
[146] J.C. Stinville, M.A. Charpagne, R. Maaß, H. Proudhon, W. Ludwig, P.G. Callahan, F. Wang, I.J. Beyerlein, M.P. Echlin, T.M. Pollock, Insights into Plastic Localization by Crystallographic Slip from Emerging Experimental and Numerical Approaches, Annu. Rev. Mater. Res. 53 (2023) 275–317. https://doi.org/10.1146/annurev-matsci-080921-102621.
[147] J.C. Stinville, N. Vanderesse, F. Bridier, P. Bocher, T.M. Pollock, High resolution mapping of strain localization near twin boundaries in a nickel-based superalloy, Acta Mater. 98 (2015) 29–42. https://doi.org/10.1016/j.actamat.2015.07.016.
[148] F. Bourdin, J.C. Stinville, M.P. Echlin, P.G. Callahan, W.C. Lenthe, C.J. Torbet, D. Texier, F. Bridier, J. Cormier, P. Villechaise, T.M. Pollock, V. Valle, Measurements of plastic localization by heaviside-digital image correlation, Acta Mater. 157 (2018) 307–325. https://doi.org/10.1016/j.actamat.2018.07.013.
[149] X. Xu, D. Lunt, R. Thomas, R.P. Babu, A. Harte, M. Atkinson, J.Q. da Fonseca, M. Preuss, Identification of active slip mode in a hexagonal material by correlative scanning electron microscopy, Acta Mater. 175 (2019) 376–393. https://doi.org/10.1016/j.actamat.2019.06.024.
[150] H. Hu, F. Briffod, T. Shiraiwa, M. Enoki, Automated slip system identification and strain analysis framework using high-resolution digital image correlation data: Application to a bimodal Ti-6Al-4V alloy, Int. J. Plast. 166 (2023) 103618. https://doi.org/10.1016/j.ijplas.2023.103618.
[151] A. Guery, F. Hild, F. Latourte, S. Roux, Slip activities in polycrystals determined by coupling DIC measurements with crystal plasticity calculations, Int. J. Plast. 81 (2016) 249–266. https://doi.org/10.1016/j.ijplas.2016.01.008.
[152] S. Isavand, A. Assempour, Strain localization and deformation behavior in ferrite-pearlite steel unraveled by high-resolution in-situ testing integrated with crystal plasticity simulations, Int. J. Mech. Sci. 200 (2021) 106441. https://doi.org/10.1016/j.ijmecsci.2021.106441.
[153] M. Yaghoobi, Z. Chen, A.D. Murphy-Leonard, V. Sundararaghavan, S. Daly, J.E. Allison, Deformation twinning and detwinning in extruded Mg-4Al: In-situ experiment and crystal plasticity simulation, Int. J. Plast. 155 (2022) 103345. https://doi.org/10.1016/j.ijplas.2022.103345.
[154] J.M. Hestroffer, M.I. Latypov, J.-C. Stinville, M.-A. Charpagne, V. Valle, M.P. Miller, T.M. Pollock, I.J. Beyerlein, Development of grain-scale slip activity and lattice rotation fields in Inconel 718, Acta Mater. 226 (2022) 117627. https://doi.org/10.1016/j.actamat.2022.117627.
[155] B. Yang, Y. Lai, X. Yue, D. Wang, Y. Zhao, Parametric Optimization of Laser Additive Manufacturing of Inconel 625 Using Taguchi Method and Grey Relational Analysis, Scanning. 2020 (2020) 1–10.

https://doi.org/10.1155/2020/9176509.
[156] Y. Bai, Y. Yang, D. Wang, M. Zhang, Influence mechanism of parameters process and mechanical properties evolution mechanism of maraging steel 300 by selective laser melting, Mater. Sci. Eng. A. 703 (2017) 116–123. https://doi.org/10.1016/j.msea.2017.06.033.
[157] M. Simonsen, Strain Tensors and Criteria in Vic, (2023). https://correlated.kayako.com/article/2-strain-tensors-and-criteria-in-vic (accessed September 30, 2025).
[158] H. Cao, Z. Luo, C. Wang, J. Wang, T. Hu, L. Xiao, J. Che, The Stress Concentration Mechanism of Pores Affecting the Tensile Properties in Vacuum Die Casting Metals, Materials (Basel). 13 (2020) 3019. https://doi.org/10.3390/ma13133019.
[159] G.N. Haidemenopoulos, 9 Fracture, fatigue, and creep of metals, in: Phys. Metall. Princ. Des., CRC Press, 2018: pp. 335–388. https://doi.org/10.1201/9781315211220.
[160] K. Oura, M. Katayama, A. V. Zotov, V.G. Lifshits, A.A. Saranin, 14. Growth of Thin Films, in: Surf. Sci., 2003: pp. 357–387. https://doi.org/10.1007/978-3-662-05179-5_14.
[161] Z.-H. Li, E.-S. Cho, S.J. Kwon, Molybdenum thin film deposited by in-line DC magnetron sputtering as a back contact for Cu(In,Ga)Se2 solar cells, Appl. Surf. Sci. 257 (2011) 9682–9688. https://doi.org/10.1016/j.apsusc.2011.06.101.
[162] P. Huang, C. Huang, M. Lin, C. Chou, C. Hsu, C. Kuo, The Effect of Sputtering Parameters on the Film Properties of Molybdenum Back Contact for CIGS Solar Cells, Int. J. Photoenergy. 2013 (2013) 1–8. https://doi.org/10.1155/2013/390824.
[163] F. Bachmann, R. Hielscher, H. Schaeben, Grain detection from 2d and 3d EBSD data—Specification of the MTEX algorithm, Ultramicroscopy. 111 (2011) 1720–1733. https://doi.org/10.1016/j.ultramic.2011.08.002.
[164] MTEX, MTEX, (2024). https://mtex-toolbox.github.io/ (accessed September 30, 2025).
[165] MTEX, Kernel Average Misorientation (KAM), (2024). https://mtex-toolbox.github.io/EBSDKAM.html (accessed September 30, 2025).
[166] W. Soboyejo, Dislocations and Plastic Deformation, in: Mech. Prop. Eng. Mater., CRC Press, 2002: pp. 176–223. https://doi.org/10.1201/9780203910399.
[167] G.N. Haidemenopoulos, 7 Plastic Deformation and Annealing, in: Phys. Metall. Princ. Des., CRC Press, 2018: pp. 261–300. https://doi.org/10.1201/9781315211220.
[168] MTEX, The Schmid Factor, (2024). https://mtex-toolbox.github.io/SchmidtFactor.html (accessed September 30, 2025).
[169] MTEX, Grain Orientation Parameters, (2024). https://mtex-toolbox.github.io/GrainOrientationParameters.html (accessed September 30, 2025).
[170] R.R. Shen, P. Efsing, Overcoming the drawbacks of plastic strain estimation based on KAM, Ultramicroscopy. 184 (2018) 156–163. https://doi.org/10.1016/j.ultramic.2017.08.013.
[171] MTEX, Subgrain Boundaries, (2024). https://mtex-toolbox.github.io/SubGrainBoundaries.html (accessed September 30, 2025).

[172] MTEX, Grain Shape Parameters - Basic Properties, (2024). https://mtex-toolbox.github.io/ShapeParameters.html (accessed September 30, 2025).
[173] S. Shamsdini, M.H. Ghoncheh, M. Sanjari, H. Pirgazi, B.S. Amirkhiz, L. Kestens, M. Mohammadi, Plastic deformation throughout strain-induced phase transformation in additively manufactured maraging steels, Mater. Des. 198 (2021) 109289. https://doi.org/10.1016/j.matdes.2020.109289.
[174] T. Tekin, G. Ischia, F. Naclerio, R. Ipek, A. Molinari, Effect of a direct aging heat treatment on the microstructure and the tensile properties of a 18Ni-300 maraging steel produced by Laser Powder Bed Fusion, Mater. Sci. Eng. A. 872 (2023) 144921. https://doi.org/10.1016/j.msea.2023.144921.
[175] D. Agius, A. Kareer, A. Al Mamun, C. Truman, D.M. Collins, M. Mostafavi, D. Knowles, A crystal plasticity model that accounts for grain size effects and slip system interactions on the deformation of austenitic stainless steels, Int. J. Plast. 152 (2022) 103249. https://doi.org/10.1016/j.ijplas.2022.103249.
[176] Z. Xiong, I. Timokhina, E. Pereloma, Clustering, nano-scale precipitation and strengthening of steels, Prog. Mater. Sci. 118 (2021) 100764. https://doi.org/10.1016/j.pmatsci.2020.100764.
[177] J.H.K. Tan, S.L. Sing, W.Y. Yeong, Microstructure modelling for metallic additive manufacturing: a review, Virtual Phys. Prototyp. 15 (2020) 87–105. https://doi.org/10.1080/17452759.2019.1677345.
[178] V.P. Narayana Samy, M. Schäfle, F. Brasche, U. Krupp, C. Haase, Understanding the mechanism of columnar–to-equiaxed transition and grain refinement in additively manufactured steel during laser powder bed fusion, Addit. Manuf. 73 (2023) 103702. https://doi.org/10.1016/j.addma.2023.103702.
[179] J. Hebert, M. Khonsari, The application of digital image correlation (DIC) in fatigue experimentation: A review, Fatigue Fract. Eng. Mater. Struct. 46 (2023) 1256–1299. https://doi.org/10.1111/ffe.13931.
[180] W.-N. Hsu, E. Polatidis, M. Šmíd, N. Casati, S. Van Petegem, H. Van Swygenhoven, Load path change on superelastic NiTi alloys: In situ synchrotron XRD and SEM DIC, Acta Mater. 144 (2018) 874–883. https://doi.org/10.1016/j.actamat.2017.11.035.